2015

Behavior of hollow-core fiber reinforced polymer-concrete-steel bridge columns under extreme loading

Omar I. Abdelkarim

BEHAVIOR OF HOLLOW-CORE FIBER REINFORCED POLYMER-CONCRETE-STEEL BRIDGE COLUMNS UNDER EXTREME LOADING

by

OMAR I. ABDELKARIM

A DISSERTATION

Presented to the Faculty of the Graduate School of the

MISSOURI UNIVERSITY OF SCIENCE AND TECHNOLOGY

In Partial Fulfillment of the Requirements for the Degree

DOCTOR OF PHILOSOPHY

in

CIVIL ENGINEERING

2015

Approved by:

Mohamed A. ElGawady, Advisor
Roger A. LaBoube
Kamal H. Khayat
Lesley H. Sneed
K. Chandrashekhara

PUBLICATION DISSERTATION OPTION

This dissertation has been prepared in the style such that the individual sections may be submitted for publication in the *Journal of Structural Engineering, Journal of Composites for Construction,* and *Journal of Bridge Engineering* published by the American Society of Civil Engineers (ASCE), the *Journal of Composites Part B: Engineering* published by ELSEVIER, and the *Journal of ACI special publication* published by American Concrete Institute (ACI).

Paper I (pages 20-66) is a manuscript entitled "Behavior of Hollow-Core FRP-Concrete-Steel Columns under Static Cyclic Axial Compressive Loading." This manuscript was submitted for publication in the *Journal of Composites Part B: Engineering*.

Paper II (pages 67-109) is a manuscript entitled "Analytical and Finite-Element Modeling of FRP-Concrete-Steel Double-Skin Tubular Columns." This manuscript was published in the *Journal of ASCE Bridge Engineering.*

Paper III (pages 110-154) is a manuscript entitled "Behavior of Hollow-Core FRP-Concrete-Steel Columns under Static Cyclic Flexural Loading." This manuscript was submitted for publication in the *Journal of ASCE Composites for Construction*.

Paper IV (pages 155-204) is a manuscript entitled "Seismic Performance of Innovative Hollow-Core FRP-Concrete-Steel Bridge Columns." This manuscript was submitted for publication in the *Journal of ASCE Bridge Engineering.*

Paper V (pages 205-242) is a manuscript entitled "Hollow-Core FRP-Concrete-Steel Tubular Columns Subjected to Seismic Loading." This manuscript was submitted for publication in the *Journal of ACI Special Publication*.

Paper VI (pages 243-294) is a manuscript entitled “Analyses of Reinforced Concrete Bridge Columns Subjected to Vehicle Collisions.” This manuscript was submitted for publication in the *Journal of ASCE Bridge Engineering*.

Paper VII (pages 295-347) is a manuscript entitled “Hollow-Core FRP-Concrete-Steel Bridge Columns Subjected to Vehicle Collision.” This manuscript was submitted for publication in the *Journal of ASCE Structural Engineering*.

ABSTRACT

This study introduces an investigation of the behavior of innovative, resilient, and quickly-constructed hollow-core fiber reinforced polymer-concrete-steel (HC-FCS) bridge columns under extreme loading. The HC-FCS column consists of a concrete wall sandwiched between an outer fiber reinforced polymer (FRP) tube and an inner steel tube. The steel tube was embedded into a reinforced concrete footing with an embedded length of 1.6-1.8 times the diameter of the steel tube. The FRP tube only confined the concrete wall and truncated at the top of the footing level. The hollow steel tube was the only reinforcement for shear and flexure inside the HC-FCS column. The steel and FRP tubes act together as stay-in-place formworks. The results obtained from testing the HC-FCS columns under seismic loading have been compared with those from testing the conventional reinforced concrete (RC) column. Results showed that the HC-FCS column exhibited a high lateral drift reaching 15.2%, while the well-detailed solid cross-section RC column reached a drift of 10.9%. The HC-FCS column dissipated energy reaching 1.9 times that of the RC column. A simple analytical model and preliminary design guidelines were presented to help implement this new technology. Vehicle collision with RC and HC-FCS bridge columns was also presented in this study using LS-DYNA software. The first equation for estimating the equivalent static force of the vehicle collision, based on the vehicle's mass and velocity, was developed. This approach will allow departments of transportation (DOTs) to design different bridge columns for different impact force demands depending on the anticipated truck loads and velocities from roads survey. In general, the peak dynamic force values of the HC-FCS columns were lower than those of the RC columns when they were subjected to vehicle collision, which could save lives and reduce damage to the bridge column and the vehicle.

ACKNOWLEDGMENTS

First and above all, I praise God, the almighty, for providing me this opportunity and granting me the capability to proceed successfully. I am deeply indebted to my advisor, Dr. Mohamed ElGawady, for his great advising to my doctoral work. Dr. ElGawady provided me with every bit of guidance, assistance, and expertise that I needed. He encouraged me to work hard. This study would not have been as enjoyable as it was without his great help, advising, motivation, and encouragement. Words cannot express how grateful I am to have such an amazing advisor.

I would like to thank the members of my advisory committee: Dr. Roger LaBoube, Dr. Kamal Khayat, Dr. Lesley Sneed, and Dr. K. Chandrashekhara. Each member provided valuable knowledge, great technical experience, and suggestions that continuously improved my knowledge and understanding.

I would also like to acknowledge my fellow graduate students in the civil department: Sujith Anumolu, Ahmed Gheni, and Mohanad Abdulazeez. Thanks also go to the civil department staff: Brian Swift, Gary Abbott, John Bullock, and Scott Parker. They offered a tremendous amount of technical assistance and support.

I could not have survived the duration of this study without my family. I would like to thank my mother for providing me with her love and prayers. I would like to thank my first tutor, “my father” who taught me a lot in my life. I would also like to thank my brothers and sisters for their love, support, and encouragement. I want to express my gratitude and deepest appreciation to my lovely wife for her great patience and understanding. I am sure that without her support and encouragement, I could not have finished this work.

TABLE OF CONTENTS

LIST OF ILLUSTRATIONS

Page

PAPER II

PAPER III

PAPER IV

PAPER V

PAPER VI

PAPER VII

LIST OF TABLES

Page

PAPER I

PAPER II

PAPER III

PAPER IV

PAPER V

PAPER VI

PAPER VII

SECTION

1. INTRODUCTION

1.1. RESEARCH OVERVIEW

A significant amount of research has recently been devoted to developing new materials and construction methods for cost-effective accelerated bridge construction (ABC) systems. The ABC systems improve site constructability, reduce total project delivery time, enhance work zone safety for the traveling public, reduce traffic disruptions, and reduce life-cycle costs. This research introduces an innovative, resilient, durable, and quickly-constructed hollow-core fiber reinforced polymer-concrete-steel (HC-FCS) bridge column. The cross-section of the HC-FCS column consists of a concrete shell sandwiched between an inner steel tube and an outer fiber reinforced polymer (FRP) tube (Figure 1.1).

The HC-FCS column has several distinct advantages over the conventional column constructed out of reinforced concrete (RC). The HC-FCS column uses 60 to 75% less concrete material since it has a hollow core. The HC-FCS column needs 90% less construction time. The HC-FCS column also requires a lower freight cost when implemented with precast construction. The inner steel and outer FRP tubes provide continuous confinement for the concrete shell; hence, the concrete shell achieves significantly higher strain, strength, and ductility compared to the unconfined concrete of the conventional column. The HC-FCS column represents a compact engineering system; the steel and FRP tubes act together as stay-in-place formworks. The steel tube acts as a flexural and shear reinforcement. Due to the protection afforded by the corrosion-free

outer FRP tube and concrete core, the HC-FCS column has high corrosion resistance. This research investigates the HC-FCS column under extreme loading (seismic and impact loadings) and compares the results with those of the conventional columns.

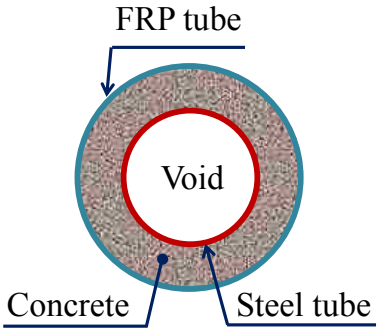

Figure 1.1. HC-FCS column's cross-section

Accidents can have serious repercussions with regard to both human life and transportation systems. These collisions often result in either a complete or partial bridge collapse. Many vehicle collision events involving bridge piers have been reported throughout the United States. Harik et al. (1990) explained that 14% of bridge failures reported in the United States between the years of 1951 and 1988 were the result of truck collisions. Lee et al. (2013) stated that vehicle collision was the third cause of bridge failures in the United States between the years of 1980 and 2012 as it was the reason of approximately 15% of bridge failures during this period. The constant impact load used in the current American Association of State Highway and Transportation Officials Load

and Resistance Factor Bridge Design Specifications (AASHTO-LRFD 2012) does not consider the vehicle's mass or the vehicle's velocity. Hence, it may be anticipated that the impact load given by AASHTO-LRFD will be conservative in some occasions and unconservative in other occasions. This research also proposes the first equation to directly calculate the impact load, given a vehicle's mass and velocity, without the need to run a crash analysis based on conducted parametric studies. This approach will allow departments of transportation (DOTs) to design different bridge columns according to different impact force demands dependent on the anticipated truck loads and velocities for a specific road.

1.2. OBJECTIVES

1. To identify the strength and ductility of the HC-FCS columns under seismic loading
2. To propose preliminary design of the HC-FCS columns under seismic loading
3. To propose new equations to design the bridge columns under vehicle collision
4. To compare the behavior of the HC-FCS columns with well detailed solid reinforced concrete (RC) columns under extreme loading

1.3. METHODOLOGY

This research investigates the behavior of the HC-FCS columns under extreme loading, starting with studying their constitutive models. HC-FCS columns were preliminarily designed using finite element and analytical models. Four large-scale HC-

FCS columns and one conventional RC-column were tested under seismic loading. An extensive finite element parametric study was conducted to better understand the behavior of the HC-FCS columns under seismic loading. Moreover, impact analysis was conducted to investigate the behavior of the HC-FCS and conventional RC columns under vehicle impact. The behavior of the HC-FCS columns under extreme loadings is compared to those of conventional RC columns having solid cross sections. Finally, design guidelines for the HC-FCS columns under seismic loading are introduced. This research also proposes the first design equation to predict the impact load of vehicle collision with bridge columns. Figure 1.2 illustrates the interaction between the research tasks through a flowchart.

1.4. RESEARCH TASKS

Task 1: Conducting a literature review

The purpose of this task is to collect the data from related previous studies.

Task 2: Investigating experimentally small-scale HC-FCS columns under static axial loading

The purpose of this task is to investigate important parameters that may affect the behavior of the HC-FCS columns under axial loading. Thirteen small-scale columns were tested during this study.

Task 3: Investigating experimentally large-scale columns under seismic loading

The purpose of this task is to study the behavior of large-scale HC-FCS columns under seismic loading. Important construction details were investigated as well to help

implementing this new technology. Five large-scale columns were tested as free cantilevers under seismic loading. The first column was a conventional RC column and the others were HC-FCS columns.

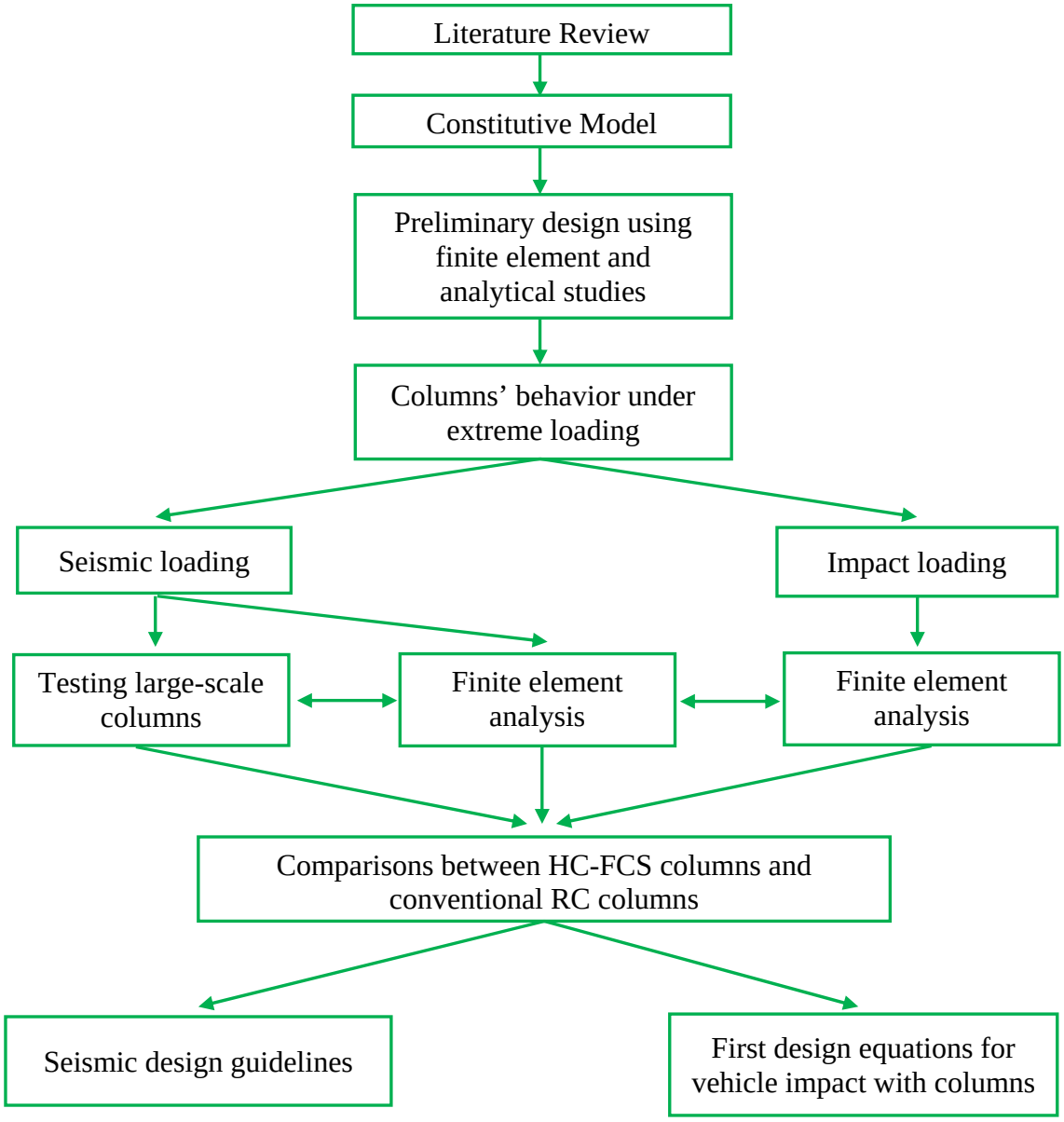

Figure 1.2. Flowchart of the research plan

Task 4: Investigating the rapid repair of large-scale HC-FCS columns

The purpose of this task is to investigate whether the new system is repairable. During this research, after one of HC-FCS columns was tested, the specimen was repaired and retested under seismic loading. This research proposed a rapid repair technique that could be completed in 6 hours.

Task 5: Conducting a finite element parametric study on HC-FCS columns under seismic loading

The purpose of this task is to better understand the behavior of the HC-FCS columns under seismic loading and to identify the factors affecting their behavior. LS-DYNA software was used to conduct the parametric study. Fifty columns were investigated during this study.

Task 6: Investigating numerically full-scale RC columns under vehicle impact

The purpose of this task is to cover a wide spectrum of parameters that would affect the behavior of the conventional RC columns under vehicle impact. Most of the investigated parameters have not been addressed in previous studies. Fifty full-scale columns were investigated during this study. LS-DYNA software was used to conduct the parametric study.

Task 7: Investigating numerically full-scale HC-FCS columns under vehicle impact

The purpose of this task is to investigate the behavior of the HC-FCS columns under vehicle impact. An extensive parametric study was conducted to investigate the effect of important parameters on the HC-FCS columns' behavior under vehicle impact.

Thirty-four full-scale columns were investigated during this study. LS-DYNA software was used during this study.

Task 8: Comparing RC and HC-FCS columns under extreme loading

The purpose of this task is to identify the efficiency of the HC-FCS columns comparable to the conventional RC columns under extreme loading (seismic and impact loadings).

Task 9: Exploring preliminary design guidelines for HC-FCS columns under seismic loading

The purpose of this task is to explore preliminary design guidelines for the selection of the HC-FCS columns' dimensions and to explain the procedure used to calculate their flexural strength.

Task 10: Proposing design equations for bridge columns under vehicle impact

This research proposes the first equation that can be used to directly calculate the impact load of the vehicle collision, given the vehicle's mass and velocity, without the need to run a crash analysis. This equation is based on the conducted parametric studies.

2. LITERATURE REVIEW

2.1. CONCRETE-FILLED TUBE COLUMNS

Concrete-filled steel tubes (CFSTs) are widely used in Japan, China, and Europe to work as bridge columns that not only accelerate construction but also obtain superior seismic performance. In the US., CFSTs are used as piles and bridge piers. Their applications, however, are limited because of inconsistent design code provisions (Moon et al. 2013). Incorporated CFST members have several advantages over either steel or reinforced concrete (RC) members. The steel tubes act as a stay-in-place formwork, flexural and shear reinforcement, and a confinement to the inside concrete core, increasing the member's ductility and strength. The tubes prevent concrete spalling so that the concrete core continues to function as a bracing for the steel tube. Therefore, the concrete core delays both local and global buckling under compression loads (Hajjar 2000).

The CFST members dissipate more energy than those made from either traditional steel or RC members. On a strength-per-dollar basis, CFST members are cheaper than traditional steel members; they are comparable in price to traditional RC members. A concrete core can be reinforced with steel rebar to further improve the member's performance while facilitating connections to other members. However, limited performance data is available for steel rebar reinforced CFST columns (Moon et al. 2013; Hajjar 2000).

FRP tubes have gained acceptance as an alternative to steel tubes in concrete-filled tubes. Concrete-filled fiber tubes (CFFT) have benefits that are similar to those of CFSTs. However, unlike steel tubes, FRP tubes have a lighter weight-to-strength ratio

and a higher corrosion resistance than steel tubes. Several researchers investigated the seismic behavior of CFFT columns (Zhu et al. 2006). Shin and Andrawes (2010) investigated the behavior of CFFTs that were confined by a shape memory alloy. ElGawady et al. (2010) and ElGawady and Sha'lan (2011) conducted static cyclic tests on both segmental precast post-tensioned CFFT columns and two-column bents. Upon conducting finite element analysis, ElGawady and Dawood (2012) and Dawood and ElGawady (2013) developed a design procedure for precast post-tensioned CFFTs.

2.2. HOLLOW-CORE COLUMNS

Hollow-core concrete columns are often used for very tall bridge columns in seismic areas including California, New Zealand, Japan, and Italy. Hollow-core cross-sections reduce the mass of the column which reduces the bridge self-weight contribution to the inertial mode of vibration during an earthquake. The hollow-core columns also reduce the foundation dimensions, thereby reducing the construction costs substantially. These advantages have increased the use of hollow-core columns instead of similar solid members. Hollow-core reinforced concrete columns have been investigated (Lee et al. 2014; Hoshikuma and Priestley 2000; Mander et al. 1983).

Mander et al. (1983) investigated hollow-core concrete columns that have two layers of longitudinal and transverse reinforcement placed near in-/outside faces and cross ties placed throughout the wall's thickness (Figure 2.1). These columns can exhibit a ductile behavior (Figure 2.2). However, they increase the labor cost making them a non-cost-effective construction option.

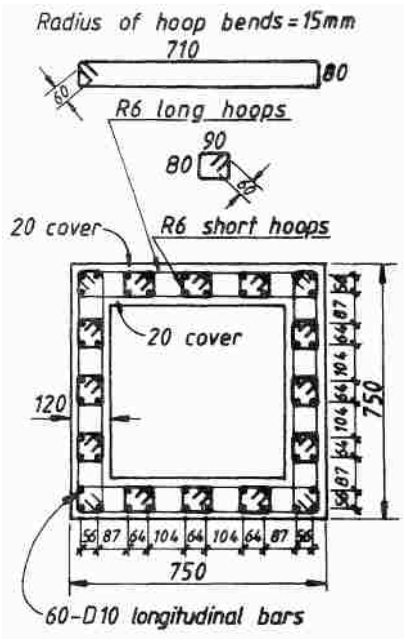

Figure 2.1. Cross-section of the hollow-core concrete column with two layers of reinforcement (Mander et al. 1983)

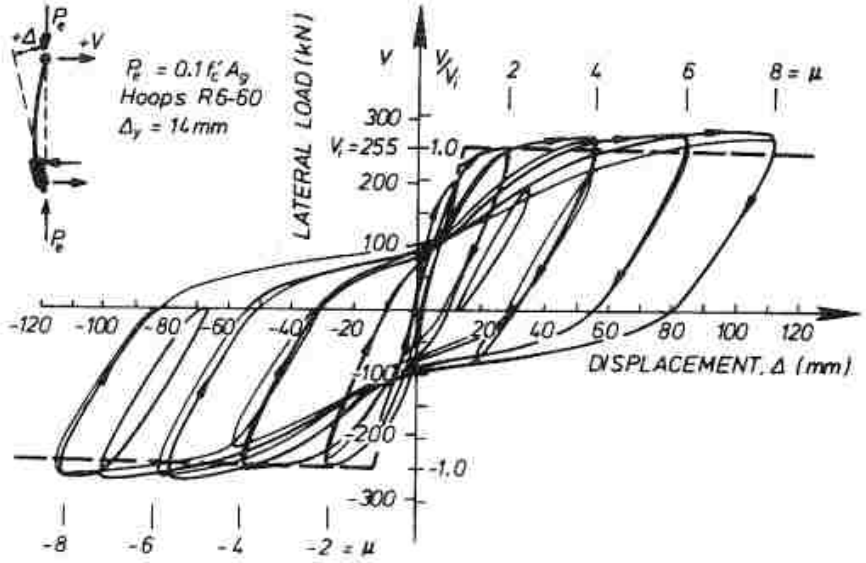

Figure 2.2. Load-displacement relationship of the hollow-core concrete column with two layers of reinforcement (Mander et al. 1983)

Hoshikuma and Priestley (2000) investigated hollow-core concrete columns that contain one layer of longitudinal reinforcement (Figure 2.3). The peak lateral force occurred at a ductility of approximately 2.0. It dropped significantly at a ductility of 3.5 in the push direction (where the inside concrete was crushed, see Figure 2.4). The lateral force began to deteriorate at a ductility of 3.3 in the pull direction. Both test observations and experimental hysteretic responses indicated that the failure that occurred inside the face concrete severely degraded the response. Therefore, the ultimate ductility capacity was 3.3, providing a 50% reserve of displacement capacity. This study indicated that a deficiency of the hollow-core concrete columns with one layer reinforcement is the low curvature ductility due to early concrete spalling because of the void.

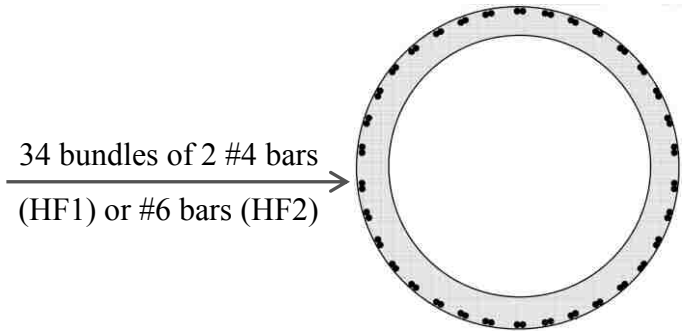

Figure 2.3. Cross-section of the hollow-core concrete column with one layer of reinforcement (Hoshikuma and Priestley 2000)

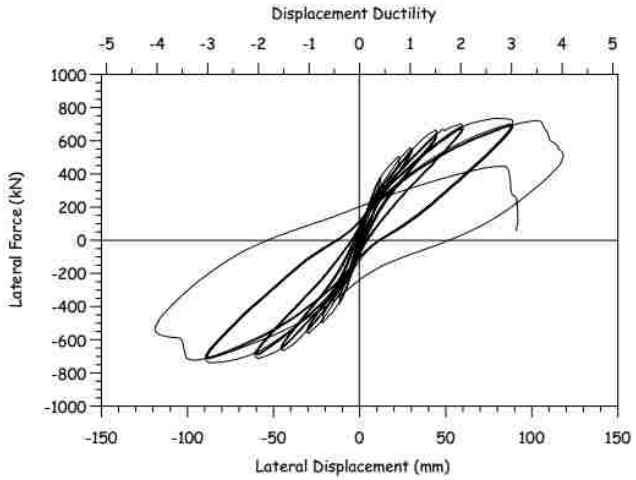

Figure 2.4. Load-displacement relationship of the hollow-core concrete column with one layers of reinforcement (Hoshikuma and Priestley 2000)

Montague (1978) combined the benefits of concrete-filled tube columns with the benefits of hollow-core concrete columns to develop a double-skin tubular column (DSTC). These columns consist of a concrete wall that is sandwiched between two generally concentric steel tubes; they have been studied extensively in Asia (Huang et al. 2013; Yagishita 2000; Shakir-Khalil & Illouli 1987). More recently, Teng et al. (2004) used FRP as an outer tube and steel as an inner tube in the double-skin tubular elements. This system combines and optimizes the benefits of all three materials; FRP, concrete, and steel, in addition to the benefits of the hollow-core concrete columns to introduce hollow-core FRP-concrete-steel columns (HC-FCS).

A number of investigators have studied the behavior of HC-FCS columns, in the form of beams and columns, under different static and cyclic loading conditions (Teng et al. 2005, 2007; Yu et al. 2006, 2010; Wong et al. 2008; Abdelkarim and ElGawady 2014a; Abdelkarim and ElGawady 2014b). The results of the experimental tests

conducted under axial compression, flexure, and a combination of axial compression and flexure showed high concrete confinement and ductility (e.g., see Figures 2.5 and 2.6).

Han et al. (2010) tested HC-FCSs in a beam-column arrangement, under cyclic flexural loading, with constant axial compression loading. The column's elastic stiffness increased as the applied axial load increased. The post-elastic stiffness increased as the FRP stiffness increased. The elastic stiffness, however, did not increase. The column's residual bending strength (after the FRP ruptured) increased as the applied axial load level increased. Zhang et al. (2012) and Ozbakkaloglu and Idris (2014) investigated the behavior of small-scale HC-FCSs under combined axial compression and lateral cyclic loading. These previous studies were carried out on small-scale specimens using manual wet layup unidirectional FRP, a low diameter-to-thickness (D_i/t_s) ratio of the steel tube (e.g., $D_i/t_s = 35$), and thick concrete wall thickness (i.e., low void ratio). The results of the studies showed high concrete confinement and ductility of the HC-FCS columns under axial compression or flexure loading.

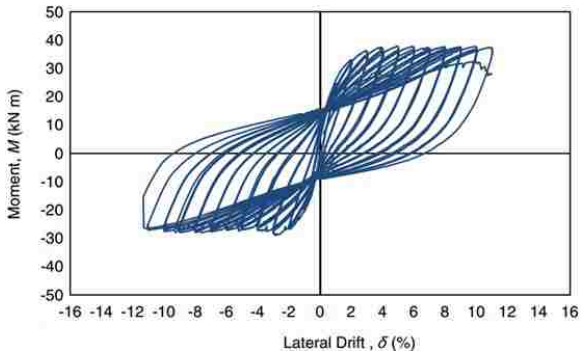

Figure 2.5. Moment-lateral drift relationship of HC-FCS column (Ozbakkaloglu and Idris 2014)

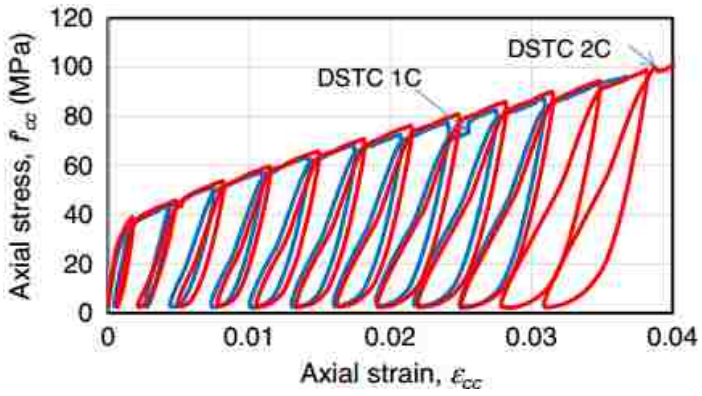

Figure 2.6. Axial strain-axial stress relationship of HC-FCS column (Albitar et al. 2013)

2.3. IMPACT ANALYSIS OF VEHICLE COLLISION

The accidents can have serious implications with regard to not only human lives but also transportation systems. Harik et al. (1990) reported that 17 of the 114 bridge failures reported in the United States were the result of truck collisions over the period of 1951-1988. Many vehicle collision events involving bridge piers have been reported throughout the US. In July 1994, a tractor cargo-tank semitrailer hit a road guardrail, and the cargo tank collided into a column of the Grant Avenue overpass over Interstate 287 in White Plains, New York (Agrawal 2011). Twenty-three people were injured, the driver was killed, and a fire was extended over a radius of approximately 400 ft. In 2008, a tractor trailer driving at a high rate of speed collided with a bridge pier on IH-30 near Mount Pleasant, Texas (Figure 2.7; Buth et al. 2010). The bridge pier consisted of three columns. These columns had 30-inch diameters, longitudinal reinforcements of 8#9, and #3 spiral stirrups with a 6 in pitch. Although this bridge did not collapse entirely, one column did fail. Another example is the two trains that collided at a rail intersection just

outside of Scott City in southeast Missouri in May of 2013. Numerous train cars were derailed, and seven people were injured (Figure 2.8). The derailed cars hit a highway overpass, causing it to collapse. The preliminary estimated cost to replace the overpass was approximately $3 million (McGrath 2013).

Figure 2.7. Truck-tractor-trailer accident–FM 1401 Bridge, Texas, 2008 (Buth et al. 2010)

Figure 2.8. Trains accident-overpass outside of Scott City, Missouri, 2013 (McGrath 2013)

According to the American Association of State Highway and Transportation Officials- *Load and Resistance Factor Design* (*AASHTO-LRFD*) *Bridge Design Specifications,* abutments and piers located within a distance of 30 ft from the roadway edge should be designed to allow for a collision load. AASHTO-LRFD *Bridge Design Specifications,* 5th edition, required the collision load to be an equivalent static force (ESF) of 400 kips (1800 kN). El-Tawil et al. (2005) used the commercial software LS-DYNA to numerically examine two bridge piers impacted by both Chevrolet pickup trucks and Ford single unit trucks (SUTs). Data was collected from structural plans on vulnerable bridges currently in use in Florida. Four different velocities were studied: 34 mph, 56 mph, 69 mph, and 84 mph. The ESF was calculated to produce the same deflection at the point of interest as that caused by the impact force. These results suggested that the AASHTO-LRFD could be unconservative and that the ESF should be higher than 400 kips.

Buth et al. (2010, 2011) studied the collision of large trucks, SUTs, and tractor-trailers with bridge piers. This study included not only experimental work but also finite element analysis (FEA) conducted with LS-DYNA. The experimental work investigated the collision of a tractor trailer into a rigid column constrained at both the top and the bottom. FEA was used to conduct a parametric study on SUTs. The data from this study has been used to suggest that the design guidelines for vehicle collisions with bridges be changed. The design requirements were updated in the 6th edition of AASHTO-LRFD *Bridge Design Specifications* (2012) as follows: “abutments and piers located within a distance of 30.0 ft to the edge of roadway shall be investigated for collision” and “the design choice is to provide structural resistance. The pier or abutment shall be designed

for an equivalent static force of 600 kip, which is assumed to act in a direction of zero to 15 degrees with the edge of the pavement in a horizontal plane, at a distance of 5.0 ft above ground."

Experiments conducted on vehicle collisions with concrete columns are both difficult and expansive to perform. FEA is considered an attractive approach because it is cheap, trustable (because lots of validations were done), and easy to implement. Numerous researchers have used LS-DYNA software to investigate the modeling of concrete columns under extreme loading (Abdelkarim and ElGawady 2014b; Sharma et al. 2012; Fouche and Bruneau 2010; Thilakarathna et al. 2010).

Sharma et al. (2012) used a performance-based response to investigate the effect of a vehicle's impact on a reinforced concrete column. They suggested that four different damage levels and three different performance levels be used to evaluate the column's response. Agrawal et al. (2013) investigated the effects of different seismic design details on a pier's response to vehicle impact loading. They proposed that a new procedure be used to calculate the ESF; this procedure is based on the vehicle's mass and velocity. A proposed equation was used to calculate the PDF. The ESF was calculated by dividing the calculated PDF by the damage ratio (which is dependent on the required performance level being 2, 5, and > 5 for minor, moderate, and high damage levels, respectively). This procedure produced variable values of ESF rather than the constant ESF recommended by AASHTO-LRFD.

No consensus exists among researchers with regard to calculating an ESF from a PDF. Three approaches to investigating the ESF were considered during the course of this research. In the first approach (SB_{ESF}; Stiffness-Based ESF) the ESF was defined as

the force needed to produce the same maximum displacement by a collision event at the point of impact (El-Tawil et al. 2005). In the second approach (EC_{ESF}; EuroCode ESF) the ESF was calculated by a Eurocode:

$$ESF = \frac{KE}{\delta_c + \delta_d} \tag{2.1}$$

$$KE = \frac{1}{2}\, m\, v_r^2 \tag{2.2}$$

where KE is the vehicle's kinetic energy, m = the vehicle's mass, v_r = the vehicle's velocity, δ_c = the vehicle's deformation, and δ_d = the column's deformation. The third approach (PTMSA; Peak of Twenty-five Milli Second moving Average) recommended by Buth et al. (2011), referenced to the 50 millisecond moving average frequently used in automotive crash analyses.

2.4. CLASSIFICATION OF IMPACT

The material response under external loading could be defined by both the loading time and the strain rate. The strain rate is the change in a material's strain with regard to time. Sierakowsi and Chaturved (1997) stated that the static load typically occurs within a time duration that is more than 10^4-10^6 seconds and a strain rate that is lower than 10^{-8}-10^{-6} s^{-1}. However, the impact load typically occurs within a time duration that is between 10^{-6} and 10^{-4} and a strain rate that is between 10^2 and 10^4 s^{-1}.

The structural system's response could be defined by the pulse duration relative to the structure's natural period. If the pulse duration is lower than a quarter of the

structure's natural period, the system's response is impacted. However, if the pulse duration is larger than four times the structure's natural period, the system's response is quasi-static.

In a vehicle collision event with bridge piers, the bridge pier (the body that is struck) is considered to be the target while the vehicle (the body that impacts the target) is considered to be the projectile. The collision's relative degree of softness/hardness classifies the type of impact that occurs. Therefore, the impact type can be classified by the projectile/target interaction into the following categories: hard/soft, hard/hard, soft/hard, and soft/soft. This classification significantly affects the induced dynamic contact force between the projectile and the target. If a soft projectile interacts with a rigid target, the stress waves propagate within the projectile upon contact, damaging the projectile. When this interaction occurs, the projectile absorbs most of the impact's kinetic energy in the form of plastic deformation. If a hard projectile interacts with a soft target, the stress waves propagate within the target upon contact. Hence, the target absorbs most of the impact's kinetic energy in the form of plastic deformation. Consequently, absorbing the kinetic energy from the projectile's mass and velocity is the key parameter when preparing the impact analysis.

PAPER

I. BEHAVIOR OF HOLLOW-CORE FRP-CONCRETE-STEEL COLUMNS UNDER STATIC CYCLIC AXIAL COMPRESSIVE LOADING

Omar I. Abdelkarim [a], S.M. ASCE; Mohamed A. ElGawady [b,*]

a Ph.D. Candidate, Dept. of Civil, Architectural, and Environmental Engineering, Missouri University of Science and Technology, Rolla, MO. 65401; oiafgc@mail.mst.edu
b Benavides Associate Professor, Dept. of Civil, Architectural, and Environmental Engineering, Missouri University of Science and Technology, Rolla, MO. 65401; elgawadym@mst.edu

ABSTRACT

This paper presents the behavior of hollow-core fiber reinforced polymer-concrete-steel (HC-FCS) columns under axial compressive loading. The typical HC-FCS column consists of a concrete wall sandwiched between an outer fiber reinforced polymer (FRP) tube and an inner steel tube. The inner steel and outer FRP tubes provide continuous confinement for the concrete shell; hence, the concrete shell achieves a significantly higher strain, strength, and ductility compared to the unconfined concrete in conventional columns. The HC-FCS column represents a compact engineering system; the steel and FRP tubes act together as stay-in-place formworks. The effect of the fiber orientation and the steel tube diameter-to-thickness ratio (D_i/t_s) on the compressive behavior of HC-FCS columns was investigated. Ten HC-FCS cylinders with different steel tube D_i/t_s ratios and three concrete-filled fiber tubular (CFFT) cylinders were manufactured and tested under static cyclic axial compressive loading. The behavior of the HC-FCS columns was complicated and related mainly to the stiffness of the FRP and steel tubes which controlled the direction of the concrete dilation under axial load. HC-FCS columns with FRP tubes made with fibers oriented at $\pm$ 45° showed a low axial compressive strength

and a high ultimate strain. HC-FCS columns with wet lay-up FRP tubes that had ±45° and 0° (hybrid FRP) exhibited high axial strengths and strains. The failure of the HC-FCS columns with hybrid FRP tubes consisted of two stages. The first stage was the rupture of the unidirectional FRP (outer tube), and the second stage was the reorientation of the angle-plied FRP exhibiting high axial strains.

Keywords: Bridge Columns, Precast Columns, Composite Columns, Hollow Columns, Axial Loading

1. Introduction

Recently, a significant amount of research has been devoted to developing accelerated bridge construction (ABC) systems. Concrete-filled steel tubes (CFST) are widely used as bridge columns in Japan, China, and Europe to not only accelerate construction but also to obtain superior seismic performance. In the U.S., CFSTs are also used as piles and bridge piers. Their application, however, is limited, primarily as a result of inconsistent design code provisions [1]. Incorporated CFST members have several advantages over both steel and reinforced concrete (RC) members. The steel tubes act as a stay-in-place formwork, a shear reinforcement, and a confinement to the inside concrete core, increasing the member's ductility and strength. The tubes prevent concrete spalling so that the concrete core continues act as bracing for the steel tube. Therefore, the concrete core delays the local and global buckling under compression loads [2].

In the last few decades, concrete-filled fiber tubes (CFFT) have been employed widely in the U.S., Japan, China, and Europe. CFFTs have many benefits, including light weight-to-strength ratio, high confinement, and corrosion resistance. The seismic behavior of the CFFT columns has been studied extensively [e.g., 3, 4]. Dawood et al.

[5], ElGawady and Sha'lan [6], and ElGawady et al. [7] studied the CFFT columns under seismic loading as well.

Hollow-core concrete columns have been utilized for very tall bridge columns in seismic areas including New Zealand, Japan, and Italy. The use of hollow-core cross-sections reduces the mass of the column, which in turn reduces the self-weight of the bridge that contributes the inertial forces. Hollow-core columns also reduce the required foundation dimensions substantially, thereby lowering the construction costs.

Recently, Teng et al. [8] combined hollow-core columns with concrete-filled tube columns to create hollow-core FRP-concrete-steel columns (HC-FCS). An HC-FCS column consists of an outer FRP tube and an inner steel tube sandwiching a concrete shell between them. This system combines and optimizes the benefits of all three materials, FRP, concrete, and steel, in addition to the existing benefits of the hollow-core concrete columns. The HC-FCS columns have been investigated extensively under axial compression loading [9-14]. The results of the axial compression experiments showed high concrete confinement and ductility. However, these studies were conducted using unidirectional FRP tubes steel tubes with a low diameter-to-thickness ratio.

In an HC-FCS system, the concrete wall between the outer FRP tube and the inner steel tube is usually thin. Self-consolidating concrete (SCC) represents a good option for preventing honeycomb and lessening the problem of consolidating and vibrating concrete. SCC has a high flowability and a moderate viscosity, giving it the ability to self-consolidate. A balance between dosages of superplasticizers or high range water reducers (HRWR) must be achieved to increase the flowability and dosages of viscosity modifying agents (VMA) to enhance stability and reduce segregation [15].

2. Research significance

This paper investigates the behavior of the HC-FCS columns under cyclic axial compressive loading. The HC-FCS column has several benefits such as its use of 60 to 75% less concrete material than the solid cross-sectional column, the steel and FRP tubes acting together as stay-in-place formworks. The corrosion-free outer tube and concrete core provide the HC-FCS with high corrosion resistance. However, the inner steel tube may require additional corrosion protection from an anti-corrosion agent similar to those used in concrete-filled steel tubes. The FRP and steel tubes protect the concrete core from shrinkage, as they do not absorb any water. The investigated HC-FCS columns were constructed with a thin to thick concrete wall thickness (25% to 38% of the column diameter), low to high diameter-to-thickness ratios of the steel tube (D_i/t_s = 32 to 64), and low to high FRP confinement. The fiber direction and hybrid FRP system were investigated as well.

3. Experimental program

3.1. Test specimens

A total of 10 HC-FCS and 3 CFFT cylinders were manufactured and tested under cyclic axial compressive loading. All of the tested specimens had an outer diameter of 210 mm and a height of 406 mm (Fig. 1, and Table 1). The thirteen specimens were sorted in four groups. The specimen's label used in the current study consists of four syllabi. The first syllabus is referring to the type of the specimen where "HC" refers to the HC-FCS cylinders and "CFFT" refers to concrete-filled fiber tubes. The second

syllabus refers to the type of FRP, where "C" is for carbon and "G" is for glass; this is followed by the number of layers in *Latin* letters and the direction of fibers (45^o or 0^o or a combination). In the case of the combination of angle-plied FRP and the unidirectional FRP, the unidirectional FRP was always in the outer surface. The third syllabus refers to the percent of the concrete wall thickness relative to the outer diameter. The fourth syllabus refers to the diameter-to-thickness (D_i/t_s) ratio of the steel tube. The third and fourth syllabi do not exist in the case of the CFFTs.

Group (A) consisted of three HC-FCS cylinders and one CFFT cylinder. The FRP tubes of this group were made of three layers of $\pm 45^o$ carbon fibers, while the steel tubes of the HC-FCS cylinders had diameters of 101.6 mm, 76.2 mm, and 50.8 mm with diameter-to-thickness (D_i/t_s) ratios of 64, 38, and 32, respectively. Group (B) consisted of three HC-FCS cylinders and one CFFT cylinder. The FRP tubes of this group were made of three layers of $\pm 45^o$ glass fibers, while the steel tubes of the HC-FCS cylinders were same as in Group (A). Group (C) consisted of three HC-FCS cylinders and one CFFT cylinder.

The FRP tubes of this group were made of two layers of $\pm 45^o$ glass fibers and one layer of unidirectional glass fiber, while the steel tubes of the HC-FCS cylinders were same as in Group (A). Group (D) consisted of one HC-FCS cylinder that had an FRP tube made of one layer of $\pm 45^o$ glass fibers and two layers of unidirectional glass fiber, while the steel tube had a diameter of 101.6 mm with D_i/t_s of 64. All of the FRP tubes were prepared manually by a wet-layup process on sonotube and were used as a mold for concrete pouring. The last wrapped layer of the FRP tube was provided with 30% overlap to prevent premature debonding failure.

3.2. Material properties

Table 2 shows the mix design of the SCC that was used. The average cylindrical concrete compressive strength (f_c') at 56 days was 55 MPa.

According to ASTM D3039 [16], longitudinal and radial coupons with widths of 25 mm were cut from a one-layer FRP tube. One horizontal and one vertical strain gauge were attached to the mid height of the longitudinal FRP coupon, as shown in Fig. 2(a). Two strain gauges were attached to the middle of the radial disk, as shown in Fig. 2(b). Under tensile tests with a displacement loading rate of 1.27 mm/min., all of the FRP coupons and radial samples failed by debonding between the two 45^o plies [$\pm 45^o$] without fiber rupture, as shown in Figs. 3c and 3d. The ultimate tensile stress for the specimens was about 73.0 MPa. This low value of the stress was because the saturated FRP tube with a fiber orientation at 45^o had a structure dependent on fibers in two perpendicular directions [$\pm 45^o$] with adhesive material between them. Therefore, this type of laminate would work globally. Also, this type of fibers that oriented at $\pm 45^o$ was non-woven fabric. As a result, the fibers did not work in the samples as the width of the strip was only 25 mm and did not allow fiber continuity. The properties of the FRP tubes are referenced in the manufacturer data sheet and are summarized in Table 3.

Standard coupons were cut longitudinally from a steel tube for tensile tests according to ASTM A1067 [17]. The steel coupon tests were conducted under a displacement control of 0.76 mm/min. A strain gauge was attached to the mid height of the steel coupons (Fig. 3(a)). All steel coupons failed by yielding in the neck (Fig. 3(b)). The

results showed that the yield stress, tensile stress, the Young's modulus, and the ultimate strain of the steel tubes were 620 MPa, 620 MPa, 200 GPa, and 0.4%, respectively.

Three hollow steel tubes similar to those used in the HC-FCS cylinders were tested under monotonic axial compression. Two strain gauges in the hoop direction and two vertical strain gauges were mounted on the outer surfaces of the steel tubes, as shown in Fig. 4. Steel Tube A, of a diameter of 101.6 mm, and Tube B, of a diameter of 76.2 mm, failed at ultimate axial loads of 302 kN and 296 kN, respectively by local buckling in the elephant's foot mode as shown in Figs. 5a and 5b, respectively. This corresponded to maximum stresses of 592 MPa and 617 MPa, respectively (Figs. 6a and 6b, respectively). However, Steel Tube C failed by global buckling and local buckling in the elephant's foot mode as shown in Fig. 5c, at a load of 83 kN corresponding to a stress of 315 MPa (Fig. 6c). The failure load of Tube C was significantly lower than the other tubes because the global buckling occurred early. In general, the behavior of the steel tubes were similar, started with linear behavior till axial compressive strain ranged from 0.4% to 0.5%. After that, the stress hardened with a lower stiffness until the maximum axial stress, and then each steel tube suffered stress softening due to the local or global buckling until the end of the test.

3.3. Instrumentation and test setup

Compression tests were carried out using an MTS machine with a loading rate of 0.5 mm/min. All test data, including the strains, loads, and displacements, were recorded simultaneously using a data acquisition system. Two horizontal and two vertical strain gauges were installed on the outer surface at the mid-height of the FRP tube. Likewise,

two horizontal and two vertical strain gauges were installed on the outer surface at the mid-height of the steel tube. In addition, two string potentiometers were attached on the outer surface of the FRP tube to obtain the axial deformation of the middle region of 140 mm for each specimen. Fig. 7 illustrates the test setup of the investigated cylinders.

3.4. Loading protocol

All specimens were tested under compression loading on a cyclic scheme, as shown in Fig. 8. The cyclic compression involved full loading/unloading cycles, where the unloading of each cycle was designed to terminate at 0.4 kN (near zero) and the reloading of each cycle was designed to terminate at the unloading displacement of the same cycle. The loading scheme followed nine steps, beginning at an axial strain of 0.125%. The axial strain was increased gradually until specimen failure or maximum displacement of the machine, which corresponded to an overall strain of the cylinder of 11.25%. Each loading step was repeated for three cycles.

4. Results and discussions

4.1. General behavior

Figs. 9 to 12 illustrate the axial strain versus axial load hysteretic curves for the specimens of all groups. The axial compressive strains were obtained from the average readings of the two string potentiometers and were represented in (–ve) values.

4.1.1. Group A (three layers of $\pm$ 45 carbon FRP)

The specimens in this group were prepared with carbon FRP tubes with fibers oriented at $\pm 45^{o}$. For the specimen HC-CIII45-25-64, the load increased almost linearly

until the peak axial load of 1,356 kN which was at an axial strain of approximately 0.14% (Fig. 9a). The load softened with increasing the strain directly after the peak axial load without any hardening unlike the regular confined concrete cylinders. This behavior was mainly because of the weak confinement from the [± 45] FRP tube. The axial load dropped to 800 kN with a loss of approximately 41% at an axial strain of 0.02. The load had some hardening after an axial strain of 0.02 until the axial strain of 0.04 where the axial load increased to 910 kN. The load softened again after an axial strain of 0.04 until the axial strain of 0.067 where the axial load dropped to 718 kN. After that, the axial load was almost constant until the maximum displacement applied from the machine without any rupture of the FRP tube (Fig. 13). The specimen reached high axial strains of 0.13 due to the fiber reorientation where the fiber reoriented from 45^{o} toward the 0^{o} direction [18]. The investigation after the test showed that the steel tube severely buckled locally (Fig. 13). The steel tube local buckling was the second reason of the softening of the axial load.

For the specimen HC-CIII45-32-38, the load increased almost linearly until the peak axial load of 1,610 kN which was at an axial strain of approximately 0.5% (Fig. 9b). The softening occurred after that until the ultimate axial strain of 0.06 where the axial load dropped to almost 800 kN at the maximum displacement applied from the machine without any rupture of the FRP tube (Fig. 13). The ultimate axial strain of this cylinder was considerably lower than that of the HC-CIII45-25-64 cylinder. This behavior explained that the deformation within the middle part of the HC-CIII45-32-38 was lower than that of the HC-CIII45-25-64. This indicated that the main deformation of such cylinders wrapped with [± 45] FRP does not have to be in the middle part unlike the

cylinders wrapped with unidirectional FRP. Also, the investigation after the test showed that the steel tube severely buckled locally.

The overall behavior of the specimens HC-CIII45-38-32 and CFFT-CIII45 was very similar to that of the specimen HC-CIII45-25-64. The load of these two specimens increased almost linearly until the peak axial loads of 1,440 kN and 1,830 kN, respectively which were at axial strains of approximately 0.14% and 0.30%, respectively (Fig. 9c and 9d). These two specimens reached to high axial strains of 0.115 and 0.12, respectively without any rupture of the FRP tube (Fig. 13).

4.1.2. Group B (three layers of ± 45 glass FRP)

The specimens in this group were prepared with glass FRP tube with fibers oriented at $\pm 45^{o}$. For the specimen HC-GIII45-25-64, the load increased almost linearly until the peak axial load of 1,522 kN which was at an axial strain of approximately 0.80% (Fig. 10a). The load softened with increased strain directly after the peak axial load without any hardening similar to the behaviors of the specimens in Group A. The axial load dropped to 635 kN with a loss of approximately 58% at an axial strain of 0.044. After that, the axial load was almost constant until the displacement of 33.0 mm which was the maximum displacement applied from the machine on this specimen only without any rupture of the FRP tube (Fig. 13). The specimen reached to axial strains of 0.08. The steel tube buckled locally as occurred in the other specimens.

The behavior of the specimens HC-GIII45-32-38 and HC-GIII45-38-32 were very similar to that of the specimen HC-GIII45-25-64. The load of the specimens HC-GIII45-32-38 and HC-GIII45-38-32 increased almost linearly until the peak axial loads of 1,540 kN and 1,670 kN, respectively which were at axial strains of approximately 0.2% and

0.3%, respectively (Figs. 10b and 10c). The softening occurred after that until the ultimate axial strains of 0.10 and 0.09, respectively where the axial load dropped to almost 310 kN and 495 kN when the FRP ruptured (Fig. 13). Also, the investigation after the test showed that the steel tube severely buckled locally.

The specimen CFFT-GIII45 reached the peak axial load of 1,965 kN at an axial strain of 0.14% (Fig. 10d). The axial load dropped severely after the peak axial load to an axial load of 731 kN at an axial strain of 0.035 when the FRP tube ruptured (Fig. 13). This behavior indicated the good effect of using steel tube in the HC-FCS columns over the CFFT in the displacement ductility. However, this behavior was highly related to the amount of FRP confinement comparable to the steel tube thickness.

4.1.3. Group C (two layers of ± 45/one layer of unidirectional glass FRP)

The specimens in this group were prepared with glass FRP tubes made with two layers of fiber oriented at $\pm 45^{o}$ and one layer of unidirectional fibers. For the specimen HC-GII45/I0-25-64, the load increased almost linearly until the axial load of 1,546 kN which was at an axial strain of approximately 0.76% (Fig. 11a). After this strain, the load hardened with increased strain until the peak axial load of 1,770 kN at an axial strain of 0.02. The axial load after the peak load dropped to 700 kN with a loss of approximately 60% at an axial strain of 0.027. This drop occurred because the unidirectional FRP ruptured while the oriented FRP did not. After that, the axial load was almost constant until an axial strain of 0.045. After that, the load softened again until the failure of the specimen by the rupture of the oriented FRP layers at an axial strain of 0.11 (Fig. 13). The steel tube buckled locally as occurred in the other specimens.

The behavior of the specimens HC-GII45/I0-32-38 and HC-GII45/I0-38-32 was very similar to each other. The load of the specimens HC-GII45/I0-32-38 and HC- GII45/I0-38-32 increased almost linearly until the axial loads of 860 kN and 740 kN, respectively, which were at axial strains of approximately 0.36% and 0.26%, respectively (Figs. 11b and 11c). After that, the loads increased with a lower stiffness until the peak axial loads of 1,906 kN and 2,000 kN, respectively at axial strains of 1.15% and 0.65%, respectively. After the peak load, the unidirectional FRP started to rupture in different locations. The rupture of the unidirectional FRP of these two specimens was earlier than the specimen HC-GII45/I0-25-64. This behavior was because the steel tubes of these two specimens had low D_i/t_s ratios. Therefore, the steel tubes under axial loading bulged outward. This behavior pushed the concrete dilation toward the FRP tube leading to early rupture. The softening occurred after the rupture of the unidirectional FRP until the ultimate axial strains of 0.10 and 0.072 of the specimens HC-GII45/I0-32-38 and HC-GII45/I0-38-32, respectively. Both specimens failed by the rupturing of both the oriented and unidirectional FRPs (Fig. 13). Also, the investigation after the test showed that the steel tube buckled locally.

The specimen CFFT-GIII45 behaved linearly until an axial load of 1,975 kN at an axial strain of 0.5% (Fig. 11d). The axial load increased slightly with increasing the axial strain until the peak axial load of 2,015 kN at an axial strain of 1.1%. At an axial strain of 1.3% the unidirectional FRP started to rupture, then the axial load suffered softening. The specimen failed when the both types of FRPs failed at an axial strain of 0.068 (Fig. 13).

The behavior of the specimens in this group revealed that when the concrete wall thickness increased, the concrete dilation increased, and as a result the concrete lateral

pressure on FRP and steel tubes increased. Therefore, the ultimate strains could be reduced when the concrete wall thickness increased.

4.1.4. Group D (one layer of ± 45/two layers of unidirectional glass FRP)

The specimen in this group (HC-GI45/II0-25-64) was prepared with a glass FRP tube made with one layer of FRP oriented at $\pm 45^{o}$ and two layers of unidirectional FRP. For this specimen, the load increased almost linearly until the axial load of 1,720 kN which was at an axial strain of approximately 0.33% (Fig. 12). After this strain, the load hardened with increasing the strain until the peak axial load of 2,285 kN at an axial strain of 1.5%. The axial load after the peak load dropped to 670 kN with a loss of approximately 70% at an axial strain of 0.021. This drop occurred because of the rupture of the unidirectional FRP while the oriented FRP remained unruptured. After that, the axial load softened until the ultimate axial strain of 0.11 when the specimen failed by rupture of the oriented FRP layers (Fig. 13). The steel tube buckled locally as occurred in the other specimens.

4.2. Axial-hoop strains relation

Figs. 14 to 17 illustrate the hysteretic axial and hoop strains versus the axial load of all the groups' specimens. In these figures, the compressive strains are denoted with negative signs and vice versa.

The behaviors of the axial and hoop strains for the specimens in Groups A and B were very similar (Figs. 14 and 15). In general, the axial and hoop strains for the specimens of these two groups increased simultaneously. The axial and hoop strains were close in values and opposite in signs because of the $\pm 45^{o}$ fiber orientation.

During the first cycles, before ultimate load, the hoop and axial strains increased linearly. At this stage, the concrete expansion under axial loading mainly occurred outwardly. At the ultimate load, the failure mainly occurred when the concrete lateral pressure broke the structure of the $\pm 45^{o}$ fibers and the epoxy. After this stage the fiber orientation occurred and the specimen could not achieve higher strength. However, the axial and hoop strains did not reach to very high strains. This behavior was because of the steel tube's local buckling. When the steel tube buckled locally, the concrete expansion went inwardly and outwardly. This behavior released some pressure on the FRP tube.

Despite the fact that the ultimate axial and hoop strains of the specimens of Group A and B were very close in values, most of the specimens in Group B failed by FRP rupture while those of Group A did not. This behavior was because the FRP tubes of the specimens in Group A were made with carbon fibers where the single carbon fiber had a lower diameter than the single glass fiber. Hence, the fiber impregnation with epoxy was better in the case of glass than that in the case of carbon. Therefore, the bond breakage of the structure of the $\pm 45^{o}$ fibers and the epoxy occurred earlier in the case of the carbon fiber. For this reason, the carbon fibers reoriented more than the glass fibers. This behavior caused the lower axial capacity of the specimens in Group A than those of Group B.

The specimens of the Groups C and D had almost the same behavior in axial and hoop strains (Figs. 16 and 17). At the same axial load, the hoop strains were higher in value than the axial strains. This behavior indicated that the unidirectional outer FRP layers stopped the fiber reorientation of the $\pm 45^{o}$ FRP inner layers.

4.3. Change in FRP confinement

Fig. 18 illustrates comparisons among the specimens that were similar in the steel tube and concrete wall thickness and different in FRP confinement. This figure shows the axial strain versus the normalized axial load that was calculated as the axial load over the nominal axial capacity (P_o) of the specimen. P_o was calculated according to ACI-318 [19] using equation 1 as below:

$$P_o = A_s f_y + 0.85\, f_c'(A_c - A_s) \quad (1)$$

where A_s = the cross-sectional area of the steel tube, A_c = the cross-sectional area of the concrete shell, f_y = the yield stress of the steel tube, and f_c' = the cylindrical concrete's unconfined compressive stress.

Fig. 18a illustrates the relation of the axial strain versus the normalized axial load for the specimens that had a concrete wall thickness of 25% of the outer diameter. The normalized axial load increased from approximately 0.8 to 1.3 when the FRP tube was made with one layer of $\pm 45^{o}$/two layers of unidirectional glass fibers instead of three layers of carbon fiber oriented at $\pm 45^{o}$. The normalized axial load increased from approximately 0.8 to 1.04 when the FRP tube was made with two layers of $\pm 45^{o}$/one layer of unidirectional glass fibers instead of three layers of carbon fiber oriented at $\pm 45^{o}$.

Fig. 18b illustrates the relation of the axial strain versus the normalized axial load for the specimens that had a concrete wall thickness of 32% of the outer diameter. The normalized axial load increased from approximately 0.86 to 1.02 when the FRP tube was

made with two layers of $\pm 45^{o}$/one layer of unidirectional glass fibers instead of three layers of carbon fiber oriented at $\pm 45^{o}$. However, the ultimate axial strains changed slightly.

Fig. 18c illustrates the relation of the axial strain versus the normalized axial load for the specimens that had a concrete wall thickness of 38% of the outer diameter. The normalized axial load increased from approximately 0.76 to 1.04 when the FRP tube was made with two layers of $\pm 45^{o}$/one layer of unidirectional glass fibers instead of three layers of carbon fiber oriented at $\pm 45^{o}$. However, the ultimate axial strains slightly changed.

Fig. 18d illustrates the relation of the axial strain versus the normalized axial load for the CFFT specimens. The normalized axial load increased from approximately 0.97 to 1.06 when the FRP tube was made with two layers of $\pm 45^{o}$/one layer of unidirectional glass fibers instead of three layers of carbon fiber oriented at $\pm 45^{o}$. The ultimate axial strains significantly changed (from 0.035 to 0.12) with changing the FRP type.

These comparisons indicated that increasing the FRP confinement improved the axial compressive strength of the HC-FCS specimens more than that of the CFFT specimens. However, the FRP confinement slightly affected the ultimate strains of the HC-FCS specimens, it significantly affected the ultimate strains of the CFFT specimens.

4.4. Change in concrete wall thickness

Fig. 19 illustrates the axial strain versus the normalized axial load of the specimens those had concrete wall thickness of 32% and 38% of the outer diameter for all of the groups. These two specimens of each group were selected for investigating the effect of

the concrete wall thickness on the axial capacity of the HC-FCS specimens. These specimens had close D_i/t_s ratios of steel tubes. Hence, the effect of the steel tube D_i/t_s ratio could be excluded from these comparisons. The figure shows that changing of the concrete wall thickness had a negligible effect on the normalized axial capacity of the HC-FCS specimens if the steel tube D_i/t_s ratio slightly changed.

4.5. Local buckling of the steel tubes

The effect of using a D_i/t_s ratio is a very significant parameter in the study of HC-FCS columns. Most of the previous studies were conducted on the HC-FCS columns using low steel tube D_i/t_s ratios [10-12, 20]. Table 4 summarizes results of some previous studies on the HC-FCS columns under axial compressive loading using a low steel tube D_i/t_s ratio. In general, an increase in capacity for such cylinders was achieved or, at least, no reduction in capacity occurred. Hence, higher values of the D_i/t_s ratio, ranging from 32 to 64, were investigated. The capacity of the tested specimens ranged from 0.76 to 1.30 of the nominal axial capacity P_o.

The steel tube local buckling occurred due to the bidirectional pressure that was applied on the steel tube; axially from the applied load and laterally from the concrete dilation. Fig. 20 illustrates the hoop strains on the steel tubes of the specimens HC-CIII45-25-64 and HC-GI45/II0-25-64. Both steel tubes were similar and were subjected to compressive hoop strains due to the concrete dilation. However, the hoop compressive strains of the steel tube of the specimen HC- GI45/II0-25-64 were much higher than that of the specimen HC-CIII45-25-64. The hoop compressive strain of steel tube of the specimen HC-GI45/II0-25-64 was approximately 2,600 microstrain, while it was approximately 200 microstrain for the steel tube of the specimen HC-CIII45-25-64. This

indicated that when the FRP confinement increased, the concrete pressure on the steel tube significantly increased. This indicated that the behavior of the HC-FCS columns under axial load is complicated and it is related to the interaction between the FRP and steel stiffness.

The normalized D_i/t_s can be defined as the ratio between the D_i/t_s and the D_i/t_s of AISC Manual [21] for the steel hollow section under compression as per the following equation:

$$\text{Normalized } (D_i/t_s) = D_i/t_s \,/(0.07\ \frac{E}{F_y}) \tag{2}$$

where E and F_y are the Young's modulus and the yield stress of the steel tube, respectively.

As shown in Table 4 and Fig. 21, the local buckling occurred when the D_i/t_s ratio was higher than the AISC Manual value. The D_i/t_s ratio for the tested cylinder relative to the AISC Manual value was between 1.37 and 2.74. However, this ratio in the specimens gathered from the literature relative to the AISC manual was lower than 1.0, as shown in Fig. 21. That explained the local buckling that occurred for the steel tubes of the tested specimens, even for the specimens with a steel tube D_i/t_s ratio of 32.

5. Findings and summary

This paper studied the behavior of the hollow-core fiber reinforced polymer-concrete-steel columns (HC-FCS) under cyclic axial compressive loading. The HC-FCS columns consisted of a concrete wall sandwiched between an outer FRP tube and an inner steel tube. Ten HC-FCS cylinders with different steel tube D_i/t_s ratios and three concrete-filled

fiber tuber (CFFT) cylinders were manufactured and tested under static cyclic axial compressive loading. The effects of using steel tubes with different D_i/t_s ratios and the effect of the FRP tube's fiber orientation on the behavior of the HC-FCS columns under axial load were investigated. The behavior of the HC-FCS columns were complicated and related mainly to the stiffness of the FRP and steel tubes which controlled the direction of the concrete dilation under axial load. HC-FCS columns with FRP tubes made with fibers oriented at $\pm$ 45° showed a low axial compressive strength and a high ultimate strain. HC-FCS columns with wet lay-up FRP tubes that had $\pm$ 45° and 0° (hybrid FRP) exhibited high axial strengths and strains. The failure of the HC-FCS columns with hybrid FRP tubes consisted of two stages. The first stage was the rupture of the unidirectional FRP (outer tube), and the second stage was the reorientation of the $\pm$ 45° fibers exhibiting high axial strains.

Acknowledgement

This research was supported by Missouri Department of Transportation (MoDOT) and Mid-American Transportation Center (MATC). In kind contribution from the National University Transportation Center (NUTC) at Missouri University of Science and Technology (Missouri S&T). However, any opinions, findings, conclusions, and recommendations presented in this paper are those of the authors and do not necessarily reflect the views of the sponsors.

References

[1] Moon, J., Lehman, D., Roeder, C., and Lee, H. (2013). "Strength of Circular Concrete-Filled Tubes with and without Internal Reinforcement under Combined Loading." J. Structural Engineering, 139(12).

[2] Hajjar J. (2000). “Concrete-filled steel tube columns under earthquake loads.” Structural Engineering and Materials; 2(1):72–82.

[3] Shin, M. and Andrawes, B. (2010). “Experimental Investigation of Actively Confined Concrete Using Shape Memory Alloys.” J. Eng. Struct. 32:3, 656-664.

[4] Zhu, Z., Ahmad, I., and Mirmiran, A. (2006). “Seismic performance ofconcrete-filled FRP tube columns for bridge substructure.” J. Bridge Eng., 11(3), 359–370.

[5] Dawood, H., ElGawady, M., and Hewes, J. (2012). “Behavior of Segmental Precast Post-Tensioned Bridge Piers under Lateral Loads.” ASCE Journal of Bridge Engineering, Vol. 17, No. 5, pp. 735-746.

[6] ElGawady, M. and Sha’lan, A. (2011). “Seismic Behavior of Self-Centering Precast Segmental Bridge Bents.” J. Bridge Eng., 16(3), 328–339.

[7] ElGawady, M., Booker, A., and Dawood, H. (2010). “Seismic Behavior of Posttensioned Concrete-Filled Fiber Tubes.” J. Compos. Constr., 14(5), 616–628.

[8] Teng, J.G., Yu, T., and Wong, Y.L. (2004). “Behavior of Hybrid FRP-Concrete-Steel Double-Skin Tubular Columns.” Proc. 2nd Int. Conf. on FRP Composites in Civil Engineering, Adelaide, Australia, 811-818.

[9] Li, W., Han,L. H., Chan, T. (2014). “Tensile behaviour of concrete-filled double-skin steel tubular members.” Journal of Constructional Steel Research, Volume 99, 35-46.

[10] Yu, T., Wong, Y.L., Teng, J.G., and Dong, S.L., (2004). “Structural behavior of hybrid FRP-concrete-steel double-skin tubular columns.” ANCER Annual Meeting: Networking of Young Earthquake Engineering Researchers and Professionals, Honolulu, Hawaii.

[11] Yu T, Wong YL, Teng JG. (2010). “Behavior of hybrid FRP-concrete-steel double-skin tubular columns subjected to eccentric compression.” Advances in Structural Engineering; 13(5):961-74.

[12] Wong, Y.L., Yu, T., Teng, J.G., and Dong, S.L. (2008). "Behavior of FRP-confined Concrete in Annular Section Columns." Composites: Part B Engineering, 39, 451-466.

[13] Teng, J.G., Yu, T., Wong, Y.L., and Dong, S.L. (2005). "Innovative FRP-Steel-Concrete Hybrid Columns." Advances in Steel Structures, 1, 545-554.

[14] Teng, J. G., Yu, T., Wong, Y. L., and Dong, S. L. (2007). "Hybrid FRP concrete-steel tubular columns: Concept and behavior." Constr. Build. Mater., 21(4), 846–854.

[15] Khayat, K.H. (1999). "Workability, Testing, and Performance of Self-Consolidating Concrete." ACI Materials Journal, 96 (3), 346-354.

[16] ASTM Standard D3039. (2008). "Standard Test Method for Tensile Properties of Polymer Matrix Composite Materials." ASTM International, West Conshohocken, PA, 2008, 10.1520/D3039_D3039M-08.

[17] ASTM Standard A1067. (2012). "Test Coupons for Steel Castings." ASTM International, West Conshohocken, PA, 10.1520/A1067_A1067M-12A.

[18] Au, C. and Buyukozturk, O. (2005). "Effect of Fiber Orientation and Ply Mix on Fiber Reinforced Polymer-Confined Concrete." J. Compos. Constr., 9(5), 397–407.

[19] ACI Committee 318 (2011). "Building Code Requirements for Structural Concrete (ACI318-11) and Commentary (318R-11)." American Concrete Institute, Farmington Hills, Mich., 509 pp.

[20] Ozbakkaloglu, T. and Fanggi, B. (2013). "Axial Compressive Behavior of FRP-Concrete-Steel Double-Skin Tubular Columns Made of Normal- and High-Strength Concrete." J. Compos. Constr., 10.1061/(ASCE)CC.1943-5614.0000401 , 04013027.

[21] American Institute of Steel Construction, Manual of Steel Construction, 14th Edition. Chicago: AISC, 2011.

Table 1.

Description of the tested specimens

Group No.	Specimen Number	Outer FRP tube	Inner steel tube D_i (t_s) (mm)	Concrete wall thickness (mm)
A	HC-CIII45-25-64	CFRP- Three layers 45^o	101.6 (1.6)	54
	HC-CIII45-32-38		76.2 (2.0)	67
	HC-CIII45-38-32		50.8 (1.6)	80
	CFFT-CIII45		—	—
B	HC-GIII45-25-64	GFRP- Three layers 45^o	101.6 (1.6)	54
	HC-GIII45-32-38		76.2 (2.0)	67
	HC-GIII45-38-32		50.8 (1.6)	80
	CFFT-GIII45		—	—
C	HC-GII45/I0-25-64	GFRP- Two layers 45^o + One Layer 0^o	101.6 (1.6)	54
	HC-GII45/I0-32-38		76.2 (2.0)	67
	HC-GII45/I0-38-32		50.8 (1.6)	80
	CFFT-GII45/I0		—	—
D	HC-GI45/II0-25-64	GFRP- One layer 45^o + Two Layers 0^o	101.6 (1.6)	54

Table 2.

SCC mixture proportions

w/cm	Cement (kg/m^3)	Fly Ash (kg/m^3)	Water (kg/m^3)	Fine aggregate (kg/m^3)	Coarse aggregate (kg/m^3)	HRWRA (kg/m^3)	VEA (kg/m^3)
0.38	350	174	198	830	830	2.1	0.7

Table 3.

Properties of saturated FRP according to manufacturer's data

Material	Nominal thickness/layer (mm)	Young's modulus, E (GPa)	Tensile strength (MPa)	Ultimate strain
CFRP-45^{o}	0.86	47.9	661	1.40 %
GFRP-45^{o}	0.86	18.6	279	1.50 %
GFRP-0^{o}	1.30	26.1	575	2.20 %

Table 4.

Steel tube D_i/t_s ratio of HC-FCS columns of literature and of current study

	D_o (mm)	D_i (mm)	t_s (mm)	D_i/t_s	$(D_i/t_s)_{AISC}$	Normalized (D_i/t_s)	P_u/P_o
Current Study	210	101.6	1.6	64	23.3	2.74	0.8
		101.6	1.6	64	23.3	2.74	0.89
		101.6	1.6	64	23.3	2.74	1.04
		101.6	1.6	64	23.3	2.74	1.3
		76.2	2.0	39	23.3	1.67	0.86
		76.2	2.0	39	23.3	1.67	0.82
		76.2	2.0	39	23.3	1.67	1.02
		50.8	1.6	32	23.3	1.37	0.76
		50.8	1.6	32	23.3	1.37	0.87
		50.8	1.6	32	23.3	1.37	1.04
Ozbakkaloglu and Fanggi [20]	150	101.6	3.2	31.75	35	0.91	1.31
		101.6	3.2	31.75	35	0.91	2.07
		101.6	3.2	31.75	35	0.91	1.05
		76.2	3.2	23.78	35	0.68	1.16
		76.2	3.2	23.78	35	0.68	1.17
		38.1	3.2	11.91	35	0.34	1.1
		38.1	1.6	23.81	35	0.68	1.27
		38.1	1.6	23.81	35	0.68	1.16
Yu et al. [11]	205	140.2	5.3	26.47	42.1	0.63	1.26
						0.63	1.23
Yu et al. [10]	152	76.2	3.2	23.78	41.1	0.58	0.99
						0.58	1.27
						0.58	1.48
Wong et al. [12]	152	41.9	2.3	18.26	38.7	0.47	1.35
		75.9	3.3	23.03	41.1	0.56	0.99
		75.9	3.5	21.71	34.2	0.63	1.14
		87.9	2.1	41.9	43.3	0.97	1.1
		115.1	5.2	22.12	39.5	0.56	1.17

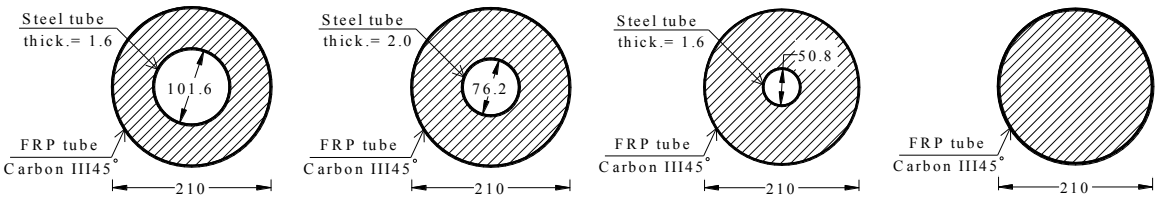

HC-CIII45-25-64 HC-CIII45-32-38 HC-CIII45-38-32 CFFT-CIII45

(a)

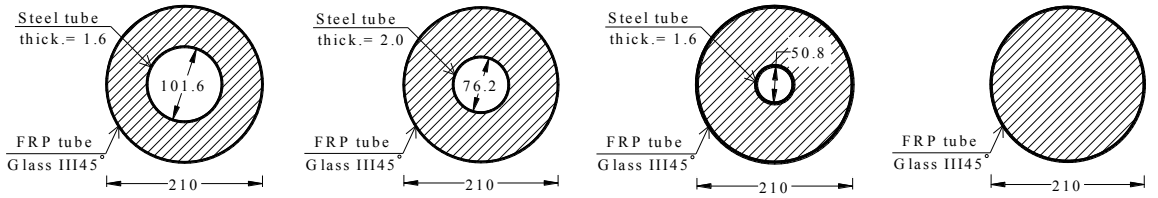

HC-GIII45-25-64 HC-GIII45-32-38 HC-GIII45-38-32 CFFT-GIII45

(b)

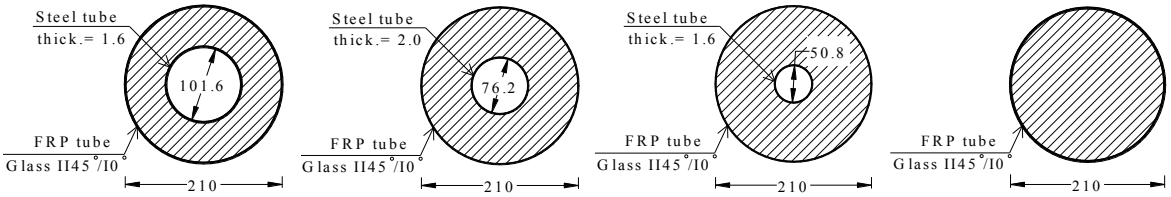

HC-GII45/I0-25-64 HC-GII45/I0-32-38 HC-GII45/I0-38-32 CFFT- GII45/I0

(c)

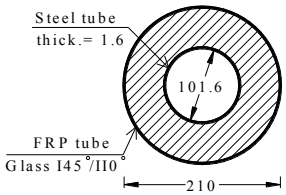

HC-GI45/II0-25-64

(d)

Fig. 1. Cross-sections of the test specimens in groups: (a) Group A, (b) Group B, (c) Group C, and (d) Group D

(a)

(b)

(c)

(d)

Fig. 2. FRP coupon and ring tensile tests: (a) testing of FRP coupon, (b) testing of FRP ring, (c) rupture of FRP coupon, and (d) rupture of FRP ring

(a) (b)

Fig. 3. Steel coupon tests: (a) testing of steel coupon and (b) rupture of steel coupons

Fig. 4. Testing of steel tube under compressive loading

(a) (b) (c)

Fig. 5. Modes of failure of the steel tubes under compressive loading: (a) elephant foot of tube A of diameter 101.6 mm, (b) elephant foot of tube B of diameter 76.2 mm, and (c) global buckling and elephant foot of tube C of diameter 50.8 mm

Note: rings are drawn around the local or global buckling

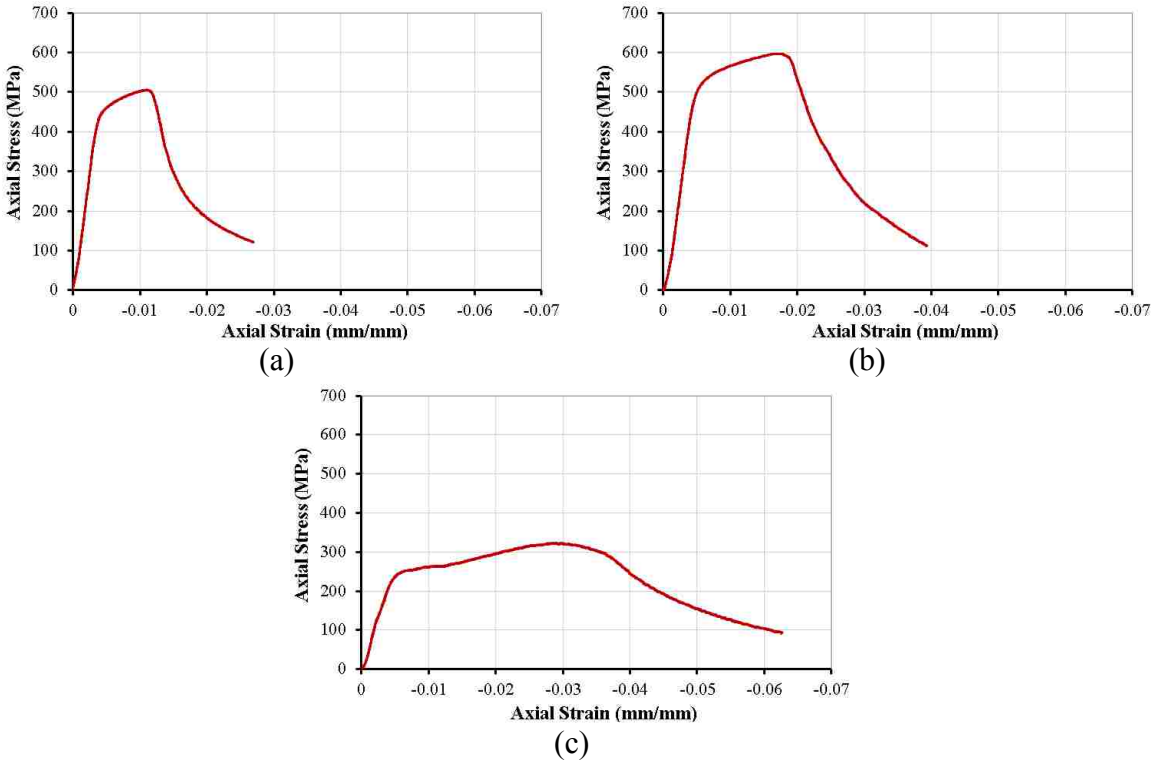

Fig. 6. Strain-stress relation of the steel tubes: (a) tube A, (b) tube B, and (c) tube C

Fig. 7. Test setup of the investigated specimens

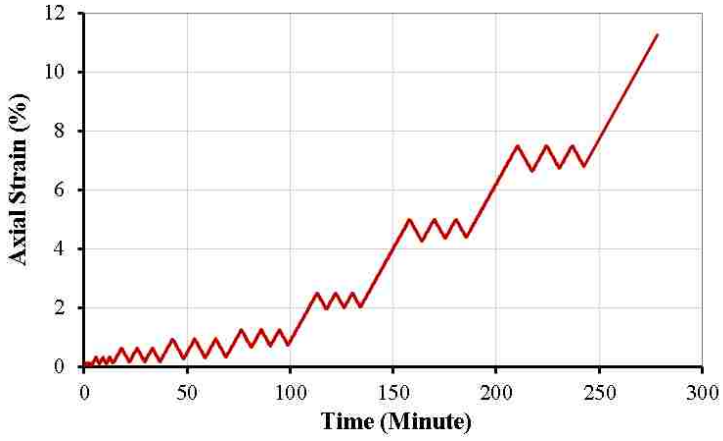

Fig. 8. Cyclic loading scheme

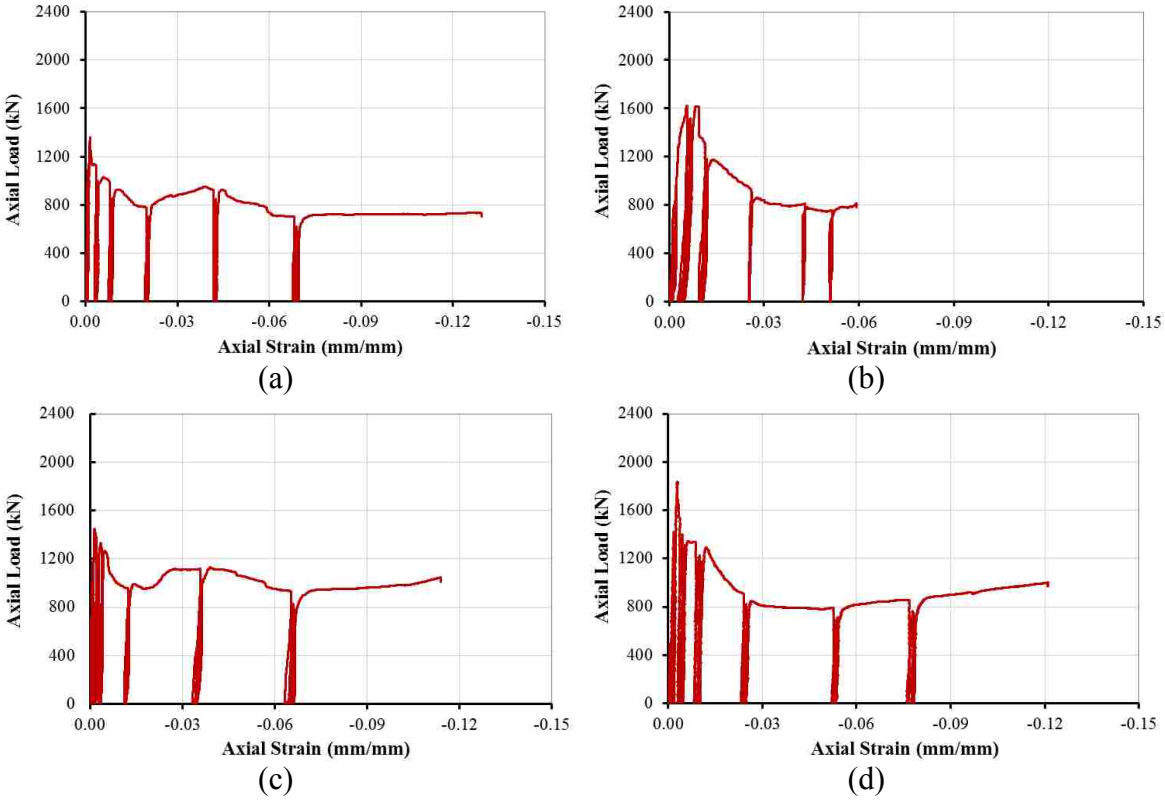

Fig. 9. Axial strain-axial load relation of the cylinders in Group A: (a) HC-CIII45-25-64, (b) HC-CIII45-32-38, (c) HC-CIII45-38-32, and (d) CFFT-CIII45

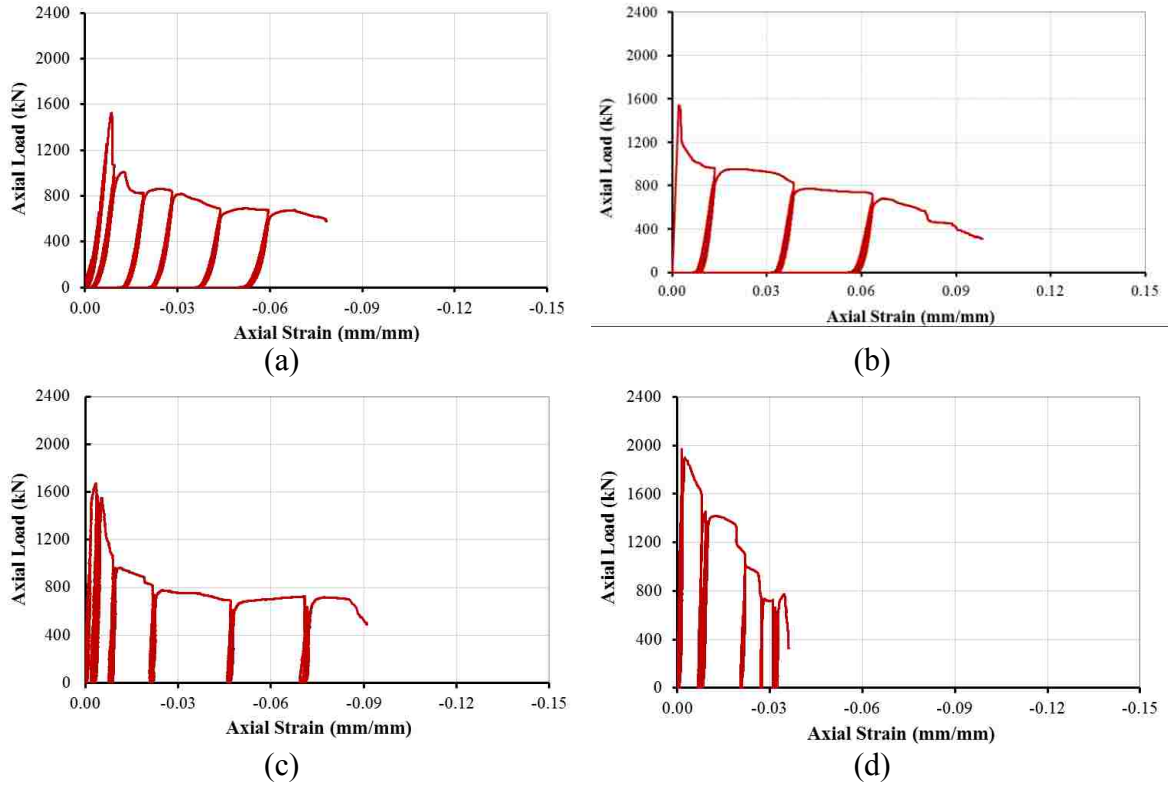

Fig. 10. Axial strain-axial load relation of the cylinders in Group B: (a) HC-GIII45-25-64, (b) HC-GIII45-32-38, (c) HC-GIII45-38-32, and (d) CFFT-GIII45

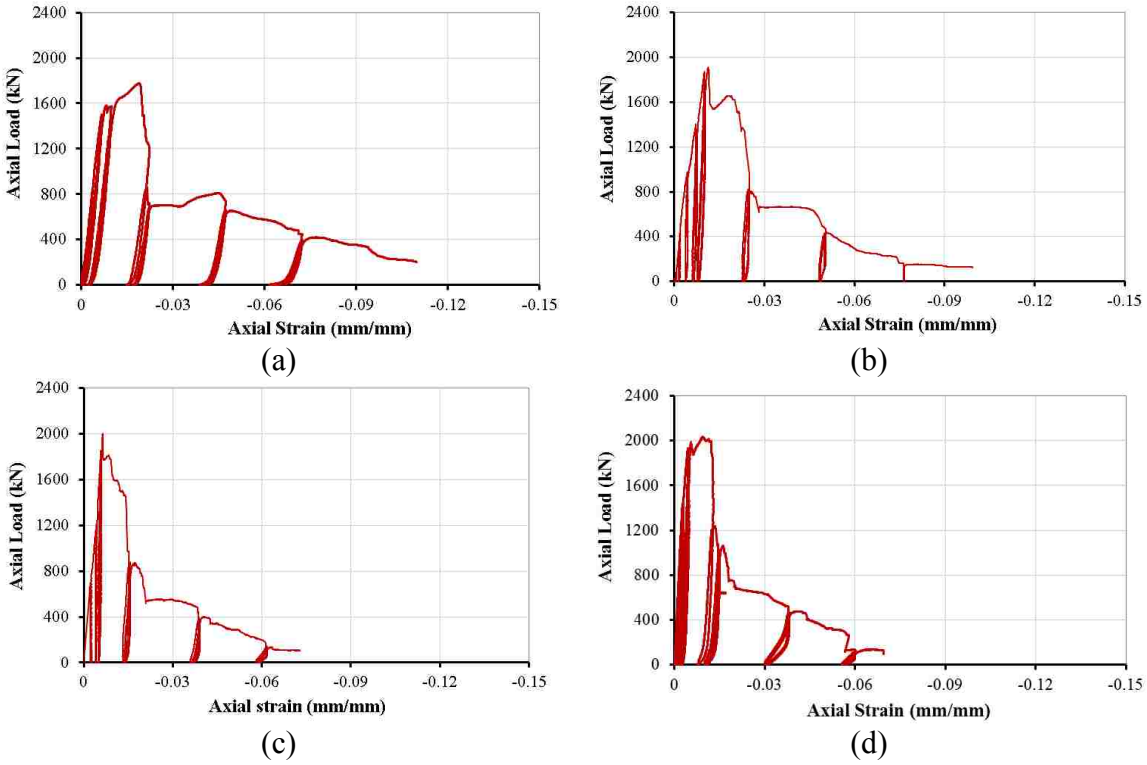

Fig. 11. Axial strain-axial load relation of the cylinders in Group C: (a) HC-GII45/I0-25-64, (b) HC- GII45/I0-32-38, (c) HC- GII45/I0-38-32, and (d) CFFT- GII45/I0

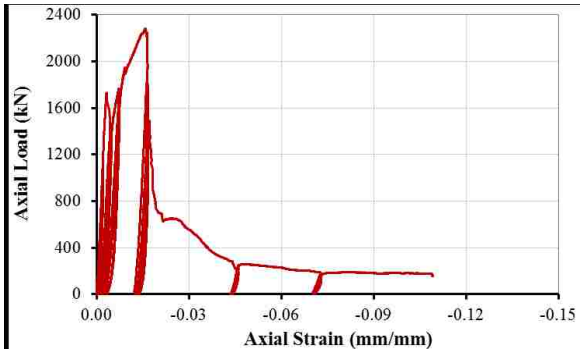

Fig. 12. Axial strain-axial load relation of the cylinders in Group D (HC-GI45/I0-25-64)

Fig. 13. Modes of failure of all of the specimens and their steel tube local buckling

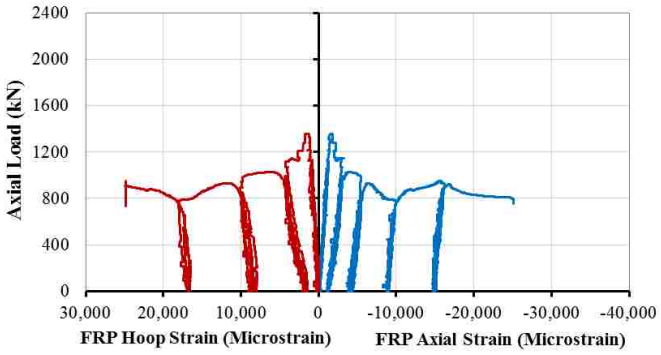

(a)

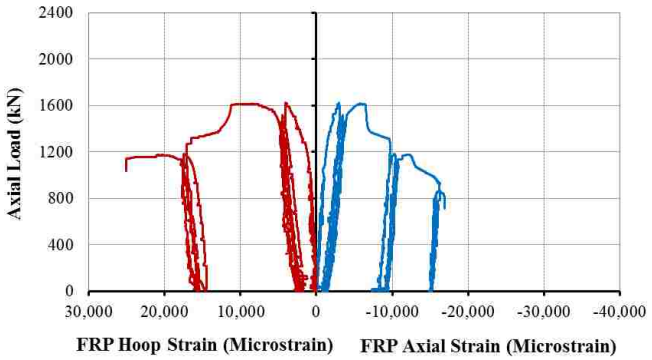

(b)

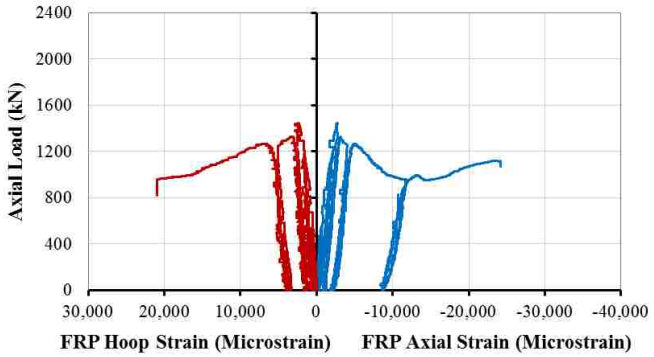

(c)

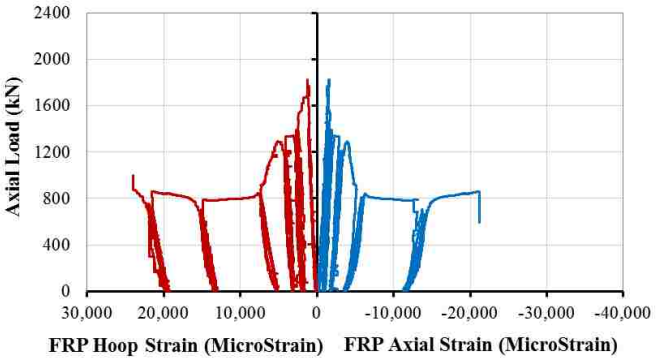

(d)

Fig. 14. FRP hoop strain and axial strain versus axial load relations of the cylinders in Group A: (a) HC-CIII45-25-64, (b) HC-CIII45-32-38, (c) HC-CIII45-38-32, and (d) CFFT-CIII45

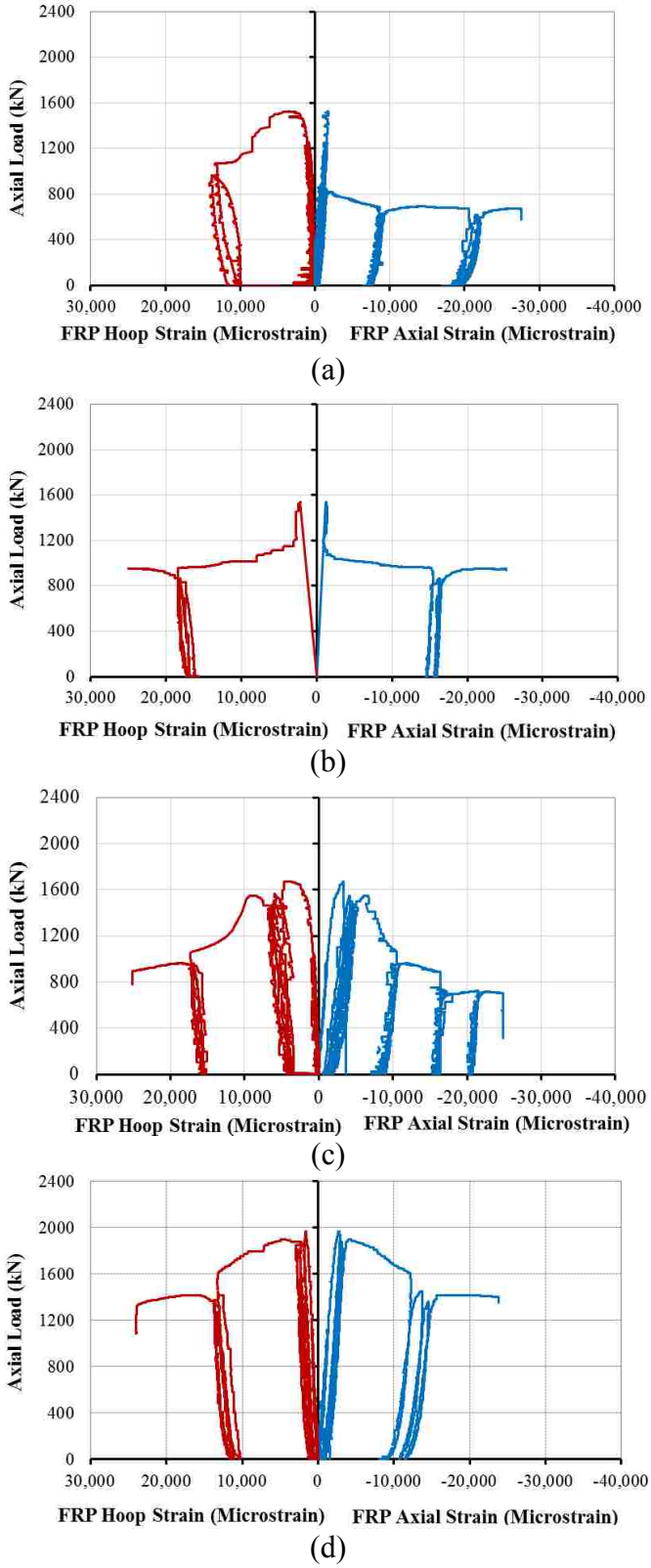

Fig. 15. FRP hoop strain and axial strain versus axial load relations of the cylinders in Group B: (a) HC-GIII45-25-64, (b) HC-GIII45-32-38, (c) HC-GIII45-38-32, and (d) CFFT-GIII45

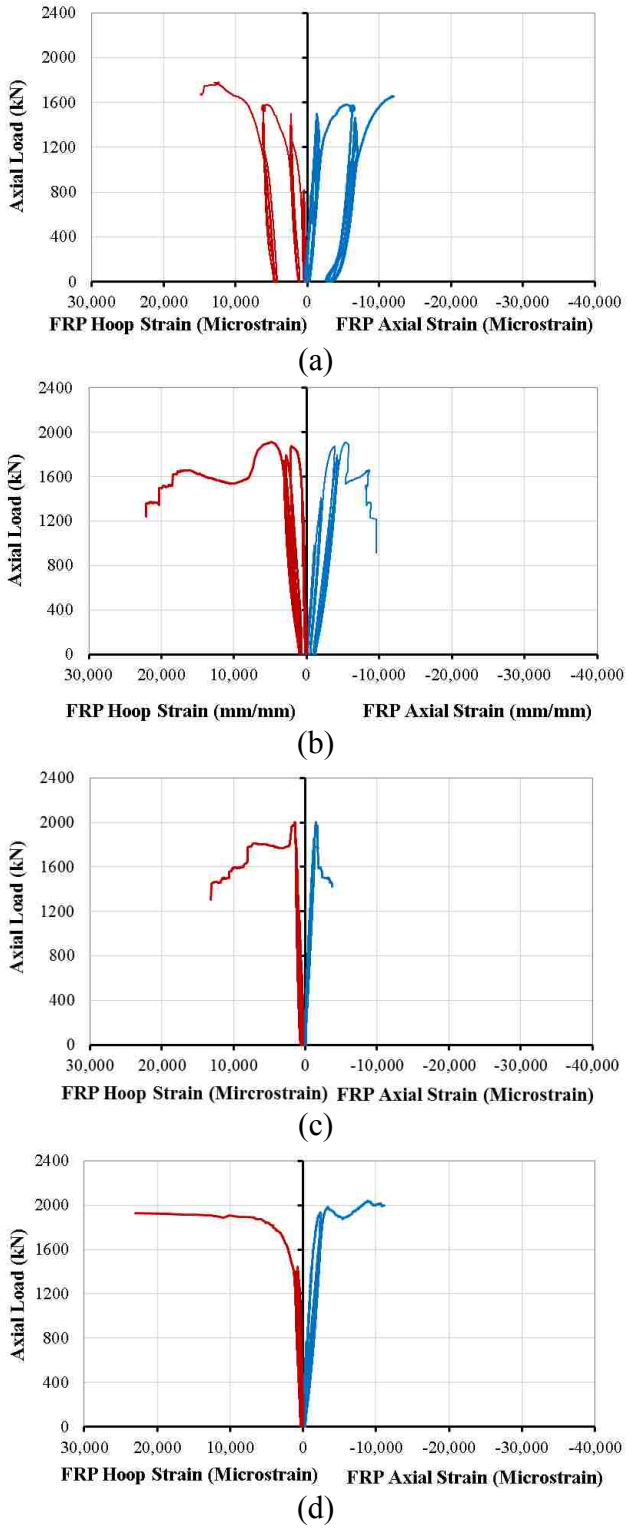

Fig. 16. FRP hoop strain and axial strain versus axial load relations of the cylinders in Group C: (a) HC-GII45/I0-25-64, (b) HC- GII45/I0-32-38, (c) HC- GII45/I0-38-32, and (d) CFFT-GII45/I0

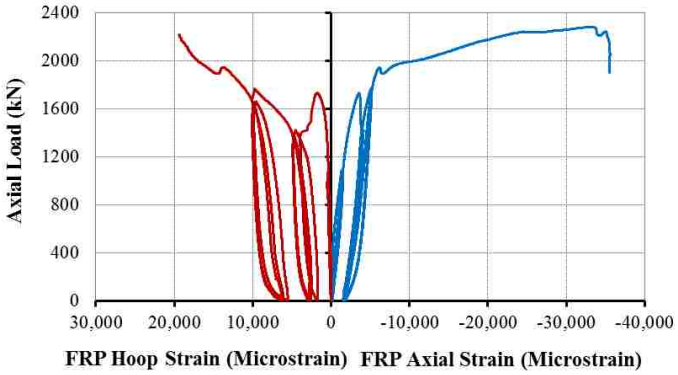

Fig. 17. FRP hoop strain and axial strain versus axial load relations of the cylinders in Group D (HC-GI45/I0-25-64)

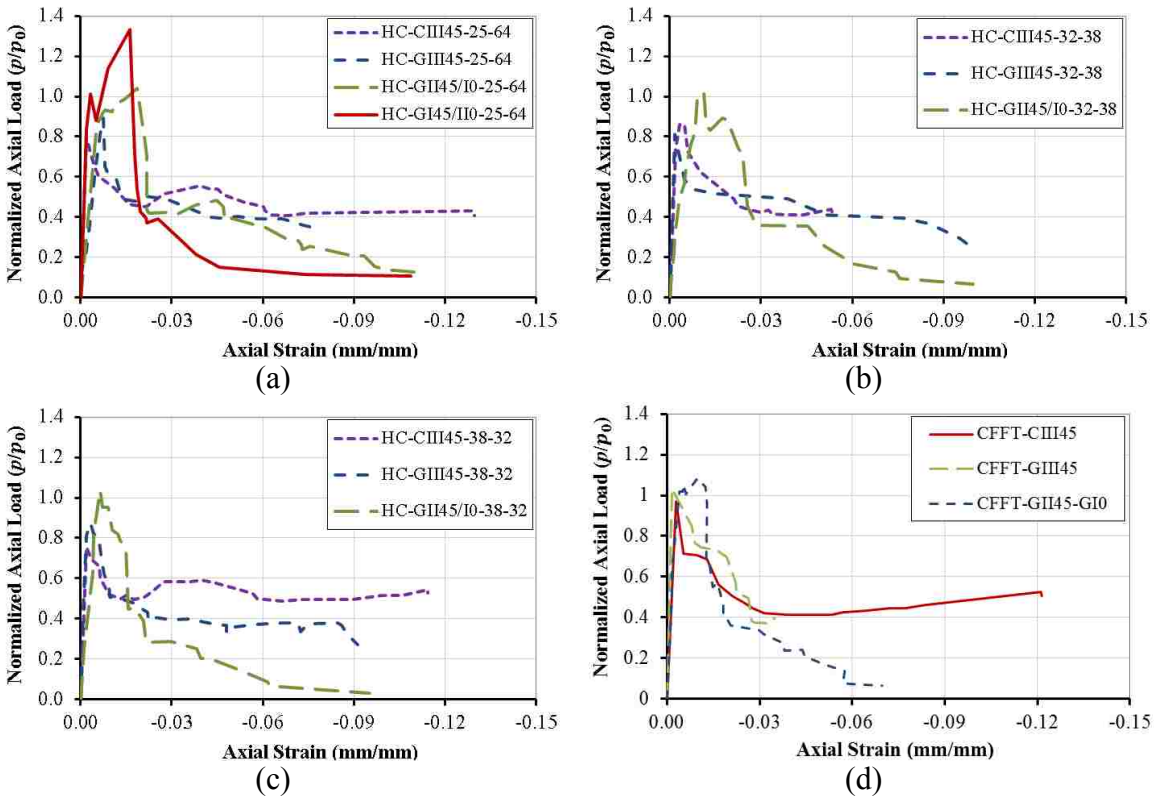

Fig. 18. Axial strain-normalized load relation of: (a) HCs with steel tube D/t ratio of 64, (b) HCs with steel tube D/t of 38, (c) HCs with steel tube D/t of 32, and (d) CFFTs

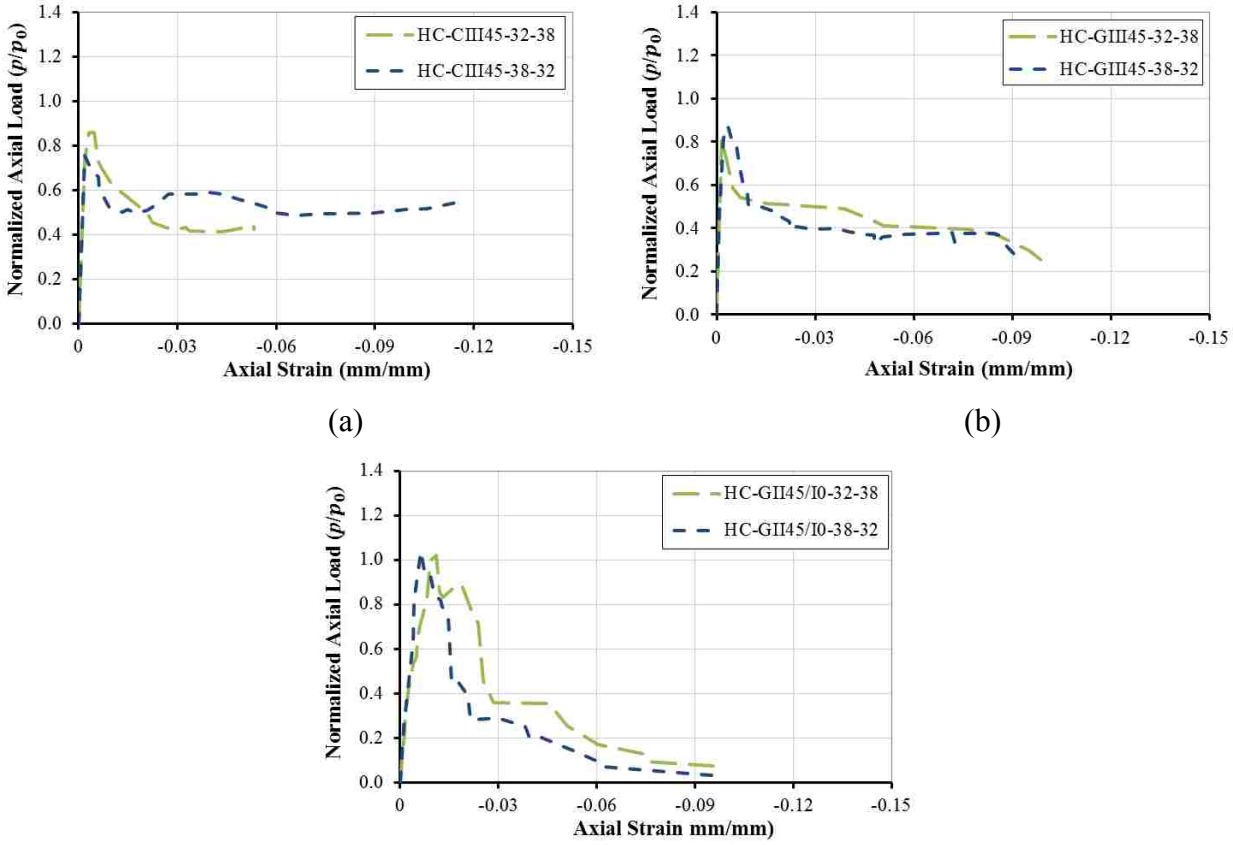

Fig. 19. Axial strain-normalized load relations of the two specimens of concrete wall thicknesses of 32% and 38% of: (a) Group A, (b) Group B, and (c) Group C

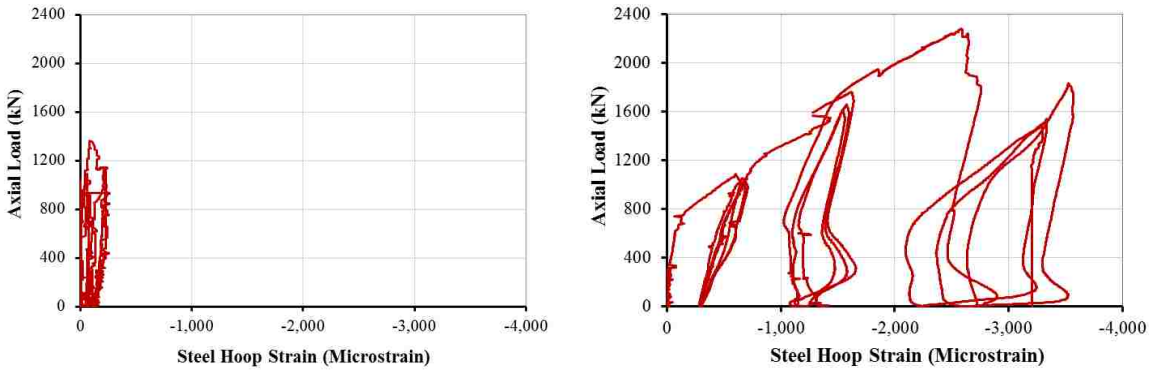

Fig. 20. Steel hoop strain- axial load relation of the specimens: (a) HC-CIII45-25-64 and (b) HC-GI45/II0-25-64

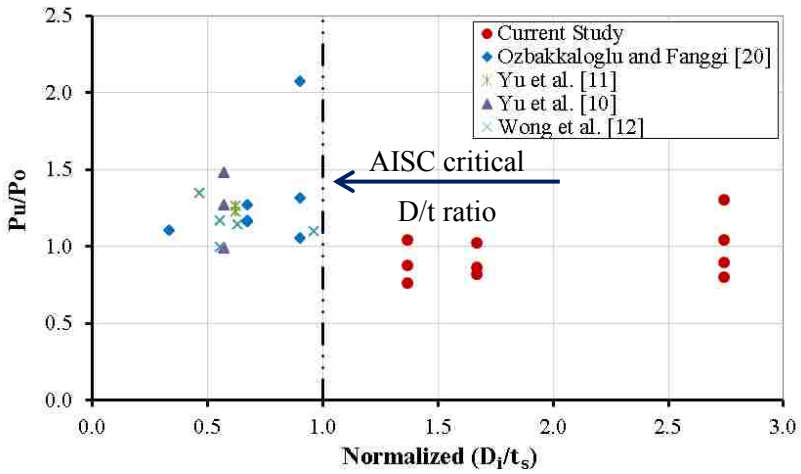

Fig. 21. Actual steel diameter-thickness ratios relative to the AISC manual value versus increase in capacity

II. ANALYTICAL AND FINITE-ELEMENT MODELING OF FRP-CONCRETE-STEEL DOUBLE-SKIN TUBULAR COLUMNS

Omar I. Abdelkarim[1], S.M. ASCE; Mohamed A. ElGawady[2]§

Abstract

This paper presents a finite element analysis of hybrid fiber reinforced polymer (FRP)-concrete-steel double-skin tubular columns (FSDTs). This FSDT consists of a concrete wall sandwiched between an outer FRP tube and an inner steel tube. LS-DYNA was used to develop a pushover analysis of three-dimensional FSDT models to simulate seismic loading. Finite element (FE) models were validated against the experimental results gathered from seven FSDT columns tested under cyclic loading. The FE analysis results were in good agreement with the experimental backbone curves. The maximum error was 9% in predicting the bending strengths of the columns. A parametric study was used to evaluate the effect of axial load level, concrete wall thickness, concrete strength, the diameter-to-thickness of the steel tube (D/t), and the number of FRP layers on the FSDT column's behavior. This study revealed that the behavior of FSDTs is quite complex. It also revealed that this behavior is controlled by the interactions that occur between the steel tube's stiffness, the concrete wall's stiffness, and the FRP hoop's stiffness. Local buckling occurred in all of the specimens examined. This buckling caused the FSDT system to rupture. Two modes of failure were defined: steel/concrete compression failure and FRP rupture. Compression failure was relatively gradual while

1 Ph.D. Candidate, Dept. of Civil, Architectural, and Environmental Engineering, Missouri University of Science and Technology, Rolla, MO. 65401; oiafgc@mail.mst.edu

2 Benavides Associate Professor, Dept. of Civil, Architectural, and Environmental Engineering, Missouri University of Science and Technology, Rolla, MO. 65401; elgawadym@mst.edu

§Corresponding author

failure due to FRP rupture was quite abrupt. Finally, the bending strength increased as the applied axial load, concrete compressive strength, and number of FRP layers increased. The bending strength also increased as both the concrete wall's thickness and the D/t ratio decreased.

Introduction

A significant amount of research has recently been devoted to developing accelerated bridge construction (ABC) systems. These ABC systems offer several benefits, including reduced construction time, minimal traffic disruptions, reduced life-cycle costs, improved construction quality, and improved safety (Dawood et al. 2012). Concrete-filled steel tubes (CFST) are widely used as bridge columns in Japan, China, and Europe to not only accelerate construction but also obtain superior seismic performance. In the U.S., CFSTs are used as piles and bridge piers. Their application, however, is limited, primarily, as a result of inconsistent design code provisions (Moon et al. 2013). Incorporated CFST members have several advantages over either steel or reinforced concrete (RC) members. The steel tubes act as a stay-in-place formwork, a shear reinforcement, and a confinement to the inside concrete core, increasing the member's ductility and strength. The tubes prevent concrete spalling so that the concrete core continues to function like a bracing for the steel tube. Therefore, the concrete core delays the local and global buckling under compression loads (Hajjar 2000).

Concrete-filled steel tube members dissipate more energy than those made from either traditional steel or RC members. On a strength-per-dollar basis, CFST members are cheaper than traditional steel members; they are comparable in price to traditional RC members. A concrete core can be reinforced with steel rebar to further improve the

member's performance while facilitating connections to other members. Limited performance data is available, however, for steel rebar reinforced CFST columns (Moon et al. 2013; Hajjar 2000).

Fiber reinforced polymer (FRP) tubes have gained acceptance as an alternative to steel tubes in CFST. Concrete-filled fiber tubes (CFFT) have benefits similar to those of CFST. Unlike steel tubes, FRP tubes have a light weight-to-strength ratio and a higher corrosion resistance than steel tubes have. Several studies have been conducted to investigate the seismic behavior of CFFT columns (Zhu et al. 2006). Shin and Andrawes (2010) investigated the behavior of CFFTs that were confined by a shape memory alloy. ElGawady et al. (2010) and ElGawady and Sha'lan (2011) conducted static cyclic tests on both segmental precast post-tensioned CFFT columns and two-column bents. Upon conducting finite element analysis, ElGawady and Dawood (2012) and Dawood and ElGawady (2013) developed a design procedure for precast post-tensioned CFFTs.

Montague (1978) developed another version of concrete-filled tubular columns: double-skin tubular column (DSTC). These columns consist of concrete wall sandwiched between two generally concentric steel tubes. They have been studied extensively in Asia (Shakir-Khalil & Illouli 1987; Yagishita 2000). More recently, Teng et al. (2004) used the FRP as an outer tube; they used steel as an inner tube within the double-skin tubular elements. This system combines and optimizes the benefits of all three materials: FRP, concrete, and steel.

In recent years, many investigators have studied the behavior of FRP-steel double-skin tubes (FSDT), in the form of beams and columns, under different static and cyclic loading conditions (Teng et al. 2005, 2007; Yu et al. 2006, 2010; Wong et al. 2008; Lu et

al. 2010; Huang et al. 2013; Abdelkarim & ElGawady 2014; Li et al. 2014a; Li et al. 2014b). Han et al. (2010) tested FSDTs in a beam-column arrangement, under cyclic flexural loading, with constant axial compression loading. The column's elastic stiffness increased as the applied axial load increased. The post-elastic stiffness increased as the FRP stiffness increased. The elastic stiffness, however, did not. The column's residual bending strength, after the FRP ruptured, increased as the applied axial load level increased. Zhang et al. (2012) and Ozbakkaloglu and Idris (2014) investigated the behavior of small-scale FSDTs under combined axial compression and lateral cyclic loading. The results of the conducted experimental tests revealed a high concrete confinement and ductility.

This study utilized finite element modeling to analyze FSDT's behavior under a constant axial compression load and lateral pushover. The LS-DYNA software was used to design and verify the models against the experimental results gathered from seven FSDT columns tested by Ozbakkaloglu and Idris (2014). These columns had a concrete compressive strength (f_c') that was between 95 MPa (13,775 psi) and 130 MPa (18,850 psi). Either aramid (AFRP) or carbon (CFRP) was used to manufacture the FRP tubes (see Table 1). The columns were tested under axial loads (P) between 410 kN (92.2 kips) and 690 kN (155.1 kips). These loads were corresponding to 0.34 to 0.45 of the columns nominal axial capacity (P_o) where P_o is calculated as follows (ACI-318 2011):

$$P_o = A_s f_y + 0.85 f_c' A_c \quad (1)$$

Where A_s = the cross-sectional area of the steel tube, A_c = the cross sectional area of the concrete column, f_y = the yield strength of the steel tube, f_c' = the cylindrical concrete unconfined compressive strength.

These models were next used to conduct a parametric study investigating the effects of the applied axial load level, concrete strength, concrete wall thickness, the steel tube's diameter-to-thickness ratio (D/t), and the number of FRP layers on the FSDT column's behavior. Analytical models were used to predict the column's flexural strength.

FE Modeling

Geometry

The columns under consideration in this study were tested as free cantilevers under both a constant axial compression load and cyclic lateral loading. The tested columns were symmetrical about the vertical plane. Thus half of each column was modeled and analyzed in LS-DYNA (Figs. 1 and 2). Each column had a circular cross-section with an outer diameter of 150 mm (5.90 in.) and an inner diameter of 88.9 mm (3.50 in.). The column height (measured from the top of the footing to the top of the column) was 1200 mm (47.25 in.); the lateral load (measured from the top of the column's footing) was applied at a height of 1000 mm (39.37 in.). A steel tube was extended inside the footing while the FRP tube was stopped at the top of the footing. The FRP tube of specimen DST-2 stopped at 20 mm (0.79 in.) above the top of the footing. The specimens did not include any flexural reinforcement except the steel tubes. Each FE model had 5,248 elements and 6,840 nodes. A sensitivity analysis was conducted before the final form of the finite element model to optimize the elements' sizes achieving an acceptable accuracy.

Each column's concrete core was modeled by solid elements. These elements had a height of 25.00 mm (0.98 in.). Both the outer FRP tube and the inner steel tube were simulated by shell elements. A typical element height for the FRP tube was 25.00 mm

(0.98 in.); each steel tube was 25.00 mm x 8.68 mm (0.98 in. x 0.34 in.). A rigid cylinder, modeled by solid elements, was placed on top of the concrete column to apply the axial load. Each column was supported on a concrete footing, which was also modeled by solid elements. All solid elements were modeled with constant-stress and one-point quadrature integration to reduce the computational time. Hourglass control was used to avoid spurious singular modes for solid elements. The hourglass value for all models was taken as the default value of 0.10.

Contact elements surface-to-surface were used to simulate the interface between the concrete column and the FRP tube. They were also used between the concrete column and the steel tube. This type of contact considers slip and separation that occurs between master and slave contact pairs. Hence, slip/debonding will be displayed if either occurs between the concrete wall's surface and the tube's surface.

This type of contact was used between the concrete footing and the steel tube. Node-to-surface contact elements were used between the loading stub and the concrete wall, the FRP tube, and the steel tube. Similarly, this contact type was used to simulate the contact between the concrete wall and the FRP tube to the footing. The coefficient of friction for all of the contact elements was taken as 0.6.

Material Models

Concrete

Different material models are available in LS-DYNA to simulate concrete materials. The Karagozian and Case Concrete Damage Model Release 3 (K&C model) was used in this study because it exhibited good agreement with the experimental results gathered in

previous studies (Ryu et al. 2014). This model, developed from the theory of plasticity, has three shear failure surfaces: yield, maximum, and residual (Malvar et al. 1997).

This study used the automatic generation option for the failure surface, where f_c' was the main input to the model. Another input to the model, the fractional dilation parameter (ω), considers any volumetric change in concrete. The fractional dilation parameter was taken as the default value of 0.50. The equation of state (EOS), which controls the compressive behavior of the concrete under triaxial stresses, was automatically generated, given f_c' and ω.

FRP Tube

The FRP material used was modeled as an orthotropic material using "002-orthotropic_elastic" material. Such material model uses total Lagrangian-based to model the elastic-orthotropic behavior of solids, shells, and thick shells. This material is defined by several engineering constants: elastic modulus (E), shear modulus (G), and Poisson's ratio (PR), in the three principle axes (a, b and c). The fiber orientation is defined by a vector. Table 2 is a summary of FRP's properties. The following characteristics, based on Ozbakkaloglu and Idris (2014) were implemented in the FE. The elastic moduli of the AFRP and CFRP tubes in the hoop directions (Ea) was 125.7 GPa (18,226 ksi) and 251.0 GPa (36,404 ksi), respectively. The ultimate tensile strain of the AFRP and CFRP tubes in the hoop directions was 0.0212 and 0.0144, respectively. The major Poisson's ratio was 0.25. The shear moduli of the AFRP and CFRP tubes in the transverse directions (Gab) was 9.25 GPa (1,341 ksi) and 9.60 GPa (1,392 ksi), respectively. The failure criterion for the FRP, defined as "000-add_erosion," was assigned the ultimate strain of FRP in "EFFEPS" card.

Steel Tube

The material model "003-plastic_kinamatic" was used to identify the steel tube's elasto-plastic stress-strain curve. Three parameters were needed to define this material model according to the material's properties: the elastic modulus (E), the yield stress (SIGY), and Poisson's ratio (PR). The elastic modulus and the yield stress were 205.0 GPa (29,725 ksi) and 350.0 MPa (50,750 psi), respectively, for all columns except DST-7. A different steel tube with a different thickness was used in this column. Thus, its elastic modulus and yield stress were different: 206.3 GPa (29,906 ksi) and 412.5 MPa (59,813 psi), respectively.

Boundary Conditions and Loading

Displacement in the Y direction and rotations about both the X and Z axes at the plane of symmetry were restrained. Displacements and rotations in all directions at the nodes of the footing's bottom were prevented.

The loading was applied in two different steps. An axial compressive load was applied to the top of the loading stub during the first step. These loads were half of those listed in Table 1 due to symmetry. During the second step, lateral displacement was applied at the middle nodes of the common surface, between the column and the loading stub, until failure occurred due to rupture of the FRP tube or compression failure.

Results and Discussion

The lateral drift of each column was obtained by dividing the lateral displacement, measured at 1000 mm (39.37 in.) above the footing top, by 1000 mm (39.37 in.). The

moment at the base of the column was also obtained from FE analysis; the sum of the reactions at the footing time was multiplied by a column height of 1000 mm (39.37 in.). The moment versus drift (obtained from FE analyses) is plotted in Fig. 3. This figure also depicts the experimental drift versus the moment for each column. Table 3 includes a summary of the finite element results versus the experimental results for all columns. This table also includes the error in predicting the ultimate moment of each test specimen. This error was calculated as the absolute value of the difference between the experimental and the FE ultimate moments divided by the experimental ultimate moment. The error was between 1.3% and 8.9%. All simulated columns behaved in a manner similar to the tested columns up to failure.

Overall, the FE models were able to capture the test specimen's behavior (Fig. 3). Column DST-1 reached peak bending strengths of 36.5 kN.m (26.9 kip-ft) and 33.8 kN.m (24.9 kip-ft) during the experimental work and the FE analysis, respectively (Fig. 3a). The difference between the experimental strength and the FE strength was 7.4%. The column reached its peak strength at drifts of 5.8% and 5.7% during the experimental and FE analysis, respectively. However, during the experimental work and beyond a drift of 6.0%, the column failed abruptly when the FRP tube ruptured. This column failed by compression failure during the FE analysis at a lateral drift of 8.9%.

The FE predicted the initial stiffness until a drift of 1.0% (see Fig. 3a). At that drift, both the experimental and the FE analysis revealed a significant nonlinear behavior up to failure. The FE analysis revealed that the nonlinear behavior began when the concrete column began to uplift at the footing level. This connection had no continued reinforcement and, therefore, had no tensile strength. Thus, at some point during flexural

loading, the connection between the column and the footing uplifted at the tension side. As a result, the contact area of the column with the footing reduced nonlinearly as the neutral axis shifted toward the compression zone (Fig. 4). As the neutral axis continued to shift, the compression in the concrete increased caused the concrete volumetric dilation to increase. This increase, in turn, increased the strain in the FRP tube.

The FE analysis revealed a confined concrete compressive strength (f'_{cc}) of 178 MPa (25,810 psi) just before failure (Fig. 5). This value indicates that the concrete's strength increased 87%, signaling good confinement. Yu et al. (2010) developed a confinement model for FSDT. For the given cross-section, this model predicted an f'_{cc} that was equal to 160 MPa (23,235 psi), a value close to the f'_{cc} observed during the FE analysis.

The strain profile of the FRP tube at the bottom 450 mm (17.7 in.) of column DS-1 was obtained from the FE analysis and is compared with the experimental profile at a lateral drift of 5.0% (Fig. 6). Three strain profiles taken from the FE are plotted in Fig. 6. These profiles represent the peak, average, and minimum strains, respectively. The average profile of the strains obtained from the FE is close to those obtained during the experimental work. Both the FE and the experimental work revealed a strain concentration at the bottom 50 mm (1.97 in.).

Column DST-2 reached a bending strength of 28.6 kN.m (21.1 kip-ft) and a lateral drift of 5.0% during the experimental work (Fig. 3b); it reached a bending strength of 30.7 kN.m (22.7 kip-ft) and a drift of 7.8% during the FE analysis. This represents an error of 7.6% in predicting the bending strength. During the experimental work, strength degradation occurred after a 2% lateral drift. This degradation was the result of a 20 mm (0.8 in.) gap that was present between the FRP tube and the footing during the

experimental work. Hence, a slight difference occurred in the behavior between the FE results and the experimental results after 2.0% lateral drift. The FE model demonstrated both a higher moment capacity and a higher lateral drift. This column failed by FRP rupture in both the experimental and the FE studies.

Column DST-3 reached bending strengths of 32.6 kN.m (24.0 kip-ft) and 32.1 kN.m (23.7 kip-ft) during the experimental work and the FE analysis (Fig. 3c), respectively. These values correspond to an error of 1.3%. Both the FE and the experimental analysis revealed that failure occurred when the FRP ruptured. The FE analysis predicted the column's behavior accurately up to a drift of 9.0%. Beyond that level, the FE analysis exhibited slow strength degradation while the experimental work presented a nearly constant strength. Degradation in the bending strength during FE analysis occurred as a result of local buckling in the steel tube.

Columns DST-5 and DST-6 failed during the experimental work at bending strengths of 40.7 kN.m (30.0 kip-ft) and 42.0 kN.m (31.0 kip-ft), respectively. The FE analyses of both columns predicted peak bending loads of 39.0 kN.m (28.8 kip-ft) and 39.6 kN.m (29.2 kip-ft), respectively. This corresponds to errors of 4.0% and 5.8% for the columns DST-5 and DST-6, respectively. However, while the experimental work showed that these columns failed at drifts of 6.0% and 7.0% for DST-5 and DST-6, respectively, the FE analyses showed that these columns failed at drifts of 9.4% and 9.7%. Both columns failed numerically as a result of compression failure at a confined concrete strength of 180 MPa (26,100 psi).

During FE analysis, local buckling in the steel tube occurred at a lateral drift of 5.7%. Hence, the concrete stresses increased considerably because of the significant reduction

in the participation of the steel tube to bending resistance. The experimental work revealed a strength reduction, likely due to steel buckling, at a drift of 5.0%. The FRP also ruptured, however, after the steel buckled.

Column DST-7 reached a bending strength of 39.7 kN.m (29.3 kip-ft) during the experimental work. The FE analysis was in close agreement with the experimental results; the column reached a bending strength of 43.3 kN.m (31.9 kip-ft; Fig. 3f), corresponding to an error of 8.9%. The FE analysis and the experimental work revealed stiffness degradation at a lateral drift of 5.0% and 5.5%, respectively. Moreover, the post-elastic stiffness of column DST-7 was significantly higher than that of all other specimens. This column was displaced laterally up to 6.0% experimentally and up to 9.0% numerically. The FRP rupture occurred experimentally within the first 4.0 in. (approximately 100 mm) from the footing's top. The FE model simulated this behavior very well, as illustrated in Fig. 7. The FRP failed more gradually, however, during the numerical analysis. Both the FE and the experimental work revealed significantly higher post-elastic due to the thicker steel tube and higher yield stress.

Column DST-9 reached bending strengths of 41.0 kN.m (30.3 kip-ft) and 43.9 kN.m (32.3 kip-ft) during the experimental and FE analysis, respectively, (see Fig. 3g) corresponding to an error of 6.6%. The FE analysis predicted the column's behavior accurately up to failure. The column failed experimentally at a 12.0% lateral drift without any visible fiber rupture. It could not, however, endure more applied lateral load. Likewise, the column failed numerically because of the concrete strength degradation, up to compression failure, without fiber rupture, at a lateral drift of 10.2%. The FE analysis

revealed that the maximum confined concrete strength for this column was 225.0 MPa (32,625 psi) with an increase in the unconfined concrete strength of 73.0%.

Parametric Study

The FSDT column is a new system that has only recently been investigated. The FE models developed in this work were used to examine the effects of the applied axial load level, concrete wall thickness, and unconfined concrete nominal compressive strength (f_c'). They were also used to study both the diameter-to-thickness of the steel tube (D/t) as well as the number of FRP layers on the FSDT column's strength, ultimate drift, and mode of failure. The FE model of column DST-1 was used as the reference for this parametric study. Each parameter was studied independently, resulting in an analysis of 36 columns. The results from this study provided an in-depth understanding of FSDT's behavior under combined vertical and lateral loadings.

The columns' overall behavior was as follows. Steel tubes yielded under tension and compression. This yielding was followed by an onset of local buckling at the section just above the concrete footing. Two modes of failure were observed; both modes were triggered by local buckling of the steel. This buckling led to stiffness degradation of the steel tube, placing higher compression demands on the concrete.

The first mode of failure displayed by columns with a higher FRP confinement ratio, defined as the ratio of the ultimate FRP confining pressure normalized by f_c'; the onset of local steel buckling was followed by a propagation of local buckling leading to excessive compressive load demand on concrete and gradual failure of the system due to steel/concrete failure. This mode of failure is referred to here as compression failure. The

second mode of failure displayed by columns having lower confinement ratio, the onset of the local buckling placed higher compression and dilation demands on the concrete where the FRP can't effectively confine the concrete leading to abrupt rupture of the FRP. This mode of failure is referred to here as FRP failure. A specimen was identified as having failed when either the specimen's lateral resistance dropped by 20% of its peak strength or the FRP ruptured, whichever occurred first.

Table 4 includes summary of the parametric study results collected. The backbone curves and the change in bending strengths of the investigated columns are presented in Figs. 8 and 9, respectively. Different limit states are given in Fig. 8. These states include the onset of compression and tension yielding in the steel tube, the presence of local buckling in the steel tube, and FRP rupture if occurred. The ultimate lateral drift (δ) for each column is also presented in Figs. 8 and 9.

Effects of Axial Load Level on the Behavior of FSDT

The behavior of four columns, namely, DST-1, DST-2A, DST-3A, and DST-4A were studied with different values of applied axial load levels of 45%, 30%, 15% and 7.5% of P_o, respectively, where P_o was defined by equation 1. As shown in Figs. 8(a), 9(a) and Table 4, the effects of the axial load on the nominal moment capacity, ultimate drifts, and modes of failure were substantial with the nominal bending strength increased with increasing the applied axial load level. Decreasing the applied axial load level by 83% i.e., from 45%P_o to 7.5% P_o decreased the bending strength by 39% i.e., from 33.8 kN.m (24.9 kip-ft) for the DST-1 to 20.7 kN.m (15.2 kip-ft) for the DST-4A. This behavior resembled the behavior of conventional reinforced concrete short columns under the

combined effect of small applied axial load and large bending moment where increasing the applied axial load would increase the moment capacity of the column.

These specimens failed in two distinct failure modes. Column DST-1 failed as a result of compression failure when an axial load of 45% P_o was applied while the other columns failed as a result of FRP failure. As explained earlier, local buckling of the steel tubes triggered failures of the columns. Expectedly, the higher the applied axial is the smaller drift at local buckling. Columns that had been subjected to axial loads of 15% P_o or higher locally buckled at drifts of 3% to 5%; the steel tube in column DST-4A locally buckled at a drift of 10.6%. After local buckling occurred, it propagated leading to a gradual degradation in concrete confinement and, ultimately, failure of the columns. This propagation of the local buckling was relatively quick in columns that had higher levels of applied axial loads (i.e., 30% P_o and 45% P_o). Excessive local buckling placed higher compressive stress demands on the concrete while the steel tube was not able to effectively confine the concrete leading to gradual concrete crushing at smaller drifts. For example, the concrete in column DST-1sustained an axial compressive stress of 187% f_c'. Degradation in concrete stresses occurred beyond that point.

Columns that were subjected to low axial loads (i.e., DST-4A) experienced a delay in local buckling, allowing the concrete to remain effectively confined and the concrete sustained axial compressive stress of 240% f_c'. These high stresses led to excessive dilation demands on the FRP and, ultimately, abrupt FRP rupture. As shown in Figs. 8(a) and 9(a), the lateral drift capacity significantly increased as the applied axial load level decreased. Moreover, the backbone curves reflect the differences in the modes of failure. Compression failure occurred quite gradually. Thus, the backbone curve displayed a post-

peak descending branch while the FRP failure displayed abrupt termination of the backbone curves.

The applied axial load level also had a significant effect on the initiation of the nonlinear behavior, tensile yielding of the tubes, and stiffness degradation. Nonlinear behavior initiated when uplift began on the tension side of the footing-column connection (Fig. 10). Thus, for columns subjected to lower level of applied axial load, the interface joint opened early leading to early stiffness degradation and early yielding of the steel tubes. The steel tubes in this group exhibited tensile yielding at drifts between 1.4% and 2.6%. Expectedly, the higher the applied axial load is the higher drift at tensile yielding of the tube.

Effects of Concrete Wall Thickness on the Behavior of FSDT

Four columns, namely, DST-1, DST-2B, DST-3B, and DST-4B were studied with different concrete wall thicknesses of 30.5 mm (1.2 in.), 20.3 mm (0.8 in.), 40.6 mm (1.6 in.), and 50.8 mm (2.0 in.), respectively. As shown in Figs. 8(b) and 9(b) as well as Table 4, as the concrete wall thickness decreased, the column strength increased. Decreasing the concrete wall thickness by 60% i.e., from 50.8 mm (2.0 in.) to 20.3 mm (0.8 in.) increased the bending strength 30% i.e., from 29.2 kN.m (21.5 kip-ft) in column DST-4B to 38.1 kN.m (29.8 kip-ft) in column DST-2B.

The increase in the strength of columns having smaller wall thickness occurred since the lever arm between the tensile forces in the steel tube and the compression forces in concrete and steel tube increased with decreasing the concrete wall thickness. Moreover, since all columns have the same FRP and steel rigidities, confinement of columns having smaller concrete wall thickness was relatively higher. The concrete in the case of column

DST-2B sustained compressive stresses up to 175 MPa (25,382 psi) while the concrete in columns DST-3B and DST-4B sustained peak stresses of 168 MPa (24,366 psi) and 161 MPa (23,351 psi), respectively.

Local buckling occurred at drifts of 2% to 3%. Columns with a thicker concrete wall thickness locally buckled at higher drifts since the initial axial stresses on the steel tubes due to the applied axial load will be smaller on columns having thicker concrete wall. Moreover, for columns having thicker concrete walls (DST-3B and DST-4B), the confinement was not as effective as the columns having thinner concrete walls. Hence, for columns DST-3B and DST-4B, concrete reached their peak stresses at smaller drifts of 3% to 5% when the columns began to approach their peak strengths. This was followed by concrete strength gradual degradation and the local buckling in the steel tubes propagated rapidly leading to compression failure in the columns. Column that had a smaller concrete wall thickness (i.e., column DST-2B) were more confined, leading to the gradual propagation of local steel buckling. Hence, the concrete sustained higher stresses and placed higher dilation demand on the FRP, causing the FRP to rupture.

It is worth noting that the steel tubes in all of the specimens, except specimen DST-4B, yielded in tension. The steel tube in specimen DST-4B had the thickest concrete wall was the only tube in the specimens presented in this manuscript that did not reach tensile yielding.

Effects of Column Concrete Strength (f'_c) on the Behavior of FSDT

Four columns, namely, DST-1, DST-2C, DST-3C, and DST-4C were studied with different concrete compressive strengths (f'_c) of 95.0 MPa (13,775 psi), 69.0 MPa

(10,000 psi), 51.7 MPa (7,500 psi), and 34.5 MPa (5,000 psi), respectively. As shown in Figs. 8(c) and 9(c) as well as Table 4, by increasing the concrete compressive strength, the bending strength increased while the lateral drift decreased. Increasing the concrete compressive strength by 175% i.e. from 34.5 MPa (5000 psi) to 95 MPa (13775 psi) increased the bending strength by 56% i.e. from 21.7 kN.m (16.0 kip-ft) for column DST-4C to 33.8 kN.m (24.9 kip-ft) for column DST-1 and the maximum lateral drift decreased from 11.3% for column DST-4C to 8.9% for column DST-1.

The concrete's compressive strength had an insignificant effect on the onset of steel tube local buckling. All tubes locally buckled at drifts of 2.5% to 3.0%. However, once locally buckled the rate of strength degradation in the compression steel in the columns that have lower values of f_c' was slightly slower than those having higher values of f_c'. This occurred since for a given number of FRP layers, the lower the concrete compressive strength is the highest confinement effectiveness and ductility.

Expectedly, the concrete in column DST-4C, which had a f_c' of 34.5 MPa (5,000 psi), sustained compressive stress up to 248% f_c' at a drift of approximately 6.1%, while the concrete in column DST-1, which had a f_c' of 95 MPa (13,775 psi), sustained compressive stress up to 187% f_c' at a drift of 5%. Beyond these drifts, the columns strengths decreased gradually due to compression failure.

Effects of D/T Ratio of the Steel Tube on the Behavior of FSDT

Five columns, namely, DST-1, DST-2D, DST-3D, DST-4D, and DST-5D were studied with the diameter-to-thickness (D/t) of 27.8, 45.0, 60.0, 75.0 and 90.0, respectively. As shown in Figs. 8(d), and 9(d) as well as Table 4, the bending strength decreased linearly

and the drift decreased nonlinearly as the D/t increased. Increasing the D/t by 224% (i.e., from 27.8 to 90.0) decreased the bending strength by 19% from 33.8 kN.m (24.9 kip-ft) to 27.4 kN.m (20.2 kip-ft) for columns DST-1 and DST-5D, respectively. Similarly, the drift decreased by 17% from 8.9% to 7.4% for columns DST-1 and DST-5D, respectively.

All columns in this group failed by compression failure. Similar to the other columns, local buckling occurred at drifts of 2.8% to 3.1% and tensile yielding at drifts of 2.6% to 3.2%. Local buckling propagated quite slowly for thicker steel tubes allowing their columns to display higher ultimate drifts than thinner steel tubes. Local buckling led to concrete crushing.

Effects of the Number of FRP Layers on the Behavior of FSDT

Four columns, namely, DST-1, DST-2E, DST-3E, and DST-4E had 3, 5, 7, and 9 FRP layers, respectively. Expectedly, both the bending strength and the lateral drift increased as the number of layers increased as shown in Figs. 8(e) and 9(e) as well as Table 4. However, the increase in the lateral drift was more pronounced than the increase in the bending strength. Increasing the FRP layers by 200% (i.e., from 3 to 9 layers) increased the bending strength by 17% i.e., from 33.8 kN.m (24.9 kip-ft) to 39.5 kN.m (29.1 kip-ft) while increased the lateral drift by 31% i.e., from 8.9% to 11.7%. All of the specimens in this set failed due to compression failure.

Increasing the number of FRP layers increased the confined concrete strength and stiffness, which increased the concrete contribution to the lateral load resistance mechanism delaying the onset of the steel tube local buckling. For column DST-1 local

buckling occurred at a drift of 2.8%; tripling the number of FRP layers in column DST-4E, the local buckling occurred at a drift of 4.0%. Moreover, while the concrete in column DST-1, which has 3 layers of FRP, sustained an axial stress up to 187% f_c', column DST-3E, which has 7 layers of FRP, sustained an axial stress up to 205% f_c'. Increasing the number of FRP layers to 9 layers did not improve the concrete confinement compared to the column having 7 layers since confinement does not depend exclusively on FRP rigidity but also on the steel rigidity. Since the steel rigidity was the same in this set of column, there seems that there is a threshold on FRP rigidity beyond which increasing FRP rigidity does not significantly improve the column behavior. Finally, local buckling in the steel tubes led to a gradual reduction in the steel tube compressive stresses leading to more axial load demand on the concrete in compression. For columns with low number of FRP layers, once local buckling occurred, concrete began to dilate more rapidly loosing the confinement effect. In the case of DST-4E, beyond the initiation of local buckling concrete was still well-confined sustaining the high compressive stresses.

Effects of the Number of FRP Layers Combined with D/t ratio

The number of FRP layers versus D/t ratios of the steel tubes was investigated last. Twenty columns were investigated numerically as stated in Table 5. Four different numbers of FRP layers of 3, 5, 7, and 9 were studied in a matrix with five steel tube D/t ratios of 27.8, 45.0, 60.0, 75.0, and 90.0. The bending strength increased as the number of layers increased regardless of the steel tube D/t ratio as presented in Fig. 9(f). However, the bending strength decreased as the steel tube D/t ratio increased for the same number

of FRP layers. The relationship between the number of FRP layers and the bending strength nearly linear, regardless of the steel tube D/t ratio. It is worthy noted that, for a given number of FRP layers, the rate of increase in the bending decrease with increasing D/t ratio.

Flexural Analysis of FSDT Columns

Nonlinear analysis, considering Navier-Bernoulli's assumptions and strains compatibility, was used to calculate the flexural strength of FSDT columns. The main assumptions in the analysis were as follows: a) The plane section remained plane both before and after deformation occurred; b) Full composite action between the steel tube and concrete; c) The stress-strain relationship of steel was assumed elastic-perfectly plastic; d) the stress-strain relationship of concrete in the FRP-concrete-steel double skin sections (developed by Yu et al. 2010) was adopted. Moment-curvature analysis (including the applied axial load effects) was conducted and the lateral load capacity was determined for each column.

The bending strengths calculated using the analytical procedure for the specimens tested by Ozbakkaloglu and Idris (2014) are presented in Table 6 and Fig. 3. The analytical procedure overestimated the strength for all of the specimens. The average, standard deviation, and range of errors in predicting the specimens' strengths were 8.2%, 8%, and 0.5% to 19.4%, respectively. The error in the strength prediction increased as the number of FRP layers increased. However, the error decreased as the steel tube D/t ratio increased.

This analytical procedure was also used to calculate the bending strengths of the specimens that were used for the parametric studies. Tables 4 and 5 list the bending strengths obtained from the finite element models as well as the analytical procedure. The analytical procedure systematically over-predicted the strength (as compared to the FE results). The average, standard deviation, and range of errors in predicting the strengths of the specimens were 6%, 4%, and -0.1% to 13.0%, respectively.

Conclusions

This paper discusses the finite element analysis of hybrid FRP-concrete-steel double-skin tubular columns (FSDTs) using LS-DYNA software. The FSDTs examined consisted of a concrete wall sandwiched between an outer FRP tube and an inner steel tube. The finite element analysis was validated against experimental results available in the corresponding literature. The proposed model was able to predict the FSDT column's behavior very well in both ultimate moment and lateral drift. The Karagozian and Case Concrete Damage Model Release 3 (K&C model), with automatically generated parameters, produces good results for concrete modelling, including high strength concrete. An analytical model based on Navier-Bernoulli's assumptions and strains compatibility was also used to predict the FSDT's strength. Based on the finite element analyses and analytical model, it is concluded that:

1. The behavior of FSDT column is complex and is controlled by the interaction of the steel tube stiffness, the concrete wall stiffness, and the FRP hoop stiffness. Local buckling occurred in all of the specimens investigated using the finite element analysis, which triggered the rupture of the FSDT system. The rate of

local buckling propagation depends on the FRP confinement ratio, the steel tube diameter/ steel tube thickness (D/t), concrete unconfined compressive strength, and the concrete wall thickness.

2. Two modes of failure were defined, namely, steel/concrete compression failure and FRP rupture. Compression failure is relatively gradual while failure due to FRP rupture is quite abrupt. However, FRP rupture occurs at higher drifts than does concrete crushing.
3. The bending strength increases as the applied axial load, concrete compressive strength, and number of FRP layers increase.
4. The bending strength increases as the concrete wall thickness and the D/t ratio decrease.
5. The columns' drifts increase as the applied axial load, unconfined concrete compressive strength, and steel tube D/t decrease. The columns' drifts increase as the FRP layers increase.
6. The bending strength increases as the number of layers increases regardless of the steel tube D/t ratio within the range of the parameters investigated in this study.

Acknowledgement

This research was conducted by Missouri University of Science and Technology and was supported by Missouri Department of Transportation (MoDOT) and Mid-American Transportation Center (MATC). This support is gratefully appreciated. However, any opinions, findings, conclusions, and recommendations presented in this paper are those of the authors and do not necessarily reflect the views of the sponsors.

References

Abdelkarim, O. and ElGawady, M. (2014). "Behavior of Hybrid FRP-Concrete-Steel Double-Skin Tubes Subjected to Cyclic Axial Compression." Structures Congress 2014: pp. 1002-1013.

ACI Committee 318 (2011). "Building Code Requirements for Structural Concrete (ACI318-11) and Commentary (318R-11)." American Concrete Institute, Farmington Hills, Mich., 509 pp.

Dawood, H., ElGawady, M. (2013). "Performance-based seismic design of unbonded precast post-tensioned concrete filled GFRP tube piers." Composites Part B: Engineering, Volume 44, Issue 1, Pages 357-367.

Dawood, H., ElGawady, M., and Hewes, J. (2012). "Behavior of Segmental Precast Post-Tensioned Bridge Piers under Lateral Loads." ASCE Journal of Bridge Engineering, Vol. 17, No. 5, pp. 735-746.

ElGawady, M. and Dawood, H. (2012). "Analysis of segmental piers consisted of concrete filled FRP tubes." Engineering Structures, Vol. 38, pp. 142-152.

ElGawady, M., Booker, A., and Dawood, H. (2010). "Seismic Behavior of Posttensioned Concrete-Filled Fiber Tubes." J. Compos. Constr., 14(5), 616–628.

ElGawady, M. and Sha'lan, A. (2011). "Seismic Behavior of Self-Centering Precast Segmental Bridge Bents." J. Bridge Eng., 16(3), 328–339.

Hajjar J. (2000). "Concrete-filled steel tube columns under earthquake loads." Structural Engineering and Materials; 2(1):72–82.

Han, L.H., Tao, Z., Liao, F.Y., and Xu, Y. (2010). "Tests on Cyclic Performance of FRP-Concrete –Steel Double-Skin Tubular Columns." Thin-Walled Structures, 4, 430-439.

Huang, H., Han, L. H., Zhao, X. (2013). "Investigation on concrete filled double skin steel tubes (CFDSTs) under pure torsion." Journal of Constructional Steel Research, Volume 90, 221-234.

LS-DYNA. (2007). "Keyword user's manual." Livermore Software Technology Corporation, CA.

Li, W., Han,L. H., Chan, T. (2014a). "Tensile behaviour of concrete-filled double-skin steel tubular members." Journal of Constructional Steel Research, Volume 99, 35-46.

Li, W., Han,L. H., Chan, T. (2014b). "Numerical investigation on the performance of concrete-filled double-skin steel tubular members under tension." Thin-Walled Structures, Volume 79, 108-118.

Lu, H., Zhao, X., Han, L. H. (2010). "Testing of self-consolidating concrete-filled double skin tubular stub columns exposed to fire." Journal of Constructional Steel Research, Volume 66, Issues 8–9, 1069-1080.

Malvar, L., Crawford, J., Wesevich, J., and Simons, D. (1997). "A plasticity concrete material model for DYNA3D." Int. J. Impact Eng., 19(9–10), 847–873.

Montague, P., (1978). "Experimental behavior of double-skinned, composite, circular cylindrical-shells under external-pressure." Journal of Mechanical Engineering Science, 20(1), pp. 21–34.

Moon, J., Lehman, D., Roeder, C., and Lee, H. (2013). "Strength of Circular Concrete-Filled Tubes with and without Internal Reinforcement under Combined Loading." J. Structural Engineering, 139(12).

Ozbakkaloglu, T. and Idris, Y. (2014). "Seismic Behavior of FRP-High-Strength Concrete–Steel Double-Skin Tubular Columns." J. Struct. Eng., 140(6), 04014019.

Ryu, D., Wijeyewickrema, A., ElGawady, M., and Madurapperuma, M. (2014). "Effects of Tendon Spacing on In-Plane Behavior of Post-Tensioned Masonry Walls." J. Struct. Eng., 140(4), 04013096.

Shakir-Khalil, H., and Illouli, S. 1987. "Composite columns of concentric steel tubes." Proc., Conf. on the Design and Construction of Non-Conventional Structures, Vol. 1, London, pp. 73–82.

Shin, M. and Andrawes, B. (2010). “Experimental Investigation of Actively Confined Concrete Using ShapeMemory Alloys.” J. Eng. Struct. 32:3, 656-664.

Teng, J.G., Yu, T., and Wong, Y.L. (2004). “Behavior of Hybrid FRP-Concrete-Steel Double-Skin Tubular Columns.” Proc. 2nd Int. Conf. on FRP Composites in Civil Engineering, Adelaide, Australia, 811-818.

Teng, J.G., Yu, T., Wong, Y.L., and Dong, S.L. (2005). “Innovative FRP-Steel-Concrete Hybrid Columns.” Advances in Steel Structures, 1, 545-554.

Teng, J. G., Yu, T., Wong, Y. L., and Dong, S. L. (2007). “Hybrid FRP concrete-steel tubular columns: Concept and behavior.” Constr. Build. Mater., 21(4), 846–854.

Wong, Y. L., Yu, T., Teng, J. G., and Dong, S. L. (2008). “Behavior of FRP-confined concrete in annular section columns.” Compos. B Eng., 39(3), 451–466.

Yagishita F, Kitoh H, Sugimoto M, Tanihira T, Sonoda K. (2000). “Double-skin composite tubular columns subjected cyclic horizontal force and constant axial force.” Proceedings of the Sixth ASCCS Conference, Los Angeles, USA, March 22–24, pp. 497–503.

Yu, T., Wong, Y., Teng, J., Dong, S., and Lam, E. (2006). “Flexural Behavior of Hybrid FRP-Concrete-Steel Double-Skin Tubular Members.” J. Compos. Constr., 10(5), 443–452.

Yu, T., Teng, J., and Wong, Y. (2010). “Stress-Strain Behavior of Concrete in Hybrid FRP-Concrete-Steel Double-Skin Tubular Columns.” J. Struct. Eng., 136(4), 379–389.

Zhang, B., Teng, J. G. and Yu, T. (2012). “Behaviour of hybrid double-skin tubular columns subjected to combined axial compression and cyclic lateral loading.” Sixth International Conference on FRP Composites in Civil Engineering (pp. 1-7). Rome, Italy.

Zhu, Z., Ahmad, I., and Mirmiran, A. (2006). “Seismic performance of concrete-filled FRP tube columns for bridge substructure.” J. Bridge Eng., 11(3), 359–370.

Table 1. Summary of columns variables (reproduced after Ozbakkaloglu and Idris 2014)

Column	f_c'	FRP tube		Inner steel tube	P	P/P_o
	(MPa (psi))	Material	n*	t (mm (in.))	(kN (kips))	
DST-1	95 (13,775)	AFRP	3	3.2 (0.126)	545 (122.5)	0.45
DST-2	95 (13,775)	AFRP	2	3.2 (0.126)	410 (92.2)	0.34
DST-3	95 (13,775)	AFRP	3	3.2 (0.126)	410 (92.2)	0.34
DST-5	115 (16,675)	AFRP	4	3.2 (0.126)	625 (140.5)	0.45
DST-6	115 (16,675)	CFRP	5	3.2 (0.126)	625 (140.5)	0.45
DST-7	95 (13,775)	AFRP	3	5.5 (0.217)	675 (151.7)	0.45
DST-9	130 (18,850)	AFRP	6	3.2 (0.126)	690 (155.1)	0.45

*n: number of FRP layers

Table 2. Summary of orthotropic material properties for FRP tubes

Material properties	AFRP tube	CFRP tube
Elastic modulus in the hoop direction (Ea) (GPa (ksi))	125.7 (18,226)	251.0 (36,404)
Ultimate tensile hoop strain	0.0212	0.0144
Shear modulus (Gab) (GPa (ksi))	9.25 (1,341)	9.60 (1,392)
Poisson's ratio (PR)	0.25	0.25

Table 3. Summary of experimental results vs. finite element results

Column	$M_{capacity}$				Percentage of error**	Mode of failure	
	EXP.		FE			EXP.	FE
	kN.m	kip-ft	kN.m	kip-ft			
DST-1	36.5	26.9	33.8	24.9	7.4	FRP rupture	Compression failure
DST-2	28.6	21.1	30.7	22.7	7.6	FRP rupture	FRP rupture
DST-3	32.6	24.0	32.1	23.7	1.3	FRP rupture	FRP rupture
DST-5	40.7	30.0	39.0	28.8	4.0	FRP rupture	Compression failure
DST-6	42.0	31.0	39.6	29.2	5.8	FRP rupture	Compression failure
DST-7	39.7	29.3	43.3	31.9	8.9	FRP rupture	FRP rupture
DST-9	41.0	30.3	43.9	32.3	6.6	N/A*	Compression failure

*Not reported

**The percentage of the absolute value of the difference between the experimental and the FE ultimate moments divided by the experimental ultimate moment

Table 4. Summary of the parametric study results

Group	Model name	Description		FE results			Analytical results	
				$M_{capacity}$		Lateral drift	$M_{capacity}$	
				kN.m	kip-ft		kN.m	kip-ft
A	DST-1	Load Level	45.0% P_o	33.8	24.9	8.9	36.7	27.1
	DST-2A		30.0% P_o	30.8	22.7	9.5	32.4	23.9
	DST-3A		15.0% P_o	24.9	18.4	13.0	26.0	19.2
	DST-4A		7.5% P_o	20.7	15.2	13.0	22.1	16.3
B	DST-1	Wall thick	30.5 mm (1.2 in.)	33.8	24.9	8.9	36.7	27.1
	DST-2B		20.3 mm (0.8 in.)	38.1	28.1	7.5	39.7	29.3
	DST-3B		40.6 mm (1.6 in.)	31.0	22.9	8.3	33.6	24.8
	DST-4B		50.8 mm (2.0 in.)	29.2	21.5	7.7	31.5	23.2
C	DST-1	f_c'	95.0 MPa (13,775 psi)	33.8	24.9	8.9	36.7	27.1
	DST-2C		69.0 MPa (10,000 psi)	28.7	21.2	9.3	31.5	23.3
	DST-3C		51.7 MPa (7,500 psi)	25.2	18.6	10.0	27.8	20.5
	DST-4C		34.5 MPa (5,000 psi)	21.7	16.0	11.3	24.8	18.3
D	DST-1	$\frac{D}{t}$	27.8	33.8	24.9	8.9	36.7	27.1
	DST-2D		45.0	30.2	22.3	8.1	31.9	23.6
	DST-3D		60.0	28.8	21.3	7.7	29.8	22.0
	DST-4D		75.0	28.0	20.7	7.5	28.4	20.9
	DST-5D		90.0	27.4	20.2	7.4	27.5	20.3
E	DST-1	Number of FRP layers	3	33.8	24.9	8.9	36.7	27.1
	DST-2E		5	36.3	26.8	10.3	40.4	29.8
	DST-3E		7	38.2	28.2	11.2	43.0	31.7
	DST-4E		9	39.5	29.1	11.7	44.9	33.1

Table 5. Results summary of number of FRP layers versus steel tube D/t ratios

Group	Model name	Description		FE $M_{capacity}$		Analytical $M_{capacity}$	
		Number of FRP layers	D/t	kN.m	kip-ft	kN.m	kip-ft
F	DST-1	3	27.8	33.8	24.9	36.7	27.1
	DST-2E	5		36.3	26.8	40.4	29.8
	DST-3E	7		38.2	28.2	43.0	31.7
	DST-4E	9		39.5	29.1	44.9	33.1
	DST-2D	3	45	30.2	22.3	31.9	23.6
	DST-2F	5		32.5	23.9	34.7	25.6
	DST-3F	7		34.0	25.1	36.6	27.0
	DST-4F	9		35.6	26.2	38.0	28.0
	DST-3D	3	60	28.8	21.3	29.8	22.0
	DST-5F	5		30.9	22.8	33.1	23.7
	DST-6F	7		32.4	23.9	33.8	24.9
	DST-7F	9		33.8	25.0	35.0	25.8
	DST-4D	3	75	28.0	20.7	28.4	20.9
	DST-8F	5		29.9	22.1	30.5	22.5
	DST-9F	7		31.4	23.2	32.0	23.6
	DST-10F	9		32.7	24.1	33.1	24.4
	DST-5D	3	90	27.4	20.2	27.5	20.3
	DST-11F	5		29.4	21.7	29.5	21.7
	DST-12F	7		30.9	22.8	30.8	22.7
	DST-13F	9		32.1	23.7	31.8	23.5

Table 6. Summary of experimental results vs. simplified analytical method

Column	$M_{capacity}$				Percentage of error*
	EXP.		Analytical		
	kN.m	kip-ft	kN.m	kip-ft	
DST-1	36.5	26.9	36.7	27.1	0.5
DST-2	28.6	21.1	31.9	23.5	11.5
DST-3	32.6	24.0	33.5	24.7	2.8
DST-5	40.7	30.0	42.3	31.2	3.9
DST-6	42.0	31.0	42.6	31.4	1.4
DST-7	39.7	29.3	47.4	34.9	19.4
DST-9	41.0	30.3	48.2	35.6	17.6

*The percentage of the absolute value of the difference between the experimental and the analytical ultimate moments divided by the experimental ultimate moment

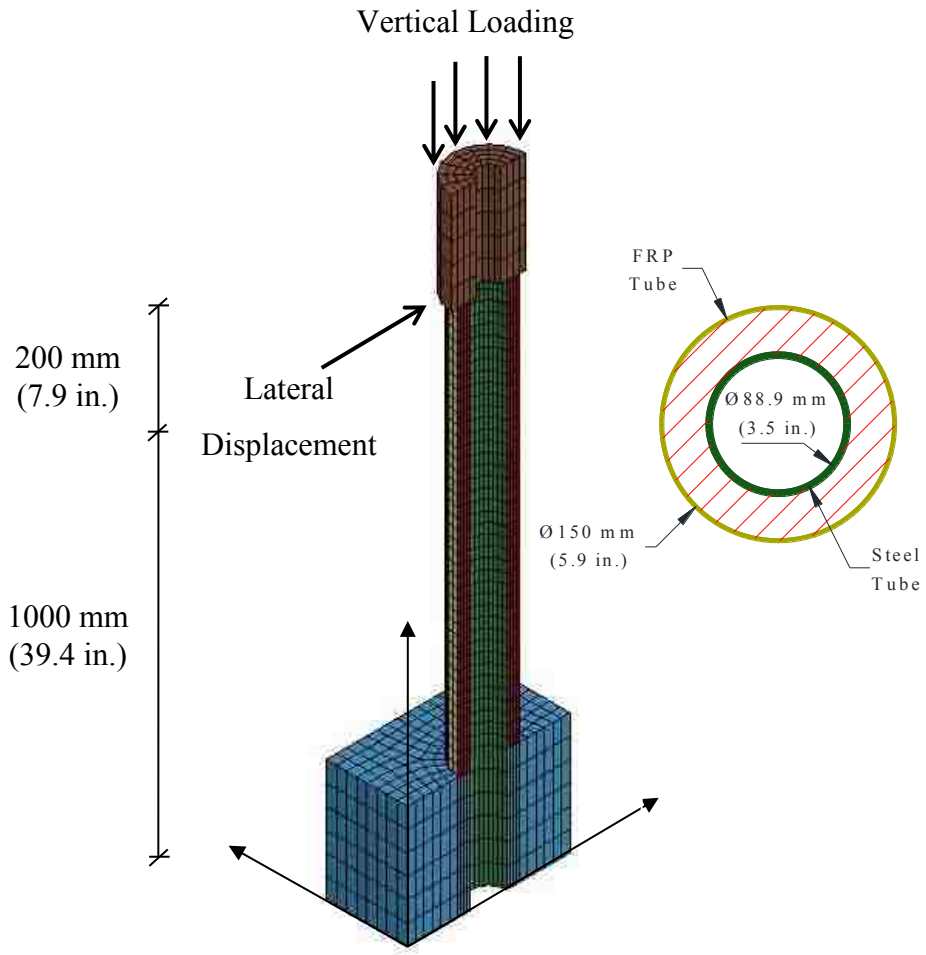

Fig. 1. 3D view of simulated FSDT column

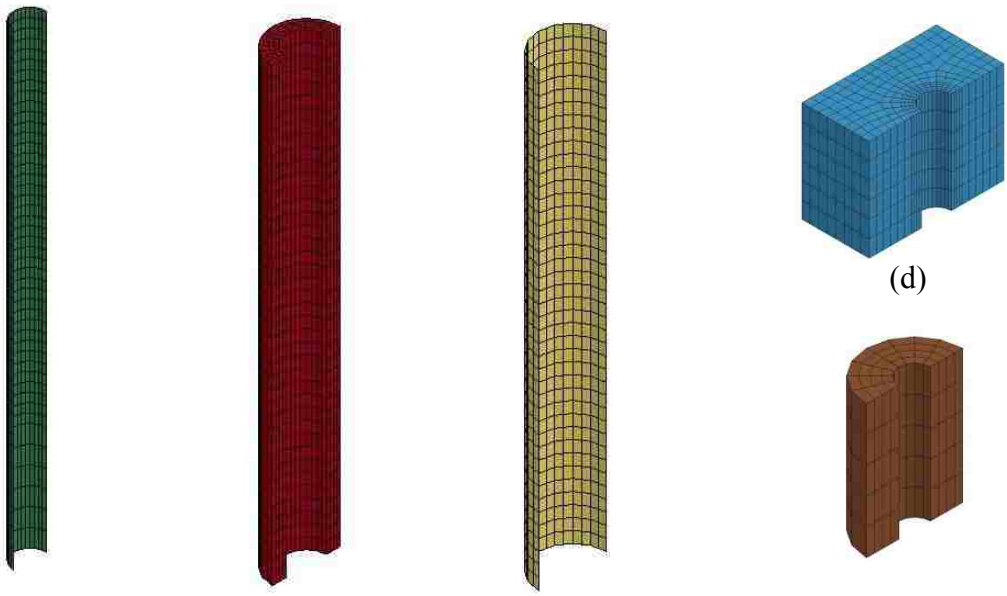

Fig. 2. (a) Steel tube, (b) Concrete column, (c) FRP tube, (d) Concrete footing, (e) Loading stub

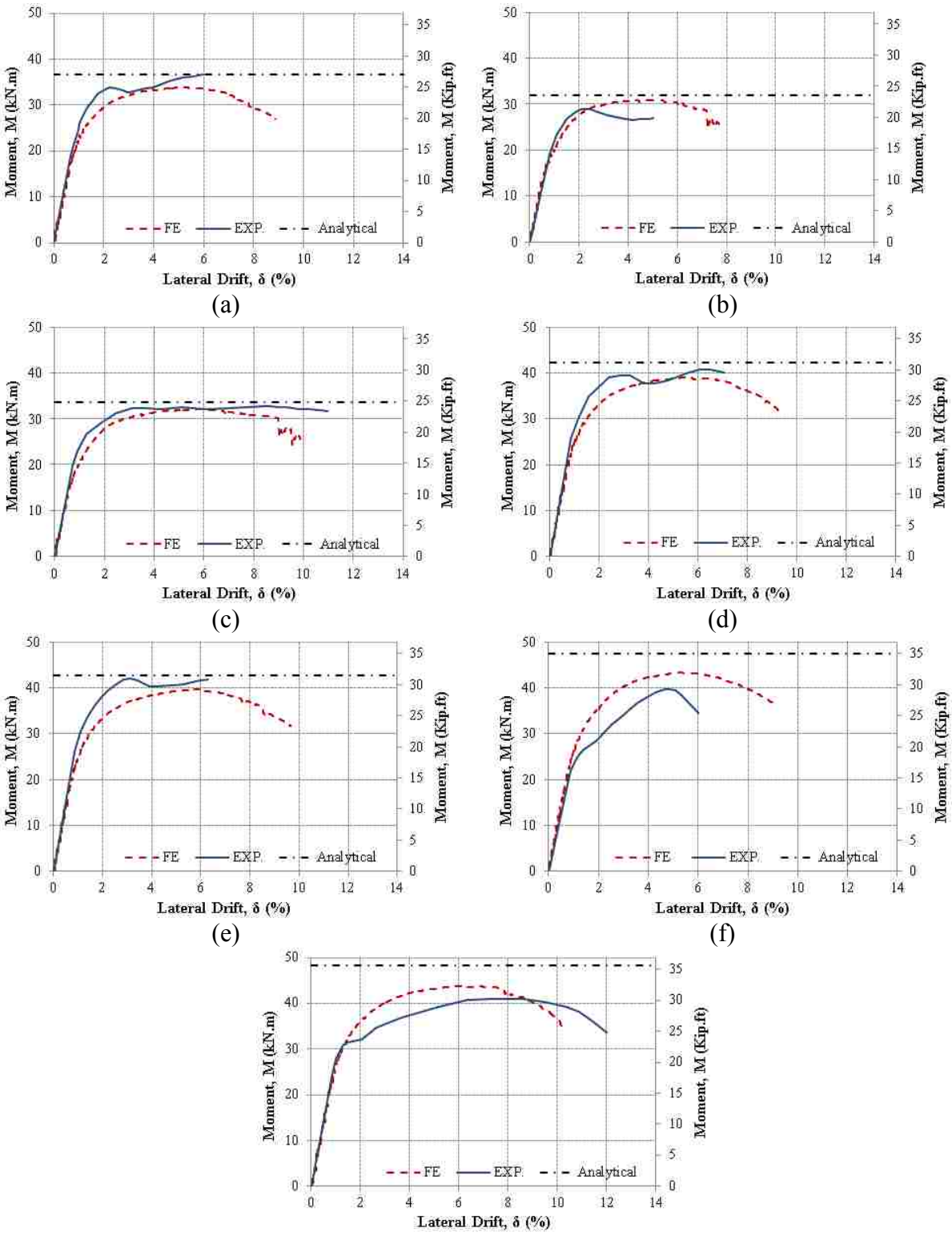

Fig. 3. Experimental (Ozbakkaloglu and Idris 2014 ©ASCE) vs. FE backbone curves for specimens: (a) DST-1, (b) DST-2, (c) DST-3, (d) DST-5, (e) DST-6, (f) DST-7, (g) DST-9

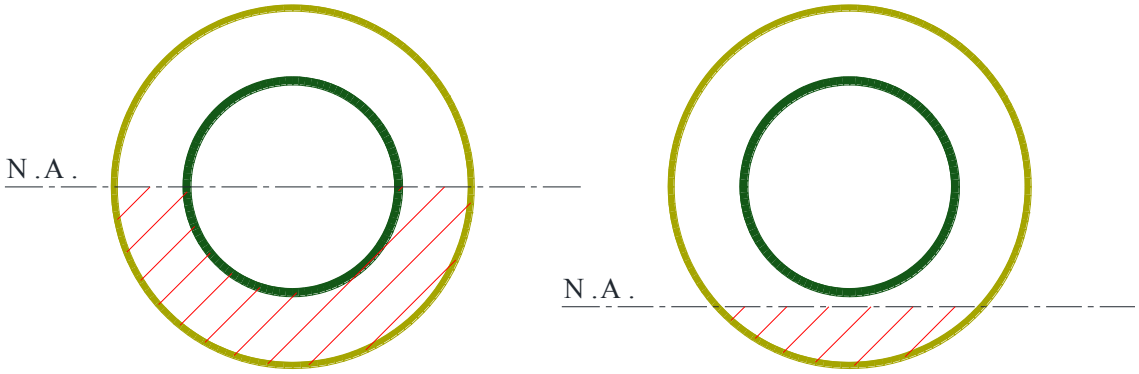

Fig. 4. Moving of neutral axis (N.A.) under lateral loading (hatched area is the compression side)

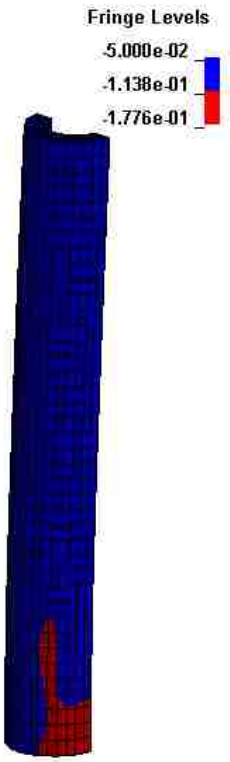

Fig. 5. Maximum confined concrete stress of the column DST-1 in GPa. (1 GPa = 145 ksi)

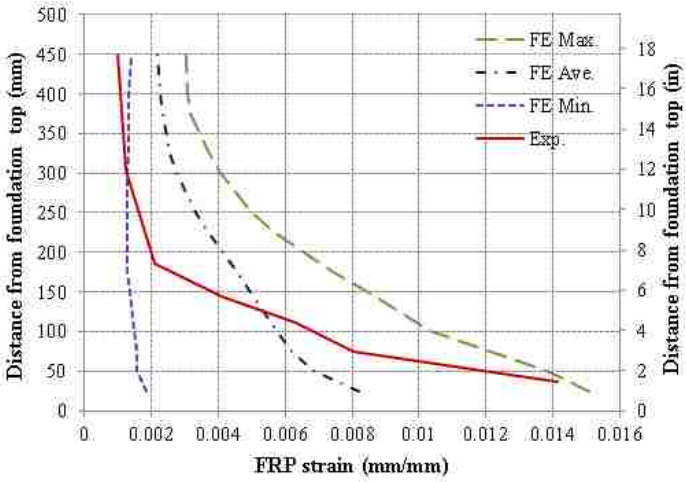

Fig. 6. FE vs. experimental (Ozbakkaloglu and Idris 2014 ©ASCE) strain profile of the FRP tube of column DST-1

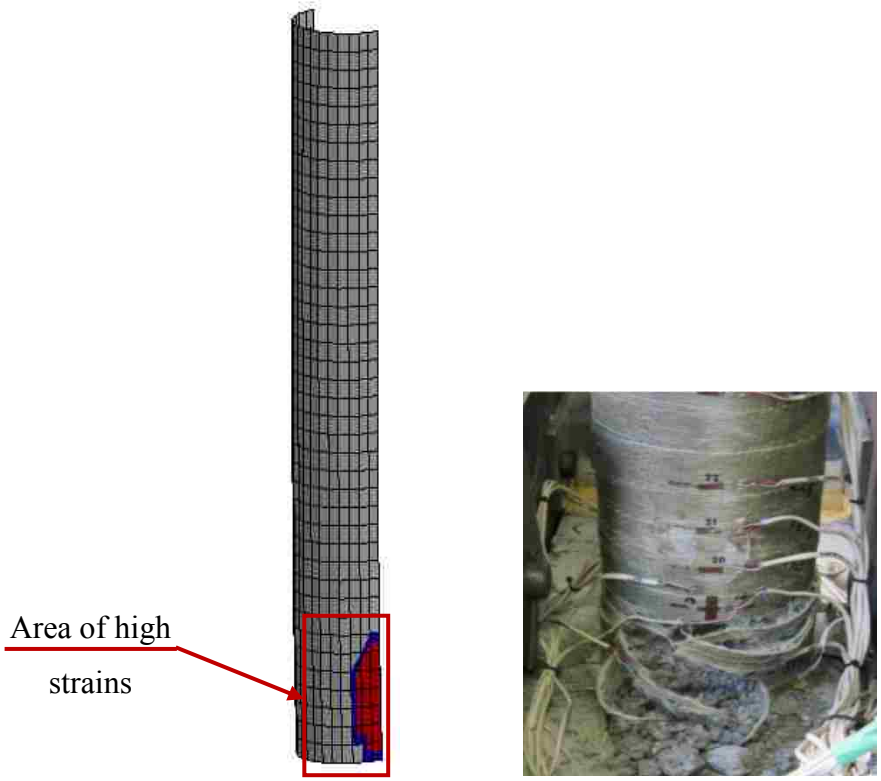

Fig. 7. Fiber rupture of FRP tube of the column DST-7; (a) FE result and (b) Experimental result (Ozbakkaloglu and Idris 2014 ©ASCE)

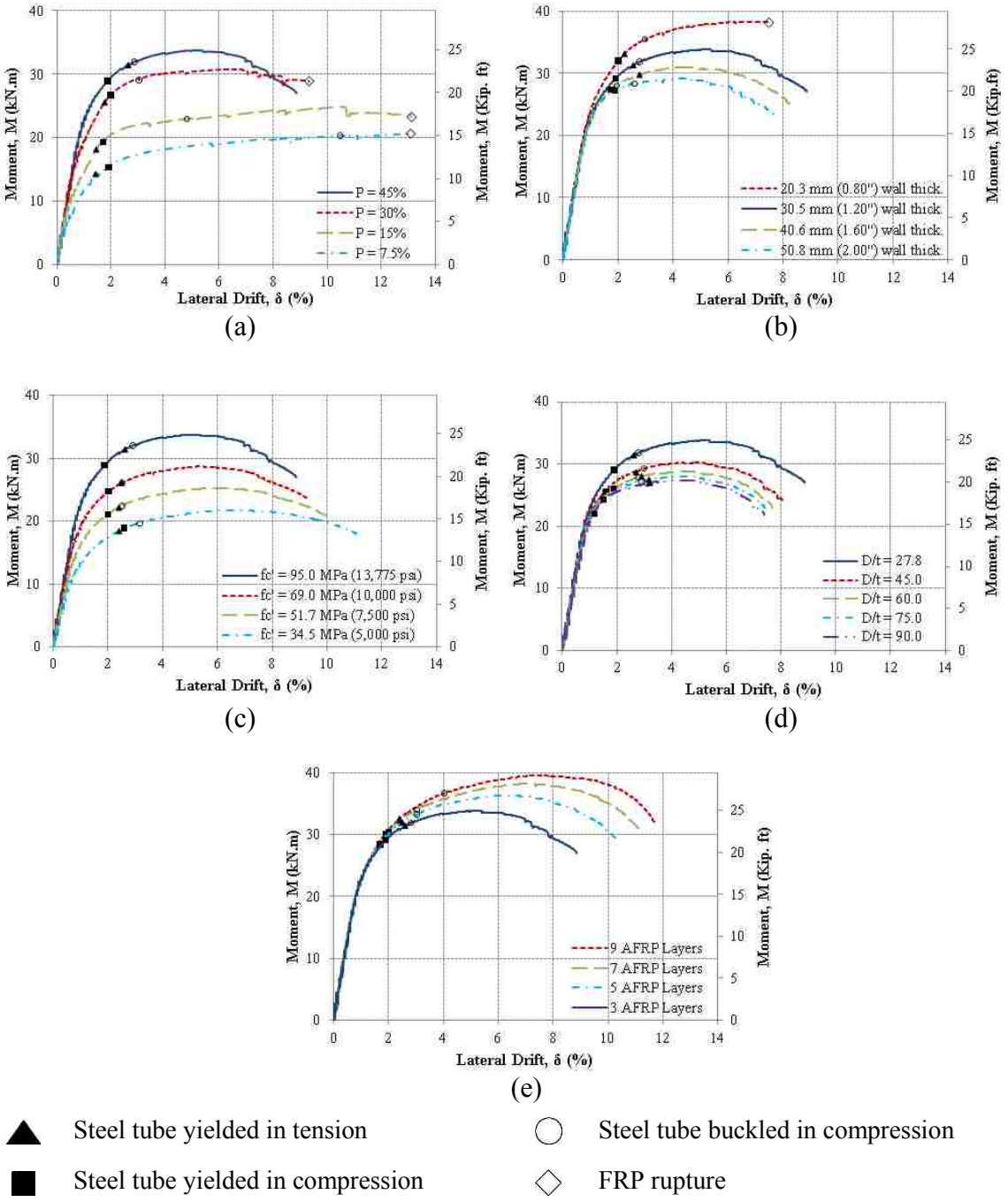

Fig. 8. Lateral drift vs. Moment for finite element parametric study: (a) Load level change, (b) Concrete wall thickness change, (c) Concrete strength change, (d) D/t for steel tube change, (e) Number of FRP layers change

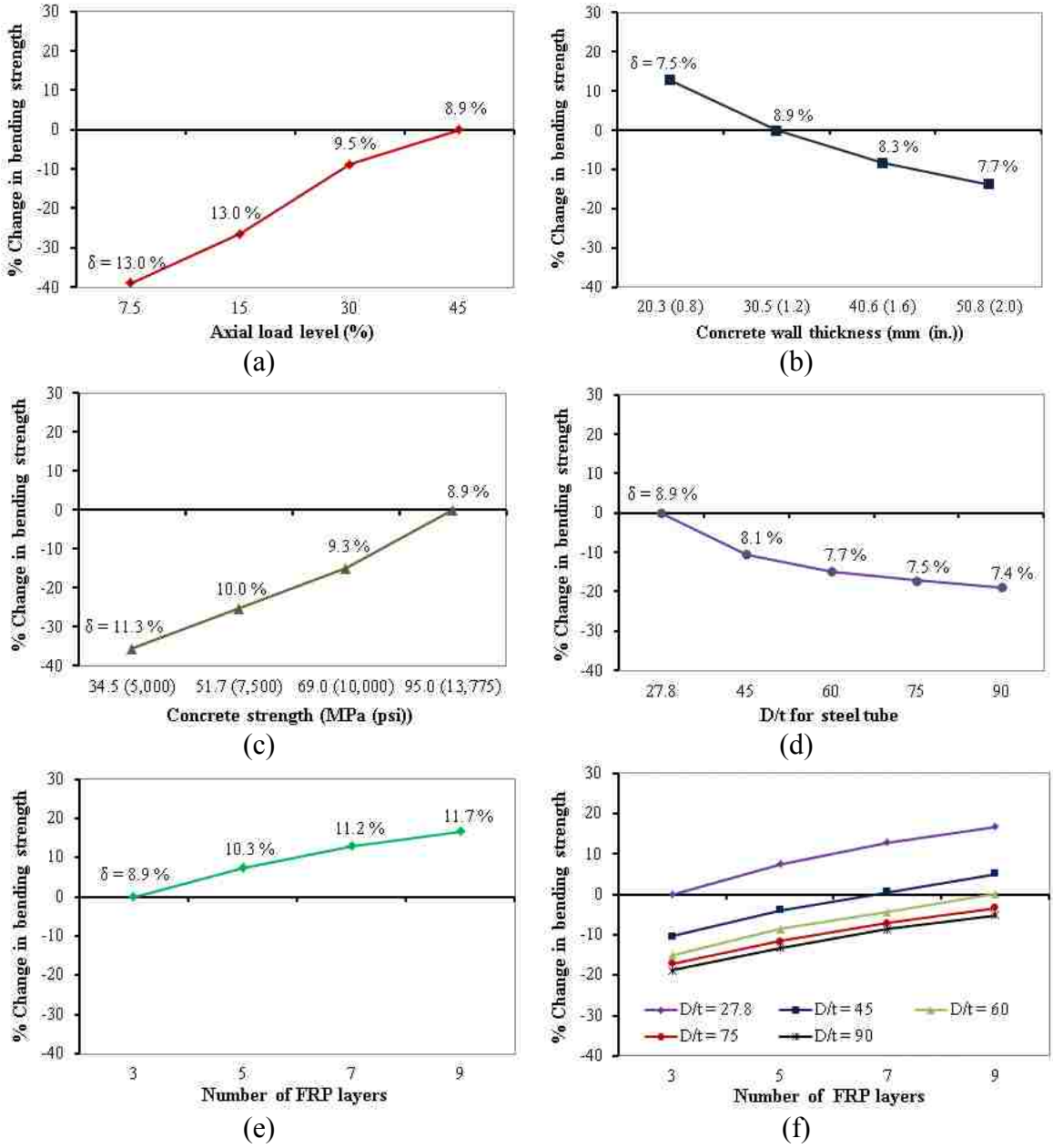

Fig. 9. Percentage change of the bending strength and the maximum lateral drift versus; (a) Loading level, (b) Concrete wall thickness, (c) Concrete strength, (d) D/t for steel tube, (e) Number of FRP layers, (f) Number of FRP layers with different steel tube D/t

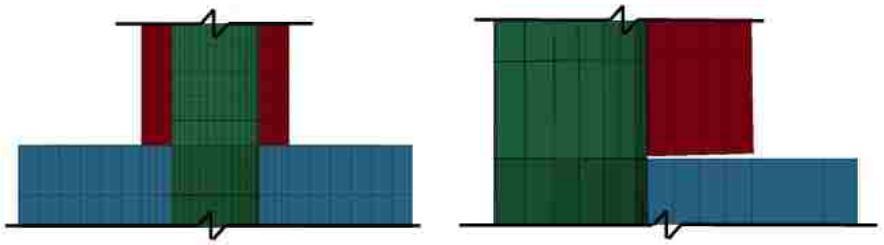

(a) (b)

Fig. 10. Column-footing connection (a) closed connection, (b) uplift of the heel of the connection

III. BEHAVIOR OF HOLLOW-CORE FRP-CONCRETE-STEEL COLUMNS UNDER STATIC CYCLIC FLEXURAL LOADING

Omar I. Abdelkarim[1], S.M. ASCE; Mohamed A. ElGawady[2]§, PhD, M. ASCE; Sujith Anumolu[3]; Ahmed Gheni[4]; Gregory E. Sanders, P.E[5]

Abstract

This paper presents the seismic behavior of hollow-core fiber reinforced polymer-concrete-steel (HC-FCS) columns. The typical HC-FCS column consists of a concrete wall sandwiched between an outer fiber reinforced polymer (FRP) tube and an inner steel tube. The HC-FCS column represents a compact engineering system; the steel and FRP tubes act together as stay-in-place formworks. The steel tube acts as a flexural and shear reinforcement. Three large-scale columns, including one RC column having a solid cross-section and two HC-FCS columns, were investigated during this study. Each column had an outer diameter of 610 mm (24 inches) and a height-to-diameter ratio of 4.0. The steel tube was embedded into reinforced concrete footing with an embedded length of 1.6 times the steel tube diameter, while the FRP tube only confined the concrete wall thickness and truncated at the top of the footing. The HC-FCS columns exhibited high lateral drift reaching to 15.2%, and failed gradually due to concrete crushing and local steel tube buckling, followed by FRP rupture. The reference RC column failed at a drift

1 Ph.D. Candidate, Dept. of Civil, Architectural, and Environmental Engineering, Missouri University of Science and Technology, Rolla, MO. 65401; oiafgc@mail.mst.edu

2 Benavides Associate Professor, Dept. of Civil, Architectural, and Environmental Engineering, Missouri University of Science and Technology, Rolla, MO. 65401; elgawadym@mst.edu
§Corresponding author

3 Graduate Research Assistant, Dept. of Civil, Architectural, and Environmental Engineering, Missouri University of Science and Technology, Rolla, MO. 65401; sat6f@mst.edu

4 Ph.D. Candidate, Dept. of Civil, Architectural, and Environmental Engineering, Missouri University of Science and Technology, Rolla, MO. 65401; aagmr6@mst.edu

5 Structural Development and Support Engineer Bridge Division, Central Office Missouri Dept. of Transportation, Jefferson City, MO. 65400, Gregory.Sanders@modot.mo.gov

of 10.9% due to rebar fracture. The HC-FCS column dissipated high energy, reaching 1.9 times that of the RC column.

Keywords: Bridge Columns, Precast Columns, Composite Columns, Hollow Columns, Seismic Loading

Introduction

Hollow-core concrete columns have been used for very tall bridge columns in seismic areas including New Zealand, Japan, and Italy. Using hollow-core cross-sections reduces the mass of the column, which reduces the bridge self-weight contributing to the inertial forces. Hollow-core columns also reduce the required foundation dimensions substantially, thereby reducing construction costs.

Researchers investigated the seismic behavior of hollow-core concrete columns that have two coaxial layers of reinforcement connected using a significant amount of cross ties placed throughout the wall's thickness (Mander et al. 1983; Yeh et al. 2001; Lee et al. 2014). While such columns exhibited ductile behavior, they require extensive manpower during construction. Montague (1978) introduced a new form of hollow-core column, which consists of a concrete wall that is sandwiched between two generally concentric steel tubes. These columns have been investigated extensively (Huang et al. 2013; Fouche and Bruneau 2010; Uenaka et al. 2010; Yagishita 2000; Hajjar 2000; Han et al. 2004; Shakir-Khalil & Illouli 1987). These columns have distinct advantages over conventional members like steel or reinforced concrete (RC). The steel tubes act as a stay-in-place formwork, longitudinal and shear reinforcements, and a continuous confinement to the concrete core, which increase the member's ductility and strength

compared to conventional hollow-core columns. Furthermore, the concrete core delays the local buckling of the steel tubes.

Fiber reinforced polymer (FRP) tubes have gained acceptance as an alternative to steel tubes in concrete-filled tube columns. Concrete-filled FRP tubes have benefits that are similar to those of concrete-filled steel tubes. However, FRP unlike steel tubes, FRP tubes have a higher strength-to-weight ratio and a higher corrosion resistance compared to steel tubes. Several researchers investigated the behavior of concrete-filled FRP tube columns under extreme loads (Qasrawi et al. 2014; Moon et al. 2013; ElGawady and Dawood 2012; ElGawady and Sha'lan 2011; Sadeghian and Fam 2010; ElGawady et al. 2010; Zhu et al. 2006; Shao and Mirmiran 2005; Fam et al. 2003; Zhang and Shahrooz 1997). More recently, Teng et al. (2004) used a section similar to that of Montague et al. (1983); however, FRP was used as an outer tube and steel as an inner tube. The hollow-core FRP-concrete-steel column (HC-FCS) system combines the benefits of all three materials: FRP, concrete, and steel, in addition to the benefits of the hollow-core concrete columns.

The HC-FCS columns have been investigated extensively under axial compression loading (e.g., Abdelkarim and ElGawady 2014a; Li et al. 2014; Yu et al. 2006, 2010; Wong et al. 2008; Teng et al. 2005, 2007). Fewer researchers investigated the performance of HC-FCS columns under flexure loading using numerical analysis (Abdelkarim and ElGawady 2014b) or experimental work (Ozbakkaloglu and Idris 2014; Zhang et al. 2012). These previous studies were carried out on small-scale specimens using manual wet layup unidirectional FRP, a low diameter-to-thickness (D_i/t_s) ratio of the steel tube (e.g., $D_i/t_s = 35$), and thick concrete wall thickness (i.e., low void ratio). The

results of the studies showed high concrete confinement and ductility of the HC-FCS columns under axial compression or flexure loading.

This manuscript investigates the first large-scale HC-FCS columns under seismic loading and compares the results with those of a conventional RC column. The investigated HC-FCS columns were constructed out of filament-wound FRP tubes with a thin concrete wall thickness (16% of the column diameter) and a steel tube with a high diameter-to-thickness ratio (D_i/t_s = 64).

Experimental Program

Three large-scale columns were tested as free cantilevers under both constant axial compression loading and cyclic lateral loading. Table 1 and Fig. 1 summarize the dimensions and variables of the test specimens. As shown in the figure and table, the first column was a conventional (RC) column having a solid cross-section, and the other two columns were HC-FCS columns. Each column had a circular cross-section with an outer diameter (D_o) of 610 mm (24 inch; Fig. 1) and a nominal inner diameter of 406 mm (16 inch). Each column had a height of 2,032 mm (80 inch). The lateral load was applied at a height (H) of 2,413 mm (95 inch) measured from the top of the footing, resulting in a shear-span-to-depth ratio (H/D_o) of approximately 4.0.

The column's label used in the current study consists of three syllabi. The first syllabus is a letter F referring to flexural testing followed by the column's height-to-outer diameter ratio (H/D_o). The second syllabus refers to the column's outer diameter (D_o) in inches. The third syllabus refers to the GFRP matrix, using E for epoxy and P for Iso-Polyster base matrices; this is followed by the GFRP thickness in a multiplication of 3.2

mm (1/8 inch), steel thickness in a multiplication of 3.2 mm (1/8 inch), and concrete wall thickness in a multiplication of 25.4 mm (1.0 inch). In the case of the reinforced concrete column, the third syllabus is replaced with RC. For example, a third syllabus of F4-24-E324 corresponds to an epoxy-based matrix for a GFRP tube having a wall thickness of 9.5 mm (0.375 inch), a steel tube having a wall thickness of 6.4 mm (0.25 inch), and concrete having a wall thickness of 102 mm (4 inch).

The F4-24-RC column had a longitudinal reinforcement of 8 φ 22 mm (8 # 7), corresponding to approximately 1.1% of the concrete cross-sectional area, and it had a transverse spiral reinforcement of φ 13 mm @ 76 mm (#4 @ 3 inch), corresponding to a volumetric reinforcement ratio of 1.0%. The concrete cover beyond the spiral reinforcement was 12.7 mm (0.5 inch; Fig. 1(a)). The column reinforcement details were selected to match the construction details used by the Missouri Department of Transportation (MoDOT).

The F4-24-E324 column was constructed using an outer filament-wound glass FRP tube with a wall thickness (t_{FRP}) of 9.5 mm (0.375 inch), an inner steel tube with an outer diameter (D_i) of 406 mm (16 inch) and a wall thickness (t_s) of 6.4 mm (0.25 inch) with a steel tube diameter-to-thickness (D_i/t_s) ratio of 64, and a concrete wall with a thickness (t_c) of 102 mm (4.0 inch; Fig. 1(b)). The F4-24-P124 column was similar to the F4-24-E324 except that the outer filament GFRP tube had a wall thickness of 3.2 mm (0.125 inch; Fig. 1(b)) and was made out of Iso-polyester matrix.

The inner steel tube of each of the HC-FCS columns was extended inside the footing and the column loading stub using an embedded length (L_e) of 635 mm (25 inch), representing 1.6 D_i. The FRP tube was truncated at the top surface of the footing and at

the bottom surface of the column's loading stub. The steel tube embedded length was determined based on a preliminary finite element analysis (Abdelkarim and ElGawady 2014b). None of the HC-FCS columns included any shear or flexure reinforcement except the steel tube.

Each column's footing had a length, width, and depth of 1,524 mm (60 inch), 1,219 mm (48 inch), and 864 mm (34 inch), respectively. The footing of the F4-24-RC column had bottom reinforcements of 7 φ 22 mm (7 # 7), top reinforcements of 4 φ 22 mm (4 # 7), and a shear reinforcement of φ13 mm @ 64 mm (#4 @ 2.5 inch; Fig. 1(a)). Each of the footings of the columns F4-24-E324 and F4-24-P124 had bottom reinforcements of 7 φ 22 mm (7 # 7), top reinforcements of 6 φ 22 mm (6 # 7), and shear reinforcement of φ13 mm @ 64 mm (#4 @ 2.5 inch; Fig. 1(b)).

Material Properties

Table 2 summarizes the unconfined concrete cylindrical strengths (f_c') for the columns and the footings at 28 days and on the days of the tests.

Three standard coupons were cut longitudinally from a steel tube for tensile tests according to ASTM A1067. The steel coupon tests were conducted under a displacement control of 0.76 mm/min. (0.03 inch/min). The steel tube had a yield stress, ultimate stress, yield strain, and ultimate strain of 324 MPa (47,000 psi), 483 MPa (70,000 psi), 1.6%, and 19.0%, respectively. The steel bars had a yield stress, ultimate stress, yield strain, and ultimate strain of 413 MPa (60,000 psi), 620 MPa (90,000 psi), 2.1%, and 8.0%, respectively.

According to ASTM D3039, three longitudinal FRP coupons were cut from each type of FRP tube. Each FRP coupon was subjected to a tensile test with a displacement loading rate of 1.27 mm/min. (0.05 in/min.). All of the FRP coupons failed by debonding between the FRP layers without fiber rupture. The ultimate stress was 65.5 MPa (9,500 psi). The saturated FRP with a fiber orientation at $\pm 53^{o}$ has a structure that depends on fibers in two directions [$\pm 53^{o}$] with adhesive material between them. The width of the strip is only 25 mm (1.0 inch), so there is no fiber continuity. As a result, the fibers delaminated in the coupon test. Therefore, the properties of the FRP were referenced based on the manufacturer's data sheet. Table 3 summarizes the properties of the FRP tubes.

Test Instrumentations

Fig. 2 shows the typical test instrumentations. Fifteen linear variable displacement transducers (LVDTs) and string potentiometers (SPs) were used to measure the displacement of each column. Two more LVDTs were attached to each footing to measure any potential sliding and uplift. A total of fourteen electrical strain gauges (SGs) were also symmetrically installed, on the two northmost and southmost longitudinal steel rebars in the RC column. Seventy-two strain gauges were symmetrically installed inside the steel tube of each HC-FCS column at nine levels at 127 mm (5 inch) intervals. Forty-eight strain gauges were installed on each FRP tube at six levels at 127 mm (5 inch) intervals. Two webcams were installed inside the steel tube of the F4-24-P124 column to monitor the deformations of the steel tubes (Fig. 3).

Test Setup and Loading Protocol

A constant axial load (P) of 490 kN (110 kips) representing 5% of the RC column axial capacity (P_o) was applied to each of the columns using six 12.7 mm (0.5 inch) external prestressing strands. P_o was calculated using Equation 1 (ACI 318-11).

$$P_o = A_s f_y + 0.85 f_c'(A_c - A_s) \quad (1)$$

where A_s = the cross-sectional area of the longitudinal steel reinforcements, A_c = the cross-sectional area of the concrete column, f_y = the yield stress of the longitudinal steel reinforcements, and f_c' = the cylindrical concrete's unconfined compressive stress.

The strands were installed outside the column at the east and west sides of the centers of the columns (Fig. 3). The prestressing strands were supported by a rigid steel beam atop the column head and at the column's footing. The prestressing force was applied and kept constant during the test using two automated hydraulic jacks.

After the axial load was applied, cyclic lateral loading was applied in a displacement control following FEMA 2007, using two hydraulic actuators connected to the column's loading stub in one end and to the strong wall at the other end (Fig. 3). Two cycles were executed per each displacement amplitude (Fig 4). The load was applied until failure of a test specimen.

Results and Discussion

General Behavior

Fig. 5 illustrates the hysteretic moment-lateral drift relation of all of the columns. The lateral drift of each column was obtained by dividing the lateral displacement, measured

from the actuators and corrected for any footing sliding, or uplift, by the height of the lateral load (i.e., 2,413 mm (95 inch)). The moment at the base of the column was obtained by multiplying the sum of the lateral forces, measured by the actuators' loading cells, by the column's height of 2,413 mm (95 inch). Figs. 6 and 7 show the columns' profiles and the damaged area at the failure, respectively. Table 4 presents a summary of the maximum moments, the lateral drift at maximum moment, and the maximum lateral drift of each column.

In this manuscript, the lateral loads and drifts are given using average values of the pull and push directions. As shown in Fig. 5(a), the average peak moment of the column F4-24-RC was 594.0 kN.m (438.0 kip.ft) at a lateral drift of 5.1%. Generally, the column demonstrated linear behavior up to 0.5%. Then, the stiffness of the column displayed gradual stiffness degradation up to a lateral drift of approximately 2.0%. Beyond that drift, significant stiffness softening started. Concrete spalling at the bottommost section of the column started at 3.0%. The failure of the column occurred at a lateral drift of approximately 10.9% due to the fracture of the farthest longitudinal rebars at the north and south sides of the column (Fig. 6a). Two more rebars at each side fractured during cycling the column toward the second cycle of a 10.9% lateral drift. At this stage, the column suffered severe damage in the form of concrete crushing and spalling, buckling and fracture of longitudinal rebars, and excessive lateral deformation of the spiral reinforcement (Fig. 7a). The residual moment after this damage was 196.5 kN.m (145 kip.ft) corresponding to 33% of the peak moment of the column. The height of the damaged area measured from the top of the footing ranged from 432 mm (17 inch) to 559 mm (22 inch) with the severe damage concentrated at the bottommost 229 mm (9 inch)

from the level of the footing top. The column's curvature was compatible with the column's damage as it was highest within the first 203 mm (8 inch; Fig. 8a).

For the F4-24-E324 column, the average peak moment of the column was 732.0 kN.m (540 kip.ft) at a lateral drift of 2.8% (Fig. 5b). Generally, the column behaved linearly up to 0.9%. Then, gradual stiffness degradation occurred until a drift of approximately 2.8%. The peak flexural strength of the column remained approximately constant until a drift of approximately 6.0%. Beyond that, the column's flexural strength gradually decreased until a drift of 10.9%. At this drift ratio, the column suffered an 11% strength reduction. Cycling continued beyond that until a lateral drift of 15.2%, when the FRP ruptured (Fig. 6b). The direction of the FRP rupture followed the fiber direction closely (i.e., 53^{o} (Fig. 7b)). The residual moment after the FRP rupture was 314.4 (232 kip.ft), corresponding to 43% of the peak moment of the column. At the conclusion of testing the column, the column's concrete shell was almost powder along the bottommost 152 mm (6 inch) in the north and south sides. This indicated that the steel and FRP tubes were able to confine the concrete shell, and the concrete reached its ultimate strain before the rupture of the FRP tube. The column's curvature was compatible with the column damage as it was high within the first 203 mm (8 inch) (Fig. 8b).

The opening of the interface joint between the column and footing was measured as 70 mm (2.75 inch) at a lateral drift of 14.1% (Fig. 9). This opening resulted from sliding of the FRP tube on the concrete shell, sliding of the concrete shell on the steel tube, and the concrete pull-out from the footing.

For the F4-24-P124 column, the average peak moment of the column was 748.0 kN.m (552.0 kip.ft) at a lateral drift of 2.6% (Fig. 5c). Generally, the column behaved linearly

up to 0.9%. Then, gradual stiffness degradation occurred until a drift of approximately 2.6%. Beyond that, the column suffered significant stiffness softening. The failure of the column was at a lateral drift of 5.8% when the FRP ruptured (Fig. 7c). The cameras inside the steel tube showed no visible steel tube buckling or sliding occurred between the steel tube and the column loading stub. The videos are available online in the ASCE Library (www.ascelibrary.org). Fig. 8(c) illustrates that the high column's curvature was within the first 203 mm (8 inch) of the top of the footing.

Backbone Curves

Fig. 10 illustrates the backbone of the moment-lateral drift curves of all of the columns. The figure also illustrates the limit states of steel yielding in tension or compression, steel buckling, rebar fracture, and/or FRP rupture of each column. The steel tube or rebar of the investigated columns yielded in tension at approximately the same lateral drift (1.1%-1.4%). However, the behavior of each column was different in compression whether in yielding or buckling. The farther rebars of the F4-24-RC column yielded and buckled in compression at a lateral drift of 2.0% and 7.5%, respectively. The steel tubes of columns F4-24-E324 and F4-24-P124 yielded in compression at a lateral drift of 0.8% and 2.6%, respectively. The steel tube of the F4-24-E324 column buckled at a lateral drift of 3.0% while the steel tube of the F4-24-P124 column did not buckle.

As shown in Fig. 10, the nonlinear behavior and stiffness softening started at a lateral drift of approximately 0.9% for the HC-FCS columns and at a drift of 0.5% for the RC column. Furthermore, all of the HC-FCS columns reached to lateral strengths 1.23 and 1.26 times that of the RC column. This occurred mainly due to the difference in the

longitudinal reinforcement ratio. The effects of FRP rigidity on the performance of the columns can be understood by comparing the performance of the F4-24-E324 column with the thicker FRP tube to the F4-24-P124 column with the thinner FRP tube. As shown in the Fig., both columns reached to approximately the same lateral resistance. However, the F4-24-E324 column with the thicker FRP tube reached 2.6 times the lateral displacement of that of the F4-24-P124 column. The more rigid the FRP tube is, the higher the column's lateral displacement capacity.

The radial dilation of the concrete shell imposes a significant tensile strain demand on the FRP and compression strain demand on the steel tube. This demand depends on the relative stiffness of the FRP and steel tubes (Abdelkarim and ElGawady 2014b). The concrete dilation in the F4-24-E324 column, where the high stiffness FRP tube was used, went toward the steel tube, which increased the deformation demand on the steel tube and led to early local buckling. Consequently, the FRP rupture occurred later when the concrete dilation was significantly increased. The concrete dilation in the F4-24-P124 column went toward the FRP tube because it was considerably thinner. This behavior will be explained in detail later in the FRP and steel strains section.

Energy Dissipation

For the investigated columns, the energy dissipation at each lateral drift was determined as the enclosed area of the hysteretic loop of the first cycle at this drift level. Dissipating higher hysteretic energy reduces the seismic demand on a structure. Fig. 11 illustrates the cumulative energy dissipation-lateral drift relation for all of the columns. The conventional RC and the HC-FCS columns dissipated energy due to nonlinear steel and

concrete deformations. In general, the HC-FCS columns showed better energy dissipation than the conventional RC column. The F4-24-E324 column dissipated energy of approximately 1.9 times that of the F4-24-RC column.

FRP and Steel Strains

Figs. 12 and 13 illustrate the steel strains above the top of the footing in the vertical and hoop direction for all of the columns, respectively. Throughout this manuscript, positive strain values represent tensile strain and vice versa. The figures do not show the strains until the end of each test as some strain gauges failed before the end of the tests. The longitudinal rebars of the F4-24-RC column, the steel tubes of the F4-24-E324, and the F4-24-P124 columns reached to high vertical tensile strain values of approximately 18,000 microstrain, 11,000 microstrain, and 14,000 microstrain, respectively, at a lateral drift of 4%. The longitudinal rebars of the F4-24-RC column, the steel tubes of the F4-24-E324, and the F4-24-P124 columns reached to vertical compressive strain values of approximately 5,900 microstrain, 10,500 microstrain, and 6,000 microstrain, respectively, at a lateral drift of 4%.

The residual vertical compressive and tensile strains of the longitudinal rebars of the F4-24-RC column at zero drift after a cycling lateral drift of 4% were 6,000 microstrain and 1,200 microstrain, respectively. These residual strains represented 33% and 20% of the maximum tensile and compressive strains during this cycle. The residual vertical compressive and tensile strains of the steel tube of the F4-24-E324 column at zero drift after a cycling lateral drift of 4% were 3,500 microstrain and 3,600 microstrain, respectively. These residual strains represented 32% and 34% of the maximum tensile

and compressive strains during this cycle. The residual vertical compressive and tensile strains of the steel tube of the F4-24-P124 column at zero drift after the cycling lateral drift of 4% were 7,200 microstrain and 3,200 microstrain, respectively. These residual strains represented 50% and 53% of the maximum tensile and compressive strains during this cycle. The percentages of residual strains out of the maximum strains of the F4-24-E324 column were lower than those percentages of the F4-24-P124 column because of the effect of steel tube sliding.

Figs. 14 and 15 illustrate the hysteric FRP strains in the vertical and hoop direction recorded at 127 mm (5 inch) from the top of the face of each footing for both columns. In the push direction (negative direction of lateral drift), the FRP compressive vertical and tensile hoop strains increased due to the direct compression and the concrete lateral pressure, respectively. In the pull direction (positive direction of lateral drift), the FRP had almost constant residual strains due to the fiber reorientation.

Fig. 16 illustrates the vertical and hoop strains of the FRP and steel tubes in the cross-section at 127 mm (5 inches) above the top of the footing for both HC-FCS columns. The strains are at a lateral drift of 2.8% when the columns reached their peak strengths. In this figure, the north side (N) is the tension side and the south side (S) is the compression side. The steel tube of the F4-24-E324 column was subjected to compressive hoop strain along the whole cross-section, and the FRP tube was subjected to tensile hoop strain along the whole cross-section. The FRP and steel hoop strains indicated that the concrete applies pressure on steel and FRP tubes due to concrete expansion under vertical compression. Also, the compressive hoop strains on the steel tube push it to buckle under the vertical strain. The FRP tube of the F4-24-E324 column was subjected to compressive

vertical strain along the cross-section. This indicated that the FRP tube did not move up from the footing and the steel tube slid inside the concrete column.

The vertical strain on the FRP tube of the F4-24-E324 column was significantly higher than that of the F4-24-P124 column because of the high stiffness of the FRP tube of the F4-24-E324 column. However, the F4-24-E324 and F4-24-P124 columns had almost the same peak moment, and the tension steel strain in the N side of the F4-24-E324 column was lower than that of the F4-24-P124 column. The reasons for this were the high vertical strain in the FRP tube of the F4-24-E324 column that shifted the neutral axis toward the tension side (N), and because the steel tube sliding of the F4-24-E324 column was higher than that of the F4-24-P124. However, the steel tube of the F4-24-E324 column on the S side was subjected to compressive hoop strain due to concrete expansion; the steel tube of the F4-24-P124 column was not. In addition, The FRP hoop strain of the F4-24-P124 in the S side was higher than that of the F4-24-E324. These results proved that the expansion of the concrete went toward the FRP tube, the weaker side, in the F4-24-P124 column. Also, the steel tube of the F4-24-P124 column was subjected to a higher hoop compressive strain on the N, E, and W sides than that of the F4-24-E324 column. This indicated that the concrete column worked as one unit and moved toward the FRP tube on the S side. The higher hoop tensile strain on the FRP tube on the N side of the F4-24-P124 than that of the F4-24-E324 column explains this behavior.

Fig. 17 illustrates the steel vertical strain profile of the HC-FCS columns. In the F4-24-E324 column, the steel tube buckled locally at a 3% lateral drift because the compressive strain at the lateral drift of 4% was significantly lower than that of the 3%.

The strain before local buckling was approximately 10,000 microstrain which is compatible with previous studies by Brown et al. (2014). The steel tube in the HC-FCS column would be subjected to higher hoop compressive strains than that of the steel tube in the concrete-filled steel tube. The reason is the concrete shell reached to a higher axial strain as the FRP tube in HC-FCS column provided a higher confinement than the steel tube in the concrete-filled steel tube. The low strain along the steel tube down to the level of 127 mm (5 inches) from the top of the footing proves the occurrence of steel tube sliding. It is noted in the figure that the high tension strains occurred at 254 mm (10 inches) from the top of the footing and the location did not change during cycling.

In the F4-24-P124 column, no local buckling occurred in the steel tube as the steel compressive strain did not drop until the failure of the column. Also, the maximum compressive strain was lower than 10,000 microstrain. In addition, the inside camera confirmed the previous result and did not show any local buckling (supplementary data). The level of the maximum tensile strain of the steel tube in the F4-24-P124 column moved up gradually from some consecutive lateral drifts to the next. The level of the maximum tensile strain was 0.0 mm (0.0 inches), 127 mm (5 inches), and 254 mm (10 inches) from the top of the footing at a lateral drift of 3%, 4%, and 5%, respectively. This result proves also that very little or no sliding occurred for the steel tube inside this column. The steel tube yield penetration depth into the concrete footing for the F4-24-E324 and F4-24-P124 columns was 254 mm (10 inches), which asserts that the 635 mm (25 inch) embedded length was enough.

Figs. 18 and 19 illustrate the FRP vertical and hoop strain profiles for all of the columns. The high strains were within the bottommost 254 mm (10 inches) for all of the

columns, which was compatible with the steel profiles and the columns' curvatures. The values of the hoop strains were almost 70% of that of the vertical strains at the same lateral drift. As shown in the figure, when the column in the strain gauge side was subjected to compressive stresses due to the lateral loads, the axial strains on the FRP increased significantly. However, once the applied load was reversed, the axial strains decreased but did not return to zero, indicating that the concrete core had small cracks that closed upon unloading. The FRP of the F4-24-E324 reached a vertical compressive strain and hoop tensile strain of 22,000 microstrain and 13,500 microstrain, respectively. The FRP of the F4-24-P124 reached a vertical compressive strain and hoop tensile strain of 10,000 microstrain and 7,900 microstrain, respectively.

Findings and Conclusions

This paper reported the seismic behavior of hollow-core fiber reinforced polymer-concrete-steel columns (HC-FCS). The HC-FCS columns consisted of a concrete wall sandwiched between an outer FRP tube and an inner steel tube. Three large-scale columns including one conventional RC column and two HC-FCS columns were investigated during this study. This study revealed the following findings:

1. In general, the HC-FCS columns had better seismic behavior than the conventional RC column.
2. The HC-FCS column exhibited a high lateral drift reaching 15.2%. The RC-column failed at a lateral drift of 10.9%. The RC column failed by rebar rupture, and the moment capacity suddenly dropped more than 20% after that. However,

the HC-FCS failed gradually with concrete compression failure and steel tube local buckling followed by FRP rupture.

3. The HC-FCS columns dissipated higher energy, reaching 1.9 times that of the conventional column.
4. The flexural strength of the HC-FCS column is related mainly to the steel tube thickness.
5. The maximum lateral drift of the HC-FCS column is controlled by the FRP tube thickness where the maximum lateral drift increased when the FRP tube thickness increased.
6. Thick FRP tube increased concrete pressure on steel tube leading buckling in steel tube.
7. Buckling in steel tube caused vertical sliding with the footing.

Acknowledgement

This research was supported by Missouri Department of Transportation (MoDOT) and Mid-American Transportation Center (MATC). In kind contribution from ATLAS Tube is appreciated. Discounts on FRP tubes from Grace Composites and FRP Bridge Drain Pipe are also appreciated. The authors also extend their appreciation to the National University Transportation Center (NUTC) at Missouri University of Science and Technology (Missouri S&T). However, any opinions, findings, conclusions, and recommendations presented in this paper are those of the authors and do not necessarily reflect the views of the sponsors.

Supplemental Data

The videos of the cameras inside the HC-FCS columns are available online in the ASCE Library (www.ascelibrary.org).

Reference

Abdelkarim, O. and ElGawady, M. (2014a). "Behavior of Hybrid FRP-Concrete-Steel Double-Skin Tubes Subjected to Cyclic Axial Compression." Structures Congress 2014: pp. 1002-1013.

Abdelkarim, O. and ElGawady, M. (2014b). "Analytical and Finite-Element Modeling of FRP-Concrete-Steel Double-Skin Tubular Columns." J. Bridge Eng., 10.1061/(ASCE)BE.1943-5592.0000700 , B4014005.

ACI Committee 318 (2011). "Building Code Requirements for Structural Concrete (ACI318-11) and Commentary (318R-11)." American Concrete Institute, Farmington Hills, Mich., pp. 509.

Brown, N.K., Kowalsky, M.J., and Nau, J.M. (2014). "Impact of Diameter to Thickness Ratio on The Seismic Behavior of Reinforced Concrete Filled Steel Tubes." Tenth U.S. National Conference on Earthquake Engineering Frontiers of Earthquake Engineering July 21-25, Alaska.

ElGawady, M. and Dawood, H. (2012). "Analysis of segmental piers consisted of concrete filled FRP tubes." Engineering Structures, Vol. 38, pp. 142-152.

ElGawady, M. and Sha'lan, A. (2011). "Seismic Behavior of Self-Centering Precast Segmental Bridge Bents." J. Bridge Eng., 16(3), 328–339.

ElGawady, M., Booker, A., and Dawood, H. (2010). "Seismic Behavior of Posttensioned Concrete-Filled Fiber Tubes." J. Compos. Constr., 14(5), 616–628.

Fam, A., Flisak, B., Rizkalla, S. (2003). "Experimental and analytical modeling of concrete-filled fiber-reinforced polymer tubes subjected to combined bending and axial loads." ACI Structural Journal, 100 (4), pp. 499-509.

Fouche, P. and Bruneau, M. (2010). "Non-Linear Analysis of Multi-Hazard Performance of Cylindrical Concrete Filled Steel Tubes Bridge Piers." Proceedings of 8th International Conference on Short and Medium Span Bridges, Canada.

Hajjar, J. F. (2000). "Concrete-filled steel tube columns under earthquake loads." Structural Engineering and Materials; 2(1):72–82.

Lee, J. H., Choi, J. H., Hwang, D. K., and Kwahk, I. J. (2014). "Seismic Performance of Circular Hollow RC Bridge Columns." KSCE Journal of Civil Engineering, Vol. 19(5), pp. 1456-1467.

Mander, J. B., Priestley, M. J. N., and Park, R. (1983). "Behavior of Ductile Hollow Reinforced Concrete Columns." Bulletin of the New Zealand National Society for Earthquake Engineering, Vol. 16, No. 4, December, pp. 273-290.

Montague, P., (1978). "Experimental behavior of double-skinned, composite, circular cylindrical-shells under external-pressure." Journal of Mechanical Engineering Science, 20(1), pp. 21–34.

Moon, J., Lehman, D. E., Roeder, C. W., and Lee, H. E. (2013). "Strength of Circular Concrete-Filled Tubes with and without Internal Reinforcement under Combined Loading." Journal of Structural Engineering, 139(12).

Ozbakkaloglu, T. and Idris, Y. (2014). "Seismic Behavior of FRP-High-Strength Concrete-Steel Double-Skin Tubular Columns." J. Struct. Eng., 140(6), 04014019.

Qasrawi, Y., Heffernan, P. J., & Fam, A. (2014). "Performance of Concrete-Filled FRP Tubes under Field Close-in Blast Loading." J. Compos. Constr., 10.1061/(ASCE)CC.1943-5614.0000502 , 04014067.

Sadeghian, P. and Fam, A. (2010). "Bond-Slip Analytical Formulation toward Optimal Embedment of Concrete-Filled Circular FRP Tubes into Concrete Footings." J. Eng. Mech., 136(4), 524–533.

Shakir-Khalil, H., and Illouli, S. (1987). "Composite columns of concentric steel tubes." Proc., Conf. on the Design and Construction of Non-Conventional Structures, Vol. 1, London, pp. 73–82.

Shao, Y. and Mirmiran, A. (2005). "Experimental Investigation of Cyclic Behavior of Concrete-Filled Fiber Reinforced Polymer Tubes." J. Compos. Constr., 9(3), 263–273.

Teng, J.G., Yu, T., and Wong, Y.L. (2004). "Behavior of Hybrid FRP-Concrete-Steel Double-Skin Tubular Columns." *Proc. 2nd Int. Conf. on FRP Composites in Civil Engineering*, Adelaide, Australia, 811-818.

Teng, J.G., Yu, T., Wong, Y.L., and Dong, S.L. (2005). "Innovative FRP-Steel-Concrete Hybrid Columns." Advances in Steel Structures, 1, 545-554.

Teng, J. G., Yu, T., Wong, Y. L., and Dong, S. L. (2007). "Hybrid FRP concrete-steel tubular columns: Concept and behavior." Constr. Build. Mater., 21(4), 846–854.

Wong, Y. L., Yu, T., Teng, J. G., and Dong, S. L. (2008). "Behavior of FRP-confined concrete in annular section columns." Compos. B Eng., 39(3), 451–466.

Yu, T., Wong, Y. L., Teng, J. G., Dong, S. L., and Lam, E. S. (2006). "Flexural Behavior of Hybrid FRP-Concrete-Steel Double-Skin Tubular Members." J. Compos. Constr., 10(5), 443–452.

Yu, T., Teng, J. G., and Wong, Y. L. (2010). "Stress-Strain Behavior of Concrete in Hybrid FRP-Concrete-Steel Double-Skin Tubular Columns." *J. Struct. Eng.*, 136(4), 379–389.

Zhang, W. and Shahrooz, B. M. (1997). "Analytical and Experimental Studies into Behavior of Concrete-Filled Tubular Columns." Report No. UC-CII 97/01, Cincinnati Infrastructure Institute, Department of Civil and Environmental Engineering, University of Cincinnati, College of Engineering, Cincinnati, Ohio, May.

Zhang, B., Teng, J. G. and Yu, T. (2012). "Behaviour of hybrid double-skin tubular columns subjected to combined axial compression and cyclic lateral loading." *Sixth International Conference on FRP Composites in Civil Engineering* (pp. 1-7). Rome, Italy.

Zhu, Z., Ahmad, I., and Mirmiran, A. (2006). "Seismic performance of concrete-filled FRP tube columns for bridge substructure." J. Bridge Eng., 11(3), 359–370.

Table 1. Summary of the Columns' Variables

Column		F4-24-RC	F4-24-E324	F4-24-P124
Nominal outer diameter (D_o, mm (inch))		610 (24)		
Nominal inner diameter (D_i, mm (inch))		N.A.	406 (16)	
Steel tube thickness (t_s, mm (inch))		N.A.	6.4 (0.25)	
FRP tube	Matrix	N.A.	Epoxy	Iso-Polyester
	Thickness (t_{FRP}, mm (inch))	N.A.	9.5 (0.375)	3.2 (0.125)
Longitudinal reinforcement		8 φ 22 (8 # 7)	N.A.	N.A.
Transverse reinforcement		spiral φ13 @ 76 mm (# 4 @ 3 inch)	N.A.	N.A.

Table 2. Summary of the Unconfined Concrete Strength of the Columns and the Footings

	F4-24-RC		F4-24-E324		F4-24-P124	
	Column	Footing	Column	Footing	Column	Footing
f_c' at 28 days, MPa (psi)	32.6 (4,725)	36.6 (5,300)	32.6 (4,725)	36.6 (5,300)	39.8 (5,770)	56.0 (8,117)
f_c at the day of the test, MPa (psi)	35.0 (5,075)	37.8 (5,480)	36.0 (5,215)	38.9 (5,640)	43.0 (6,235)	61.4 (8,910)

Table 3. FRP Tube Properties

	Axial compression elastic modulus (E_a, GPa (ksi))	Axial ultimate stress (f_{ar}, MPa, psi))	Hoop elastic modulus (E_h, GPa, ksi))	Hoop rupture stress (f_{hr}, psi)
Epoxy tube	4.7 (677)	83.8 (12,150)	20.8 (3,020)	276.9 (40,150)
Iso-polyester tube	9.7 (1,400)	123.4 (17,900)	15.2 (2,200)	275.9 (40,000)

Table 4. Summary of the Results of the Tested Columns

Column	Average maximum moment, kN.m (kip.ft.)	Lateral drift at the maximum moment	Lateral drift at failure
F4-24-RC	594.0 (438.0)	5.1%	10.9%
F4-24-E324	732.0 (540.0)	2.8%	15.2%
F4-24-P124	748.0 (552.0)	2.6%	5.8%

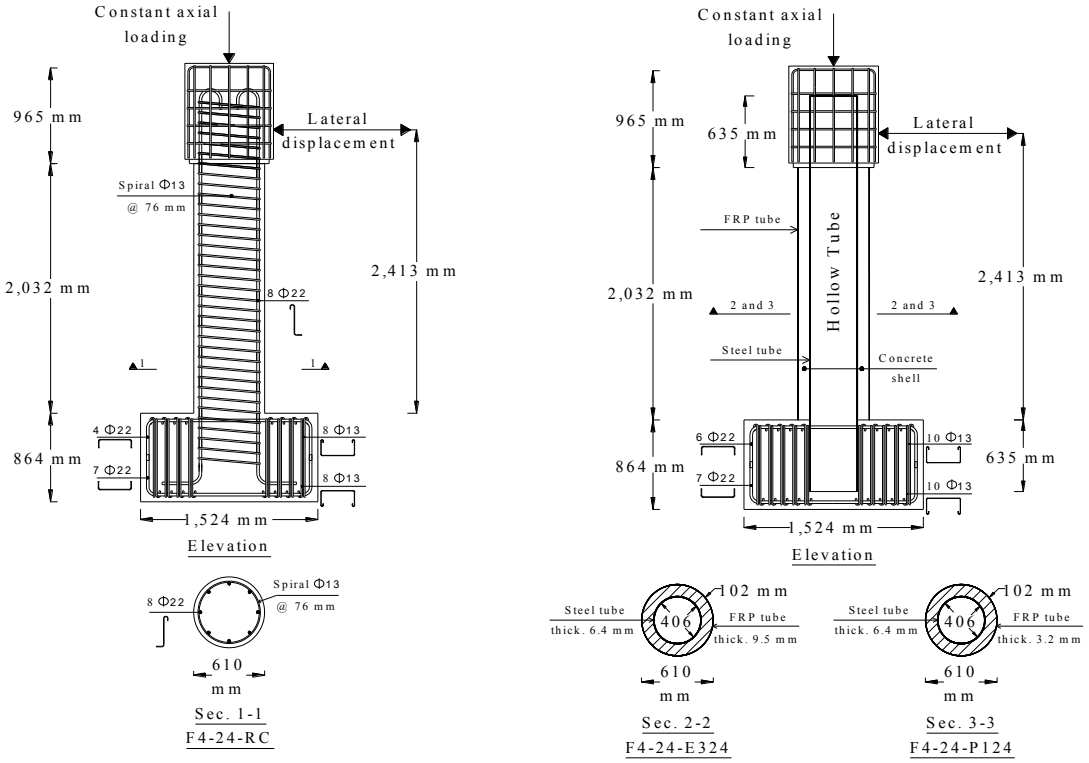

(a) (b)

Fig. 1. General arrangement and reinforcement details of the investigated columns: (a) conventional RC column and (b) HC-FCS columns

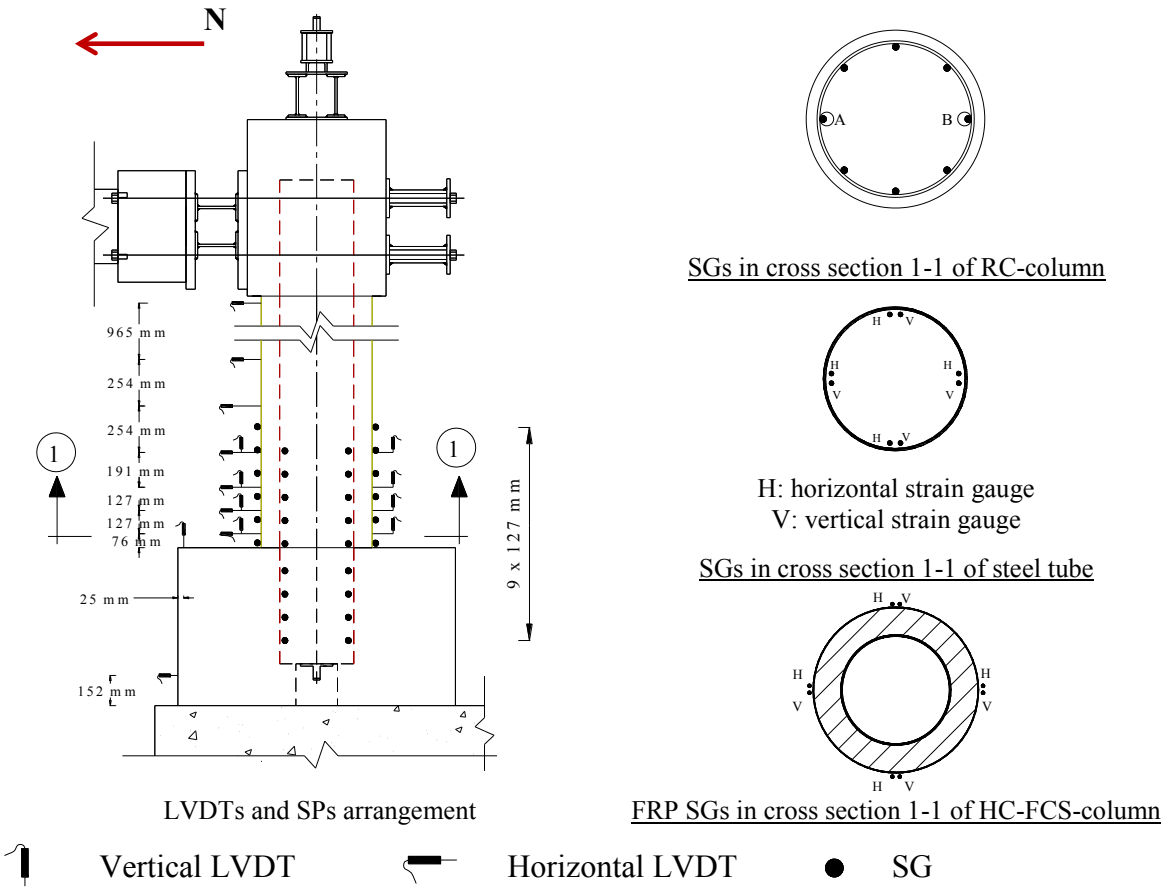

Fig. 2. Layout of the LVDTs, String potentiometers, and strain gauges (1 mm = 0.04 inch)

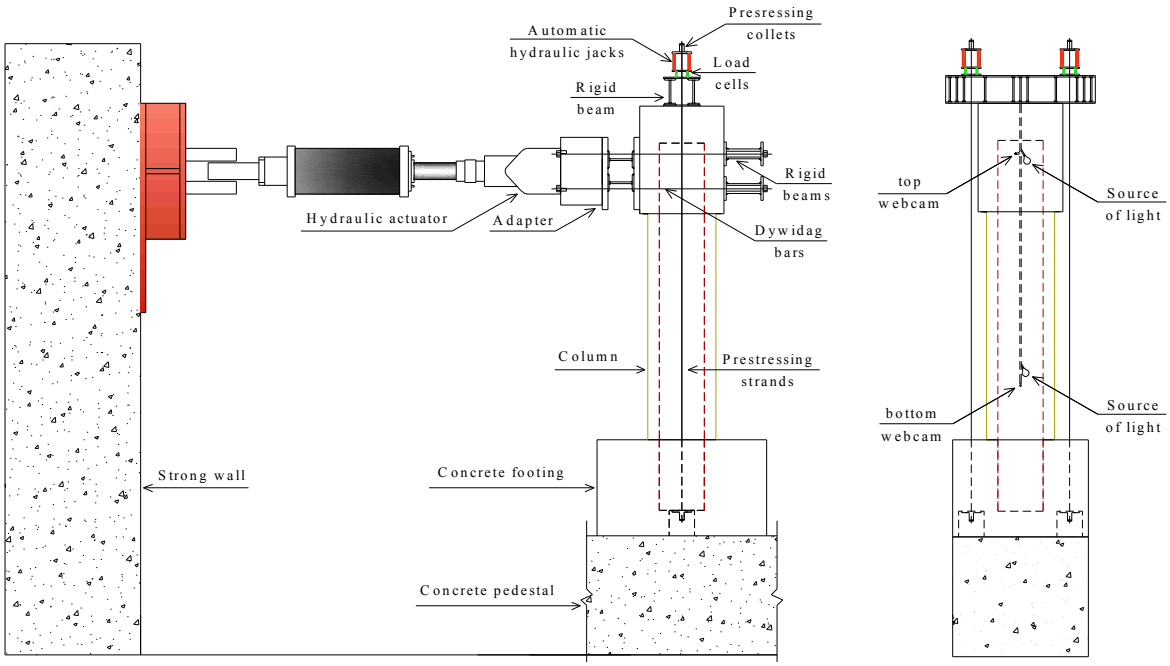

Fig. 3. Column test setup: (a) elevation, (b) side-view

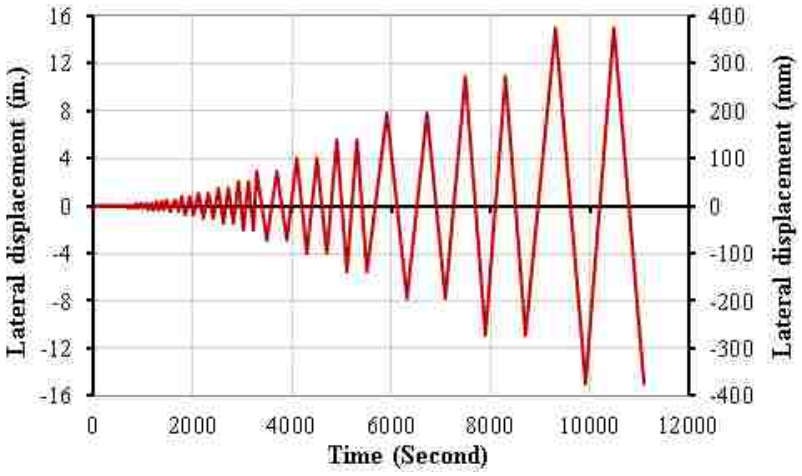

Fig. 4. Lateral displacement loading protocol

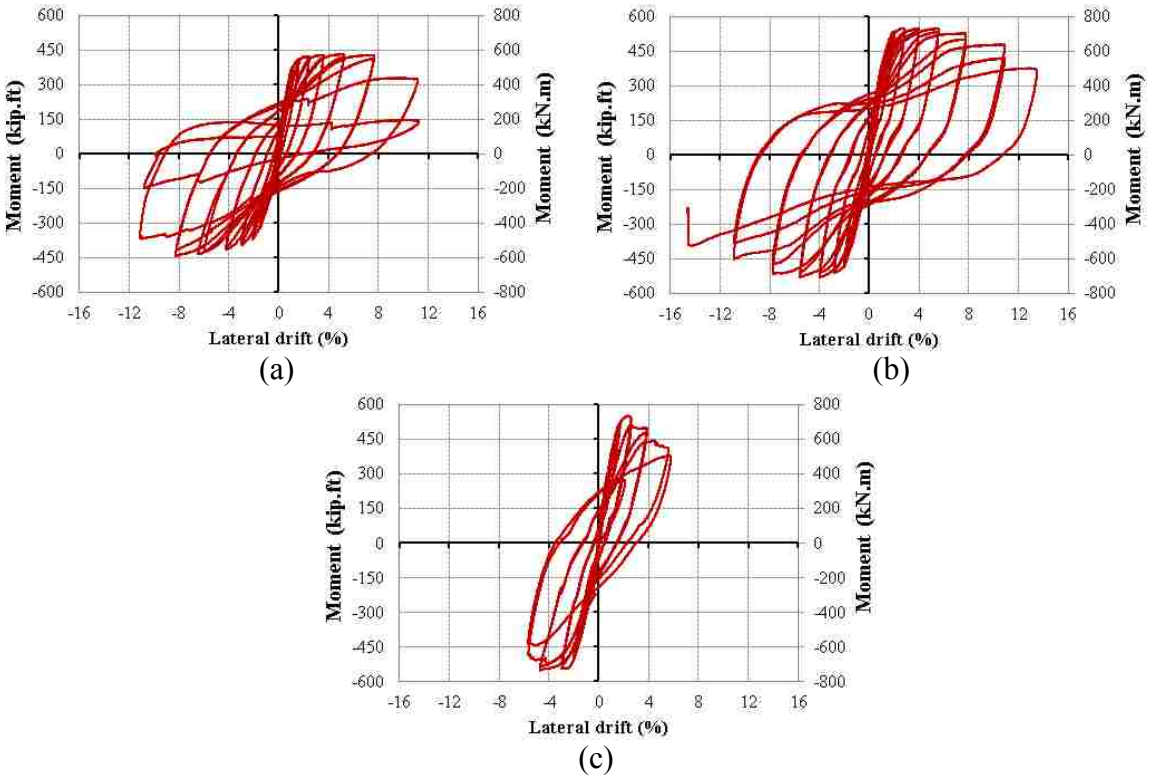

Fig. 5. Hysteretic moment-lateral drift relation: (a) F4-24-RC column, (b) F4-24-E324 column, and (c) F4-24-P124 column

(a) (b) (c)

Fig. 6. Columns' profiles: (a) F4-24-RC at 10.9% lateral drift, (b) F4-24-E324 at 15.2% lateral drift, and (c) F4-24-P124 at 5.8% lateral drift

(a) (b) (c)

Fig. 7. Columns' modes of failure: (a) F4-24-RC damage area, (b) F4-24-E324 FRP rupture, and (c) F4-24-P124 FRP rupture

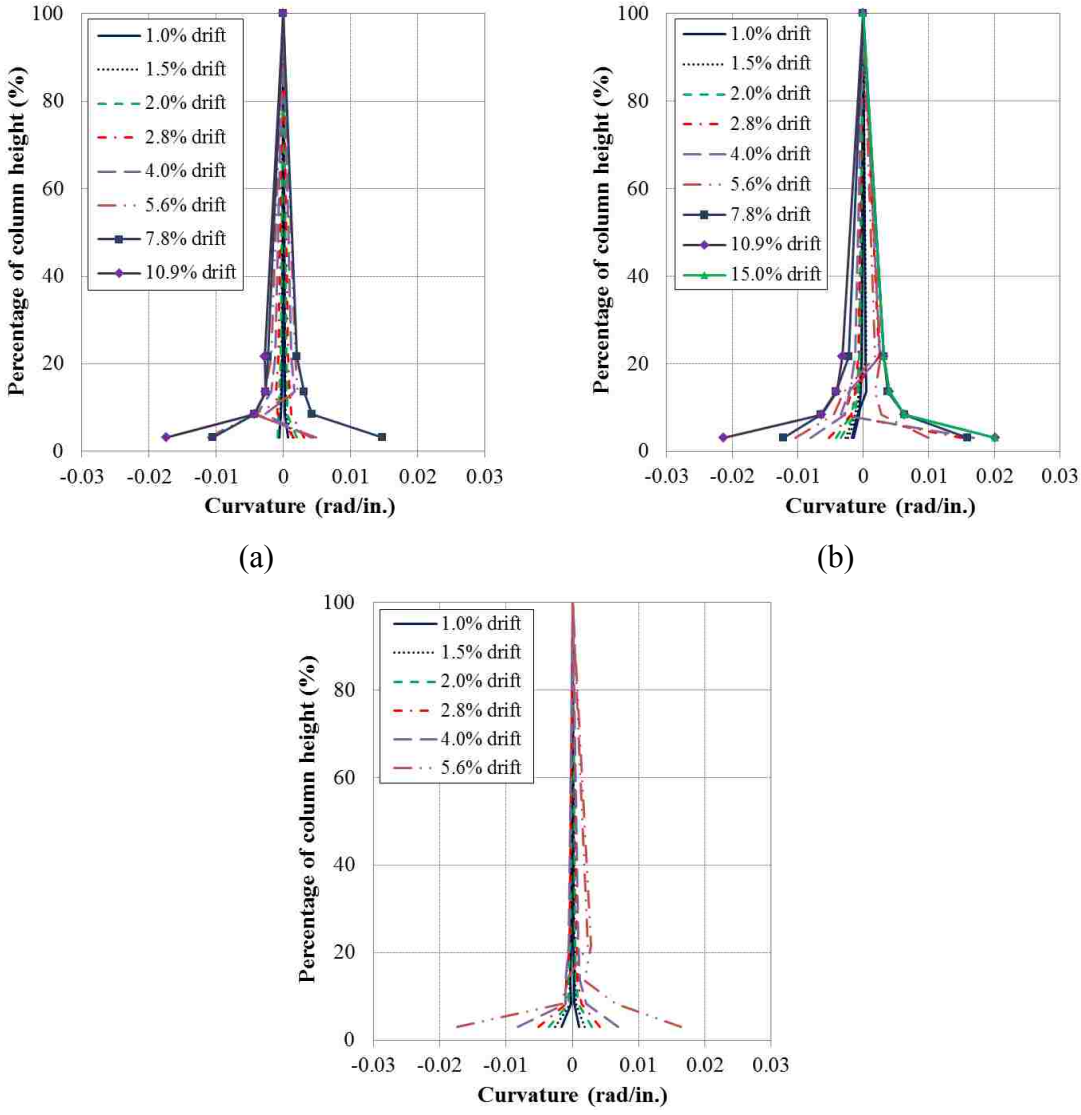

Fig. 8. Curvature along the height: (a) F4-24-RC column, (b) F4-24-E324 column, and (c) F4-24-P124 column

Fig. 9. Joint opening of the F4-24-E324 column at lateral drift of 14.1%

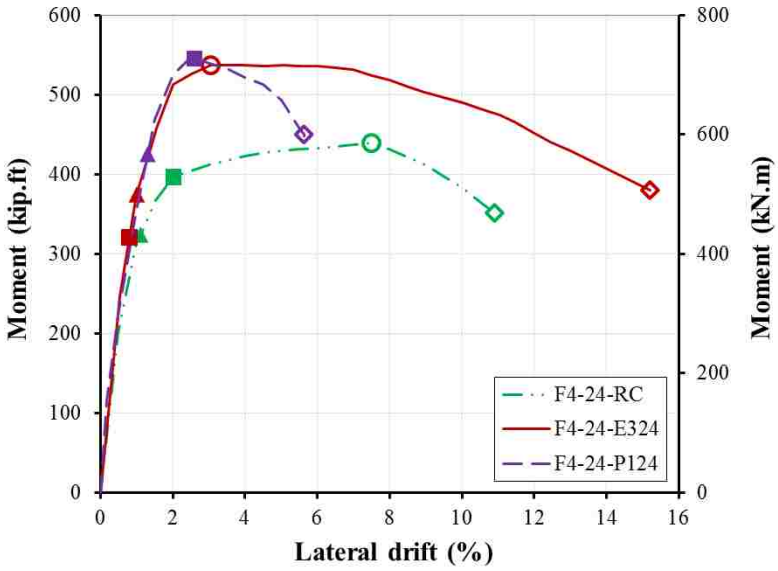

▲ Steel tube or rebar yielded in tension ◯ Steel tube or rebar buckled in compression

■ Steel tube or rebar yielded in compression ◇ FRP rupture or rebar fracture

Fig. 10. Backbone moment-lateral drift relation for all of the columns

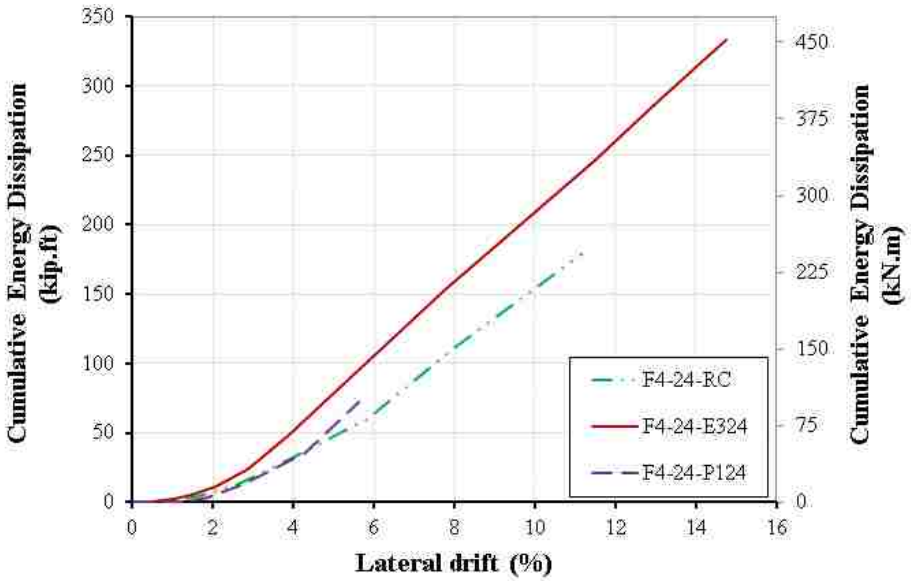

Fig. 11. Cumulative energy dissipation-lateral drift relation for all of the columns

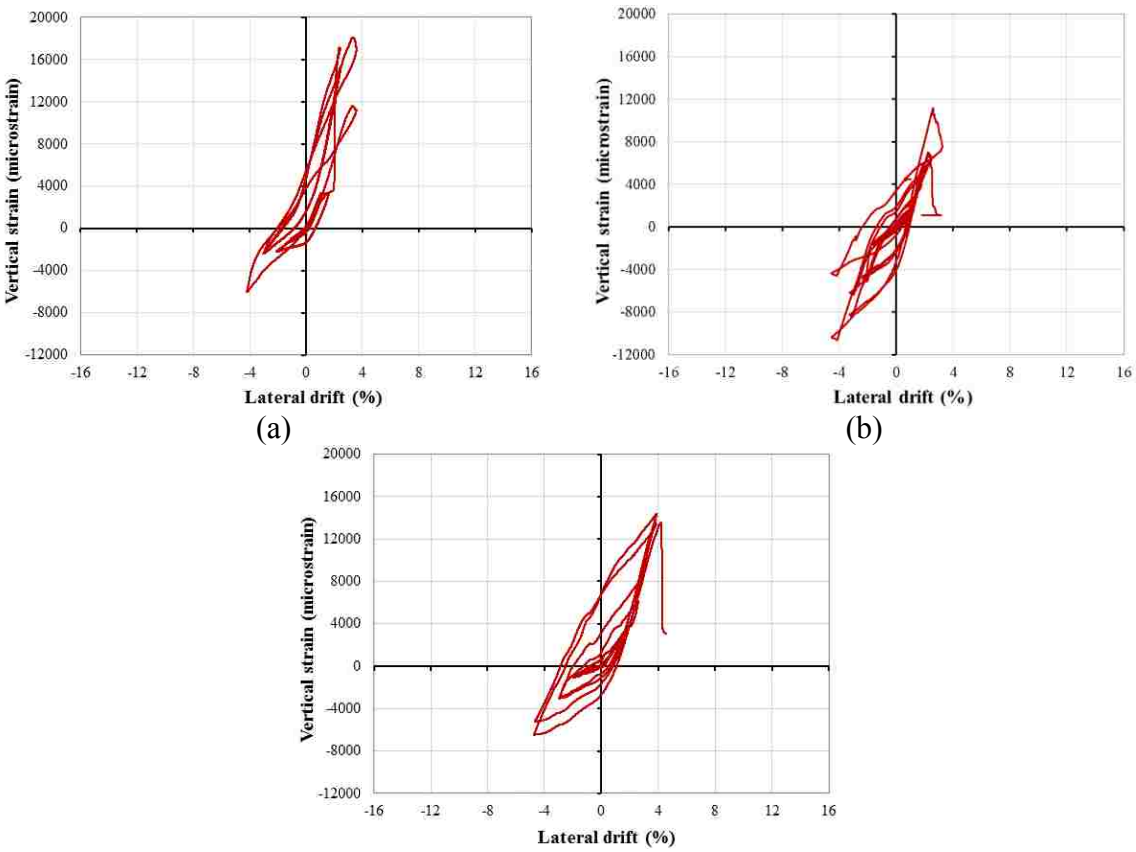

Fig. 12. Lateral drift-vertical steel strain relation within the bottommost 254 mm (10 in.) above top of footing of the columns: (a) F4-24-RC, (b) F4-24-E324, and (c) F4-24-P124

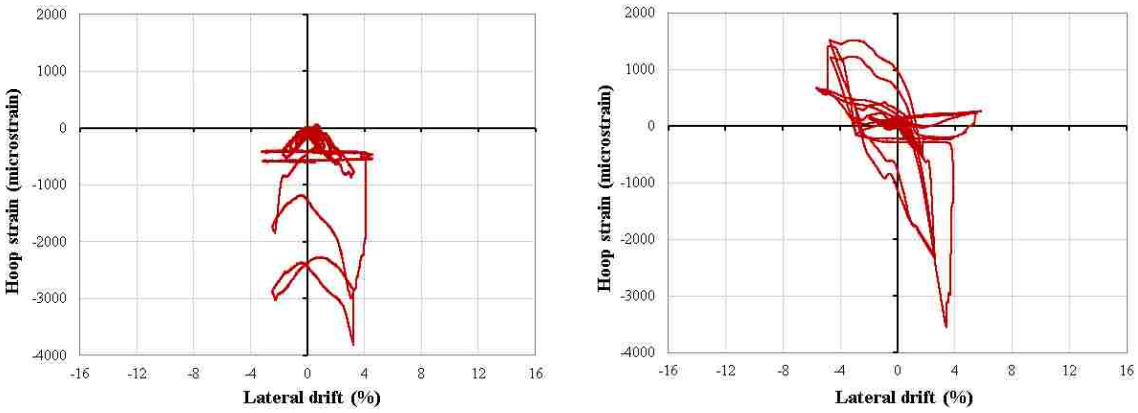

(a) (b)

Fig. 13. Lateral drift-hoop steel strain relation within the bottommost 254 mm (10 in.) above top of footing of the columns: (a) F4-24-E324 and (b) F4-24-P124

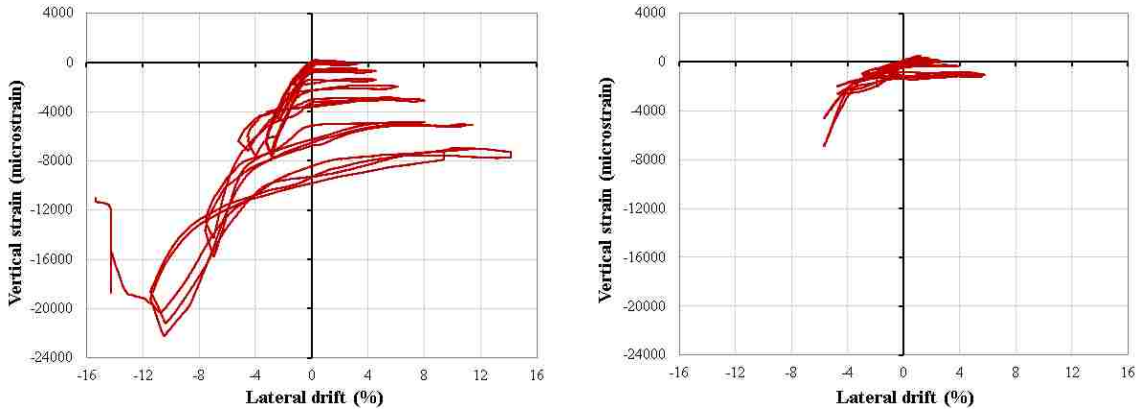

(a) (b)

Fig. 14. Lateral drift-vertical FRP strain relation at 127 mm (5 inch) from the top of the footing for the columns: (a) F4-24-E324 and (b) F4-24-P124

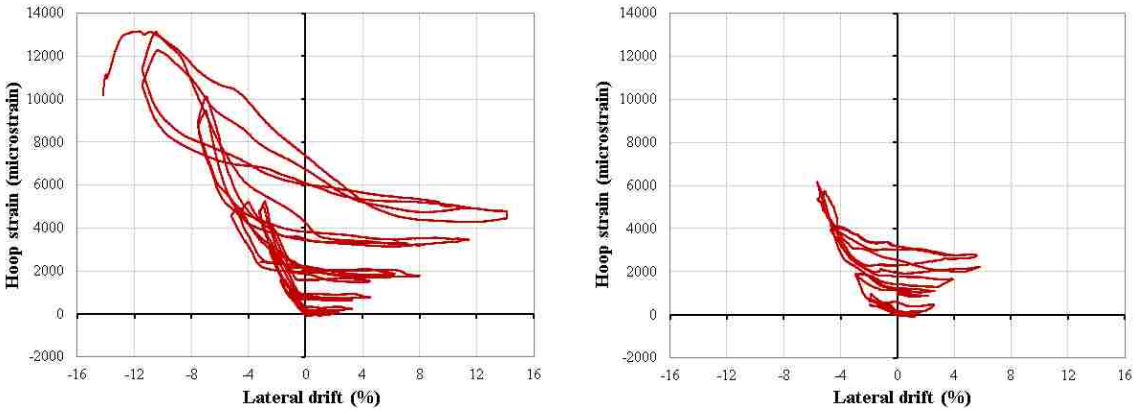

(a) (b)

Fig. 15. Lateral drift-hoop FRP strain relation at 127 mm (5 inch) from the top of the footing for the columns: (a) F4-24-E324 and (b) F4-24-P124

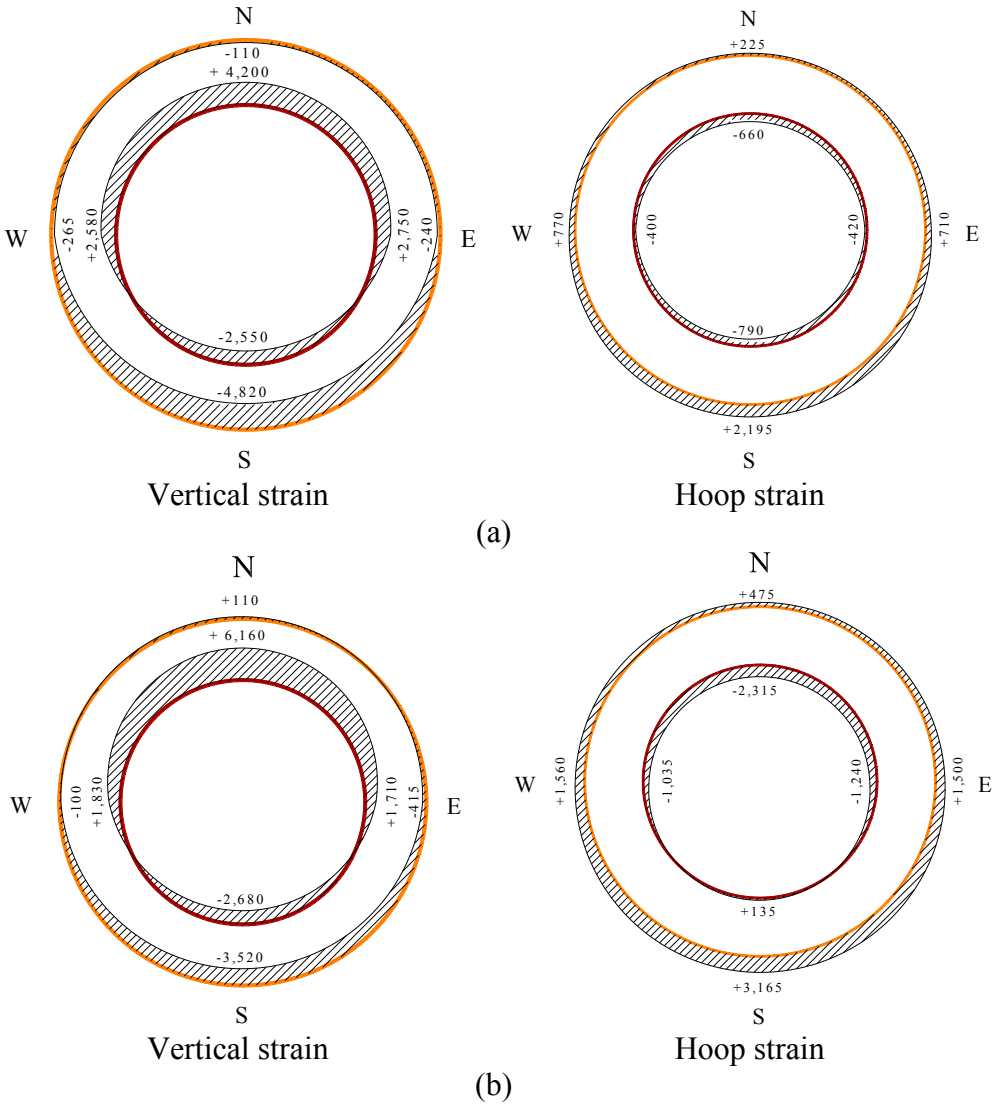

Fig. 16. FRP and steel strains in cross-section at 127 mm (5 in.) above the top of footing for the columns: (a) F4-24-E324 and (b) F4-24-P124 (Note: strains are in microstrains)

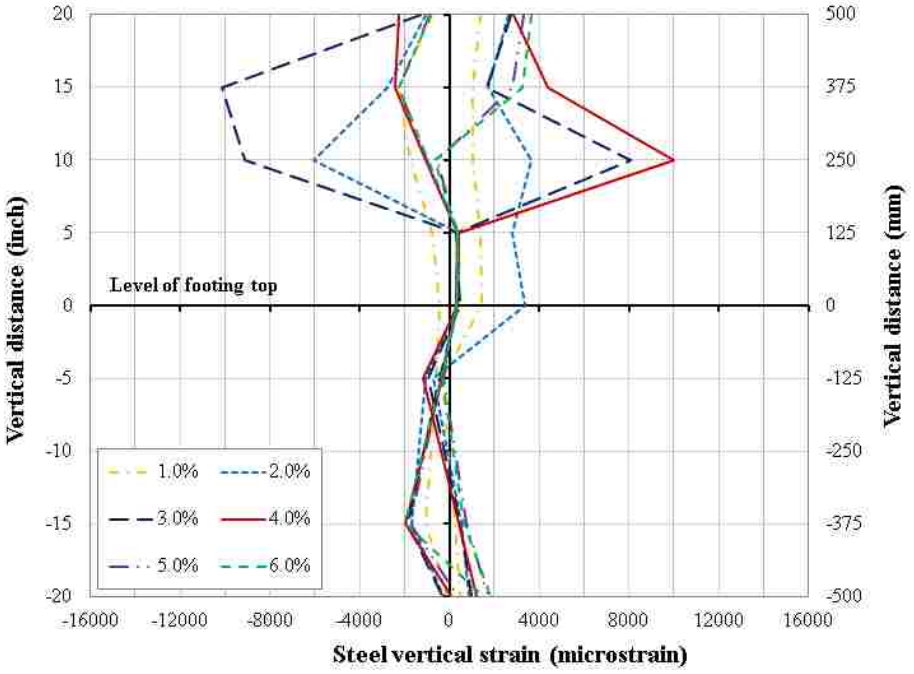

(a)

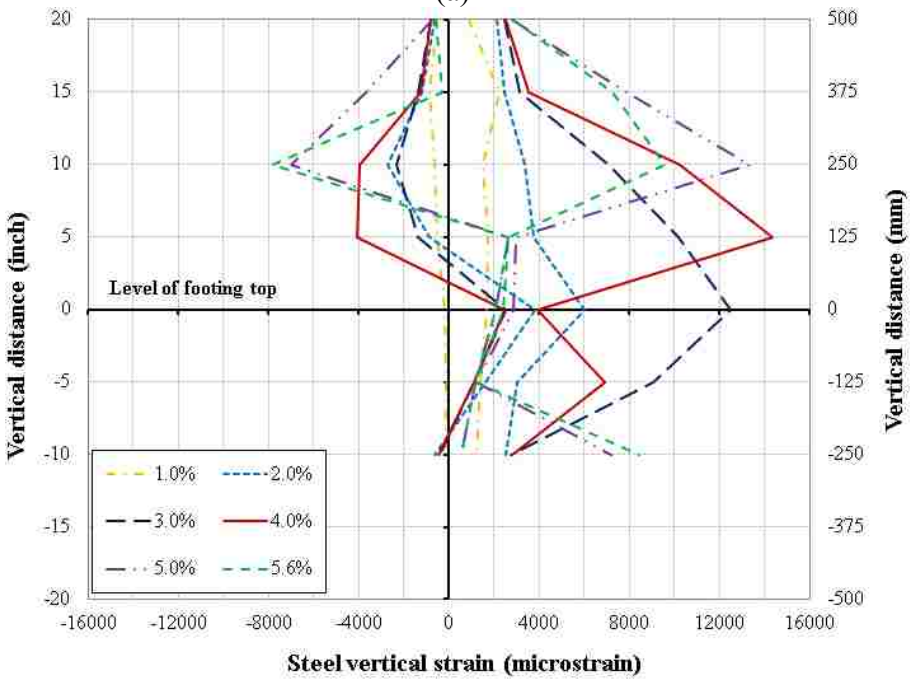

(b)

Fig. 17. Steel vertical strain profile for the columns: (a) F4-24-E324 and (b) F4-24-P124

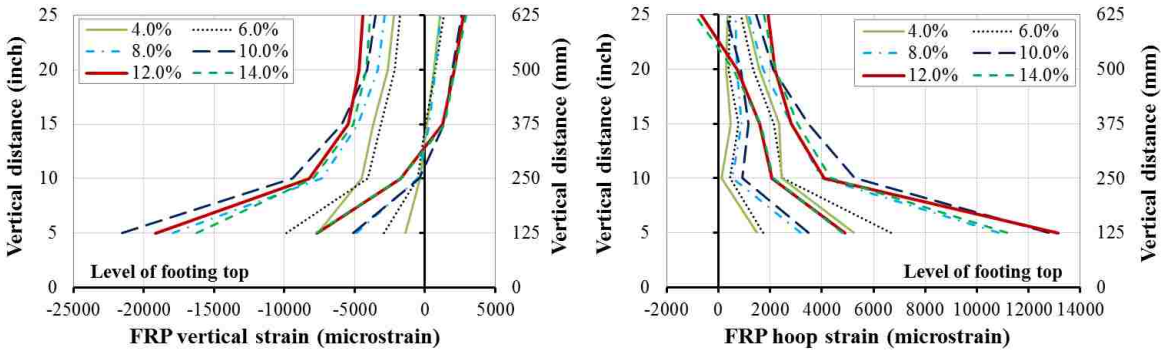

(a) (b)

Fig. 18. FRP strain of the F4-24-E324 column: (a) vertical strain and (b) hoop strain

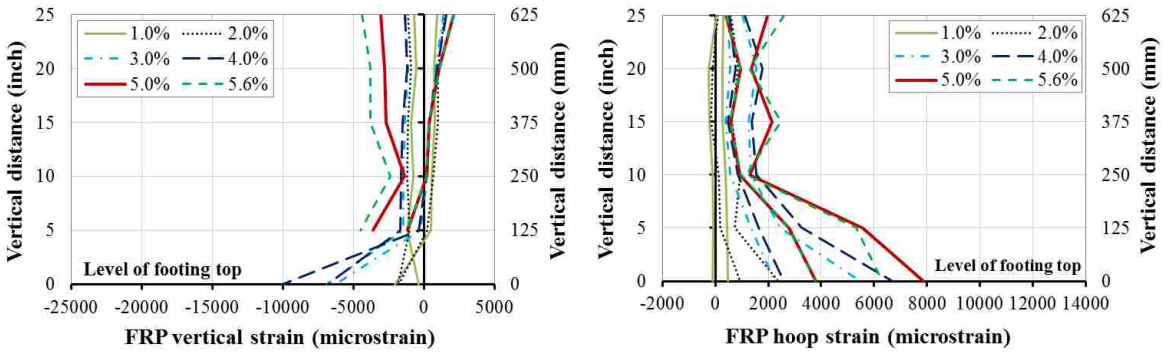

(a) (b)

Fig. 19. FRP strain of the F4-24-P124 column: (a) vertical strain and (b) hoop strain

IV. SEISMIC PERFORMANCE OF INNOVATIVE HOLLOW-CORE FRP-CONCRETE-STEEL BRIDGE COLUMNS

Omar I. Abdelkarim[1], S.M. ASCE; Mohamed A. ElGawady[2]§, PhD, M. ASCE; Ahmed Gheni[3]; Sujith Anumolu[4]; Mohanad Abdulazeez[5]

Abstract

This paper presents the seismic behavior of hollow-core fiber reinforced polymer-concrete-steel (HC-FCS) columns. The typical HC-FCS column consists of a concrete wall sandwiched between an outer fiber reinforced polymer (FRP) tube and an inner steel tube. The inner steel and outer FRP tubes provide continuous confinement for the concrete shell; hence, the concrete shell achieves significantly higher strain, strength, and ductility compared to unconfined concrete in conventional columns. Three large-scale HC-FCS columns were investigated during this study. Each column had an outer diameter of 610 mm (24 inches) and a height-to-diameter ratio of 4.0. The steel tube was embedded into reinforced concrete footing with an embedded length of 1.6-1.8 times the steel tube diameter, while the FRP tube only confined the concrete wall thickness and truncated at the top of the footing level. In general, the columns exhibited high lateral drift reaching to 11.4%, and failed gradually due to concrete crushing and local steel tube buckling. An equation to determine the steel tube development length of HC-FCS

1 Ph.D. Candidate, Dept. of Civil, Architectural, and Environmental Engineering, Missouri University of Science and Technology, Rolla, MO. 65401; oiafgc@mail.mst.edu

2 Benavides Associate Professor, Dept. of Civil, Architectural, and Environmental Engineering, Missouri University of Science and Technology, Rolla, MO. 65401; elgawadym@mst.edu

§Corresponding author

3 Ph.D. Candidate, Dept. of Civil, Architectural, and Environmental Engineering, Missouri University of Science and Technology, Rolla, MO. 65401; aagmr6@mst.edu

4 Graduate Research Assistant, Dept. of Civil, Architectural, and Environmental Engineering, Missouri University of Science and Technology, Rolla, MO. 65401; sat6f@mst.edu

5 Graduate Research Assistant, Dept. of Civil, Architectural, and Environmental Engineering, Missouri University of Science and Technology, Rolla, MO. 65401; mma548@mst.edu

columns was introduced. In addition, this paper introduced a quick repair technique for the HC-FCS columns. Also, guidelines for the preliminary design of the HC-FCS columns under seismic loading were presented to help implement this new technology.

Keywords: Bridge Columns, Precast Columns, Composite Columns, Hollow Columns, Seismic Loading

Introduction

The use of hollow-core cross-sections in bridge columns reduces the mass of the column, and therefore the overall weight of the bridge, which contributes to inertial forces during earthquakes. Several researchers (Mander et al. 1983; Yeh et al. 2001; Lee et al. 2014) have studied hollow-core concrete columns with two coaxial reinforcement layers and transversal reinforcement connected by cross ties throughout the thickness of the wall, and have shown them to exhibit ductile seismic behavior. However, these columns require extensive manpower and construction costs. Other researchers have found that hollow-core columns with one layer of longitudinal reinforcement within the wall reduce construction costs greatly, but display increased brittleness because of the concrete spalling at the inner surface of the cross-section (ElGawady et al. 2009; Hoshikuma and Priestley 2000). This limited displacement ductility makes them inappropriate for use in high seismic areas.

Montague (1978) introduced a new form of hollow-core column, consisting of a concrete wall sandwiched between two generally concentric steel tubes. These columns show a distinct advantage over conventional columns like steel or reinforced concrete (RC). The steel tubes increase the member's ductility and strength, compared to

conventional hollow-core columns. In addition, the steel tubes act as a stay-in-place formwork, longitudinal and shear reinforcement, and continual confinement to the concrete core. The concrete core also delays local buckling of the steel tubes (Fouche and Bruneau 2010; Hajjar 2000; Shakir-Khalil & Illouli 1987).

Concrete-filled fiber reinforced polymer tubes (CFFTs) are similar to concrete-filled steel tubes, and have gained wide acceptance as a viable alternative due to the higher strength-to-weight ratio and corrosion resistance of the fiber reinforced polymer (FRP). The behavior of concrete-filled FRP tube columns under extreme loads has been extensively researched (Qasrawi et al. 2014; Moon et al. 2013; ElGawady and Dawood 2012; ElGawady and Sha'lan 2011; Sadeghian and Fam 2010; ElGawady et al. 2010; Shao and Mirmiran 2005; Fam et al. 2003; Zhang and Shahrooz 1997). More recently, Teng et al. (2004) used a section similar to that of Montague et al. (1978); however, FRP was used as an outer tube and steel as an inner tube to introduce the hollow-core FRP-concrete-steel column (HC-FCS). The HC-FCS system combines the benefits of all three materials: FRP, concrete, and steel in addition to the benefits of the hollow-core concrete columns.

The HC-FCS columns have been investigated extensively under axial compression loading (e.g., Abdelkarim and ElGawady 2014a; Teng et al. 2007). Fewer researchers have investigated the performance of HC-FCS columns under flexure loading using a numerical analysis (Abdelkarim and ElGawady 2014b) or experimental work (Ozbakkaloglu and Idris 2014; Zhang et al. 2012; Han et al. 2010). These previous studies were carried out on small-scale specimens using manual wet layup unidirectional FRP, a low diameter-to-thickness (D_i/t_s) ratio of the steel tube (e.g., $D_i/t_s = 35$), and thick

concrete wall thickness (i.e., low void ratio). The results of the studies showed high concrete confinement and ductility of the HC-FCS columns under axial compression or flexure loading.

Post-earthquake, effective search and rescue and recovery efforts depend on immediate repair of local bridge networks. Quick repair to damaged bridge columns could be either temporary or long-term, but it is not anticipated that the quick repair would restore the lateral load capacity to 100%. FRP wrapping has shown sufficient restoration of strength and ductility (Fakharifar et al. 2015; He et al. 2013).

This paper introduces a resilient, durable, and quickly-constructed hollow-core bridge column. HC-FCS column offers several distinct advantages over the conventional reinforced concrete (RC) column. HC-FCS column uses 60 to 75% less concrete material, 90% reduction in construction time, the steel and FRP tubes acting together as stay-in-place formworks, and the steel tube acting as flexural and shear reinforcement. The FRP and steel tubes protect the concrete core from shrinkage, as they do not absorb any water. This research investigated large-scale HC-FCS columns under seismic loading. The investigated HC-FCS columns were constructed out of filament-wound FRP tubes with a thin concrete wall thickness (16% to 20% of the column diameter), low to high diameter-to-thickness ratios of the steel tube (D_i/t_s = 32 to 56), and low to high FRP confinement. In addition, this paper introduces guidance for the preliminary design of the HC-FCS columns for bridge engineers. A quick repair technique using FRP wrapping to a HC-FCS column is presented and investigated under seismic loading.

Experimental Program

Three large-scale HC-FCS columns were tested as free cantilevers under both constant axial compressive loading and cyclic lateral loading. Two columns were tested as virgin specimens and third one was tested as a repaired specimen (Table 1 and Fig. 1). Each column had a circular cross-section with an identical outer diameter (D_o) of 610 mm (24 inch). The nominal inner diameter of each column was 356 mm (14 inch) or 406 mm (16 inch). Each column had a height of 2,032 mm (80 inch). The lateral load was applied at a height (H) of 2,413 mm (95 inch) measured from the top of the footing, resulting in a shear-span-to-depth ratio of approximately 4.0.

The F4-24-E325 column had a concrete wall thickness (t_c) of 127.0 mm (5.0 inch; Fig. 1(a)). It was constructed using an outer filament-wound epoxy-based glass FRP tube with a wall thickness (t_{FRP}) of 9.5 mm (0.375 inch). The inner steel tube had an outer diameter (D_i) of 356 mm (14 inch) and a wall thickness (t_s) of 6.4 mm (0.25 inch) with a steel tube diameter-to-thickness (D_i/t_s) ratio of 56.

The F4-24-E344 column had a concrete wall with a thickness (t_c) of 102 mm (4.0 inch; Fig. 1(b)). It was constructed using an outer FRP tube the same as that of the F4-24-E325 column. The inner steel tube had D_i of 406 mm (16 inch) and t_s of 12.7 mm (0.50 inch) with D_i/t_s of 32.

The F4-24-P124-R column was a repaired column of Column F4-24-P124 and that originally tested as virgin specimen until rupture (Abdelkarim et al. 2015). Once the specimen failed, it was repaired and retested. The results of the repaired column are presented in this manuscript. For briefly, the original column is renamed in this manuscript as “C1.” Column C1 had t_c of 102 mm (4.0 inch; Fig. 1(c)). It was

constructed using an outer filament-wound Iso-polyester-based GFRP tube having t_{FRP} of 3.2 mm (0.125 inch). The inner steel tube had D_i of 406 mm (16 inch) and t_s of 6.4 mm (0.25 inch) with D_i/t_s of 64. The C1 column was wrapped with three layers of unidirectional FRP along the bottommost 1,140 mm (45 inch). This length was determined based on the visual inspection of FRP tube rupture in the virgin specimen (Abdelkarim et al. 2015).

The inner steel tube of each of the HC-FCS columns was extended inside its footing and stub using an embedded length (L_e) of 635 mm (25 inch), representing $1.6D_i$ in the case of specimens F4-24-E344 and F4-24-P124-R and $1.8D_i$ in the case of specimens F4-24-E325. The FRP tube was truncated at the top surface of the footing and at the bottom surface of the column's loading stub. None of the HC-FCS columns included any rebars. All of the steel tubes were hollow inside.

Each column's footing had a length, width, and depth of 1,524 mm (60 inch), 1,219 mm (48 inch), and 864 mm (34 inch), respectively. Each of the footings of the columns F4-24-E325 and F4-24-P124-R had bottom reinforcements of 7 φ 22 mm (7 # 7), top reinforcements of 6 φ 22 mm (6 # 7), and shear reinforcement of φ13 @ 64 mm (#4 @ 2.5 inch). The footing of the column F4-24-E344 had bottom reinforcements of 7 φ 25 mm (7 # 8), top reinforcements of 6 φ 25 mm (6 # 8), and shear reinforcement of φ13 @ 64 mm (#4 @ 2.5 inch).

Rapid Repair for Column C1 using FRP Wrapping

The repair of column C1 started with manually removing all disintegrated crushed concrete and vacuum dust. Three layers of unidirectional GFRP were impregnated with

two-component epoxy and were wrapped around the bottommost 1,140 mm (45 inches) of the tested column in approximately 1 hour (Fig. 2). A heat chamber using a paperboard tube was installed around the wrapped FRP and the temperature was raised to 50^{o} C using two heat guns (Fig. 2). The temperature was recorded and kept constant for 4 hours to accelerate the curing of the GFRP according to the manufacturer's recommendations. Then, the heat guns were removed and grout was injected using low pressure to replace the damaged concrete chunks (Fig. 2). The total time of the rapid repair was 6 hours; however, the column was tested 45 hours after starting the repair due to test preparation.

Material Properties

Table 1 summarizes the unconfined concrete cylindrical strengths (f_c') for the columns and the footings at 28 days and the days of the tests.

Three standard longitudinal coupons were cut from a steel tube and tested for tensile tests according to ASTM A1067. The steel tube had yield stress, ultimate stress, yield strain, and ultimate strain of 324 MPa (47,000 psi), 483 MPa (70,000 psi), 1.6%, and 19.0%, respectively.

According to ASTM D3039, three longitudinal coupons were cut from each GFRP tube. All of the GFRP coupons failed by delamination between the FRP layers without fiber rupture. The ultimate stress was 65.5 MPa (9,500 psi). The saturated FRP with a fiber orientation at $\pm 53^{o}$ has a structure that depends on fibers in two directions [$\pm 53^{o}$] with adhesive material between them. The width of the strip is only 25 mm (1.0 inch), so there is no fiber continuity. Therefore, the properties of the FRP were referenced based on the manufacturer data sheet (Tables 2 and 3).

Test Instrumentations

Fig. 3 shows the typical test instrumentations. Fifteen linear variable displacement transducers (LVDTs) and string potentiometers (SPs) were used to measure the displacements of each column. Two more LVDTs were attached to each footing to measure any potential sliding and uplift. Seventy-two strain gauges were symmetrically installed inside the steel tube of each HC-FCS column at nine levels at 127 mm (5 inch) intervals. Forty-eight strain gauges were installed on each FRP tube at six levels at 127 mm (5 inch) intervals. The joint opening of the F4-24-E325 column was measured using a string potentiometer (Fig. 3). The joint opening measures were recorded only for the F4-24-E325 column was the last tested column. Attempts, using different techniques, were used to measure the joint opening for the other columns but with no success.

Test Setup and Loading Protocol

A constant axial load (P) of 490 kN (110 kips), representing 5% of the axial capacity (P_o) of a conventional reinforced concrete column of the same outer diameter as the investigated columns with 1% of longitudinal reinforcement, was applied to each of the columns, and kept constant during the test using two automatic hydraulic jacks.

The axial load was applied using six 12.7 mm (0.5 inch) prestressing strands that were installed outside the column at the east and west sides of the centers of the columns and were supported by a rigid steel beam atop the column head and at the column's footing (Fig. 4).

After the axial load was applied, cyclic lateral loading was applied in a displacement control using two hydraulic actuators connected to the column's loading stub at one end

and to a strong wall at the other end (Fig. 4). The loading regime is based on the recommendations of FEMA 2007 where the displacement amplitude a_{i+1} of the step i+1 is 1.4 times the displacement amplitude of the proceeding step (a_i). Two cycles were executed per each displacement amplitude. Fig. 5 illustrates the loading regime of the cyclic lateral displacement. The loading rate ranged from 0.25 mm/sec. (0.01 inch/sec.) to 1.27 mm/sec. (0.05 inch/sec.). The load was applied until the failure of a test specimen.

Results and Discussion

General Behavior

Fig. 6 illustrates the hysteretic moment-lateral drift relation of all of the columns. The lateral drift of each column was obtained by dividing the lateral displacement, measured from the actuators and corrected for any footing sliding, or uplift, by the height of the lateral load (i.e., 2,413 mm (95 inch)). The moment at the base of the column was obtained by multiplying the sum of the lateral forces, measured by the actuators' loading cells, by the column's height of 2,413 mm (95 inch). Figs. 7 and 8 show the columns' profiles and the damaged area at failure, respectively. Table 4 presents a summary of the maximum moments, the lateral drift at maximum moment, and the maximum lateral drift of each column. In this manuscript, the lateral loads and drifts are given using average values of the pull and push directions.

For the F4-24-E325 column, the average peak moment of the column was 677 kN.m (499 kip.ft) at a lateral drift of 3.0% (Fig. 6a). Generally, the column behaved linearly up to 0.4%. Then, gradual stiffness degradation occurred until a drift of approximately 3.0%. The peak flexural strength of the column remained approximately constant until a drift of

approximately 6.0%. Beyond that, the column's flexural strength gradually decreased until a drift of 11.4%. At this drift ratio, the column suffered a 20% strength reduction. Cycling continued beyond that until a lateral drift of 15.6% when the column suffered a 54% strength reduction without any significant damage. The test was ended and the lateral drift of 11.4% was considered as the drift at failure. The post-test visual inspection showed that the steel tube suffered severe local buckling which led to steel tube fracture due to low cyclic fatigue. The local steel tube buckling was mainly within the bottommost 127 mm (5 inch) atop the footing surface (Fig. 8a).

For the F4-24-E344 column, the average peak moment of the column was 1,186 kN.m (875 kip.ft) at a lateral drift of 7.7% (Fig. 6b). Generally, the column behaved linearly up to 0.5%. Then, gradual stiffness degradation occurred until a drift of approximately 7.7%. The column suffered significant stiffness softening after a lateral drift of approximately 8% because the footing suffered severe damage due to pullout of the steel tube from the footing, indicating an inadequate development length (Fig. 8b). The column lost approximately 15% of its flexural strength at a lateral drift of 11.6% when the test was ended due to the severe damage of the footing.

Fig. 6c illustrates the hysteretic moment-lateral drift relation of the F4-24-P124-R and the virgin column C1 (Abdelkarim et al. 2015). The average peak moment of the virgin column was 748.0 kN.m (552.0 kip.ft) at a lateral drift of 2.6%. The F4-24-P124-R column had an average moment capacity of 693 kN.m (512 kip.ft) at a lateral drift of 8%. The repaired column showed large hysteretic loops indicating high energy dissipation. The failure of the F4-24-P124-R column occurred at a lateral drift of 13.2% due to rupture of FRP layers (Fig. 8c). This indicated the FRP wrapping well confined the

concrete core. The repaired column achieved 95% of the virgin column's strength and 61% of the virgin column's elastic stiffness. While, the flexural strength of HC-FCS column was retrieved, the elastic stiffness was not restored.

Effect of Steel Tube Thickness

The steel tube thickness plays a major role in determination of the flexural strength of HC-FCS. Fig. 9 shows the comparison between the backbone curves of specimen F4-24-E344 and specimen F4-24-E324 that was tested by Abdelkarim et al. (2015, for briefly it is called C2 in this manuscript). As shown in Fig. 9, when the steel tube thickness increased by 200%, the flexural strength of the column increased by 162%. However, the thicker steel tube led to early pullout failure and hence specimen F4-24-E344 reached 76% of the ultimate displacement of specimen C2. The figure also illustrates the limit states of steel yielding in tension or compression, steel buckling, footing damage, and FRP rupture of each column.

The steel tube of the columns F4-24-E325, F4-24-E344, C1, and C2 yielded in tension at a lateral drift ranging from 1.1%-1.8%. However, the behavior of each column was different in compression whether in yielding or buckling. The steel tubes of the columns F4-24-E325, F4-24-E344, C1, and C2 yielded in compression at a lateral drift of 0.4%, 3.6%, 2.6%, and 0.8%, respectively. The steel tubes of the F4-24-E325 and the C2 columns buckled at almost the same lateral drift of 3.0% while the steel tubes of the F4-24-E344 and the C1 columns did not buckle.

Effect of Concrete Wall Thickness and Dilation

The effect of the concrete wall thickness and the steel tube lever arm can be better understood by comparing the behavior of the F4-24-E325 and the C2 columns (Fig. 9). The concrete dilation of the F4-24-E325 was higher than that of the C2 because it was thicker in the concrete wall. Therefore, the concrete lateral pressure on the steel tube was higher in the F4-24-E325 column than in the C2 column. Increasing the concrete wall thickness from 102.0 mm (4.0 inch) in column C2 to 127.0 mm (5.0 inch) in column F4-24-E325 reduced the flexural strength by 7.5%. This occurred since both columns had the same outer diameter. Hence, increasing the concrete wall thickness reduced the lever arm and hence reduced the ultimate moment capacity. Similar observation was reported by Abdelkarim and ElGawady (2014b). Furthermore, reducing the steel tube diameter from 406.0 mm (16 inch) to 356.0 mm (14 inch) reduced the total steel area by 12.5% which increased the strain demand on the steel tube in the case of F4-24-E325.

The radial dilation of the concrete shell imposes a significant tensile hoop strain demand on the FRP and compression hoop strain demand on the steel tube. This demand depends on the relative stiffness of the FRP and steel tubes (Abdelkarim and ElGawady 2014b). The concrete dilation in the F4-24-E325 and C2 columns, where the high stiffness FRP tube was used, went toward the steel tube, which increased the deformation demand on the steel tube and led to early local buckling. Consequently, the FRP rupture occurred later when the concrete dilation was significantly increased. The concrete dilation in the C1 column went toward the FRP tube because it was considerably thinner. The concrete dilation in the F4-24-E344 column was back and forth between the steel tube side and the FRP tube side as both of them was considerably thick. This behavior

was the reason that the strength degradation of the F4-24-E344 started later than the F4-24-E325, C2, and C1 because the concrete shell was well confined from the inside thick steel tube and the outside thick FRP tube.

Steel and FRP Strains

Fig. 10 illustrates the steel vertical strain profile of all of the columns at the lateral drift of the maximum moment of each column. The figure showed that the steel tubes of the F4-24-E325 and the C2 columns suffered local buckling because their strains' profiles did not change gradually along the height. However, the F4-24-E344 and C1 columns did not suffer local buckling. These results were compatible with the backbone curves. The F4-24-E344 reached a high tensile strain of approximately 15,200 microstrain because the steel tube thickness was considerably thick.

Fig. 11 illustrates the FRP hoop strain profiles for all of the columns at the maximum lateral drift of each column. The high strains were within the bottommost 254 mm (10 inches) for all of the columns. The FRP of the F4-24-E325, F4-24-E344, C1, and C2 reached a hoop tensile strain of 10,000 microstrain, 11,800 microstrain, 7,800 microstrain, and 13,500 microstrain, respectively.

Development Length of Steel Tube

The steel tube development length into footing affected the behavior of HC-FCS column. The required development length of a concrete-filled steel tube column having a tube similar to that of the F4-24-E344 column is 610 mm (24 inch), which was calculated using equation (1) as presented by Moon et al. (2013). This development length was not

enough to fully develop the steel tube into the footing in the case of the F4-24-E344 column. This behavior is expected since the concrete-filled steel tube has two surfaces of bond between the steel tube and footing of inner and outer surfaces, while the HC-FCS column has only one outer bonding surface. This paper introduced equation (2) to determine the required development length of the steel tube into footing of HC-FCS column by using half of the bonding surface in equation (1).

$$\frac{D_i t_s F_u}{{l_e}^2 + D_o l_e} \leq 0.55\sqrt{f'_{c,FT}} \quad (1)$$

$$\frac{D_i t_s F_u}{\frac{1}{2}\left({l_e}^2 + D_i l_e\right)} \leq 0.55\sqrt{f'_{c,FT}} \quad (2)$$

where D_i is the steel tube outer diameter (mm), t_s is the steel tube thickness (mm), F_u is the ultimate stress of steel tube (MPa), D_o is the outer diameter of an annual ring welded with the bottom of steel tube of concrete-filled steel tube (mm), l_e is the development length (mm), and $f'_{c,FT}$ is the unconfined characteristic cylindrical compressive strength of the concrete footing (MPa).

Finite element (FE) analysis was conducted for the F4-24-E344 column to determine the required development length numerically. LS-DYNA software was used to implement the analysis. FE modeling of HC-FCS columns was described and validated with experimental results by Abdelkarim and ElGawady (2014b). The FE results well correlated with the experimental results as listed in Table 5. Using the FE model of the F4-24-E344 column, different values of the development length of the steel tube was studied until the fully development achieved. Fig. 12 illustrates the development length versus the flexural strength of the F4-24-E344 column. The required steel tube

development length of the F4-24-E344 column from FE was 895.0 mm (35.3 inch) as the column's flexural strength was constant after this development length. Equation (2) revealed that the required development length of the steel tube of F4-24-E344 column was 863.0 mm (35.8 inch) with an error of 1.5% over the FE result. Equation (2) was validated with the FE results of different six columns by changing their steel tube diameter, the steel tube thickness, and the steel tube ultimate stress as shown in Fig. 13. The equation showed good correlation with the FE results with an average error of 8.6%.

Joint Opening and Steel Tube Vertical Sliding

Fig. 14 illustrates the joint opening versus the lateral drift of the column F4-24-E325. Maximum joint opening was approximately 60 mm (2.4 inch). The joint started to open at a lateral drift of 0.5%. Then, it increased linearly with increasing the lateral drift. As shown in the Fig., at a lateral drift of 3.0%, the joint opening was approximately 10 mm (0.4 inch). The joint opening and steel tube vertical sliding were identified numerically using the FE analysis for the all of the columns (F4-24-E325, F4-24-E344, C1, and C2 columns). The FE model of the F4-24-E325 column well captured the joint opening (Fig. 14). Fig. 15 illustrates the joint opening of all of the columns collected from the FE. At same lateral drift, the C1 column showed the lower joint opening while the F4-24-E344 column showed the higher joint opening. For example, at a lateral drift of 5.0%, the joint opening of the C1 column was 17.8 mm (0.70 inch) while the joint opening of the F4-24-E344 column was 23.8 mm (0.94 inch). Fig. 16 illustrates the steel tube vertical sliding of all of the columns collected from the FE. The maximum steel tube vertical sliding of the F4-24-E325, F4-24-E344, C1, and C2 columns were 3.6 mm (0.14 inch), 24.4 mm (0.96

inch), 1.5 mm (0.06 inch), and 2.8 mm (0.11 inch), respectively. At same lateral drift, the C1 column showed the lower steel tube vertical sliding while the F4-24-E344 column showed the higher steel tube sliding. These results indicated that the steel tube of F4-24-E344 column was not fully developed.

Preliminary Design of HC-FCS Columns

This paper presents guidelines for the selection of the HC-FCS columns dimensions for preliminary design, based on the limited experimental investigation presented in this paper and by Abdelkarim et al. (2015), as follows:

a- Determine an initial size of the column's outer diameter (D_o).

b- Compute the minimum concrete wall thickness (t_c) based on constructability. Currently, based on the limited test data, it is recommended to select t_c as follows:

$$t_c = (0.10 \text{ to } 0.20)\, D_o \tag{3}$$

c- Compute the outer diameter of the steel tube (D_i) using Equation 4.

$$D_i = D_o - 2\, t_c \tag{4}$$

It is worth noting that increasing the steel tube diameter will decrease the column weight. However, it will increase the column's flexural strength as the lever arm of the tensile forces in the steel tube increases (Abdelkarim and ElGawady 2014b).

d- Compute the thickness of the steel tube (t_s) using Equation 5.

$$t_s = \frac{D_i}{64} \tag{5}$$

The steel tube's thickness is controlled by the diameter-to-thickness ratio (D_i/t_s). Thinner steel tubes are more susceptible to local buckling. However, a thicker steel tube would increase the column's weight, cost, and strength. The tubes that were investigated during the current research have maximum D_i/t_s of 64. Hence, until further research is available, it is recommended to keep D_i/t_s to 64.

e- Compute the FRP tube thickness (t_{FRP}) using Equations 6 and 7 for low and high seismic regions, respectively.

$$t_{FRP} = 0.035 \frac{D_o f_c'}{f_t} \tag{6}$$

$$t_{FRP} = 0.105 \frac{D_o f_c'}{f_t} \tag{7}$$

where f_t is the ultimate hoop tensile stress of the FRP tube and f_c' is the cylindrical unconfined concrete compressive strength at 28 days. A minimum f_t value of 275 MPa (40,000 psi) is recommended.

The FRP tube represents the concrete confinement which allows the column to reach higher lateral drift before failure. Two FRP tube's thicknesses were presented during the course of this study. Both thicknesses were able to display large lateral drifts of 13.0% and 5.8% before rupture. Hence, until further research is carried out, the lateral confinement pressure used in the test columns were used to develop recommendations for the FRP thickness.

f- Check the column flexural strength comparable to the ultimate applied loads using Equation (8), where the nominal strength of the HC-FCS columns (M_n) could be calculated as described in Abdelkarim and ElGawady (2015b).

$$0.9\, M_n \geq M_u \tag{8}$$

where M_u is the factored applied moment on the column due to external loads.

Findings and Conclusions

This paper presented the seismic behavior of the hollow-core fiber reinforced polymer-concrete-steel (HC-FCS) columns. The HC-FCS columns consisted of a concrete wall sandwiched between an outer FRP tube and an inner steel tube. Three large-scale columns were investigated during this study. Each column had an outer diameter of 610 mm (24 inches) and a shear span of 2,413 mm (95 inches) with a shear span-to-diameter ratio of approximately 4.0. The steel tube was extended inside the footing with an embedded length of 1.6-1.8 times the steel tube diameter. The steel tube development length affected the behavior of the HC-FCS column. Therefore, this paper introduced an equation to determine the steel tube development length. The guidelines for the preliminary design of the HC-FCS columns were presented. Also, this paper introduced a quick repair technique for the HC-FCS columns. This study revealed the following findings:

1. In general, the HC-FCS columns performed well under seismic loading.
2. The HC-FCS column exhibited a high lateral drift reaching to 11.4%.

3. The flexural strength of the HC-FCS column is related mainly to the steel tube thickness.
4. The steel tube buckling occurred when the FRP tube was considerably thicker.
5. The HC-FCS columns can be quickly repaired using FRP wrapping. The repaired column performed well under seismic loading where it retrieved 95% of the virgin column's flexural strength and 61% of the virgin column's stiffness.

Acknowledgement

This research was conducted at Missouri University of Science and Technology and was supported by the Missouri Department of Transportation (MoDOT) and Mid-American Transportation Center (MATC). In kind contribution from ATLAS Tube is appreciated. Discounts on FRP tubes from Grace Composites and FRP Bridge Drain Pipe are also appreciated. The authors also extend their appreciation to the National University Transportation Center (NUTC) at Missouri University of Science and Technology (Missouri S&T). However, any opinions, findings, conclusions, and recommendations presented in this paper are those of the authors and do not necessarily reflect the views of the sponsors.

References

Abdelkarim, O., Gheni, A., Anumolu, S., Wang, S., ElGawady, M. (2015). "Hollow-Core FRP-Concrete-Steel Bridge Columns under Extreme Loading." Missouri Department of Transportation (MoDOT), Project No. TR201408, Report No. cmr15-008, April.

Abdelkarim, O. and ElGawady, M. (2014a). "Behavior of Hybrid FRP-Concrete-Steel Double-Skin Tubes Subjected to Cyclic Axial Compression." Structures Congress 2014: pp. 1002-1013.

Abdelkarim, O. and ElGawady, M. (2014b). “Analytical and Finite-Element Modeling of FRP-Concrete-Steel Double-Skin Tubular Columns.” J. Bridge Eng., 10.1061/(ASCE)BE.1943-5592.0000700, B4014005.

ACI Committee 318 (2011). “Building Code Requirements for Structural Concrete (ACI318-11) and Commentary (318R-11).” American Concrete Institute, Farmington Hills, Mich., pp. 509.

Brown, N.K., Kowalsky, M.J. and Nau, J.M. (2014). “Impact of Diameter to Thickness Ratio on The Seismic Behavior of Reinforced Concrete Filled Steel Tubes.” Tenth U.S. National Conference on Earthquake Engineering Frontiers of Earthquake Engineering July 21-25, Alaska.

ElGawady, M. and Dawood, H. (2012). “Analysis of Segmental Piers Consisted of Concrete Filled FRP Tubes.” Engineering Structures, Vol. 38, pp. 142-152.

ElGawady, M. and Sha’lan, A. (2011). “Seismic Behavior of Self-Centering Precast Segmental Bridge Bents.” J. Bridge Eng., 16(3), 328–339.

ElGawady, M., Booker, A., and Dawood, H. (2010). “Seismic Behavior of Posttensioned Concrete-Filled Fiber Tubes.” J. Compos. Constr., 14(5), 616–628.

ElGawady, M., Cofer, W., and Shafiei-Tehrany, R. (2009). “Seismic Assessment of WSDOT Bridges with Prestressed Hollow Core Piles - Part II.” Washington State Department of Transportation, Report T4120, December.

Fakharifar, M., Chen, G., Sneed, L., and Dalvand, A. (2015). “Seismic performance of post-mainshock FRP/steel repaired RC bridge columns subjected to aftershocks.” Composites Part B: Engineering, 72, 183-198.

Fam, A., Flisak, B., Rizkalla, S. (2003). “Experimental and analytical modeling of concrete-filled fiber-reinforced polymer tubes subjected to combined bending and axial loads.” ACI Structural Journal, 100 (4), pp. 499-509.

Fouche, P., Bruneau, M. (2010). “Non-Linear Analysis of Multi-Hazard Performance of Cylindrical Concrete Filled Steel Tubes Bridge Piers.” Proceedings of 8th International Conference on Short and Medium Span Bridges, Canada.

Hajjar J. (2000). “Concrete-filled steel tube columns under earthquake loads.” Structural Engineering and Materials; 2(1):72–82.

Han, L.H., Tao, Z., Liao, F.Y., and Xu, Y. (2010). “Tests on Cyclic Performance of FRP-Concrete –Steel Double-Skin Tubular Columns.” *Thin-Walled Structures*, 4, 430-439.

He, R., Grelle, S., Sneed, L. H., and Belarbi, A. (2013). “Rapid repair of a severely damaged RC column having fractured bars using externally bonded CFRP.” Composite Structures, 101, 225-242.

Hoshikuma, J., and Priestley, M. J. N. (2000). “Flexural behavior of circular hollow columns with a single layer of reinforcement under seismic loading.” Report No. SSRP-2000/13, University of California, San Diego, La Jolla, CA.

Lee, J., Choi, J., Hwang, D., and Kwahk, I. (2014). “Seismic Performance of Circular Hollow RC Bridge Columns.” KSCE Journal of Civil Engineering, Vol. 19(5), pp. 1456-1467.

Mander, J. B., Priestley, M. J. N., and Park, R. (1983). “Behavior of Ductile Hollow Reinforced Concrete Columns.” Bulletin of the New Zealand National Society for Earthquake Engineering, Vol. 16, No. 4, December, pp. 273-290.

Montague, P., (1978). “Experimental behavior of double-skinned, composite, circular cylindrical-shells under external-pressure.” Journal of Mechanical Engineering Science, 20(1), pp. 21–34.

Moon, J., Lehman, D. E., Roeder, C. W., and Lee, H. E. (2013). “Evaluation of embedded concrete-filled tube (CFT) column-to-foundation connections.” Engineering Structures, 56, 22-35.

Ozbakkaloglu, T. and Idris, Y. (2014). “Seismic Behavior of FRP-High-Strength Concrete–Steel Double-Skin Tubular Columns.” J. Struct. Eng., 140(6), 04014019.

Qasrawi, Y., Heffernan, P., and Fam, A. (2014). “Performance of Concrete-Filled FRP Tubes under Field Close-in Blast Loading.” J. Compos. Constr., 10.1061/(ASCE)CC.1943-5614.0000502 , 04014067.

Sadeghian, P. and Fam, A. (2010). "Bond-Slip Analytical Formulation toward Optimal Embedment of Concrete-Filled Circular FRP Tubes into Concrete Footings." J. Eng. Mech., 136(4), 524–533.

Shakir-Khalil, H., and Illouli, S. 1987. "Composite columns of concentric steel tubes." Proc., Conf. on the Design and Construction of Non-Conventional Structures, Vol. 1, London, pp. 73–82.

Shao, Y. and Mirmiran, A. (2005). "Experimental Investigation of Cyclic Behavior of Concrete-Filled Fiber Reinforced Polymer Tubes." J. Compos. Constr., 9(3), 263–273.

Teng, J.G., Yu, T., and Wong, Y.L. (2004). "Behavior of Hybrid FRP-Concrete-Steel Double-Skin Tubular Columns." *Proc. 2nd Int. Conf. on FRP Composites in Civil Engineering*, Adelaide, Australia, 811-818.

Teng, J. G., Yu, T., Wong, Y. L., and Dong, S. L. (2007). "Hybrid FRP concrete-steel tubular columns: Concept and behavior." Constr. Build. Mater., 21(4), 846–854.

Yeh, Y., Mo, Y., and Yang, C. (2001). "Seismic Performance of Hollow Circular Bridge Piers." ACI Structural Journal, V. 98, No. 6, November-December.

Zhang, B., Teng, J. G. and Yu, T. (2012). "Behaviour of hybrid double-skin tubular columns subjected to combined axial compression and cyclic lateral loading." *Sixth International Conference on FRP Composites in Civil Engineering* (pp. 1-7). Rome, Italy.

Zhang, W. and Shahrooz, B. M. (1997). "Analytical and Experimental Studies into Behavior of Concrete-Filled Tubular Columns." Report No. UC-CII 97/01, Cincinnati Infrastructure Institute, Department of Civil and Environmental Engineering, University of Cincinnati, College of Engineering, Cincinnati, Ohio, May.

Table 1. Summary of the Columns' Variables

Column		F4-24-E325	F4-24-E344	F4-24-P124-R
Nominal outer diameter (D_o, mm (inch))		610 (24)		
Nominal inner diameter (D_i, mm (inch))		356 (14)	406 (16)	406 (16)
Steel tube thickness (t_s, mm (inch))		6.4 (0.25)	12.7 (0.50)	6.4 (0.25)
FRP tube	Matrix	Epoxy		Iso-Polyester
	Thickness (t_{FRP}, mm (inch))	9.5 (0.375)		3.2 (0.125)
Thickness of FRP repair wrapping (mm (inch))		——		3.8 (0.15)
f_c' of the column at 28 days, MPa (psi)		35.6 (5,160)	39.8 (5,770)	39.8 (5,770)
f_c of the column at the day of the test, MPa (psi)		36.8 (5,340)	53.7 (7,787)	43.0 (6,235)
f_c' of the footing at 28 days, MPa (psi)		52.9 (7,670)	56.0 (8,117)	56.0 (8,117)
f_c of the footing at the day of the test, MPa (psi)		56.8 (8,230)	59.3 (8,605)	61.4 (8,910)

Table 2. Properties of the GFRP tubes based on manufacturer's data

	Axial compression elastic modulus (E_a, GPa (ksi))	Axial ultimate stress (f_{ar}, MPa, psi))	Hoop elastic modulus (E_h, GPa, ksi))	Hoop rupture stress (f_{hr}, psi)
Epoxy tube	4.7 (677)	83.8 (12,150)	20.8 (3,020)	276.9 (40,150)
Iso-polyester tube	9.7 (1,400)	123.4 (17,900)	15.2 (2,200)	275.9 (40,000)

Table 3. Properties of saturated GFRP wrapping based on manufacturer's data

	Nominal thickness/layer (mm, (inch))	Young's modulus, E (GPa (ksi))	Tensile strength (MPa (ksi))	Ultimate strain
Wrapping FRP	1.3 (0.05)	26.0 (3,790)	575 (83.4 ksi)	2.2%

Table 4. Summary of the Columns' Results

Column	Average maximum moment, kN.m (kip.ft.)	Lateral drift at the maximum moment	Lateral drift at failure
F4-24-E325	677 (499)	3.0%	11.4%
F4-24-E344	1,186 (875)	7.7%	11.6%
F4-24-P124-R	940 (693)	8.0%	13.2%

Table 5. Summary of the Experimental versus FE Results

Column	$M_{capacity}$		Percentage of error in $M_{capacity}$	Lateral drift at failure		Percentage of error in lateral drift
	Exp., kN.m (kip.ft.)	FE., kN.m (kip.ft.)		Exp.	FE.	
F4-24-E325	677 (499)	595 (439)	12%	11.4%	13.0%	14.0%
F4-24-E344	1,186 (875)	1,125 (830)	5.1%	11.6%	10.7%	7.8%
C1 (Abdelkarim et al. 2015)	748 (552)	632 (466)	15.5%	5.8%	7.2%	19.4%
C2 (Abdelkarim et al. 2015)	732 (540)	680 (501)	7.1%	15.2%	14.5%	4.6%

*The percentage of the absolute value of the difference between the experimental and the analytical ultimate moments divided by the experimental ultimate moment

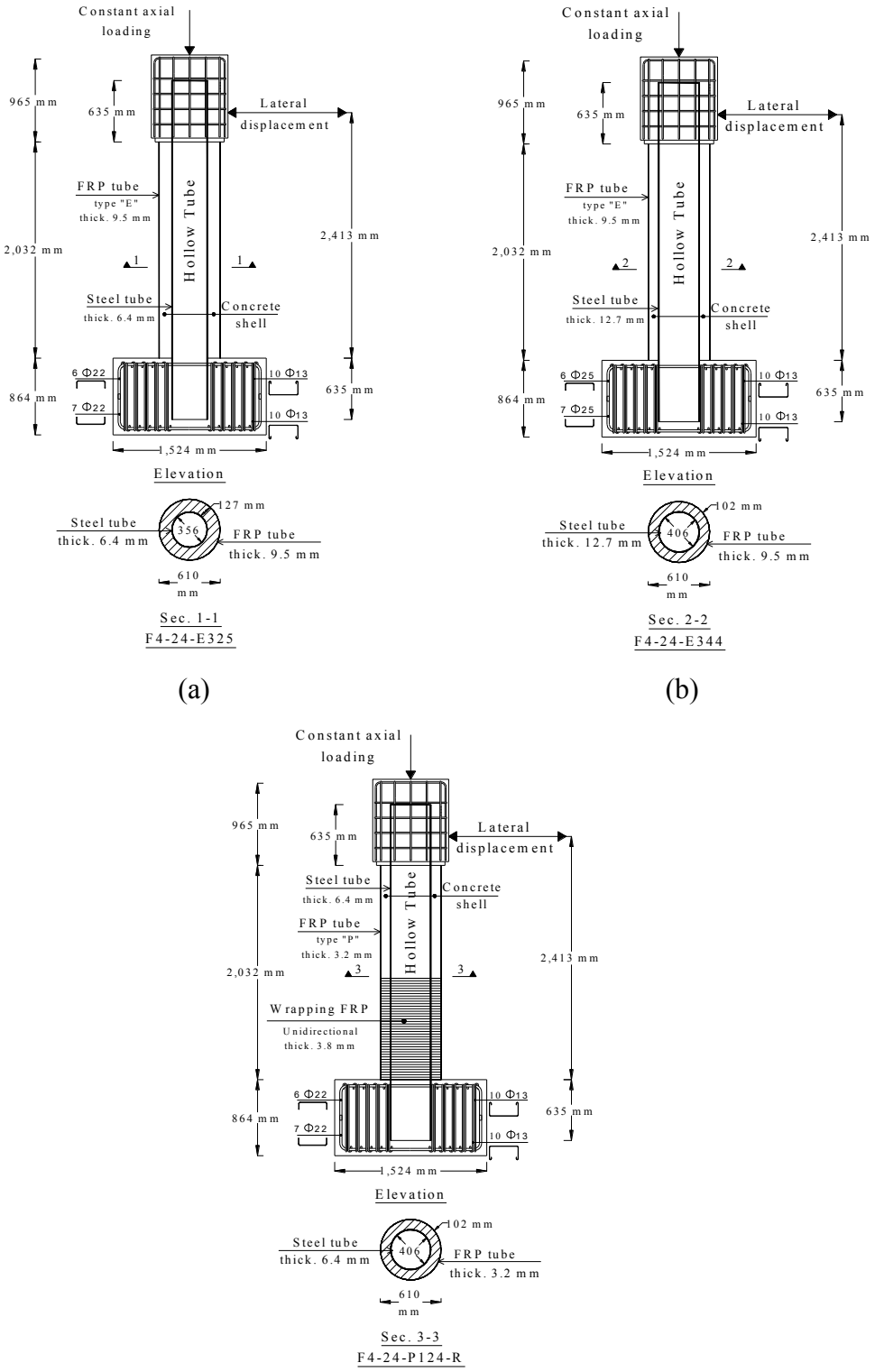

Fig. 1. General arrangement and reinforcement details of the investigated columns: (a) F4-24-E325 column, (b) F4-24-E344 column, and (c) F4-24-P124-R column

(a) (b) (c)

Fig. 2. Rapid repair of the C1 column: (a) wrapped GFRP, (b) heat chamber, and (c) grout injection

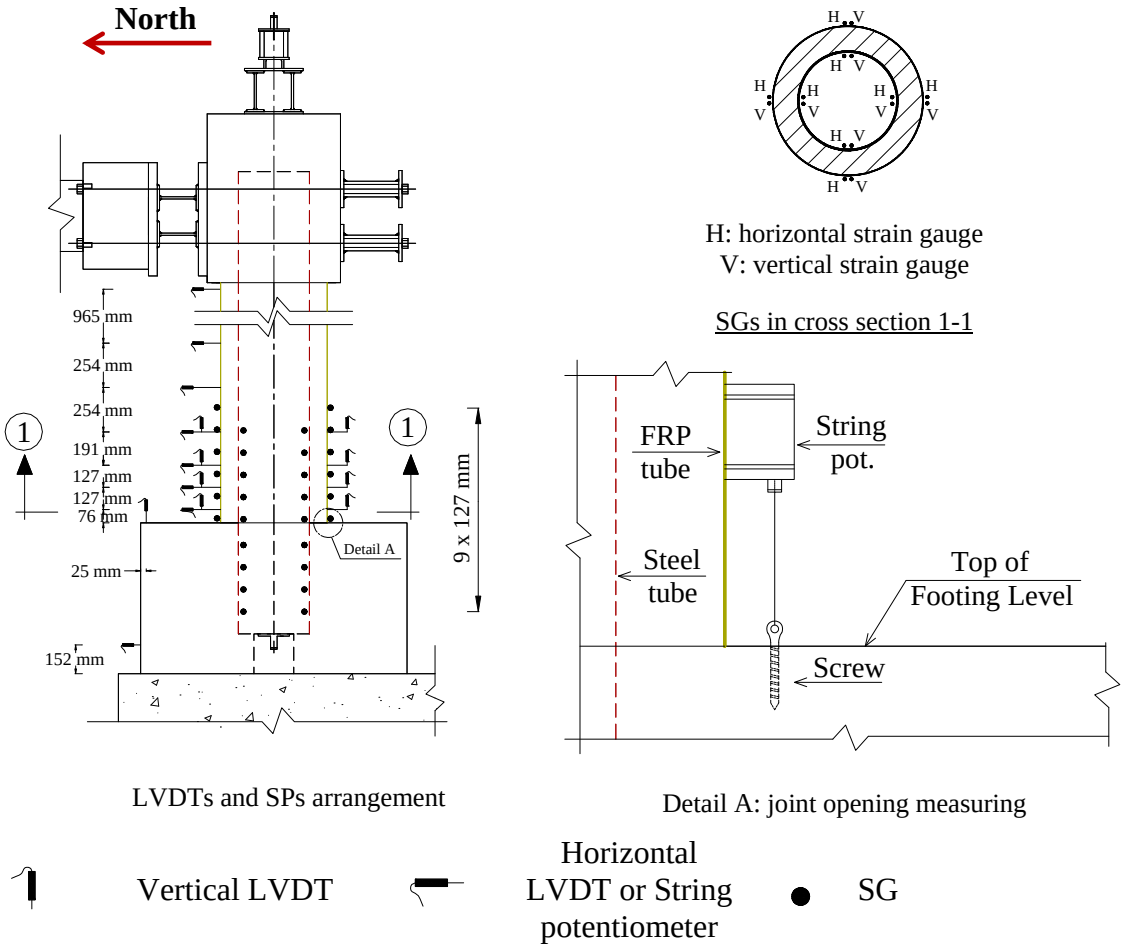

Fig. 3. Layout of the LVDTs, String potentiometers, and strain gauges

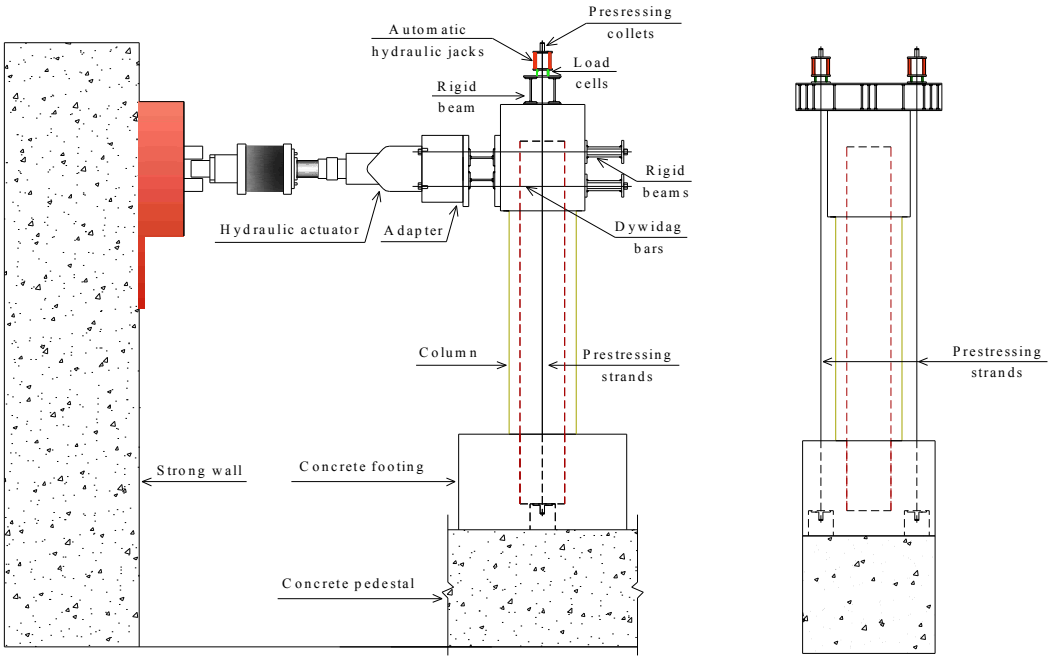

Fig. 4. Column test setup: (a) elevation, (b) side-view

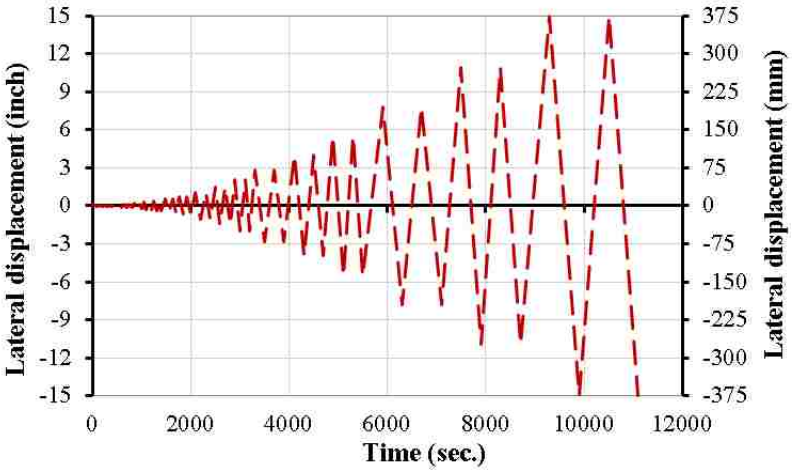

Fig. 5. Lateral displacement loading protocol

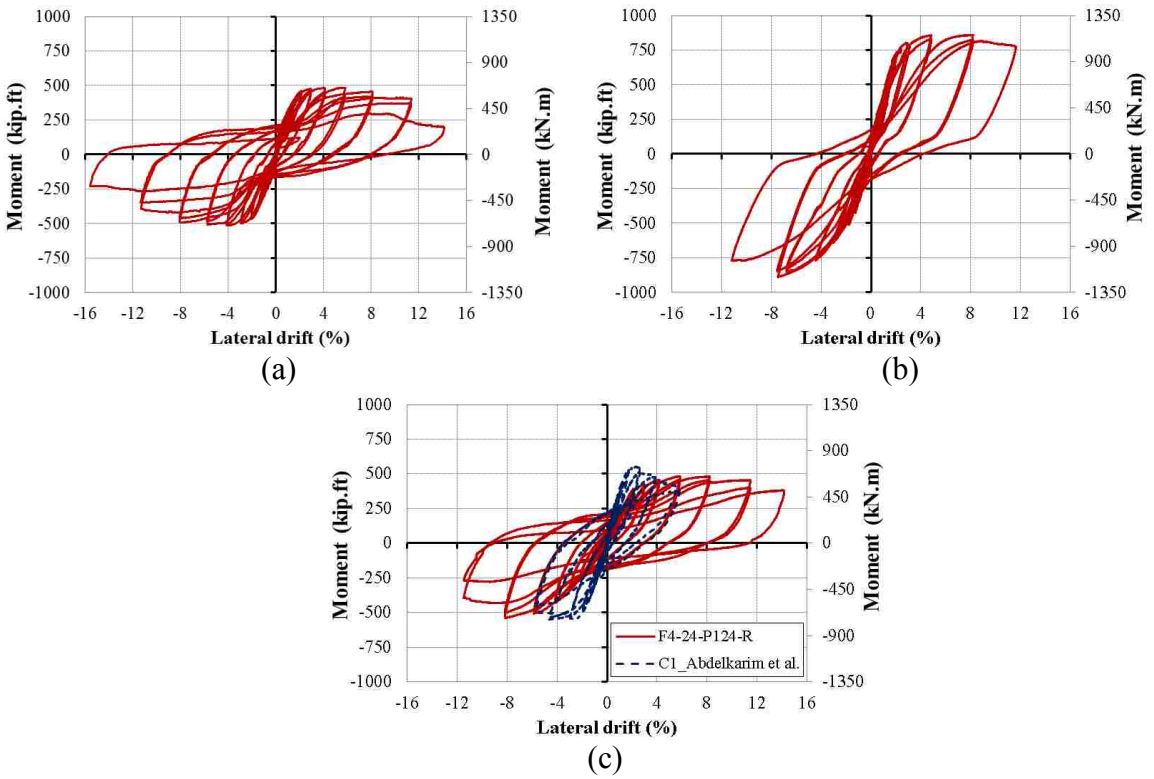

Fig. 6. Hysteretic moment-lateral drift relation: (a) F4-24-E325 column, (b) F4-24-E344 column, and (c) F4-24-P124-R column

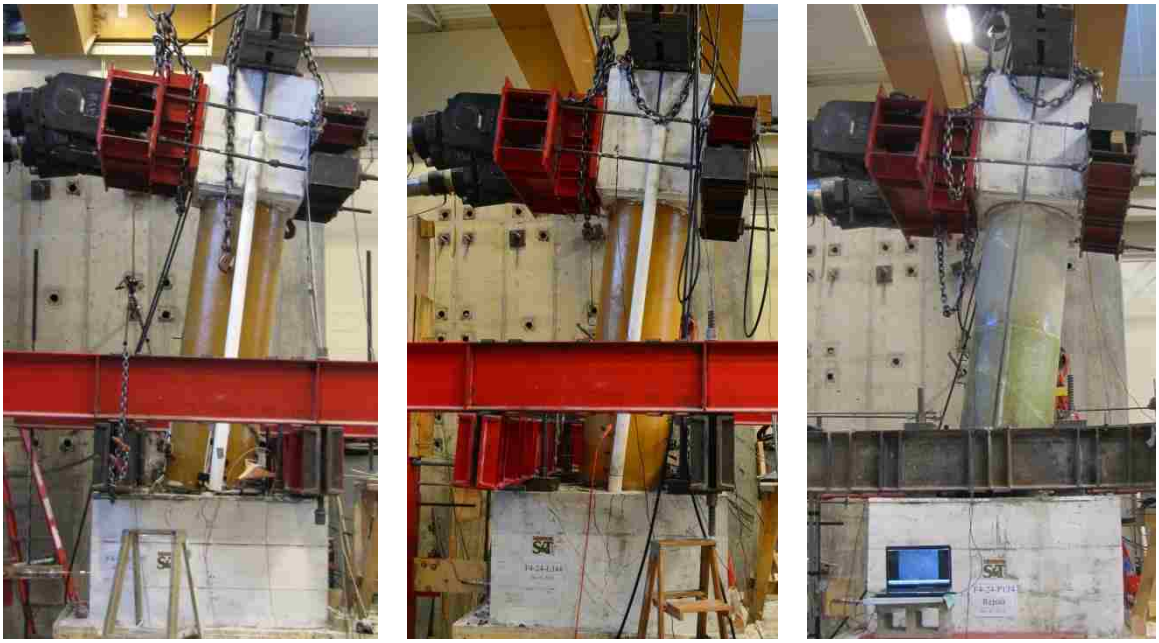

(a) (b) (c)

Fig. 7. Columns' profiles: (a) F4-24-E325 at lateral drift of 15%, (b) F4-24-E344 at lateral drift of 11.0%, and (c) F4-24-P124-R at lateral drift of 11.0%

(a) (b) (c)

Fig. 8. Columns' modes of failure: (a) steel tube fracture of the F4-24-E325 column, (b) footing damage of the F4-24-E344 column, and (c) FRP rupture of the F4-24-P124-R column

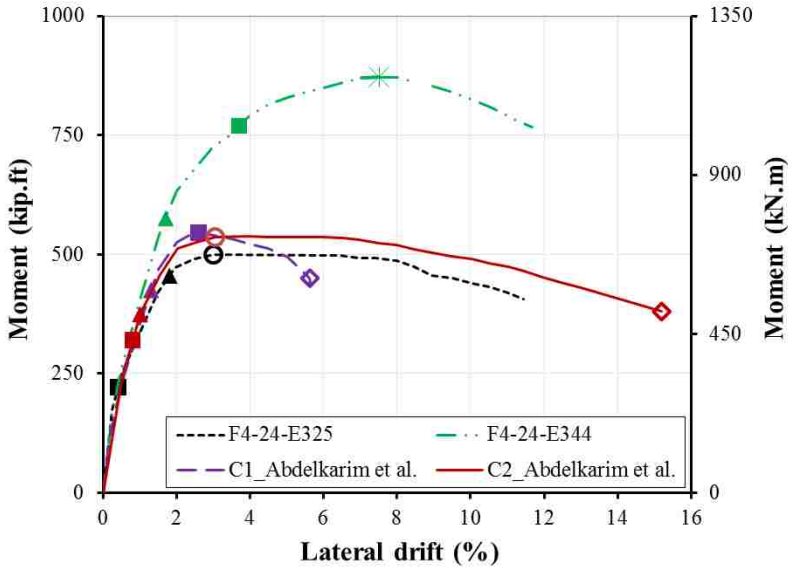

▲ Steel tube yielded in tension ◯ Steel tube buckled in compression

■ Steel tube yielded in compression ◇ FRP rupture

∗ Footing damage

Fig. 9. Backbone moment-lateral drift relation of the columns

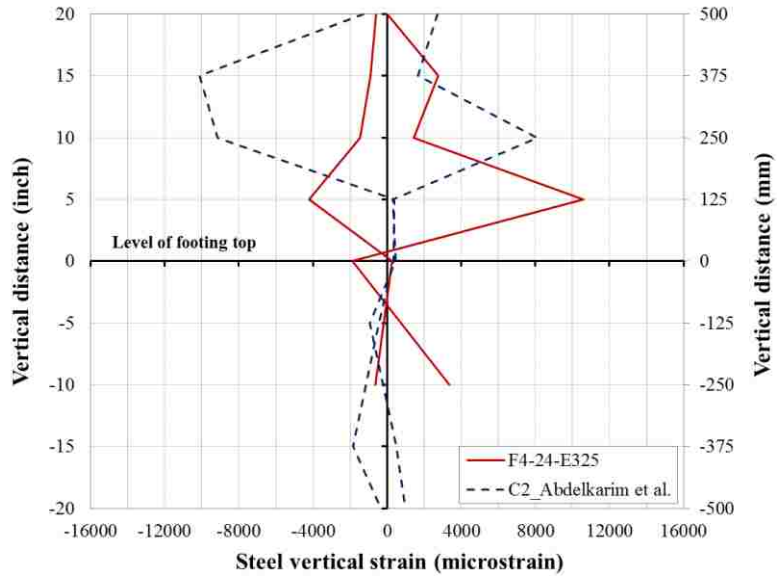

(a)

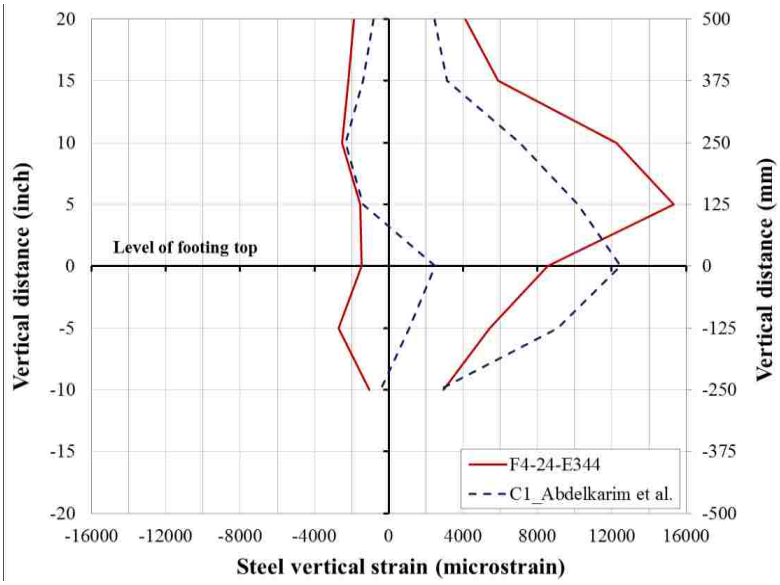

(b)

Fig. 10. Steel tube vertical strain profiles at the lateral drifts of the maximum moment of the columns: (a) F4-24-E325 and C2 by Abdelkarim et al. (2015), and (b) F4-24-E344 and C1 by Abdelkarim et al. (2015)

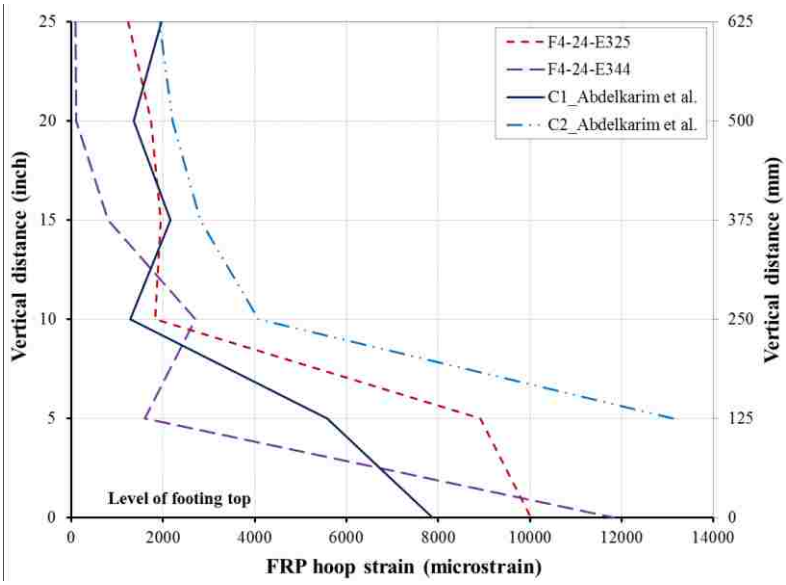

Fig. 11. FRP tube hoop strain profiles of the columns

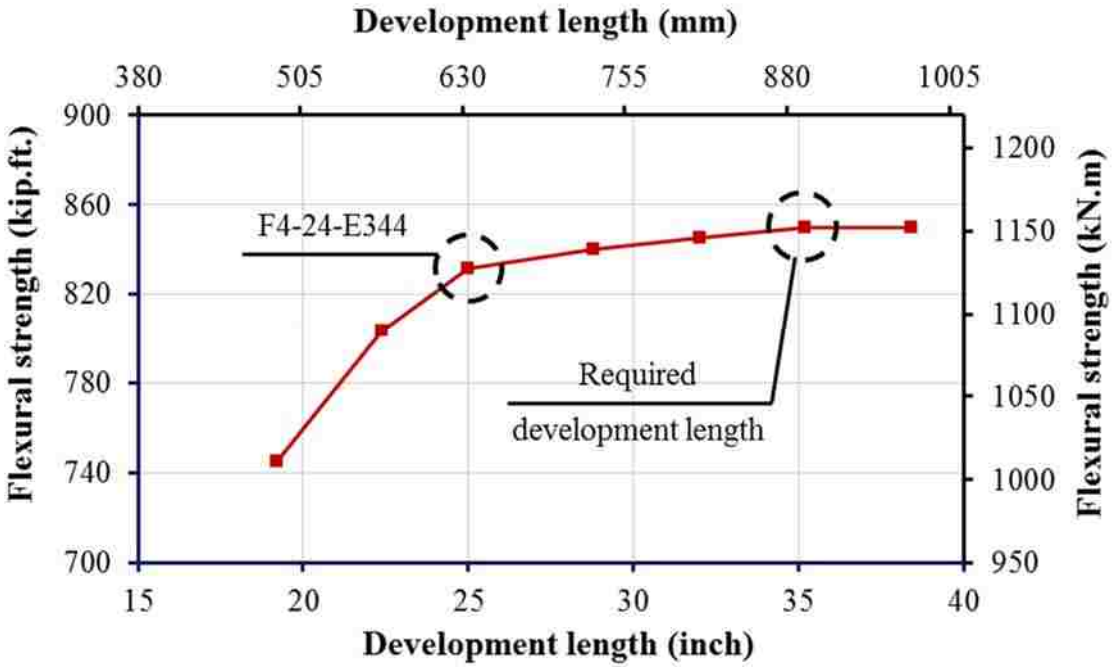

Fig. 12. Steel tube development length versus flexural strength of the column F4-24-E344

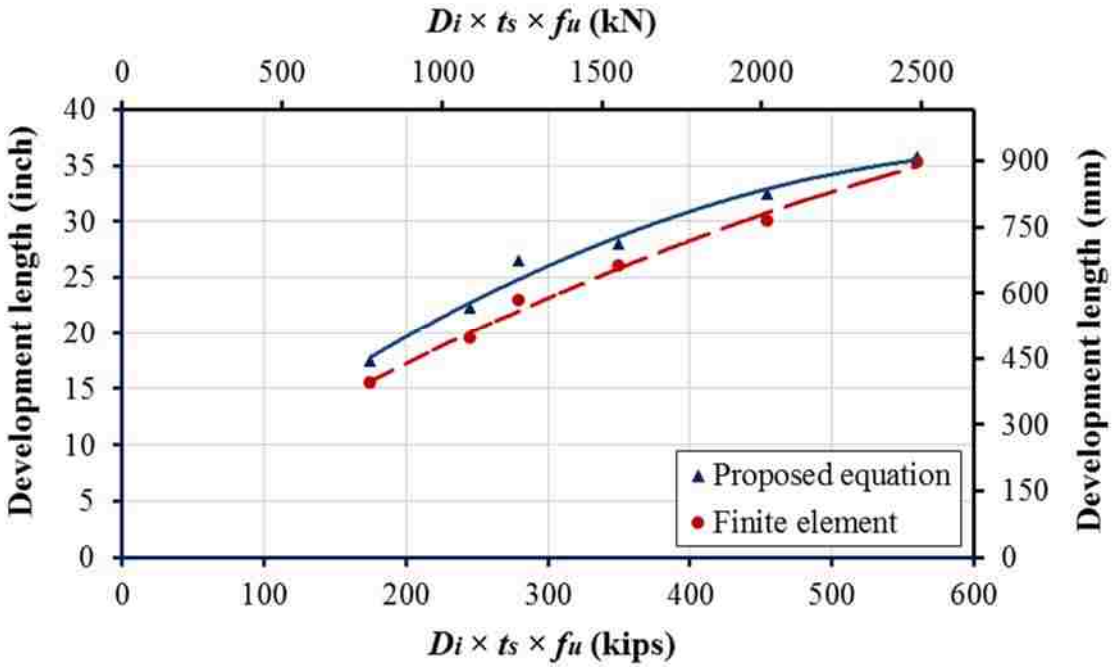

Fig. 13. Proposed equation of steel tube development length versus finite element

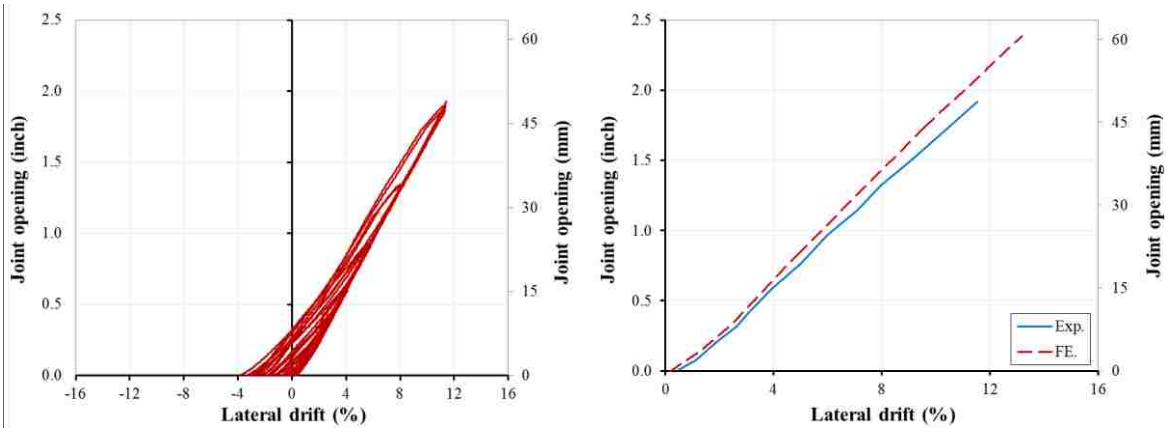

(a) (b)

Fig. 14. Joint opening-lateral drift relation of the F4-24-E325 column: (a) experimental hysteretic curve and (b) experimental and FE backbone curves

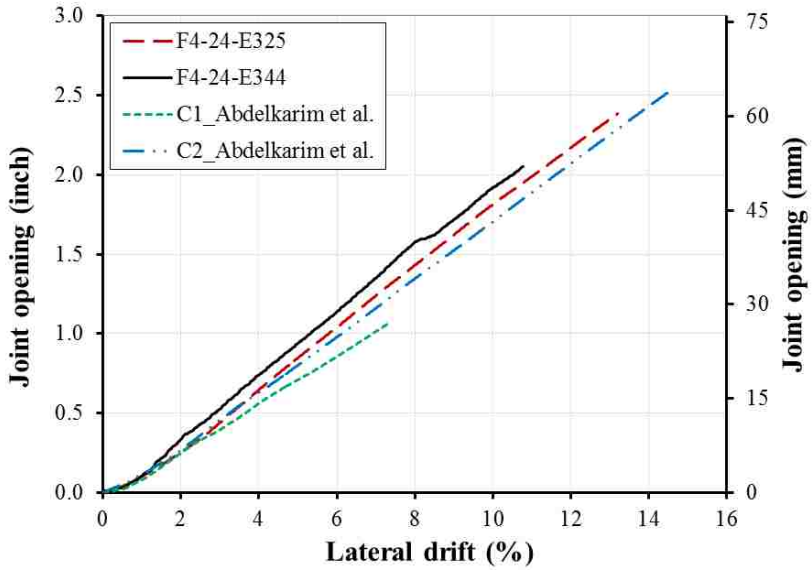

Fig. 15. Joint opening-lateral drift relation of the investigated columns from FE

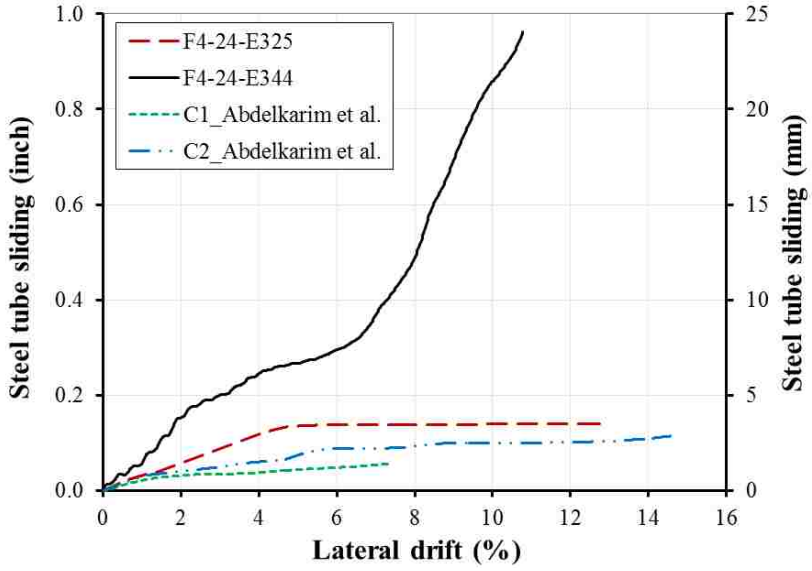

Fig. 16. Steel tube vertical sliding-lateral drift relation of the investigated columns from FE

V. HOLLOW-CORE FRP-CONCRETE-STEEL TUBULAR COLUMNS SUBJECTED TO SEISMIC LOADING

Omar I. Abdelkarim, Ahmed Gheni, Sujith Anumolu, Mohamed A. ElGawady

Synopsis

This paper describes the behavior of precast hollow-core fiber reinforced polymer (FRP)-concrete-steel columns (HC-FCS) under combined axial and lateral loading. The HC-FCS column consists of a concrete wall sandwiched between an inner steel tube and an outer FRP tube. This study investigated two large-scale columns, the traditional reinforced concrete (RC) and the HC-FCS column. The steel tube of the HC-FCS column was embedded into the footing while the FRP tube was stopped at the top of the footing level (i.e. the FRP tube provided confinement only). The hollow steel tube provided the only reinforcement for shear and flexure inside the HC-FCS column. The FRP in HC-FCS ruptured at lateral drift of 15.2% while the RC-column displayed 10.9% lateral drift at failure. The RC-column failed due to rebar rupture when the moment capacity dropped more than 20%. The HC-FCS failed gradually with concrete compression failure and steel local buckling followed by FRP rupture. Finite element (FE) analysis was conducted using LS-DYNA to develop a static cyclic analysis of a three-dimensional HC-FCS model. The FE results mirrored the experimental results. The bending strength of HC-FCS columns could easily be calculated with a high degree of accuracy using sectional analysis based on Navier-Bernoulli's assumptions and strain compatibility concepts.

Keywords: Bridge columns; precast columns; composite columns; hollow columns; seismic loading

Omar I. Abdelkarim, ACI student member, is a Ph.D. candidate at Missouri University of Science and Technology, Civil, Architectural, and Environmental Engineering Department. He received his B.Sc. and M.Sc. from Ain Shams University, Egypt. He is a student member of ACI. His research interests include seismic behavior of bridge piers, vehicle collision with bridge piers, and concrete confinement using fiber reinforced polymers (FRP).

Ahmed Gheni is a Ph.D. candidate at Missouri University of Science and Technology, Civil, Architectural, and Environmental Engineering Department. He received his B.Sc. and M.Sc. from University of Tikrit, Iraq. His research interests include seismic behavior of masonry structures.

Sujith Anumolu is a research assistant at Missouri University of Science and Technology, Civil, Architectural, and Environmental Engineering Department. He received his B.Sc. from Andha University, India. His research interests include behavior of bridge piers under torsion and concrete confinement.

Mohamed A. ElGawady is an associate professor at Missouri University of Science and Technology, Civil, Architectural, and Environmental Engineering Department. He received his B.Sc. from Cairo University, Egypt and his M.Sc. from Swiss Federal Institute of Technology (EPFL) Lausanne, Switzerland. He is a member of ACI. His research interests include seismic behavior of bridge piers and masonry structures, segmental construction, and rocking mechanics.

INTRODUCTION

Recently, several researchers have focused their efforts on the development of new materials and construction methods for cost-effective accelerating bridge construction (ABC) systems. ABC systems improve site constructability, reduce total project delivery time, enhance work zone safety for the traveling public, reduce traffic disruptions, and reduce overall life-cycle costs[1, 2, 3]. Concrete-filled steel tubes (CFST) are wide implementation in Japan, China, and Europe to accelerate construction and achieve superior seismic performance. In the U.S., CFSTs are used as piles and bridge piers. However, their applications are limited, primarily as a result of inconsistent design code provisions[4]. Incorporated CFST members have several advantages over both structural

steel and reinforced concrete (RC) members. The CFSTs' steel tubes function as stay-in-place formworks, affording shear reinforcement and continuous confinement to the inner concrete core, increasing the member's ductility and strength. The tubes prevent concrete spalling so that the concrete core, in turn, acts as bracing for the steel tube. The concrete core, therefore, delays the local and global buckling under compression loads. Furthermore, CFST columns have been found to dissipate more energy than columns made out of either structural steel or RC members[4, 5].

Fiber reinforced polymer (FRP) tubes have gained acceptance as an alternative to steel tubes in CFST. Their advantages include light weight-to-strength ratio, high confinement, and corrosion resistance when compared to steel tubes. The seismic behavior of CFFT columns has been studied extensively. Zhu[6] and Shin[7] investigated the behavior of CFFTs that were confined by a shape memory alloy. ElGawady[8, 9] conducted static cyclic tests on both segmental precast post-tensioned CFFT columns and two-column bents. After their finite element analysis, ElGawady[10] and Dawood[11] developed a design procedure for precast post-tensioned CFFTs.

Hollow-core concrete columns frequently employed for tall bridge columns to reduce column mass in moderate-to-high seismic regions such as New Zealand, Japan, and Italy. This reduction reduces the bridge self-weight contribution to the inertial force during an earthquake. Hollow-core columns also result in smaller foundation dimensions, limiting construction costs significantly.

Mander[12] showed that hollow-core concrete columns consisting of two layers of longitudinal reinforcement near the inner and outer faces of the column, and connected

using cross ties through the wall thickness, do exhibit ductile behavior under seismic loads. However, construction with two layers of reinforcement and cross ties significantly increase the labor cost. The use of a single flexural reinforcement layer at the column's outer face, while cost-effective, showed very brittle behavior under seismic loads[13]. Spalling of the inner concrete face triggered column's failure.

Montague[14] developed hollow-core CFST columns, which combine the benefits of the concrete-filled tube with those of hollow-core concrete columns, and consist of a concrete wall sandwiched between two generally concentric steel tubes. More recently, Teng[15] pioneered the use of FRP as an outer tube, and steel as an inner tube. This system combines the benefits of all three materials: FRP, concrete, and steel, while optimizing the benefits of the hollow-core concrete columns to introduce hollow-core FRP-concrete-steel columns (HC-FCS).

Few investigators have studied the behavior of hollow-core FRP-concrete-steel columns (HC-FCS), which exhibit high concrete confinement and ductility. Han[16] tested HC-FCSs in a beam-column arrangement under cyclic flexural loading, and found that the column's elastic stiffness increased as the applied axial load increased. The post-elastic stiffness increased as the FRP stiffness increased. The elastic stiffness, however, did not. Zhang's[17] and Ozbakkaloglu's[18] experiments revealed the behavior of small-scale HC-FCSs under combined axial compression and lateral cyclic loading. Abdelkarim[2] investigated numerically the behavior of the HC-FCS columns under combined axial and lateral loading through an extended parametric study.

RESEARCH SIGNIFICANCE

This paper presents innovative precast hollow-core bridge columns (HC-FCS) and their seismic behavior comparable to the behavior of the reinforced concrete (RC) columns. Such columns exhibit remarkable behavior under seismic loading while improving constructability and reducing construction time. While the FRP tube only confines the concrete wall thickness and stops at the top of footing, the steel tube of the HC-FCS column is extended inside the footing with a certain embedded length (L_e), and acts as the only reinforcement for shear and flexure inside the HC-FCS column.

EXPERIMENTAL PROGRAM

Two large scale columns were tested as free cantilevers under both constant axial compression loading and cyclic lateral displacement loading. Each column had a circular cross-section with an outer diameter (D_o) of 24 in. (610 mm) and a height of 80 in. (2,032 mm; Fig. 1). The lateral load was applied at a height (H) of 95 in. (2,413 mm) measured from the top of the footing resulting in shear-span-to-depth ratio of approximately 4.0. The first column was a conventional reinforced concrete (RC) column and the other column was HC-FCS column. Table 1 summarizes the columns' variables.

The columns' label used in the current experimental work consisted of three segments. The first segment is a letter F referring to flexural testing followed by the column's height-to-outer diameter ratio (H/D_o). The second segment refers to the column's outer diameter (D_o) in in. The third segment refers to the GFRP matrix using E for epoxy; this is followed by the GFRP thickness in 1/8 in. (3.2 mm), steel thickness in 1/8 in. (3.2

mm), and concrete wall thickness in. (25.4 mm). In the case of reinforced concrete column the third segment is replaced with RC.

The F4-24-RC column had a longitudinal reinforcement of 8#7 (8φ22 mm) corresponding to approximately 1.0% of the concrete cross-sectional area and it had a transverse spiral reinforcement of #4 @ 3 in. (φ13@76.2 mm) corresponding to volumetric reinforcement ratio of 1.0%. The concrete cover beyond the spiral reinforcement was 0.5 in. (12.7 mm; Fig. 1(a)).

The F4-24-E324 column consisted of an outer filament wound GFRP tube having a wall thickness (t_{FRP}) of 0.375 in. (9.5 mm), an inner steel tube having an outer diameter (D_i) of 16 in. (406.4 mm) and a wall thickness (t_s) of 0.25 in. (6.4 mm) with steel tube diameter-to-thickness (D_i/t_s) ratio of 64, and the concrete wall thickness (t_c) was 4 in. (101.6 mm; Fig. 1(b)). The inner steel tube was extended inside the footing and the column loading stub using an embedded length (L_e) of 25 in. (635 mm) representing 1.6 D_i while the FRP tube was stopped at the top of the footing and at the bottom of the column's loading stub. The steel tube was hollow inside. Column F4-24-E324 did not include any shear or flexure reinforcement except the steel tube.

Each column's footing had length, width, and thickness of 60 in. (1,524 mm), 48 in. (1,219.2 mm), and 34 in. (863.6 mm), respectively. The footing of the F4-24-RC column had bottom reinforcements of 7#7 (7φ22 mm), top reinforcements of 4#7 (4φ22 mm), and shear reinforcement of #4@ 2.5 in. (#13@63.5 mm; Fig. 1(a)). The footing of the column F4-24-E324 had bottom reinforcements of 7#7 (7φ22 mm), top reinforcements of 6#7 (6φ22 mm), and shear reinforcement of #4@ 2.5 in. (#13@63.5 mm; Fig. 1(b)).

Table 2 summarizes the concrete mixture proportions of the columns' components. Pea gravel of maximum aggregate size of 3/8 in. (9.5 mm) and high range water reducers (HRWR) were used for the columns only to increase the workability. Table 3 summarizes the unconfined concrete cylindrical strengths (f_c') of the columns and the footings at 28 days and the days of the tests. Table 4 summarizes the properties of the steel rebars and tubes, used during this experimental work, based on the manufacturers' data sheets. Table 5 summarizes the properties of the FRP tubes, used during this experimental work, based on the manufacturers' data sheets.

EXPERIMENTAL SET-UP AND INSTRUMENTATIONS

Fifteen Linear variable displacement transducers (LVDTs) and string potentiometers (SPs) were employed for the measurement of displacements of each column. Two more LVDTs were attached to each footing for measuring any potential sliding and uplift. A layout of the LDVTs and SPs is depicted in Fig. 2(a). Total of fourteen electrical strain gauges (SGs) were symmetrically installed, on the two north and south longitudinal steel rebars of the RC-column, at seven levels, starting at the top of footing level with an incremental spacing of 4 in. (101.6 mm; Fig. 2(b)). Seventy-two strain gauges were symmetrically installed inside the steel tube of the HC-FCS column at nine levels starting at the top of footing level with an incremental spacing of 5 in. (127 mm). Four horizontal and four vertical strain gauges were installed at each level (Fig. 2(c)). Forty-eight strain gauges were installed on each FRP tube at six levels starting at the top of the footing level with an incremental spacing of 5 in. (127 mm). Four horizontal and four vertical strain gauges were installed at each level (Fig. 2(d)).

Two webcams were installed inside the steel tube of the HC-FCS column to monitor local buckling (Fig. 3).

LOADING PROTOCOL AND TEST SETUP

Constant axial load (P) of 110 kips (490 kN) representing 5% of the RC-column axial capacity (P_o) was applied to each of the columns using six 0.5 in. (12.7 mm) external prestressing strands. The strands were installed outside the column at the east and west of the center of the columns (Fig. 3). P_o was calculated using equation (1). The prestressing strands were supported by a rigid steel beam atop the column and at the column's footing. The prestressing force was applied and kept constant during the test using two automated hydraulic jacks.

$$P_o = A_s f_y + 0.85\, f_c'(A_c - A_s) \quad (1)$$

After applying the axial load, cyclic lateral load was applied in a displacement control using two hydraulic actuators connected to the column loading stub (Fig. 3). The loading regime is based on the recommendations of FEMA[19] where the displacement amplitude a_{i+1} of the step i+1 is 1.4 times the displacement amplitude of the proceeding step (a_i). Two cycles were executed for each displacement amplitude. Fig. 4 illustrates the loading regime of the cyclic lateral displacement. Each loading cycle was applied in 100 sec. corresponding to loading rate ranged from 0.01 in./sec. (0.25 mm/sec.) to 0.05 in./sec. (1.27 mm/sec.).

RESULTS AND DISCUSSIONS

Fig. 5 illustrates the moment-lateral drift relation of the F4-24-RC and F4-24-E324 columns. The lateral drift (δ) of each column was obtained by dividing the lateral displacement measured from the actuators and corrected for any footing sliding, by the column's height of 95 in. The moment (M) at the base of the column was obtained by multiplying the force collected from the actuators' loading cells by the column's height of 95 in. Table 6 gives a summary of the maximum moments, the lateral drift at maximum moment, and the maximum lateral drift of each column.

As shown in Fig. 5(a), the average peak moment capacity of the column F4-24-RC was 438 kip.ft at lateral drift of 5.1%. The stiffness of the column displayed gradual stiffness degradation up to a lateral drift of approximately 2.0%. Beyond that drift, significant stiffness softening started. The failure of the column occurred at lateral drift approximately 10.9% due to rupture of two rebars at the north and south side of the column. Failure was defined as the column loses at least 20% of its flexural capacity.

Two more rebars ruptured during cycling the column toward the second cycle of 10.9% lateral drift. At this stage, the column suffered severe damage in the form of concrete crushing and spalling, buckling and rupture of longitudinal rebars, and lateral deformation of the spiral reinforcement. It was worthy noted that the longitudinal rebars buckled in two different directions. One direction was the usual buckling going out of the column toward the radius of the column. Other longitudinal rebars buckled toward the circumferential direction indicating effective spiral confinement (Figs. 6(a) and 6(b)). The height of the damage area measured from the top of the footing ranged from 17 in. to

22 in. However, the severe damage occurred within the first 9 in. from the top of the footing. The column's curvature was compatible with the column damage as it was high within the first 8 in. (Fig. 7(a)). However, the column was still able to carry the applied axial load.

For the F4-24-E324 column, the average moment capacity of the column was 540 kip.ft at lateral drift of 2.8% (Fig. 5(b)). Gradual stiffness degradation occurred until drift of 2%; beyond that the column suffered significant stiffness softening. The peak lateral strength of the column remained approximately constant till a drift of approximately 6.0%. Beyond that the column's flexural strength gradually decreased till drift of 10.9%. At this drift ratio the column suffered 11% strength reduction. The failure of the column was considered at lateral drift of 13% when the strength reduction exceeded 20%. Cycling continued beyond that and the FRP ruptured at lateral drift of 15.2% (Fig. 6(c)). The direction of the FRP rupture followed closely the fiber direction i.e. 53^{o} (Fig. 6(d)). The residual moment after the FRP rupture was 232 kip.ft corresponding to 43% of the peak moment capacity of the column. After testing the column, it was observed that the column's concrete shell was almost powder along the bottommost 6 in. This indicates that the steel and FRP tubes were able to confine the concrete shell and the concrete reached its ultimate strain before the rupture of the FRP tube. The column's curvature was compatible with the column damage as it was high within the first 8 in. (Fig. 7(b)).

The opening of the interface joint between the column and footing was measured as 2.75 in. at lateral drift of 14.1%. This sliding resulted from sliding of the FRP tube on the concrete shell, the sliding of the concrete shell on the steel tube, the sliding of the

concrete surfaces on each other at the damage zone, and the concrete pull-out from the footing.

FINITE ELEMENT MODELING

Geometry

Finite element (FE) modeling of the HC-FCS columns was conducted and verified with the experimental results of the F4-24-E324 column. The tested column was symmetrical about the vertical plane. Thus half of the column was modeled and analyzed in LS-DYNA[20] (Fig. 8). The column's concrete core, footing, and loading stub were modeled by solid elements. These elements had a height of 2 in. (50 mm). Both the outer FRP tube and the inner steel tube were simulated by shell elements. A typical shell elements' dimensions (height x width) were 2 in. x 2.4 in. (50 mm x 60 mm) and 2 in. x 1.6 in. (50 mm x 40 mm) for the FRP and steel tubes, respectively. All solid elements were modeled with constant-stress and one-point quadrature integration to reduce the computational time. Hourglass control was used to avoid spurious singular modes for solid elements. The hourglass value for all models was taken as the default value of 0.10.

Contact elements surface-to-surface were used to simulate the interface between the concrete column and the FRP tube. They were also used between the concrete column and the steel tube. This type of contact considers slip and separation that occurs between master and slave contact pairs. Hence, slip/debonding will be displayed if either occurs between the concrete wall's surface and the tube's surface.

This type of contact was used between the concrete footing and the steel tube. Node-to-surface contact elements were used between the loading stub and the concrete wall, the

FRP tube, and the steel tube. Similarly, this contact type was used to simulate the contact between the concrete wall and the FRP tube to the footing. The coefficient of friction for all of the contact elements was taken as 0.6.

Material models

Different material models are available in LS-DYNA to simulate concrete materials. The Karagozian and Case Concrete Damage Model Release 3 (K&C model) was used in this study because it exhibited good agreement with the experimental results gathered in previous studies[2, 21]. This model, developed from the theory of plasticity, has three shear failure surfaces: yield, maximum, and residual[22].

This study used the automatic generation option for the failure surface, where f_c' was the main input to the model. Another input to the model, the fractional dilation parameter (ω), considers any volumetric change in concrete. The fractional dilation parameter was taken as the default value of 0.50. The equation of state (EOS), which controls the compressive behavior of the concrete under triaxial stresses, was automatically generated, given f_c' and ω.

The FRP material used was modeled as an orthotropic material using "002-orthotropic_elastic" material. Such material model uses total Lagrangian-based to model the elastic-orthotropic behavior of solids, shells, and thick shells. This material is defined by several engineering constants: elastic modulus (E), shear modulus (G), and Poisson's ratio (PR), in the three principle axes (a, b, and c). The fiber orientation is defined by a

vector. The failure criterion for the FRP, defined as “000-add_erosion,” was assigned the ultimate strain of FRP in “EFFEPS” card.

The material model “003-plastic_kinamatic” was used to identify the steel tube’s elasto-plastic stress-strain curve for the pushover analysis. However, the material model “153-damage 3” was used for the static cyclic analysis because of the low cyclic fatigue.

Boundary conditions and loading

Displacement in the Y direction and rotations about both the X and Z axes at the plane of symmetry were restrained. Displacements and rotations in all directions at the nodes of the footing’s bottom were prevented.

The loading was applied in two different steps. Because of the symmetry, half of the applied axial compressive load on the tested column was applied on the FE model to the top of the loading stub during the first step. During the second step, complete cyclic lateral displacement history of the experimental was applied on the nodes of the loading stub at 95 in. (2,413 mm) from the top of the footing until failure.

ANALYTICAL INVESTIGATION

Bridge engineers can determine the bending strength of the FSDT columns using a simple method without a sophisticated analysis. Hence, an analytical model was conducted to predict the column’s bending strength using a sectional analysis based on Navier-Bernoulli’s assumptions and strains compatibility concepts. The main assumptions in the analysis were as follows: a) The plane section remained plane both

before and after deformation occurred; b) Full composite action between the steel tube and concrete; c) The stress-strain relationship of steel was assumed elastic-perfectly plastic; d) the stress-strain relationship of concrete in the FRP-concrete-steel double skin sections (developed by Yu[23]) was adopted. Moment-curvature analysis (including the applied axial load effects) was conducted and the bending strength was determined for each column.

The concrete compressive strain at the extreme fibers (ε_c) was initially assumed. Then, the distance from the neutral axis to the compressive extreme fibers (c) was incrementally increased until attaining force equilibrium ($\Sigma F_x = 0$). During the previous step, the compression and tension sides of cross-section were divided to 100 horizontal strip segments based on the polar angle of each side (Fig. 9). The stresses and forces in compressive confined concrete, steel in compression, and steel in tension were calculated at each c value. Consequently, the bending moment and the curvature were computed. The bending moment was computed around the plastic centroid which is the center of gravity (C.G.) of the cross-section as it is a symmetrical section. The concrete compressive strain at the extreme fibers (ε_c) was incrementally increased up to ultimate strain (ε_{cu}; Yu[23]).

compute the sectors' polar angles ($\theta_1, \theta_2 \& \theta_3$)

$$\theta_1 = \frac{\alpha_1}{(n)}\ , \theta_2 = \frac{\alpha_2}{(n)} \& \theta_3 = \frac{\alpha_3}{(n)} \tag{2}$$

where n is the number of strip segments = 100 in this study

compute the strain in each strip segment

$$\varepsilon_{c1n} = \frac{c - R_o\,(1 - cos\left(\alpha_{1n} + \frac{\theta_1}{2}\right))}{c}\varepsilon_c \tag{3}$$

compute the force of the whole concrete compression segment as if there is no void

$$C_{C1} = 4\,R_O^2 \int_0^{\alpha_1} sin^2\left(\alpha_{1n} + \frac{\theta_1}{2}\right) \sin\left(\frac{\theta_1}{2}\right) * \sigma_{c1n} \tag{4}$$

compute the concrete stress σ_{c1n} using Yu[23] model

compute the strain in each virtual strip segment inside the void as if there is a concrete infill

$$\varepsilon_{c2n} = \frac{c - (R_o - R_i\,cos\left(\alpha_{2n} + \frac{\theta_2}{2}\right))}{c}\varepsilon_c \tag{5}$$

compute the force of the virtual strip segment inside the void

$$C_{C2} = 4\,R_i^2 \int_0^{\alpha_2} sin^2\left(\alpha_{2n} + \frac{\theta_2}{2}\right) \sin\left(\frac{\theta_2}{2}\right) * \sigma_{c2n} \tag{6}$$

compute the concrete stress σ_{c2n} using Yu[23] model

subtract C_{C2} from C_{C1} to get the actual compression force in the concrete shell (C_C)

$$C_C = 4\,(R_O^2 \int_0^{\alpha_1} sin^2\left(\alpha_{1n} + \tfrac{\theta_1}{2}\right) \sin\left(\tfrac{\theta_1}{2}\right) * \sigma_{c1n} - R_i^2 \int_0^{\alpha_2} sin^2\left(\alpha_{2n} + \tfrac{\theta_2}{2}\right) \sin\left(\tfrac{\theta_2}{2}\right) * \sigma_{c2n}) \tag{7}$$

compute the compressive force of each segment of steel tube

$$C_{scn} = 2\int_0^{\alpha_2} t_s * R_i * \frac{\theta_2}{n} * \frac{c - (R_o - R_i\,cos\left(\alpha_{2n} + \frac{\theta_2}{2}\right))}{c}\varepsilon_c * E_s \tag{8}$$

where t_s and E_s are the thickness and the Young's modulus of the steel tube

compute the tensile force of each segment of steel tube

$$T_{stn} = 2\int_0^{\alpha_3} t_s * R_i * \frac{\theta_3}{n} * \frac{(R_o - c) + R_i\, cos\left(\alpha_{3n} + \frac{\theta_3}{2}\right))}{c} \varepsilon_c * E_s \tag{9}$$

after attending the force equilibrium ($\Sigma F_x = 0$), compute the bending moment

$$M_{ext.} = \int_0^{\alpha_1} C_{c1n} * R_o * cos\left(\alpha_{1n} + \frac{\theta_1}{2}\right) - \int_0^{\alpha_2} C_{c2n} * R_i * \ cos\left(\alpha_{2n} + \frac{\theta_2}{2}\right) + \int_0^{\alpha_2} C_{scn} * R_i * \ cos\left(\alpha_{2n} + \frac{\theta_2}{2}\right) + \int_0^{\alpha_3} T_{stn} * R_i * cos\left(\alpha_{3n} + \frac{\theta_3}{2}\right) \tag{10}$$

COMPARISON OF FINITE ELEMENT AND ANALYTICAL PREDICTIONS AND EXPERIMENTAL RESULTS

Fig. 10 illustrates the moment-lateral drift relation of the column F4-24-E324 experimentally versus that of the analytical and FE model. The analytical result was multiplied by the strength reduction factor (φ) of 0.9[24]. Column reached peak bending strength of 543 kip.ft (736 kN.m) during the analytical. The difference between the experimental strength and the analytical strength was 0.6%. Overall, the FE model was able to capture the column behavior. The hysteretic behavior and the loading and unloading stiffness of the FE was in a good agreement with the experimental. Column reached average peak bending strength of 472 kip.ft (640 kN.m) during the FE analysis. The difference between the experimental strength and the FE strength was 12.5%. The FE predicted the fiber rupture at lateral drift of 15.5% and occurred within the bottommost 10 in. (254 mm) which was compatible with the experimental fiber rupture (Fig. 11).

CONCLUSIONS

This paper investigates the behavior of the hollow-core fiber reinforced polymer (FRP)-concrete-steel tubular columns (HC-FCS) under combined axial and lateral loading. Two large scale columns, a conventionally reinforced concrete (RC) column and a HC-FCS column were investigated during this study. Each column has an outer diameter of 24 in. and the columns aspect ratio, height-to-diameter ratio, was 4.0. The HC-FCS column consisted of a concrete wall sandwiched between an outer FRP tube and an inner steel tube. The steel tube was extended inside the footing with an embedded length of 1.6 times the steel tube diameter. While the FRP tube only confined the concrete wall thickness and stopped at the top of the footing level. The hollow steel tube was the only reinforcement for shear and flexure inside the HC-FCS column. The HC-FCS column exhibited high lateral drift and the FRP ruptured at lateral drift of 15.2%. The RC-column failed at drift of 10.9% before. The RC-column failed by rebar rupture and the moment capacity suddenly dropped more than 20% after that. However, the HC-FCS failed gradually with concrete compression failure, steel tube local buckling, followed by FRP rupture. LS-DYNA was used to develop cyclic analysis of three-dimensional HC-FCS column's model to simulate seismic loading. Finite element (FE) model was validated against the tested column. The FE results were in good agreement with the experimental results. The bending strength of HC-FCS columns could be simply calculated with a good accuracy using sectional analysis based on Navier-Bernoulli's assumptions and strain compatibility concepts.

ACKNOWLEDGEMENT

This research was conducted by Missouri University of Science and Technology and was supported by Missouri Department of Transportation (MoDOT) and Mid-American Transportation Center (MATC). In kind contribution from ATLAS Tube is appreciated. Discounts on FRP tubes from Grace Composites and FRP Bridge Drain Pipe are also appreciated. However, any opinions, findings, conclusions, and recommendations presented in this paper are those of the authors and do not necessarily reflect the views of the sponsors.

References

1. Abdelkarim, O. and ElGawady, M. (2014a). "Behavior of Hybrid FRP-Concrete-Steel Double-Skin Tubes Subjected to Cyclic Axial Compression." ASCE Structures Congress 2014: pp. 1002-1013.

2. Abdelkarim, O. and ElGawady, M. (2014b). "Analytical and Finite-Element Modeling of FRP-Concrete-Steel Double-Skin Tubular Columns." Journal of Bridge Engineering, 10.1061/(ASCE)BE.1943-5592.0000700 , B4014005.

3. Dawood, H., ElGawady, M., and Hewes, J. (2012). "Behavior of Segmental Precast Post-Tensioned Bridge Piers under Lateral Loads." ASCE Journal of Bridge Engineering, Vol. 17, No. 5, pp. 735-746.

4. Moon, J., Lehman, D. E., Roeder, C. W., and Lee, H.-E. (2013). "Strength of circular concrete-filled tubes with and without internal reinforcement under combined loading." J. Struct. Eng. , 10.1061/(ASCE)ST.1943-541X.0000788, 04013012.

5. Hajjar J. (2000). "Concrete-filled steel tube columns under earthquake loads." Structural Engineering and Materials; 2(1):72–82.

6. Zhu, Z., Ahmad, I., and Mirmiran, A. (2006). "Seismic performance ofconcrete-filled FRP tube columns for bridge substructure." J. Bridge Eng., 11(3), 359–370.

7. Shin, M. and Andrawes, B. (2010). “Experimental Investigation of Actively Confined Concrete Using Shape Memory Alloys.” J. Eng. Struct. 32:3, 656-664.

8. ElGawady, M., Booker, A., and Dawood, H. (2010). “Seismic Behavior of Posttensioned Concrete-Filled Fiber Tubes.” J. Compos. Constr., 14(5), 616–628.

9. ElGawady, M. and Sha’lan, A. (2011). “Seismic Behavior of Self-Centering Precast Segmental Bridge Bents.” J. Bridge Eng., 16(3), 328–339.

10. ElGawady, M. and Dawood, H. (2012). “Analysis of segmental piers consisted of concrete filled FRP tubes.” Engineering Structures, Vol. 38, pp. 142-152.

11. Dawood, H., ElGawady, M. (2013). “Performance-based seismic design of unbonded precast post-tensioned concrete filled GFRP tube piers.” Composites Part B: Engineering, Volume 44, Issue 1, Pages 357-367.

12. Mander, J. B., Priestley, M. J. N., Park, R., “Behavior of Ductile Hollow Reinforced Concrete Columns.” Bulletin of the New Zealand National Society for Earthquake Engineering, Vol. 16, No. 4, December 1983, pp. 273-290.

13. Hoshikuma, J., & Priestley, M. J. N. (2000). “Flexural behavior of circular hollow columns with a single layer of reinforcement under seismic loading.” Report No. SSRP-2000/13, University of California, San Diego, La Jolla, CA.

14. Montague, P., (1978). “Experimental behavior of double-skinned, composite, circular cylindrical-shells under external-pressure.” Journal of Mechanical Engineering Science, 20(1), pp. 21–34.

15. Teng, J.G., Yu, T., and Wong, Y.L. (2004). “Behavior of Hybrid FRP-Concrete-Steel Double-Skin Tubular Columns.” Proc. 2nd Int. Conf. on FRP Composites in Civil Engineering, Adelaide, Australia, 811-818.

16. Han, L.H., Tao, Z., Liao, F.Y., and Xu, Y. (2010). “Tests on Cyclic Performance of FRP-Concrete –Steel Double-Skin Tubular Columns.” Thin-Walled Structures, 4, 430-439.

17. Zhang, B., Teng, J. G. and Yu, T. (2012). “Behaviour of hybrid double-skin tubular columns subjected to combined axial compression and cyclic lateral loading.” Sixth Int. Conference on FRP Comp. in Civil Engineering (pp. 1-7). Rome, Italy.

18. Ozbakkaloglu, T. and Idris, Y. (2014). “Seismic Behavior of FRP-High-Strength Concrete–Steel Double-Skin Tubular Columns.” J. Struct. Eng., 140(6), 04014019.

19. Federal Emergency Management Agency, FEMA, (2007). “Interim Protocols for Determining Seismic Performance Characteristics of Structural and Nonstructural Components Through Laboratory Testing.” FEMA 461, Federal Emergency Management Agency.

20. LS-DYNA. (2007). “Keyword user’s manual.” Livermore Software Technology Corporation, CA.

21. Ryu, D., Wijeyewickrema, A., ElGawady, M., and Madurapperuma, M. (2014). “Effects of Tendon Spacing on In-Plane Behavior of Post-Tensioned Masonry Walls.” J. Struct. Eng., 140(4), 04013096.

22. Malvar, L., Crawford, J., Wesevich, J., and Simons, D. (1997). “A plasticity concrete material model for DYNA3D.” Int. J. Impact Eng., 19(9–10), 847–873.

23. Yu, T., Teng, J., and Wong, Y. (2010). “Stress-Strain Behavior of Concrete in Hybrid FRP-Concrete-Steel Double-Skin Tubular Columns.” J. Struct. Eng., 136(4), 379–389.

24. ACI Committee 318 (2011). “Building Code Requirements for Structural Concrete (ACI318-11) and Commentary (318R-11).” American Concrete Institute, Farmington Hills, Mich., 509 pp.

Table 1. Summary of the Columns' Variables

Column		F4-24-RC	F4-24-E324
Nominal outer diameter (D_o, in. (mm))		24 (609.6)	
Nominal inner diameter (D_i, in. (mm))		—	16 (406.4)
Steel tube thickness (t_s, in. (mm))		—	0.25 (6.4)
FRP tube	Matrix	—	Epoxy
	Thickness (t_{FRP}, in. (mm))	—	0.375 (9.5)
Longitudinal reinforcement		8#7 (8φ22 mm)	—
Transversal reinforcement		spiral #4 @ 3 in. (φ13@76.2 mm)	—

Table 2. Concrete Mixture Proportions

w/c	Cement (lb/yd^3 (kg/m^3))	Fly Ash (lb/yd^3 (kg/m^3))	Water (lb/yd^3 (kg/m^3))	Fine Aggregate (lb/yd^3 (kg/m^3))	Coarse Aggregate* (lb/yd^3 (kg/m^3))	HRWR** (lb/yd^3 (kg/m^3))
0.5	590 (350)	170 (100)	380 (225)	1,430 (848)	1,430 (848)	1.90 (1.13)

*Pea gravel of maximum aggregate size of 3/8 in. (9.5 mm) was used only for columns
**HRWR was used only for columns

Table 3. Summary of the Used Unconfined Concrete Strengths

	Column	Footing
f_c' at 28 days (psi (MPa))	4,725 (32.5)	5,300 (36.5)
f_c at the day of testing (psi (MPa))	5,215 (36.0)	5,640 (38.9)

Table 4. Nominal Properties of the Rebars and Steel Tubes

	Elastic modulus (E, ksi (GPa))	Yield stress (f_y, psi (MPa))	Ultimate stress (f_u, psi (MPa))	Ultimate strain (ε_u, in./in. (mm/mm))
Steel rebar	29,000 (200)	60,000 (414)	90,000 (621)	0.08
Steel tube	29,000 (200)	42,000 (290)	58,000 (400)	0.23

Table 5. Nominal Properties of the FRP Tubes

	Axial compression elastic modulus (E_a, ksi (GPa))	Axial ultimate stress (f_{ar}, psi (MPa))	Hoop elastic modulus (E_h, ksi (GPa))	Hoop rupture stress (f_{hr}, psi (MPa))
Epoxy tube	677 (4.7)	12,150 (83.8)	3,020 (20.8)	40,150 (277)

Table 6. Summary of the Columns' Results

Column	Average maximum moment (kip.ft. (kN.m)	Lateral drift at the maximum moment	Lateral drift at failure
F4-24-RC	438 (594)	5.1%	10.9%
F4-24-E324	540 (732)	2.8%	13%

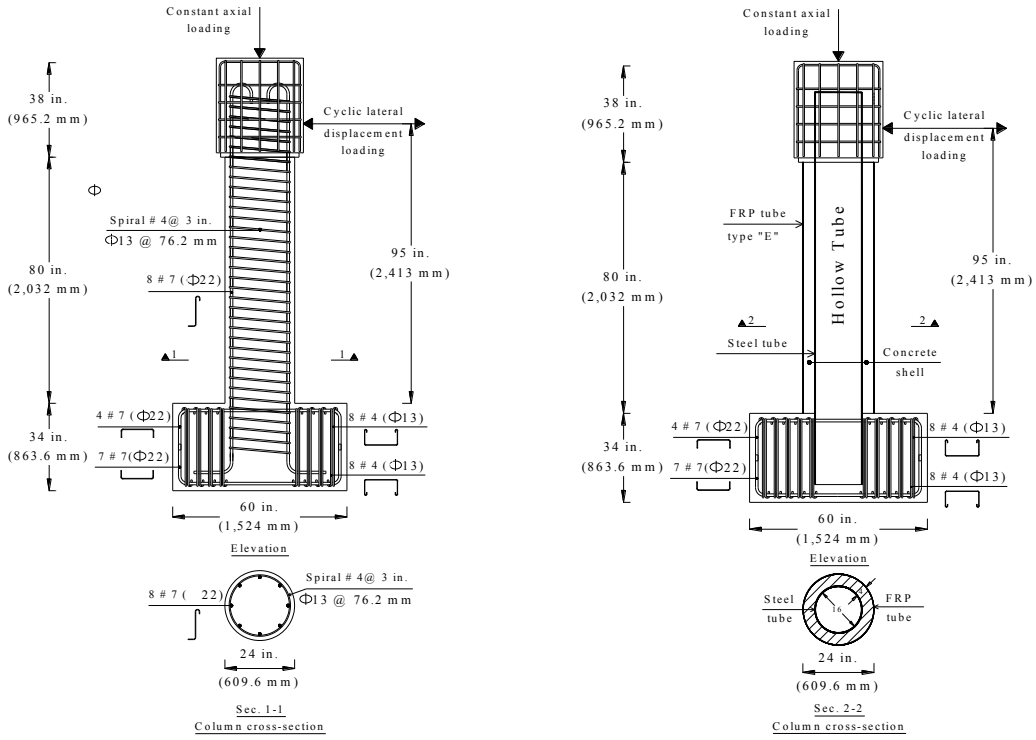

(a) (b)

Figure 1. Reinforcement details of the investigated columns: (a) F4-24-RC column and (b) F4-24-E324 column

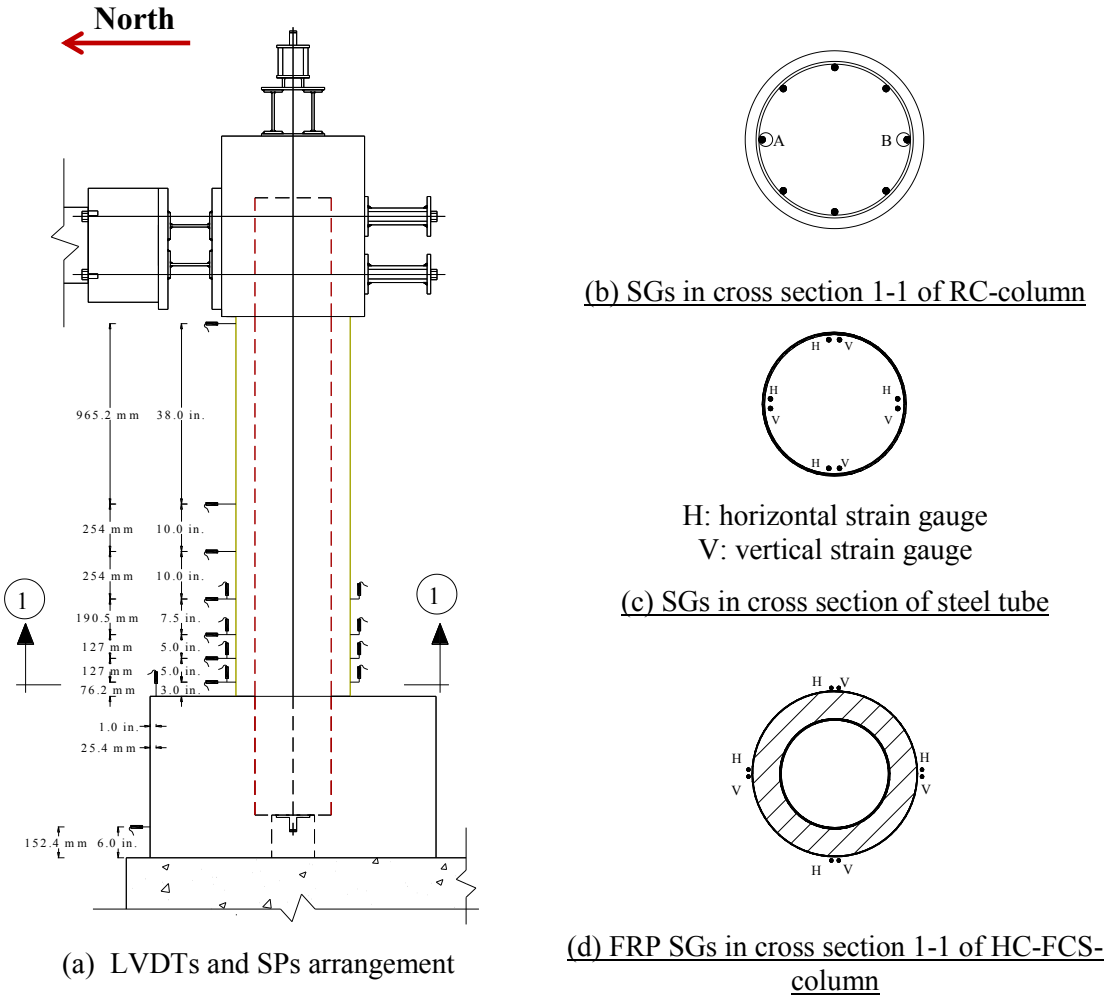

(a) LVDTs and SPs arrangement

(b) SGs in cross section 1-1 of RC-column

(c) SGs in cross section of steel tube

(d) FRP SGs in cross section 1-1 of HC-FCS-column

Figure 2. Layout of the LVDTs, SPs, and strain gauges

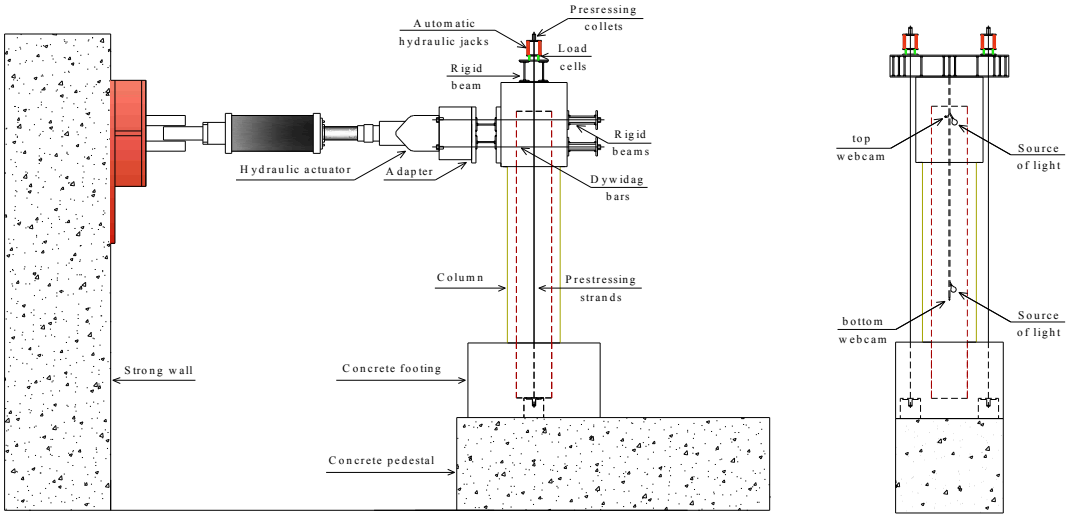

(a) (b)

Figure 3. Column test setup: (a) elevation, (b) sideview

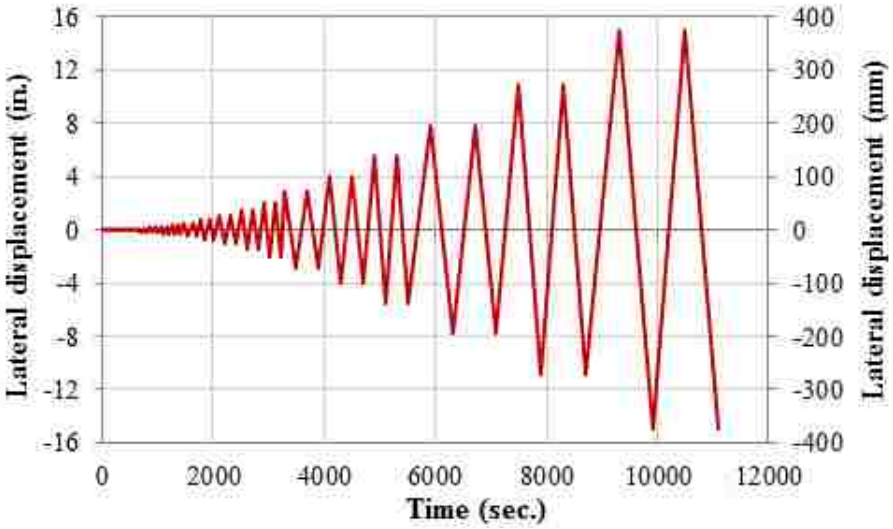

Figure 4. Lateral displacement loading regime

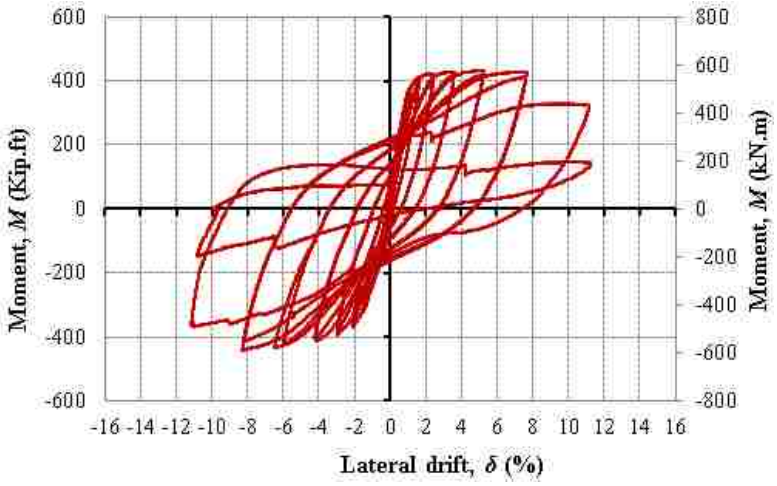

(a)

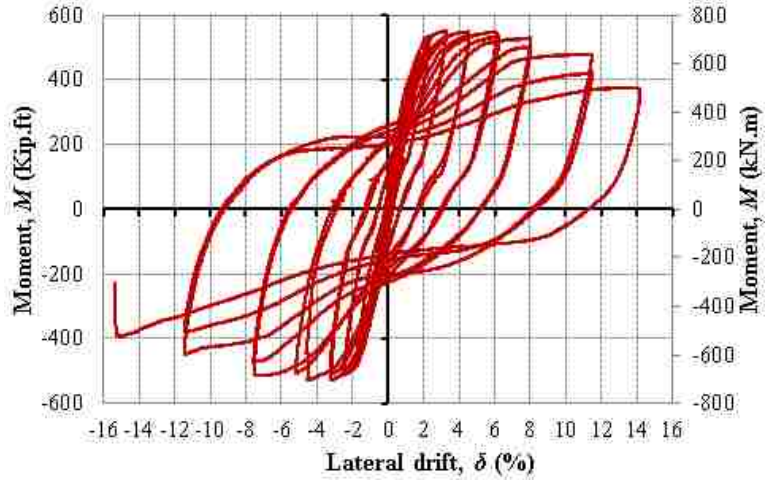

(b)

Figure 5. Moment-lateral drift relation: (a) F4-24-RC column and (b) F4-24-E324 column

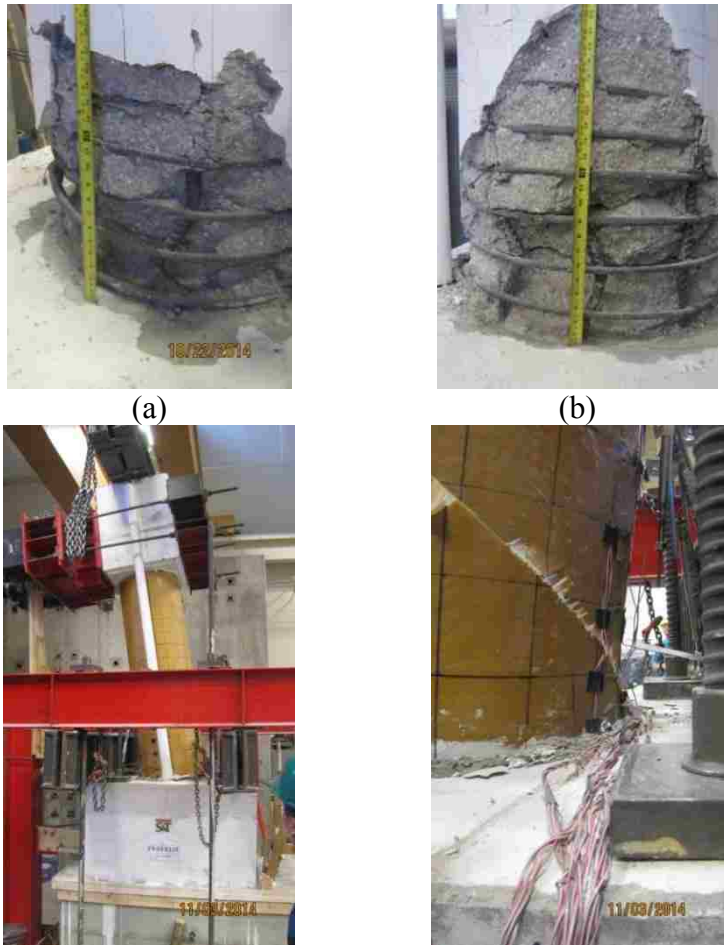

(a) (b)

(c) (d)

Figure 6. Columns' failure: (a) F4-24-RC column's damage area in north side, (b) F4-24-RC column's damage area in south side, (c) F4-24-E324 column's profile at 15.2% lateral drift, and (d) F4-24-E324 column's FRP rupture

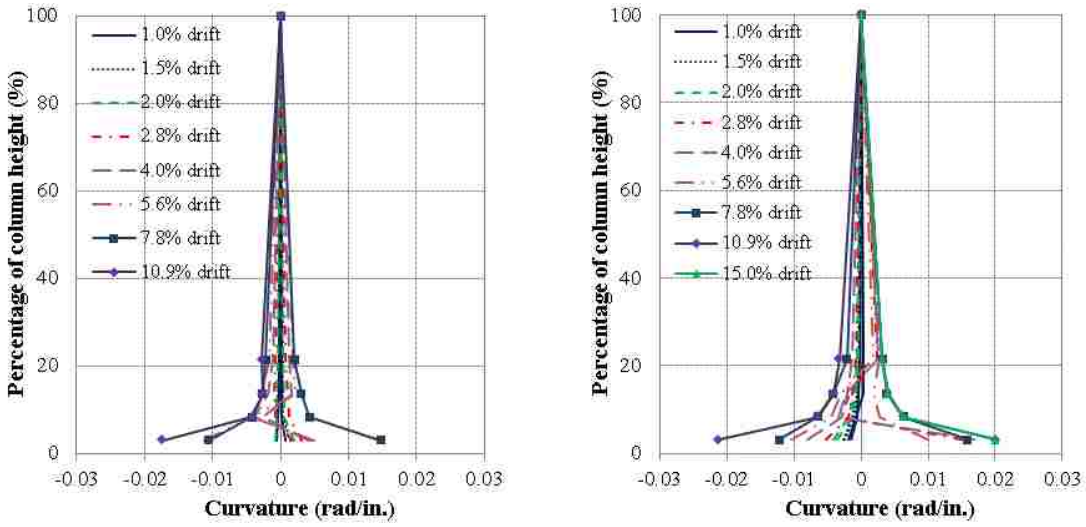

Figure 7. Curvature along the height: (a) F4-24-RC column and (b) F4-24-E324 column

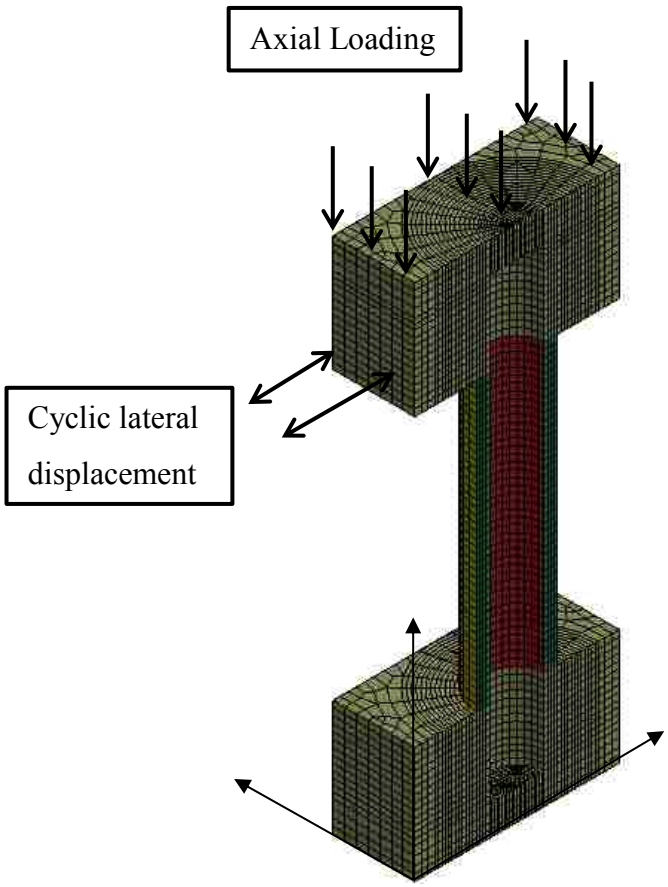

Figure 8. View of the HC-FCS column's model

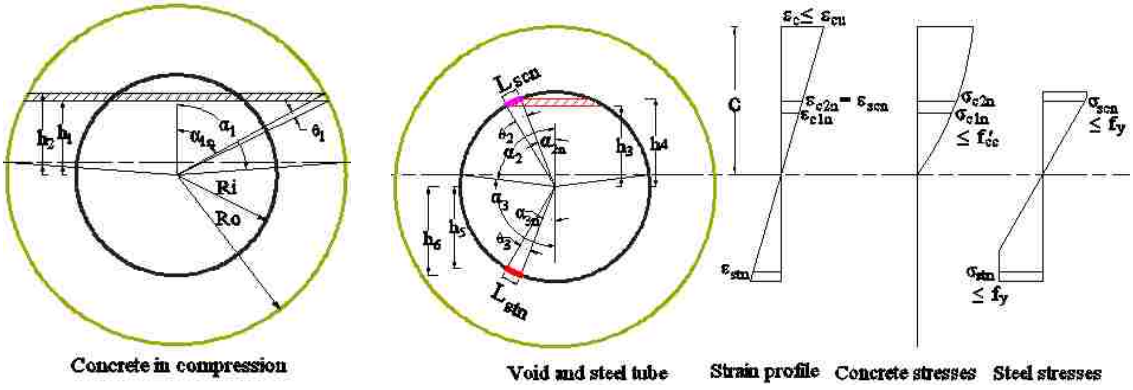

Figure 9. Cross-sectional analysis

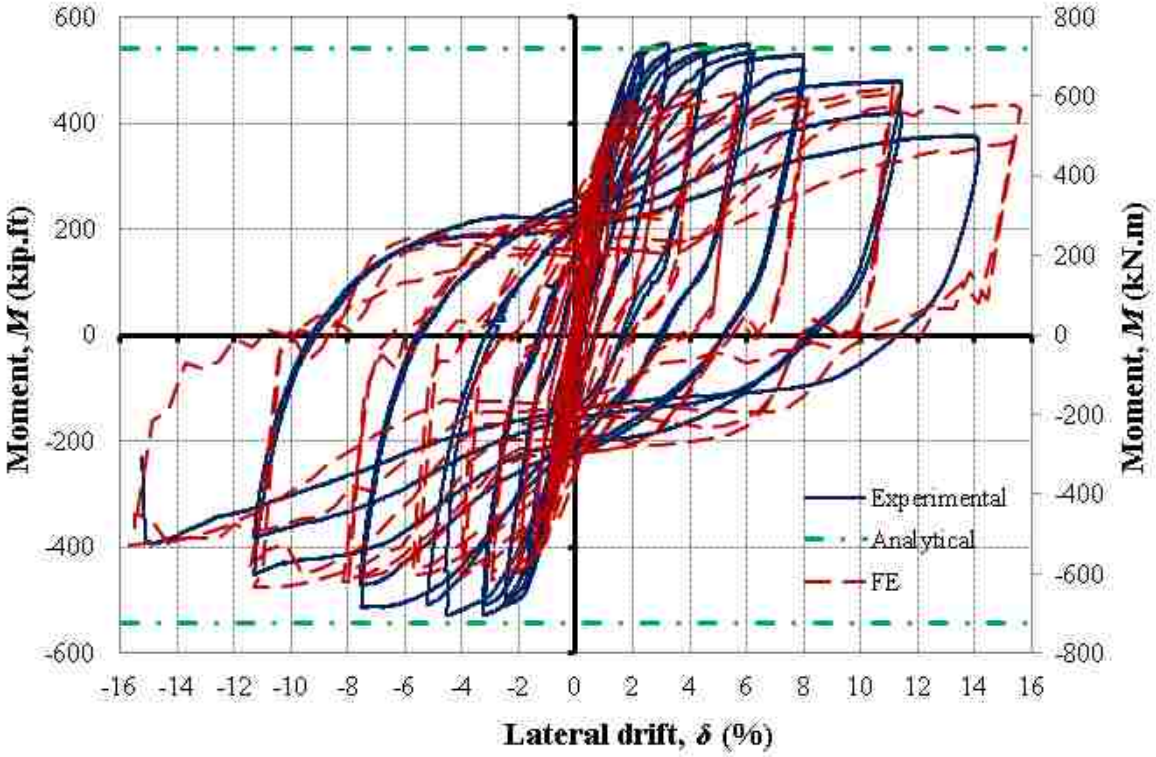

Figure 10. Moment-lateral drift relation of the analytical and FE model comparable to the experimental

Figure 11. Rupture of the FRP tube during the FE

VI. ANALYSES OF REINFORCED CONCRETE BRIDGE COLUMNS SUBJECTED TO VEHICLE COLLISIONS

Omar I. Abdelkarim[1], S.M. ASCE; Mohamed A. ElGawady[2]§, PhD, M. ASCE

Abstract

Both the peak dynamic force (PDF) and the equivalent static force (ESF) of a vehicle collision with reinforced concrete bridge columns were examined as part of an extensive finite element (FE) analyses study. An extensive parametric study of 13 parameters, including the concrete material model, the unconfined concrete compressive strength (f_c'), the material strain rate, the percentage of longitudinal reinforcement, the hoop reinforcement, the column span-to-depth ratio, the column diameter, the top boundary conditions, the axial load level, the vehicle's velocity, the vehicle's mass, the roadside distance between errant vehicle and unshielded bridge column, and the soil depth above the top of the column footing was conducted. Three approaches were used to investigate the ESF. The ESF in the first (stiffness-based) approach was defined as the static force producing the same maximum displacement that is produced by a vehicle collision at the point of impact. The ESF examined in the second approach was calculated according to the Eurocode. The ESF studied in the third approach was defined as the Peak of the Twenty-five Milli Second moving Average (PTMSA). The different ESFs were compared to the ESF in the American Association of State Highway and Transportation Officials- Load and Resistance Factor Design (AASHTO-LRFD; 2,670 kN [600 kips]).

1 Ph.D. Candidate, Dept. of Civil, Architectural, and Environmental Engineering, Missouri University of Science and Technology, Rolla, MO. 65401; oiafgc@mail.mst.edu

2 Benavides Associate Professor, Dept. of Civil, Architectural, and Environmental Engineering, Missouri University of Science and Technology, Rolla, MO. 65401; elgawadym@mst.edu

§Corresponding author

In general, the ESF calculated according to the Eurocode presented the lower bound while those from the stiffness-based approach presented the upper bound. Furthermore, the recommended ESF of the AASHTO-LRFD was found to be non-conservative for heavy and/or high speed vehicle impacts; it was found to be too conservative for light and/or slow vehicle impacts. Hence, rather than a constant design impact force, a variable design impact force should be used. An equation was developed to calculate a design impact force, which is the function in the vehicle's mass and velocity. A simplified equation based on the Eurocode equation of the ESF was proposed. These equations, however, do not require cumbersome FE analyses.

Keywords: Vehicle collision, Impact load, Bridge column, Design force, LS-DYNA

Introduction

Accidents can have serious repercussions with regard to both human life and transportation systems. Many vehicle collision events involving bridge piers have been reported throughout the US. These collisions often result in either a complete or a partial bridge collapse (Harik et al. 1990; Buth et al. 2010; Agrawal 2011). For example, in 2008, a vehicle weighs 39 tons (80 kips) and moving at a high speed collided with a bridge pier on IH-30 near Mount Pleasant, Texas (Buth et al. 2010). The bridge pier consisted of three columns. These columns had 760 mm (30 in.) diameters, longitudinal reinforcements of 8 D28 (8#9), and D10 (#3) spiral stirrups with a 152 mm (6 in.) pitch. Although this bridge did not collapse entirely, one column failed.

Numerous researchers have used LS-DYNA software to investigate the modeling of concrete columns under extreme loads such as impact and seismic loadings (Abdelkarim

and ElGawady 2015a; Abdelkarim and ElGawady 2014; Youssef et al. 2015; Sharma et al. 2012; Fouche and Bruneau 2010; Thilakarathna et al. 2010). El-Tawil et al. (2005) used LS-DYNA software to examine two bridge piers impacted by different trucks at different velocities. Both the peak dynamic force (PDF) and the equivalent static force (ESF) were evaluated. The PDF is defined as the maximum contact force of the vehicle collision with a bridge column. The American Association of State Highway and Transportation Officials- Load and Resistance Factor *Bridge Design Specifications 5th edition* (AASHTO-LRFD 2010) mandates that abutments and piers located within a distance of 9.1 m (30 ft) from the roadway edge be designed to allow for a collision load using ESF of 1,800 kN (400 kips). El-Tawil et al. (2005) found that this design force could be non-conservative in some cases, and that the ESF should be increased. However, no recommendation was made for impact load magnitude.

Buth et al. (2011) experimentally studied the collision of tractor-trailers into a rigid column that was constrained at both ends. Numerical models were used to conduct a parametric study on single unit truck (SUT). The investigated parameters included the pier's diameter, the vehicle's weight, the vehicle's velocity, and the cargo's state (rigid vs. deformable). Based on the results gathered during this study, the ESF of the AASHTO-LRFD increased to 2,670 kN (600 kips) applied to a bridge pier in a direction of zero to 15 degrees with the edge of the pavement in a horizontal plane, at a distance of 1,500 mm (5.0 ft) above ground.

Sharma et al. (2012) used a performance-based response to investigate the effect of a vehicle's impact on a reinforced concrete column. They suggested that four different damage levels and three performance levels be used to evaluate the column's response.

Agrawal et al. (2013) investigated the effects of different seismic design details on a pier's response to vehicle impact loading. They proposed that a new procedure be used to calculate the ESF based on the vehicle's mass and velocity. A proposed equation was used to calculate the PDF. The ESF was calculated by dividing the PDF by the damage factor which was taken as 2, 5, or > 5 for minor, moderate, or high damage levels, respectively. This procedure produced variable value of ESF rather than the constant ESF value recommended by the AASHTO-LRFD.

No consensus exists among researchers with regard to calculating ESF based on PDF. Hence, three different approaches were used during this study. The ESF in the first approach (SB_{ESF}) was defined as the static force needed to produce displacement equal to that of the maximum displacement by a collision vehicle at the point of impact (El-Tawil et al. 2005). The second approach is the one recommended by Eurocode 1 (2002) to calculate the ESF using the following equations:

$$ESF = \frac{KE}{\delta_c + \delta_d} \tag{1}$$

$$KE = \frac{1}{2}\, m\, v_r^2 \tag{2}$$

where KE is the vehicle's kinetic energy, m = the vehicle's mass, v_r = the vehicle's velocity, δ_c = the vehicle deformation, δ_d = the column deformation. The δc of each vehicle was calculated as the change in length between the vehicle nose and the center of mass according to NCHRP 350 (1993). The center of mass of a vehicle changes when the vehicle's mass changes. The δd of each column was calculated as the lateral displacement of the column at the point of impact load. The ESF in the third approach was defined as

the Peak of the Twenty-five Milli Second moving Average (PTMSA). Buth et al. (2011) recommended this average, which was referenced from the 50 millisecond moving average frequently used in automotive crash analyses.

Research Significance

While several researchers have investigated the issue of vehicle impact with concrete columns, few have studied the effect of different construction detailing and vehicle parameters on a column's performance. Detailed finite element analyses were used in this study to investigate the effects of 13 different parameters, including the concrete material model, the unconfined concrete compressive strength (f_c'), the material strain rate, the percentage of longitudinal reinforcement, the hoop reinforcement, the column span-to-depth ratio, the column diameter, the top boundary conditions, the axial load level, the vehicle's velocity, the vehicle's mass, the roadside distance between errant vehicle and unshielded bridge column, and the soil depth above the top of the column footing, on both dynamic and static impact forces. Comparisons were also made between the ESF of the AASHTO-LRFD (2,670 kN [600 kips]) and the ESF calculated through various approaches. The constant impact load used in the AASHTO-LRFD did not consider either the vehicle's mass or velocity. Hence, the given impact load may be conservative in some occasions and unconservative in others. A new equation is presented here that can directly calculate the ESF given the vehicle's mass and velocity without the need to run a crash analysis. A simplified equation for the Eurocode equation can also be used to directly calculate the ESF without a crash analysis.

Validating the Finite Element Modeling of a Vehicle Colliding with a Bridge Pier

Experiments conducted on vehicle collisions with concrete columns are both difficult and expensive. Finite element analysis (FEA) is considered an attractive approach because it is economical, reliable, and easy to implement. The FEA of a collision event requires a combination of vehicle and concrete structure modeling.

Bridge pier models similar to those used by El-Tawil et al. (2005) were developed during the course of this study. These models were also subjected to similar impact loads (El-Tawil et al. 2005). The results gathered by El-Tawil et al. (2005) were used to validate the developed models.

The bridge pier in these models was 9,925 mm (32.6 ft) tall (see Figs. 1 and 2). It was supported by a reinforced concrete pile cap that was 3,300 mm × 2,300 mm × 1,075 mm (10.0 ft × 7.0 ft × 3.5 ft). This pile cap was supported by 6 prestressed piles that were 450 mm (18 in.) in diameter and 10,000 mm (30 ft) in length. Fully integrated 8-node brick elements, with an elastic material (mat. 001), were used to simulate the substructure (both the pier and the pile cap). Beam_orientation type truss elements (ELFORM_3) were used to model all of the reinforced bars. These elements shared nodes with the concrete elements. A Hughes-Liu beam element type (ELFORM_2) was used to simulate the pile so that the soil/structure interaction could be examined. Each pile was supported by four discrete lateral spring elements. These elements were modeled by a spring inelastic material (mat. S08). This material provided a compression response only. Bowles' (1988) equations for the soil's compressive stiffness were used to calculate the modulus of the subgrade's reaction to the soil. The springs were spaced 440 mm (17.4 in) apart.

The bridge superstructure was comprised of a composite steel-concrete box girder. Thirty-six Belytschko-Schwer resultant beam-type (ELFORM_2) elements were used to simulate two adjacent steel girders. This superstructure's transformed steel cross-sectional area was 80,000 mm^2 (124 in^2). The strong moment of inertia (the I_{yy} about the vertical axis) was 8.3×10^{10} mm^4 (2.0×10^5 in^4), and the weak moment of inertia (the I_{zz} about the horizontal axis) was 2.8 x 10^{10} mm^4 (6.7×10^4 in^4). The superstructure's two unequal spans were 53,340 mm (175 ft) and 50,290 mm (165 ft), respectively. This superstructure was assumed to be pinned at the far ends. The Hughes-Liu beam-type element (ELFORM_2) was used to simulate the bridge bearings located under the superstructure. These bearings were 37 mm (1.5 in.) thick and 200 mm × 200 mm (8 in. × 8 in.) in the cross-section. The bridge bearing's shear modulus was 0.61 MPa (88.0 psi).

A Chevrolet pickup reduced finite element model was used to study the vehicle's collision with the bridge pier (Fig. 3a). This vehicle model was developed by the National Crash Analysis Center (NCAC) of The George Washington University under a contract with both the Federal Highway Administration (FHWA) and the National Highway Traffic Safety Administration (NHTSA) of the U.S. Department of Transportation (DOT). A surface-to-surface contact type was used between the vehicle and the bridge pier in the finite element models; the coefficient of friction was 0.3. An extensive sensitivity analysis was conducted by El-Tawil (2004) on the effect of the coefficient of friction (COF) on the impact analysis of vehicle collision with bridge pier. He concluded that the magnitude of the peak impact force did not significantly change. Also, the COF had a little effect on the 50 ms average impact force. Finally, he concluded that coefficient of friction of 0.3 is a reasonable number for steel on concrete.

The collision event of the Chevrolet pickup with the bridge pier, at a velocity of 69 mph (110 kph), at a time of 0.05 second, is illustrated in Figure 3b. The FE results from this study, in general, were close to the results reported by El-Tawil et al. (2005), as illustrated in Fig. 4 and Table 1. The percentages of difference between the PDFs from this study and those from the El-Tawil et al. (2005) study for vehicle velocities of 34 mph (55 kph), 69 mph (110 kph), and 84 mph (135 kph) were between 0.6% and 9.2% (Fig. 4). These differences occurred as a result of the number of uncertainties, such as a column's concrete cover, mesh size, the column component's material models, the vehicle nose's location at the column's face, and the values of modulus of the subgrade's reaction of the soil springs. These parameters were not accurately described by El-Tawil et al. (2005).

Parametric Study

Once the finite element model was validated, a comprehensive parametric study was conducted to numerically investigate the RC-column's behavior during a vehicle collision. This parametric study was used to develop a new design equation to calculate a design vehicle impact force, which is the function in the vehicle's mass and velocity. This study is to investigate vehicle collision with unshielded bridge columns.

The LS-DYNA software was used to examine 13 different parameters, including the following parameters:

- Concrete material model (elastic, nonlinear, and rigid)
- Unconfined concrete compressive strength (f_c') ranging from 20.7 MPa (3,000 psi) to 69.0 MPa (10,000 psi)

- Material strain rate (SR, both considered and not considered)
- Percentage of longitudinal reinforcement ($\rho_s = A_s/A_c$) ranging from 1% to 3%
- Hoop reinforcement ranging from D13@64 mm (#4@2.5 in.) to D16@305 mm (#5@12 in.), corresponding to a volumetric reinforcement ratio of between 0.54% and 0.17%
- Column span-to-depth ratio (S/D) ranging from 2.5 to 10.0
- Column diameter (D) ranging from 1,200 mm (4.0 ft) to 2,100 mm (7.0 ft)
- Column top boundary condition (free, superstructure, and hinged)
- Axial load level (P/P_o) ranging from 0% to 10%
- Vehicle velocity (v_r) ranging from 32 kph (20 mph) to 112 kph (70 mph)
- Vehicle mass (m) ranging from 2 tons (4.4 kips) to 30 tons (65 kips)
- Roadside distance between errant vehicle and unshielded bridge column (L_c) ranging from 0.0 mm (0.0 ft) to 9,140 mm (30 ft)
- Soil depth above the top of the column footing (d_s) ranging from 500 mm (1.7 ft) to 1,500 mm (5.0 ft)

Thirty-three columns (from C0 to C32) were investigated. Column C0 was used as a reference column. The range of selected variables for the columns with regard to the examined parameters is summarized in Table 2. It should be noted that some of the selected parameters may be not common in practice. They were used, however, to fully understand the column's performance under a wide spectrum of parameters.

Geometry

The columns investigated in this study were supported on a concrete footing that had a fixed boundary condition at its bottom. The soil-structure interaction was investigated in a pre-study and will be presented in the sensitivity analysis section. All of the columns but C17 and C18 were hinged at the top ends. Column C17 was free at the top end while column C18 had a superstructure attached at its top (as explained in the validation section). The mass of the superstructure of the column C18 represented to 8.8% of the column's nominal axial capacity (eqn. 3). The effect of the superstructure's mass on the behavior of the bridge columns under vehicle collision was investigated and will be presented in the sensitivity analysis section. Each column had a circular cross-section with a diameter (D) that was between 1,200 mm (4.0 ft) and 2,100 mm (7.0 ft); most had a diameter of 1,500 mm (5.0 ft; Fig. 5). The column's height (H) was between 3,810 mm (12.5 ft) and 15,240 mm (50.0 ft); most were 7,620 mm (25.0 ft) high. The column span-to-depth ratios (S/D) were between 2.5 and 10; most had a span-to-depth ratio of 5.0. The soil depth above the top of the footing (d_s) were between 500 mm (1.7 ft) and 1,500 mm (4.9 ft); most soil depths were 1,000 mm (3.3 ft).

The percentage of longitudinal steel reinforcement (ρ_s) was between 1.0% and 3.0%; most columns had ρ_s of 1.0%. The hoop reinforcement size was between D13 @ 64 mm (#4 @ 2.5 in.) and D19 @ 305 mm (#6 @ 12 in.); most columns had a hoop reinforcement of D16 @ 102 mm (#5 @ 4 in.).

The column's axial load (P) was between 0% and 10% of the column's nominal axial capacity (P_o); most columns had an axial load of 5% of P_o. The column's nominal axial capacity (P_o) was calculated as follows (AASHTO-LRFD 2012):

$$P_o = A_s f_y + 0.85\, f_c'(A_c - A_s) \quad (3)$$

where A_s = the cross-sectional area of the longitudinal steel reinforcements, A_c = the cross sectional area of the concrete column, f_y = the yield stress of the longitudinal steel reinforcements, and f_c' = the cylindrical concrete's unconfined compressive stress.

FE Columns Modeling

One-point quadrature solid elements were used to model each column's concrete core. This type of elements assumes constant stress through the element and determines the element's local deformations using hourglass control. An hourglass control was used to avoid spurious singular modes (e.g., hourglass modes). The hourglass value for each of the models was taken as the default value 0.10, with an hourglass control type_4 (Flanagan-Belytschko stiffness form). The FE results are reliable should the initial kinetic energy completely transformed into internal energy, hourglass energy, and residual kinetic energy (El-Tawil et al. 2005). The hourglass energy was calculated for each model and it was lower than 2% of the total energy. Therefore, the hourglass control did not affect accuracy of the results. The column's concrete core elements had an average dimension of 108.0 mm × 56.0 mm × 63.5 mm (4.3 in. × 2.2 in. × 2.5 in.). A rigid cylinder that was 200 mm (7.9 in.) high, modeled by solid elements, was placed atop the concrete column to avoid excessive local damage to the column's top when the axial loads were applied. Solid elements were used to model the concrete footing.

Both longitudinal and hoop reinforcements were modeled by beam_orientation elements. All of the beam elements of the reinforcement were "constrained" to the elements of the concrete column and the footing by "Lagrange in solid" which simulates

the perfect bond behavior between the concrete column and steel reinforcements. The column's concrete cover was designed to spall at an axial compressive strain exceeding 0.005 (Caltrans 2006).

Concrete Material Models

Two different concrete material models have been used in the literature to assess the impact forces on bridge columns: the elastic isotropic material mat001 and the rigid material model mat020. The use of an elastic material allows for the evaluation of the impact force, assuming that the column will remain elastic. Similarly, rigid material model does not allow any deformations to take place in the columns. Hence, both material models do not consider any energy dissipation induced by inelastic deformation in the column and the impact forces calculated with these two material models represent the impact forces' upper bounds. Both material models have been extensively used in the literature for analysis of impact problems (Buth et al. 2010, El-Tawil et al. 2005). The AASHTO-LRFD, however, considers vehicle impact to be an extreme load. Therefore, a column's nonlinear behavior is both expected and allowed. Hence, this research was conducted in attempt to investigate the effect of three different concrete material models, including elastic (mat001), rigid (mat020), and nonlinear (mat72RIII) on a bridge column's response to vehicle impact.

The elastic modulus and Poisson's ratio are the only parameters required to define an elastic material model. These parameters were also used for the rigid material to identify the sliding interface parameters of the contact elements between the vehicle and the column. The elastic modulus (E) was calculated according to ACI-318 (2011) and

considering the dynamic increase factor (DIF) factor (E = 4,750 $\sqrt{\text{DIF} * f_c'}$). The DIF factor is explained later in this section. The Poisson's ratio was taken as 0.20 (Mehta and Monteiro 2006).

A nonlinear concrete material model (mat72RIII) was used for all of the columns and footings examined in this study except the columns C1 and C2. The concrete materials of the columns C1 and C2 were elastic and rigid materials, respectively. The mat72RIII model had three shear failure surfaces: yield, maximum, and residual (Malvar et al. 1997). The yield and ultimate failure surfaces of this model were automatically generated given f_c' and ω. The fractional dilation parameter (ω) that takes into consideration any volumetric change occurring in the concrete was taken as the default value of 0.50.

Loading strain rates may play an essential role in a structure's response. The DIF is typically used to describe the increase in concrete's strength under dynamic loading as compared to static loading (Malvar and Ross 1998; Bischoff and Perry 1991; Williams 1994; Fu et al. 1991). Malvar and Ross (1998) modified the CEB model code for use with strain rate effects as in equations 4 to 11 (CEB-FIP 1990). They implemented these equations into an LS-DYNA format. For example, when concrete has a compressive strength (f_c') of 34.5 MPa (5,000 psi) and is subjected to a compressive load with a strain rate of 100 s^{-1} (common for impact loading; Sierakowsi and Chaturved 1997), the DIF will be 2.21 in compression and 7.52 in tension. The effect of a high strain rate is quite significant with regard to concrete's tensile strength (as compared to concrete's compressive strength). This behavior occurred because tension cracks do not have enough time to propagate through concrete; the loading time is too short.

$$DIF_c = \frac{f_c}{f_{cs}} = \left(\frac{\dot{\varepsilon}}{\dot{\varepsilon}_s}\right)^{1.026\,\alpha_s} \quad \text{for } \dot{\varepsilon} \leq 30\ s^{-1} \tag{4}$$

$$DIF_c = \frac{f_c}{f_{cs}} = \gamma_s \left(\frac{\dot{\varepsilon}}{\dot{\varepsilon}_s}\right)^{0.33} \quad \text{for } \dot{\varepsilon} > 30\ s^{-1} \tag{5}$$

$$\alpha_s = (5 + 9\frac{f_{cs}}{f_{co}})^{-1} \tag{6}$$

$$log\gamma_s = 6.156\,\alpha_s - 2 \tag{7}$$

Where DIF_c = compressive strength dynamic increase factor

$\dot{\varepsilon}$ = strain rate in the range of 30×10^{-6} to 300 s^{-1}

$\dot{\varepsilon_s}$ = static strain rate of 30×10^{-6} s^{-1},

f_c = the dynamic compressive strength at $\dot{\varepsilon}$

f_{cs} = the static compressive strength at $\dot{\varepsilon_s}$

f_{co} = 10 MPa = 1,450 psi

$$DIF_t = \frac{f_t}{f_{ts}} = \left(\frac{\dot{\varepsilon}}{\dot{\varepsilon}_s}\right)^{\delta} \quad \text{for } \dot{\varepsilon} \leq 1\ s^{-1} \tag{8}$$

$$DIF_t = \frac{f_t}{f_{ts}} = \beta \left(\frac{\dot{\varepsilon}}{\dot{\varepsilon}_s}\right)^{0.33} \quad \text{for } \dot{\varepsilon} > 1\ s^{-1} \tag{9}$$

$$\delta = (1 + 8\frac{f_{cs}}{f_{co}})^{-1} \tag{10}$$

$$log\ \beta = 6\,\delta - 2 \tag{11}$$

Where DIF_t = tensile strength dynamic increase factor

f_t = the dynamic tensile strength at $\dot{\varepsilon}$

f_{ts} = the static tensile strength at $\dot{\varepsilon_s}$

$\dot{\varepsilon}$ = strain rate in the range of 10^{-6} to 160 s^{-1}

$\dot{\varepsilon}_s$ = static strain rate of 10^{-6} s^{-1}

Steel Reinforcement Model

An elasto-plastic constitutive model (mat003-plastic_kinamatic) was used for steel reinforcement. The following five parameters were needed to define this material model: the elastic modulus (E), the yield stress, Poisson's ratio, the tangent modulus, and the ultimate plastic strain. These parameters were assigned the following values: 200 GPa (29,000 ksi); 420.0 MPa (60,900 psi); 0.30; 1,102 MPa (160 ksi); and 0.12, respectively (Caltrans 2006). Cowper-Symonds's (1957) model was adopted (eqn. 12) to examine the strain rate effect. Parameters p and c were assigned as a means for identifying the strain rate effect. Constants p and c were taken as 5 and 40, respectively (Yan and Yali 2012). Substituting these two constants into Cowper-Symonds's equation at a strain rate of 100 s^{-1} produced a dynamic yield stress that was 2.20 times the static yield stress. The elastic modulus of steel did not change considerably under impact loading (Campbell 1954).

$$f_{yd} = 1 + \left(\frac{\dot{\varepsilon}}{c}\right)^{\frac{1}{p}} \tag{12}$$

where $f_{yd} =$ dynamic yield stress and p and c were taken as 5 and 40, respectively

FE Vehicles Modeling

Two vehicle models were used in this study: a Ford reduced model (35,353 elements) single unit truck (SUT) and a detailed model (58,313 elements) Chevrolet C2500 Pickup (Fig. 6). These models were downloaded from the NCAC website. Experimental tests

involving head-on collisions were conducted to validate each model (Zaouk et al. 1996; Mohan et al. 2003). Both models showed good agreement with experimental results

Different vehicle speeds were investigated during this research. The vehicle's initial velocities were between 32 kph (20 mph) and 112 kph (70 mph); most had an initial velocity of 80 kph (50 mph). The interface friction between the vehicle and the ground was taken as 0.9. The mass of the vehicle was between 2 tons (4.4 kips) and 30 tons (65 kips); most was 8 tons (18 kips). The Chevrolet C2500 Pickup was used for the 2 tons (4.4 kips) mass, and the Ford SUT was used for the remaining models. Changing of the Ford SUT's mass was by changing of the cargo mass. Automatic_surface_to_surface contact elements by parts, with the contact factor SOFT=1 were used between the vehicle and the RC-column (Bala 2001). The algorithm Automatic_surface_to_surface is a penalty-based which was designed to examine each slave node for penetration through the master surface at every time step. So, if any penetration was found between the parts in contact, a nominal interface spring would apply a force proportional to the penetration depth of these interfaces to eliminate the penetration.

If the bridge pier was not located inside the clear zone which means the pier is not shielded by a crashworthy barrier, the design of the pier must include the collision force. The clear zone is the total roadside border area, beginning at the edge of the traveled way, available for safe use by an errant vehicle (AASHTO Roadside Design Guide, 2011). The effect of the roadside distance (L_c) between the vehicle and the unshielded bridge pier was examined here by studying different distances between the vehicle's nose and the column's face. This distance was taken between 0.0 mm and 9,140 mm (30.0 ft); most was 150 mm (0.5 ft).

Results and Discussion of the Parametric Study

Performance Levels

Few researchers have attempted to assign limit states to bridge columns under vehicle impact (Agrawal et al. 2013; Sharma et al. 2012). No consensus among researchers has been reached on the damage state at different limit states. Three different limit states were defined during the course of this study. Performance level P1 was assigned when no longitudinal rebar buckling took place during the analysis. Performance level P2 (heavy damage) was assigned when less than 20% of the longitudinal rebar buckled. Performance level P3 was assigned when at least 20% of the longitudinal rebar buckled (Fig. 7a). Performance level P3 was considered as column's failure.

The rebar buckling was validated with the result of a previous study of a large-scale reinforced concrete column tested under seismic loading (Figs. 7b and 7c; Abdelkarim et al. 2015b). The main differences between seismic and impact loadings are loading rate and number of reversible cycles. The seismic loading has lower loading rate and higher number of reversible cycles than the impact loading. Rebar buckling typically occurs following unloading after being subjected to high tensile strain demand. Zong and Kunnath (2008) concluded that the tensile strain is the main factor affects the onset of bar buckling. Feng et al. (2015) stated that the onset of bar buckling would occur before crack closure, which would be due to a previous high tensile strain demand. As the steel rebar model in LS-DYNA "003-plastic kinematic" can capture the tensile strain from previous studies on reinforced concrete columns under seismic loading (e.g., Youssf et al. 2015), it would capture the onset of rebar buckling. In addition, the effect of the loading rate was taken into consideration by defining the strain rate effect according to equation

of Cowper-Symonds (1957).” However, the deformed shape of the rebar buckling or fracture due to low cyclic fatigue under impact loading deserve further investigation, this manuscript identify the performance level based on the *onset* of rebar buckling only.

Performance levels for each of the columns are illustrated in Fig. 8(a) and listed in Table 3. Approximately 73%, 15%, and 12% of the columns were assigned to performance levels P1, P2, and P3, respectively. Columns C14, C21, C25, and C26 failed under the vehicle impact load. These impact cases were characterized by a small column diameter of 1,200 mm (4.0 ft), a high speed vehicle velocity of 112 kph (70 mph), and a heavy mass of either 16 tons (35 kips) or 30 tons (65 kips). Columns C3, C6, C12, C17, and C30 suffered heavy damage. These impact cases were characterized by a low concrete strength of 20.7 MPa (3,000 psi), when strain rate effect was excluded, a low column aspect ratio of 2.5, a free top boundary condition, and a long roadside distance of 9,140 mm (10 ft).

General Comparisons

The static shear capacity of each column was calculated according to AASHTO-LRFD (2012) and using the static material properties. Both the ESF and the columns’ static shear capacities normalized by the ESF of the AASHTO-LRFD (2,670 kN [600 Kips]) are illustrated in Figure 8b and listed in Table 3. The PDFs normalized by the ESF of the AASHTO-LRFD for all of the columns are listed in Table 3 as well. The differences between the ESF approaches were highly varied from case to case. The differences between the maximum and the minimum values of ESF, calculated using the different three approaches for a given column was between 7% (C2) and 140% (C14). The SB_{ESF}

represents the upper bound for 73% of the columns. The EC_{ESF} represents the lower bound for 85% of the columns. The SB_{ESF} of 27% of the columns either exceeded or equaled the ESF of the AASHTO-LRFD (2,670 kN [600 kips]). The ESF calculated with the PTMSA exceeded the ESF of the AASHTO-LRFD for 9% of the examined columns. The ESF of the Eurocode (EC_{ESF}) was typically lower than the ESF of the AASHTO-LRFD except for the columns C25 and C26 of the heavy vehicles of masses more than 16 ton (35 kips).

Columns that reached performance level P3 are referred to as "failed columns" while all other columns are referred to as "unfailed columns". As the point of the impact loading due to the vehicle collision is usually close to the point of the fixity of the column. The shear failure is the predominant mode of failure rather than the flexure failure. Therefore, if the ESF (according to a given approach) was higher than the column's static shear capacity, the column was considered a failed column. .Equations 13 and 14 summarize these characteristics as following:

Safety according to FE =

$$true\ value\ of \begin{cases} P_1 & (unfailed\ column) \\ P_2 & (unfailed\ column) \\ P_3 & (failed\ column) \end{cases} \tag{13}$$

Safety according to the different approaches =

$$true\ value\ of \begin{cases} ESF \leq shear\ capacity & (unfailed\ column) \\ ESF > shear\ capacity & (failed\ column) \end{cases} \tag{14}$$

By comparing the results from Equations 13 and 14 for a given column, an approach to calculate the ESF can be determined to be conservative or unconservative for this particular column. When Equation 13 predicted performance level P3 while Equation 14

predicted “unfailed column”; then, this approach is un-correctly predicting the performance of this column. Otherwise, the approach used to calculate ESF is considered matches well the performance of the column.

The data in Figs. 8a and 8b, as well as that in Tables 3 and 4 indicate that the PTMSA approach was the best approach for predicting the column’s performance. This approach predicted that four columns would fail (performance level P3). The PTMSAs of these columns were higher than the columns’ static shear capacities. The PTMSA was lower than the column’s static shear capacity for all of the unfailed columns. Hence, the FE results were in 100% agreement with the performance levels.

The SB_{ESF} approach predicted that six of the columns would fail, which is a higher number than that given during the FE analyses. The SB_{ESF} approach correctly predicted that columns C14, C21, C25, and C26 would fail. The SB_{ESF}, however, also indicated that columns C11 and C17 would fail. Columns C11 and C17 reached performance level P1 and P2, respectively, according to the FE analyses. Hence, the SB_{ESF} approach over-predicted the impact force on columns C11 and C17 by at least 10% and 2%, respectively. Thus, these two columns were characterized as unfailed columns.

The EC_{ESF} approach predicted that only two of the columns would fail. The EC_{ESF} approach correctly predicted that columns C14 and C26 would fail. The EC_{ESF}, however, indicated that columns C21 and C25 would not fail. Columns C21 and C25 reached performance level P3 according to the FE analyses. Hence, the EC_{ESF} approach under-predicted the impact force on columns C21 and C25 by at least 34% and 6%, respectively. Therefore, these two columns were characterized as failed columns. The EC_{ESF} correctly predicted the column’s failure for the columns are associated with impact

with the heaviest vehicle of 30 tons (65 kips) which represents the highest kinetic energy. Also, the EC_{ESF} correctly predicted the column's failure for the case of the lowest column's diameter of 1,200 mm (4.0 ft) which had the lowest shear capacity.

The AASHTO-LRFD predicted that three columns, C3, C11, and C14, would fail. The FE analysis, however, showed that the AASHTO-LRFD approach correctly predicted the state of only one column i.e. column C14. The AASHTO-LRFD approach indicated that columns C3 and C11 would fail. These columns, however, reached performance level P2 and P1, respectively, according to the FE analyses. Hence, the AASHTO-LRFD over-predicted the impact force on columns C3 and C11 by at least 2% and 13%, respectively.

The AASHTO-LRFD indicated that columns C21, C25, and C26 would not fail. These columns reached performance level P3 according to the FE analyses. Hence, the AASHTO-LRFD approach under-predicted the impact force on columns C21, C25, and C26 by at least 10%. It is worth noting that, the commentary to AASHTO-LRFD (2012) stated that "C3.6.5.1; Field observations indicate shear failures are the primary mode of failure for individual columns and columns that are 750 mm (30.0 in.) in diameter and smaller are the most vulnerable". The current study, however, indicated that columns that are 1,200 mm (48.0 in.) in diameter are also vulnerable to shear failure.

The static damage ratio (DR_s) is defined as the ESF, normalized by each column's static shear capacity. The dynamic damage ratio (DR_d) is defined as the PDF, normalized by each column's dynamic shear capacity. The dynamic shear capacity of each column was calculated according to AASHTO-LRFD (2012) and using the dynamic material properties by considering the DIFs. The column would fail when the static or the

dynamic damage ratio was > 1.0. Fig. 9 illustrates the static and dynamic damage ratios for all of the investigated columns. The figure shows that the dynamic damage ratios were in very good agreement with the columns' performance levels. The DR_d predicted that five columns would fail. However, one column, C11, its DR_d = 1.02 which was predicted as performance level P2. In summary, based on the DRs of all ESF approaches, 6 columns out of the investigated 33 columns would fail as the shear demand due to vehicle collision is greater than the shear capacity.

Sensitivity Analysis

A sensitivity analysis was conducted to investigate the effect of important parameters on the reliability of the parametric study results. The existence of the superstructure, the superstructure mass, and the soil-structure interaction were studied through this analysis.

The reference column C0 (which was hinged atop) and the column C18 (which had a superstructure atop) were collided with different vehicle's velocities and masses having kinetic energies between 980 kN.m (723 kip.ft.) and 7,600 kN.m (5,605 kip.ft.). Figure 10a illustrates the ratio between the dynamic forces of the column C0 and that of the column C18 at the different kinetic energies. Figure 10b illustrates the ratio between the static forces (PTMSAs) of the column C0 and that of the column C18 at the different kinetic energies. The results when the column was hinged atop or when the superstructure existed atop the column were very similar. The results in Figs. 10a and 10b clarify that the existence of the superstructure does not affect the dynamic and static forces. This behavior occurred since the impact duration is very small compared to the natural period of the column and hence the structure response is mainly controlled by the amplitude of

the imposed kinetic energy. Similar conclusion was drawn for pulse type loading (Chopra 2012).

The mass of the superstructure was studied by investigating four different superstructure masses resulting in axial stress ratios ranging from 5.5% of P_o to 10% of P_o. Figure 11 illustrates the normalized PDF and PTMSA to the ESF of the AASHTO-LRFD (2670 kN [600 kip]) at different superstructure masses. The results showed that within the narrow range of bridge masses investigated in this section the mass of the superstructure had almost no effect on the PTMSA and insignificant effect on the PDF.

The footing of the column C0 was fixed at its bottom assuming it was shallow footing constructed on a rock soil. The soil-structure interaction was investigated by studying column C0 when its footing rested on a loose sandy soil with a modulus of subgrade reaction of 10,000 kN/m^3 (40 psi/in.; Bowles 1988). The results of the two cases (rock and loose sand) were compared. Figure 12 illustrates the dynamic forces versus time of the two cases. The results of the two models were very similar. These results indicated that the type of the soil has limited effect on the impact forces. It should be noted that while the soil conditions do not significantly change the dynamic impact force, they will change the column response in terms of deformations.

Proposed Variable ESF for Adoption by AASHTO-LRFD

The AASHTO-LRFD uses a constant value for ESF, regardless of the vehicle's and/or column's characteristics. All other approaches presented in this manuscript use a variable ESF that is dependent on these characteristics. The AASHTO-LRFD approach for ESF is quite simple. However, Fig. 8 as well as Tables 3 and 4 showed that in some cases

AASHTO-LRFD is quite conservative and in other cases under-predicts the impact loads such as those involving heavy trucks, high speeds, and small column diameters. The other approaches, however, require a cumbersome FE analysis and iterative design. Thus, a simple equation that can predict the ESF without either a cumbersome FE or an iterative analysis would represent a significant improvement over the current AASHTO-LRFD approach. Fig. 8 and Table 3 reveal that vehicle mass and velocity are the most influential parameters on impact problems. The remaining parameters have limited effects. Therefore, developing a vehicle impact load as a function of the vehicle's mass and velocity seems reasonable. This approach will allow Departments of Transportation (DOTs) to design different bridge columns according to different impact force demands that are dependent on the anticipated truck loads and velocities for a specific road.

The PTMSA correctly predicted the performance of all the columns investigated in this study. Thus, it was selected as the basis for the newly developed equation. Based on the FE results and PTMSAs of the parametric study, using CurveExpert Professional software and SAS software, a new design equation for estimating kinetic-energy based equivalent static force (KEB_{ESF}) was developed and presented in equation (15) as below:

$$KEB_{ESF} = 33\sqrt{m\, v_r^2} = 46\sqrt{KE} \tag{15}$$

where m = the vehicle mass in ton, v_r = the vehicle velocity in m/s, and KE = kinetic energy of the vehicle in kN.m

The proposed equation's results were compared to the PTMSA's FE results. Additional 14 columns were collided with SUT trucks with different masses and velocities to investigate the accuracy of the equation with the cases of high kinetic

energies. The additional columns were collided with vehicles had masses between 8 tons (18 kips) and 40 tons (90 kips) and had velocities between 80 kph (50 mph) and 112 kph (70 mph). The ESFs of the additional 14 column were calculated and compared with the results from equation (15). The relationship between the vehicle's kinetic energy and the normalized PTMSA is illustrated in Fig. 13. The figure illustrates the relationship between the vehicle's kinetic energy and the normalized KEB_{ESF} as well. The AASHTO-LRFD over-predicted the ESF up to a KE of approximately 2,500 kN.m (1,844 kip.ft). It was quite unconservative, however, beyond that threshold of 2,500 kN.m (1,844 kip.ft). In several instances, the RC-columns were subjected to impact loads that were almost double the ESF of the AASHTO-LRFD. The proposed $KEB_{ESF} \pm 10\%$ of the KEB_{ESF} (referred to as upper and lower limits) are also shown in Fig. 13. The upper and lower limits are to visualize the error of equation (15) versus the PTMSA results. The proposed KEB_{ESF} equation exhibited good agreement with averages, standard deviations, and a coefficient of variation of 1.1, 8.7, and 8.2, respectively. Fig. 15 illustrates the normalized KEB_{ESF} (eqn. 15) comparing to the columns' static shear capacity and the ESF of AASHTO-LRFD. This data reveals that the KEB_{ESF} could correctly predict the column's performance in 100% of the cases i.e. the KEB_{ESF} predicted failure of 4 columns and the FE analyses indicate failure of these 4 columns as explained earlier in this manuscript.

Proposed Simplified ESF for Adoption by Eurocode

The EC_{ESF}, based on equation (1), is dependent on the vehicle and column deformations and the KE. The FE analyses revealed that the column's displacement was much smaller than the vehicle's displacement and, thus, can be ignored. Hence, the EC_{ESF} is dependent

on the vehicle's mass and speed. Based on the FE results of EC_{ESF} of the parametric study and using CurveExpert Professional software and SAS software, a new simplified equation for estimating momentum-based equivalent static force MB_{ESF} is developed and presented in equation (16) as below:

$$MB_{ESF} = 130\sqrt{m\, v_r} = 130\sqrt{P_m} \tag{16}$$

where m = the vehicle mass in ton, v_r = the vehicle velocity in m/s, and P_m = the momentum of the vehicle in ton.m/s

The results of the proposed equation were compared to the FE results of EC_{ESF}. Fig. 14 illustrates the relation between the vehicle's momentum and the normalized EC_{ESF}. The figure illustrates the relation between the vehicle's momentum and the normalized MB_{ESF} as well. Both the upper and lower limits (referring to $\pm$ 10% of the MB_{ESF}) are also depicted in Fig. 14. The proposed MB_{ESF} equation exhibited good agreement with averages, standard deviations, and coefficient of variation of 2.9, 6.3, and 2.2, respectively. Fig. 15 illustrates the normalized MB_{ESF} (eqn. 16) comparing to the columns' static shear capacity and the ESF of AASHTO-LRFD. This data reveals that the MB_{ESF} could predict the columns' performance by 94% and 2 out of 4 of the failed columns.

Findings and Conclusions

A detailed description of finite element modeling of vehicle collision with reinforced concrete bridge columns using LS-DYNA software was presented. Evaluation of the peak dynamic force (PDF) and the equivalent static force (ESF) through a comprehensive

parametric study were conducted. The comprehensive parametric study investigated the effects of concrete material model, unconfined concrete compressive stress (f_c'), material strain rate, percentage of longitudinal reinforcement, hoop reinforcement, column span-to-depth ratio, column diameter, the top boundary conditions, axial load level, vehicle's velocity, vehicle's mass, roadside distance between errant vehicle and unshielded bridge column, and soil depth above the top of the column footing on the behavior of the columns under vehicle collision. Three approaches were considered during the course of this research to investigate the ESF. In the first approach, SB_{ESF}, the ESF was defined as the force needed to produce the same maximum displacement by a collision event at the point of impact. In the second approach, EC_{ESF}, the ESF was calculated by Eurocode. In the third approach, PTMSA, the ESF was defined as the peak of the 25 millisecond moving average. This study revealed the following findings:

1. The AASHTO-LRFD was found to be non-conservative when the column was collided with a vehicle having kinetic energy of 2,500 kN.m (1,800 kip.ft) or more. This corresponded to heavy vehicles of a weight more than 16 ton (35 kips) or high speed vehicle of a speed more than 112 kph (70 mph).
2. This study indicated that columns that are 1,200 mm (48.0 in.) in diameter are also vulnerable for shear failure. Currently, the commentary to AASHTO-LRFD states that columns that are 750 mm (30.0 in.) in diameter and smaller are most vulnerable for shear failure under vehicle impact loads.
3. A new equation for estimating the ESF based on the vehicle's mass and velocity ($KEB_{ESF} = 33\sqrt{m\ v_r^2}$) with accuracy more than 90% was developed. This approach will allow Departments of Transportation (DOTs) to design different

bridge columns to different impact force demands depending on the anticipated truck loads and velocities.

4. This paper simplified the Eurocode equation for estimating the ESF based on the vehicle's mass and velocity ($MB_{ESF} = 130\sqrt{m\ v_r}$) with accuracy more than 90%.
5. SB_{ESF} and PTMSA exceeded the ESF of the AASHTO-LRFD for approximately 27% and 9% of the total number of the investigated columns, respectively, while the ESF of the Eurocode (EC_{ESF}) was typically lower than the ESF of the AASHTO-LRFD.
6. Approximately 12% of the investigated columns failed while 15% suffered some sort of limited damage. The remaining 73% of the columns were responded elastically with no damage.
7. PTMSA approach was the best approach for predicting the columns' performance. The PTMSA predicted the failure state of 100% of the investigated columns while the EC_{ESF} predicted the potential failure of 50% of the failed columns. Furthermore, the AASHTO-LRFD was able to predict the potential failure of 25% of the failed columns.
8. The difference between the maximum and the minimum ESF for a given column ranged from 7% to 140% depends on the approach used to calculate the ESF.
9. For the columns investigated in this study, the SB_{ESF} generally represents the upper bound for 73% of the columns while EC_{ESF} represents the lower bound for 85% of the columns.

10. The existence of superstructure, the mass of the superstructure and the type of soil have insignificant effect on the dynamic and static forces of the vehicle impact.

Acknowledgement

This research was conducted by Missouri University of Science and Technology and was partially supported by Missouri Department of Transportation (MoDOT) and Mid-American Transportation Center (MATC). This support is gratefully appreciated. However, any opinions, findings, conclusions, and recommendations presented in this paper are those of the authors and do not necessarily reflect the views of sponsors.

References

AASHTO, (2012). AASHTO-LRFD Bridge Design Specifications – Customary US Units, sixth edition, Washington, DC.

AASHTO, (2010). AASHTO-LRFD Bridge Design Specifications – Customary US Units, fifth edition, Washington, DC.

Abdelkarim, O. and ElGawady, M. (2015a). "Impact Analysis of Vehicle Collision with Reinforced Concrete Bridge Columns." Transportation Research Board (TRB) conference (2015), Washington Dc, 15-4461.

Abdelkarim, O., Gheni, A., Anumolu, S., and ElGawady, M. (2015b). "Seismic Behavior of Hollow-Core FRP-Concrete-Steel Tubular Bridge Columns." ASCE Congress (2015), Oregon.

Abdelkarim, O. and ElGawady, M. A. (2014). "Analytical and Finite-Element Modeling of FRP-Concrete-Steel Double-Skin Tubular Columns." J. Bridge Eng., 10.1061/(ASCE)BE.1943-5592.0000700 , B4014005.

ACI Committee 318 (2011). "Building Code Requirements for Structural Concrete (ACI318-11) and Commentary (318R-11)." ACI, Farmington Hills, Mich., pp. 509.

Agrawal, A. K., Liu, G., and Alampalli, S. (2013). "Effects of Truck Impacts on Bridge Piers." Advanced Materials Research, 639-640, pp.13-25.

Agrawal, A.K. (2011). "Bridge Vehicle Impact Assessment: Final Report." University Transportation Research Center and New York State Department of Transportation.

Bala, S. (2001). "Contact Modeling in LS-DYNA." Livermore Software Technology Corporation.

Bischoff, P.H., Perry, S.H., "Compressive Behavior of Concrete at High Strain Rates." Materials and Structures, Vol. 24, 1991, pp. 425-450.

Bowles, J. (1988). "Foundation Analysis and Design." McGraw-Hill Inc., United States of America, pp. 1004.

Buth, C. E., Williams, W. F., Brackin, M. S., Lord, D., Geedipally, S. R., and Abu-Odeh, A. Y. (2010). "Analysis of Large Truck Collisions with Bridge Piers: Phase 1." Texas Department of Transportation Research and Technology Implementation Office, 9-4973-1.

Buth, C. E., Brackin, M. S., Williams, W. F., and Fry, G.T. (2011). "Collision Loads On Bridge Piers: Phase 2." Texas Department of Transportation Research and Technology Implementation Office, Report 9-4973-2.

California Department of Transportation. (2006). "Seismic Design Criteria." California Department of Transportation, Rev. 1.4.

Campbell, J.D. (1954). "The yield of mild steel under impact loading." Journal of the Mechanics and Physics of Solids, 3, 54-62.

Chopra, A. K. (2012). "Dynamics of Structures- Theory and Applications to Earthquake Engineering." Prentice Hall, Upper Saddle River, NJ, USA.

Comité Euro-International du Béton. (1993). "CEB-FIP Model Code 1990." Redwood Books, Trowbridge, Wiltshire, UK.

Cowper, G. R. and Symonds, P. S. (1957). "Strain Hardening and Strain Rate Effects in Impact Loading of Cantilever Beams." Brown University, App. Math. Report No. 28.

El-Tawil, S., Severino, E., and Fonseca, P. (2005). "Vehicle Collision with Bridge Piers." J. Bridge Eng., 10(3), 345-353.

El-Tawil, S. (2004). "Vehicle collision with bridge piers." Final Report to the Florida Department of Transportation for Project BC-355-6, FDOT/FHWA publication.

Eurocode 1: Actions on structures – Part 1-1: General actions – Densities, self-weight, imposed loads for buildings, Final Draft prEN 1991-1-1, October 2002.

Fouche, P., Bruneau, M. (2010). "Non-Linear Analysis of Multi-Hazard Performance of Cylindrical Concrete Filled Steel Tubes Bridge Piers." Proceedings of 8th International Conference on Short and Medium Span Bridges, Canada.

Feng, Y., Kowalsky, M., and Nau, J. (2015). "Finite-Element Method to Predict Reinforcing Bar Buckling in RC Structures." J. Struct. Eng., 141(5), 04014147.

Fu, H.C., Erki, M.A., Seckin, M., "Review of Effects of Loading Rate on Reinforced Concrete." Journal of Stru. Eng., Vol. 117, No. 12, December 1991, pp. 3660-3679.

Harik, I., Shaaban, A., Gesund, H., Valli, G., and Wang, S. (1990). "United States Bridge Failures, 1951–1988." J. Perform. Constr. Facil., 4(4), 272–277.

LS-DYNA; "theory manual for version 971." (2006). Livermore Software Technology Corporation.

Malvar, L. J. and Ross, C. A. (1998). "Review of Strain Rate Effects for Concrete in Tension." ACI Materials Journal, 95, 735-739.

Malvar, L., Crawford, J., Wesevich, J., and Simons, D. (1997). "A plasticity concrete material model for DYNA3D." *Int. J. Impact Eng*., 19(9–10), 847–873.

Mehta, K.P., Monteiro, P.J.M. (2006). "CONCRETE: Microstructure, Properties, and Materials." 3rd Edition, McGraw-Hill Inc., United States of America, pp. 660.

Mohan, P., Marzougui, D., Kan, C. (2003). "Validation of a Single Unit Truck Model for Roadside Hardware Impacts." NCAC, The George Washington University.

Roadside Design Guide. (2011) "American Association of State Highway and Transportation Officials." Washington, DC.

Ross, H.E., Sicking, D.L., Zimmer, R.A., and Michie, J.D. (2013). "Recommended Procedures for the Safety Performance Evaluation of Highway Features." National Cooperative Research Program (NCHRP) Report No. 350, Transportation Research Board, Washington, D.C.

Sharma, H., Hurlebaus, S., Gardoni, P. (2012). "Performance-based response evaluation of reinforced concrete columns subject to vehicle impact." Inter. Journal of Impact Eng., (43), 52-62.

Sierakowsi, R. L. and Chaturved, S. K. (1997). "Dynamic Loading and Characterization of Fiber-Reinforced Composites." John Wiley & Sons, Inc., New York, USA.

Thilakarathna, H.M.I., Thambiratnam, D.P., Dhanasekar, M., Perera, N. (2010). "Numerical simulation of axially loaded concrete columns under transverse impact and vulnerability assessment." Inter. Journal of Impact Eng., (37), 1100-1112.

Williams, M.S., "Modeling of Local Impact Effects on Plain and Reinforced Concrete." ACI Structural Journal, Vol. 91, No. 2, March-April 1994, pp. 178-187.

Yan, X. and Yali, S. (2012). "Impact Behaviors of CFT and CFRP Confined CFT Stub Columns." J. Compos. Constr., 16(6), 662–670.

Youssf, O., ElGawady, M., and Mills, J. (2015). "Displacement and plastic hinge length of FRP-confined circular reinforced concrete columns." Engineering Structures, 101, 465-476.

Zaouk, A., Bedewi N.E., Kan, C.D., Marzougui, D. (1996). "Validation of a Non-Linear Finite Element Vehicle Model Using Multiple Impact Data." International Mechanical Engineering Congress and Exposition, Atlanta, GA.

Zaouk, A. K., Bedewi, N. E., Kan, C. D., and Marzoughi, D. (1996). "Evaluation of a Multi-purpose Pick-up Truck Model Using Full Scale Crash Data with Application to Highway Barrier Impact." 29th Inter. Sym. on Auto. Tech. and Auto., Florence, Italy.

Zong, Z., and Kunnath, S. (2008). "Buckling of reinforcing bars in concrete structures under seismic loads." In Proc., 14th World Conf. on Earthquake Engineering, Beijing.

Table 1. Summary of FE results of current study versus El-Tawil et al. (2005)

Vehicle velocity, kph (mph)	PDF, kN (kips)		Difference (%)	ESF, kN (kips)		Difference (%)
	Current study	El-Tawil et al. (2005)		Current study	El-Tawil et al. (2005)	
55 (34)	3,784 (851)	3,466 (779)	9.2	583 (131)	622 (140)	6.4
110 (69)	10,397 (2,337)	9,985 (2,245)	4.1	1,104 (248)	1,196 (269)	7.8
135 (84)	12,418 (2,792)	12,500 (2,810)	0.6	1,362 (306)	1,593 (358)	14.5

Table 2. Summary of the examined columns' parameters

Col.	Conc. Mat.	$f'c$ (MPa)	SR	ρ_s	Hoop RFT	S/D	D (mm)	Top Bound. Cond.	P/P$_0$	v_r (kph)	m (ton)	L_C (mm)	d_s (mm)
C0	NL	34.5	C	1%	D16@ 102 mm	5	1,500	Hinged	5%	80	8	150	1,000
C1	EL												
C2	RIG												
C3	NL	20.7											
C4		48.3											
C5		69.0											
C6		34.5	NC										
C7			C	2%									
C8				3%									
C9				1%	D13@ 64 mm								
C10					D19@ 152 mm								
C11					D16@ 305 mm								
C12					D16@ 102 mm	2.5							
C13						10							
C14						5	1,200						
C15							1,800						
C16							2,100						
C17							1,500	Free					
C18								Super-structure					
C19								Hinged	0%				
C20									10%				
C21									5%	112			
C22										56			
C23										32			
C24										80	2		
C25											16		
C26											30		
C27											8	0	
C28												300	
C29												3,050	
C30												9,140	
C31												150	500
C32													1,500

NL = nonlinear material (mat72RIII), EL = elastic material (mat001), RIG = rigid material (mat020), SR = strain rate, NC = Not Considered, C = Considered, ρ_s = the percentage of longitudinal steel reinforcement in the column's cross-section =A_s/A_c(A_s = the cross-sectional area of the longitudinal steel reinforcements, A_c = the cross sectional area of the concrete column), S/D = span-to-depth ratio, D = column diameter, P = applied axial load, P_0 = column axial compressive capacity, v_r = vehicle velocity, m = vehicle mass, L_c = clear distance in front of vehicle's nose, d_s = soil depth above the column footing.

Table 3. Summary of the normalized PDFs, ESFs, and static and dynamic shear capacities of all of the columns and their performance levels

Column	PDF	SB_{ESF}	EC_{ESF}	PTMSA	Static shear capacity	Dynamic shear capacity	Performance level
C0	1.4	0.9	0.7	0.8	1.1	2.0	P1
C1	1.6	0.6	0.7	0.7	1.1	2.0	P1
C2	1.6	N/A	0.7	0.7	1.1	2.0	P1
C3	1.1	0.7	0.6	0.8	1.0	1.7	*P2*
C4	1.4	1.1	0.7	0.7	1.2	2.2	P1
C5	1.4	1.0	0.7	0.7	1.4	2.4	P1
C6	1.1	1.0	0.7	0.8	1.1	2.0	*P2*
C7	1.4	0.8	0.7	0.7	1.1	2.0	P1
C8	1.5	0.8	0.7	0.7	1.1	2.0	P1
C9	1.5	0.9	0.7	0.8	1.1	2.0	P1
C10	1.5	0.9	0.7	0.8	1.1	1.9	P1
C11	1.3	0.9	0.7	0.7	0.8	1.3	P1
C12	1.1	0.9	0.6	0.8	1.1	2.0	*P2*
C13	1.1	0.4	0.6	0.8	1.1	2.0	P1
C14	1.3	1.4	0.6	0.8	0.7	1.1	**P3**
C15	1.5	0.7	0.7	0.9	1.5	2.6	P1
C16	1.4	0.6	0.6	0.8	1.9	3.3	P1
C17	1.4	1.1	0.7	0.7	1.1	2.0	*P2*
C18	1.5	0.7	0.7	0.7	1.1	2.0	P1
C19	1.1	1.0	0.6	0.7	1.1	2.0	P1
C20	1.4	0.8	0.7	0.7	1.1	2.0	P1
C21	3.2	1.2	0.7	1.1	1.1	2.0	**P3**
C22	0.8	0.4	0.5	0.5	1.1	2.0	P1
C23	0.6	0.4	0.5	0.5	1.1	2.0	P1
C24	1.5	0.5	0.2	0.4	1.1	2.0	P1
C25	2.2	1.5	1.0	1.1	1.1	2.0	**P3**
C26	2.8	1.6	1.2	1.4	1.1	2.0	**P3**
C27	1.5	0.9	0.7	0.7	1.1	2.0	P1
C28	1.5	0.8	0.7	0.8	1.1	2.0	P1
C29	1.2	0.8	0.7	0.8	1.1	2.0	P1
C30	1.5	0.9	0.7	0.7	1.1	2.0	*P2*
C31	1.5	0.8	0.6	0.8	1.1	2.0	P1
C32	1.5	1.1	0.7	0.7	1.1	2.0	P1

Table 4. Summary of the prediction of the different approaches including AASHTO-LRFD

Prediction	SB_{ESF}	EC_{ESF}	PTMSA	AASHTO-LRFD
% correctly predicted	94.0%	94.0%	100.0%	85.0%
% over predicted	9.0%	0.0%	0.0%	6.0%
% under predicted	0.0%	6.0%	0.0%	9.0%
No. of predicted failed columns	4 out of 4	2 out of 4	4 out of 4	1 out of 4

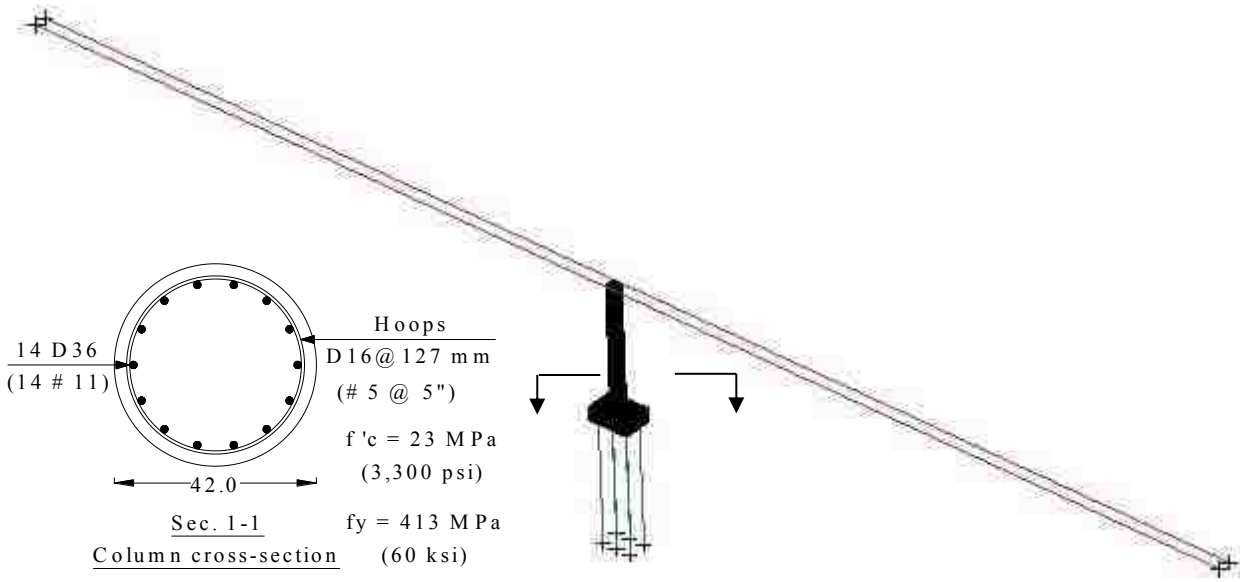

Fig. 1. 3D- view of the FE model for validation against El-Tawil's et al. (2005) results

Note: soil subgrade springs are not shown for simplicity

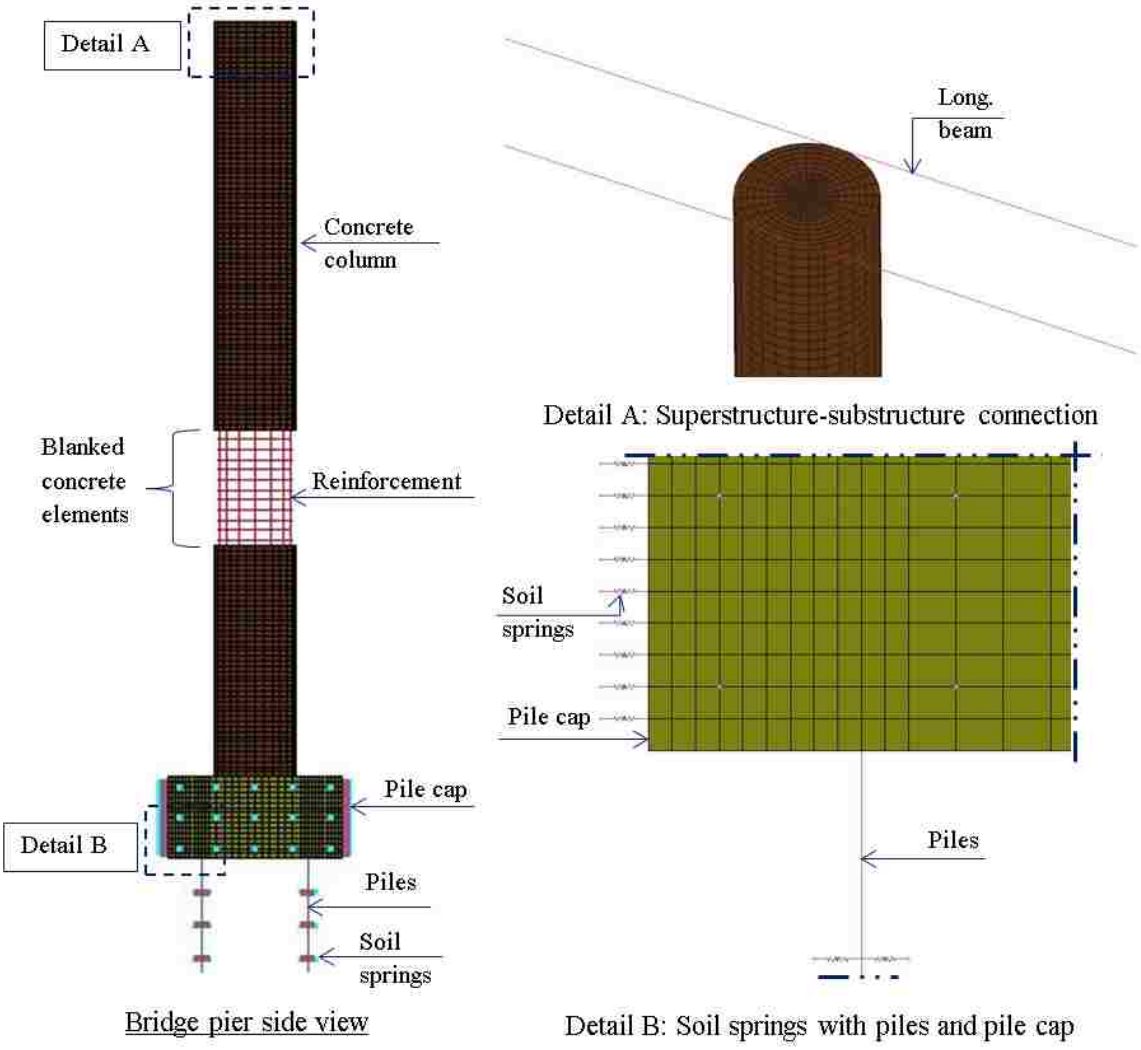

Fig. 2. Components of the FE model for validation against El-Tawil's et al. (2005) results

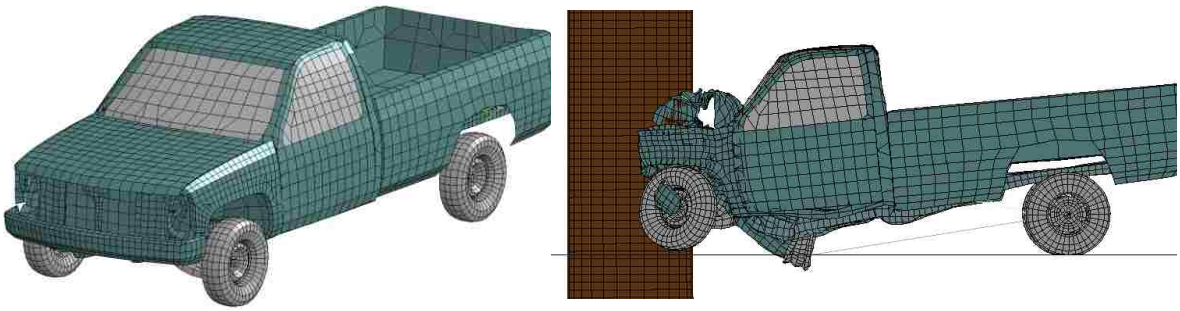

(a) (b)

Fig. 3. The reduced FE model of Chevrolet pickup: (a) 3D-view, (b) Side view of the collision event of the reduced FE model of Chevrolet pickup with bridge pier (velocity = 110 kph (69 mph) at time = 0.05 second)

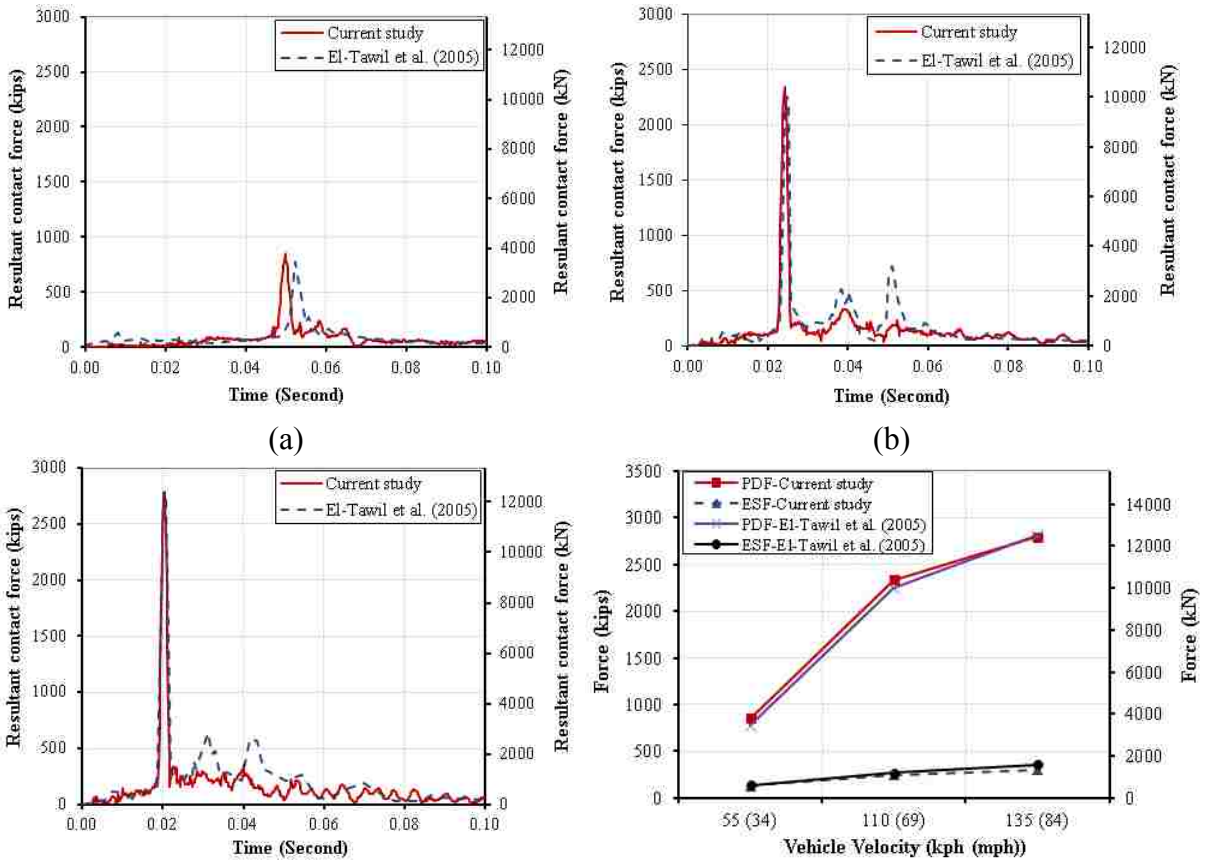

Fig. 4. FE results from current study versus those from El-Tawil et al. (2005) FE results; (a) vehicle's velocity of 55 kph (34 mph), (b) vehicle's velocity of 110 kph (69 mph), (c) vehicle's velocity of 135 kph (84 mph), and (d) PDF and ESF versus the vehicle velocities

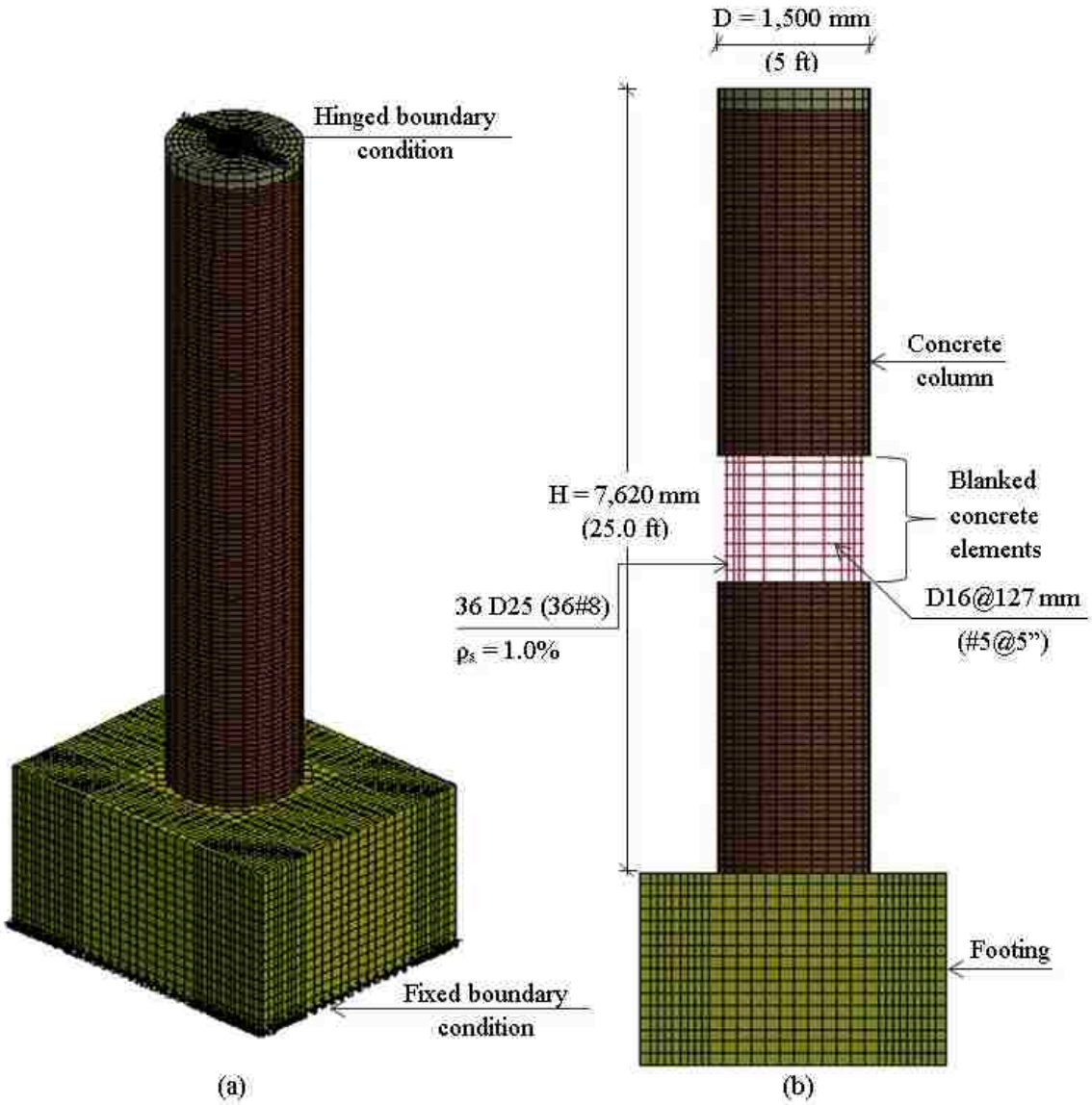

Fig. 5. F.E. model of the bridge pier "C0" for the parametric study; (a) 3D-view, (b) detailed side view of the pier components

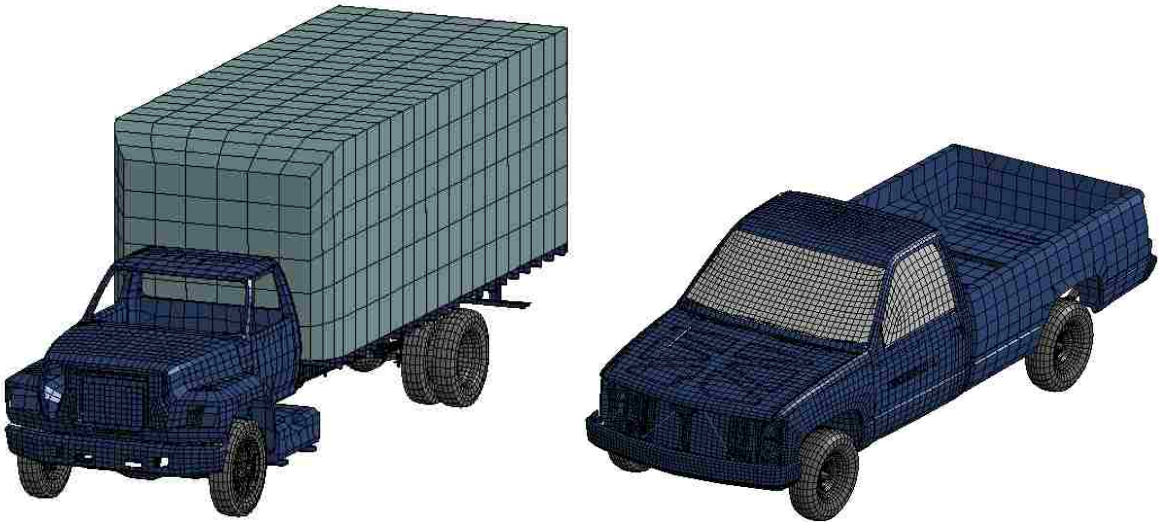

(a) (b)

Fig. 6. 3D-view of the FE model: (a) the Ford single unit truck, (b) Chevrolet pickup detailed model

(a) (b) (c)

Fig. 7. (a) Buckling of the longitudinal rebars (column C14 having a diameter of 1,200 mm [4 ft]- scaled 50 times), (b) Rebar buckling in a reinforced concrete column under seismic loading (Abdelkarim et al. 2015b), and (c) Validation of the rebar buckling with the experimental work

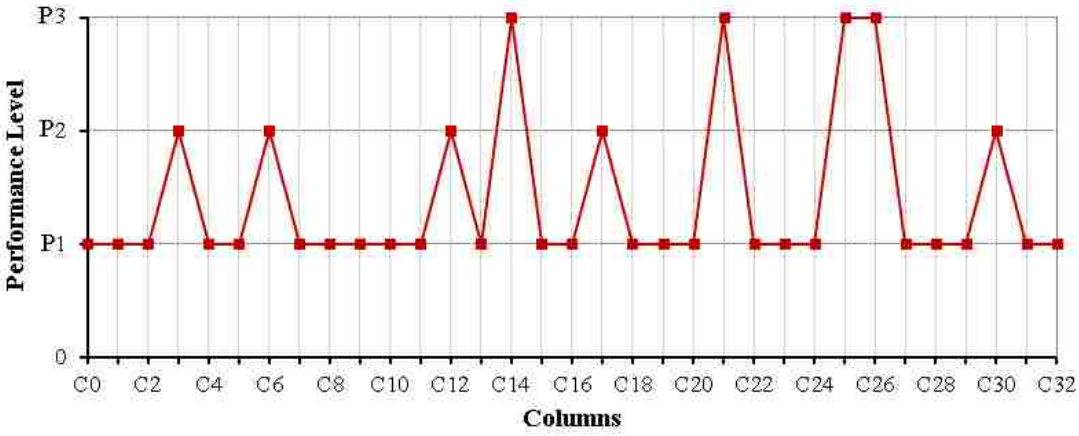

(a)

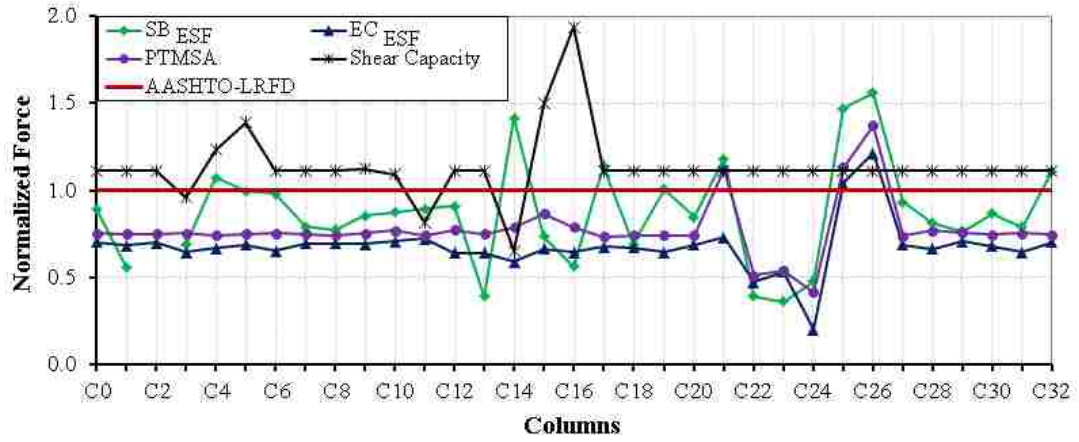

(b)

Fig. 8. (a) Performance levels of the examined columns according to the results of FE and (b) Normalized forces to the ESF of the AASHTO-LRFD (2,670 kN (600 kips))

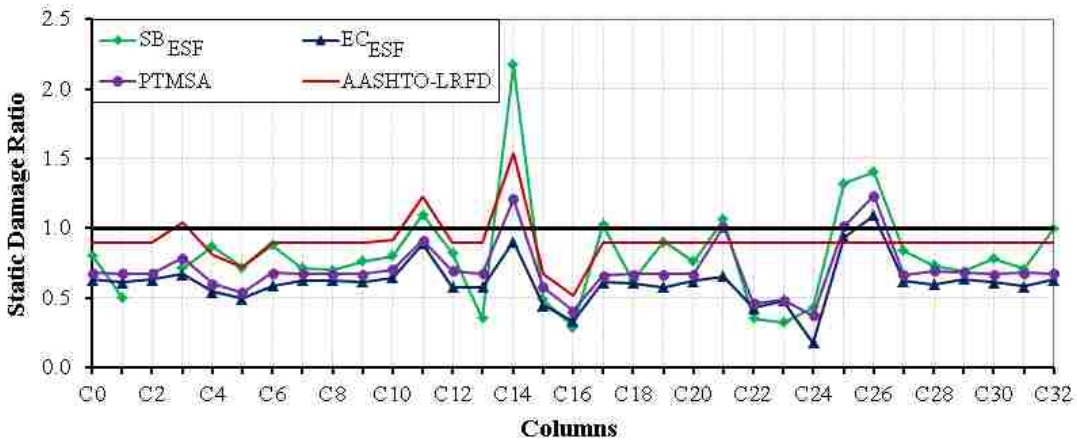

(a)

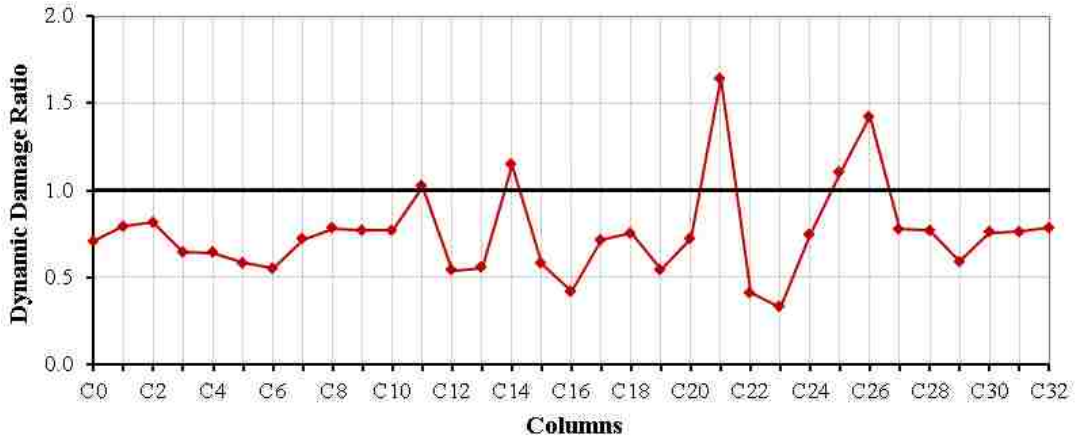

(b)

Fig. 9. (a) Static damage ratios of the ESF approaches and (b) Dynamic damage ratio of the PDF, for all of the examined columns

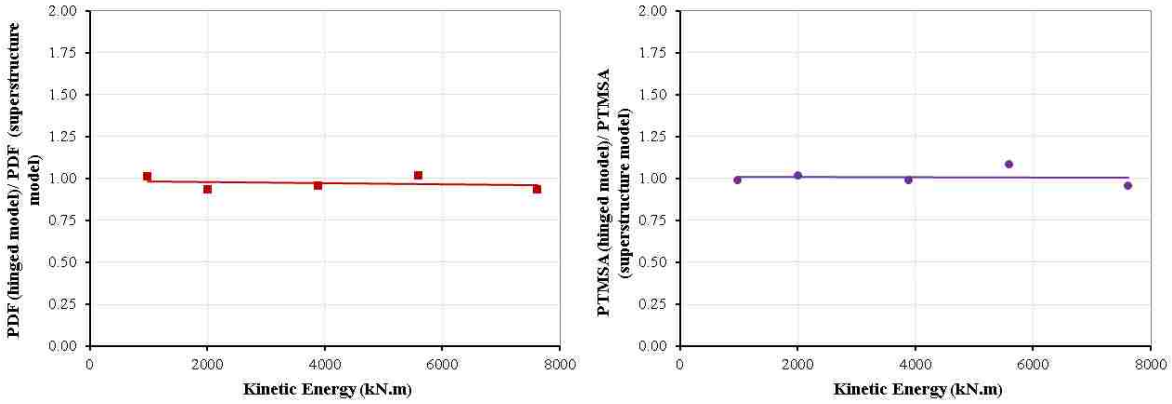

(a) (b)

Fig. 10. Kinetic energy versus dynamic and static forces of the columns C0 and C18

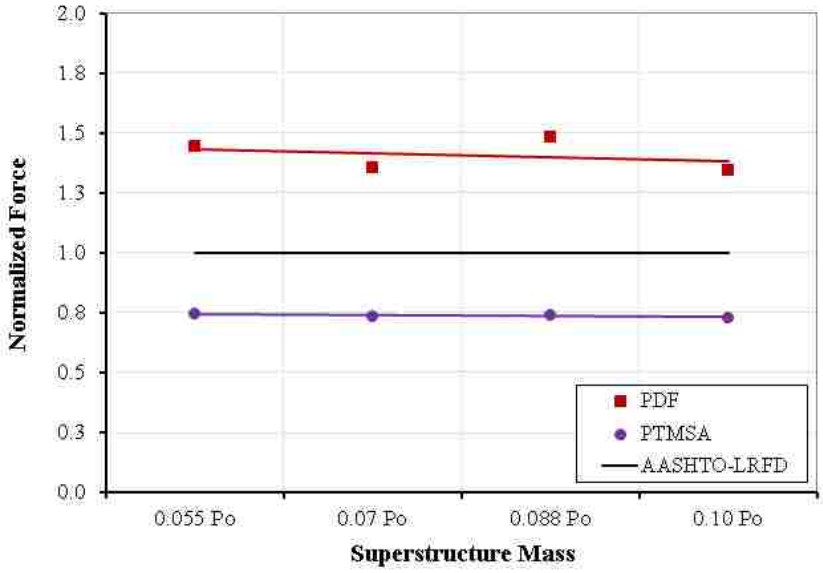

Fig. 11. Superstructure masses versus the normalized dynamic and static forces

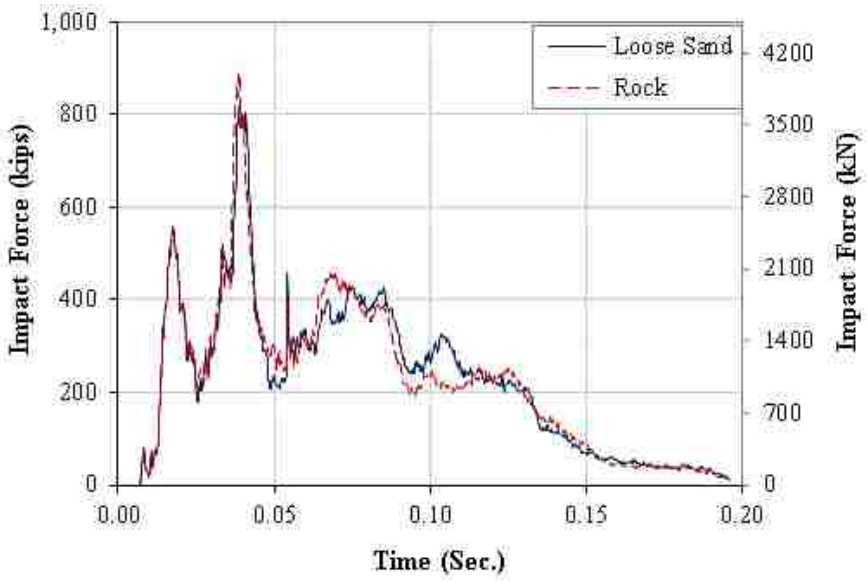

Fig. 12. Time versus impact forces when the column's footing rested on a rock or on a loose sand soil

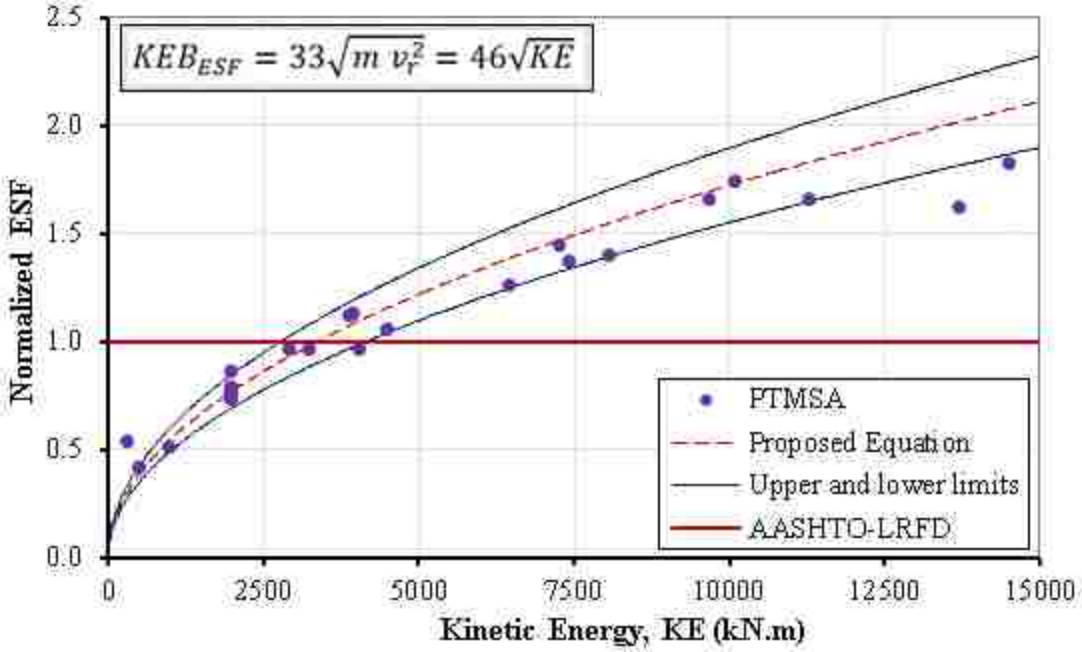

Fig. 13. Kinetic energy-ESF relation for the proposed equation of KEB_{ESF} and the FE results

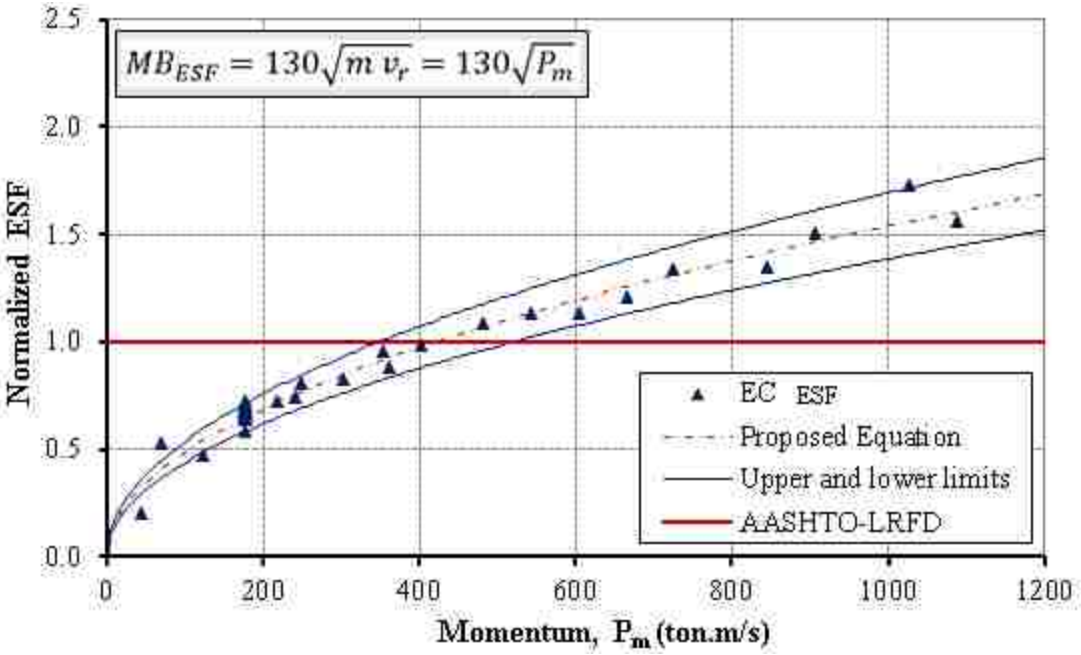

Fig. 14. Momentum-normalized ESF relation for the proposed equation of MB_{ESF} and the FE results

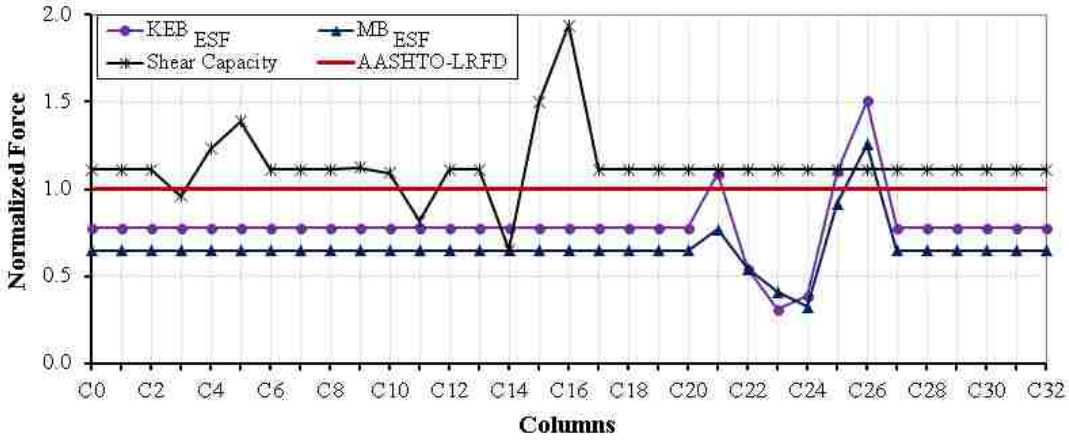

Fig. 15. Normalized forces of KEB_{ESF} and MB_{ESF} versus the normalized shear capacity and the ESF of AASHTO-LRFD

VII. HOLLOW-CORE FRP-CONCRETE-STEEL BRIDGE COLUMNS SUBJECTED TO VEHICLE COLLISION

Omar I. Abdelkarim[1], S.M. ASCE; Mohamed A. ElGawady[2]§, PhD, M. ASCE

Abstract

This paper presents the behavior of an innovative accelerated bridge construction system of hollow-core fiber reinforced polymer-concrete-steel (HC-FCS) columns under vehicle collisions using LS-DYNA software. The HC-FCS column consists of a concrete wall sandwiched between an outer fiber reinforced polymer (FRP) tube and an inner steel tube. The steel tube works as longitudinal and transverse reinforcement, and the FRP tube confines the sandwiched concrete. Detailed finite element analyses were conducted to investigate the effects of 14 different parameters including the concrete material model, the unconfined concrete compressive strength (f_c'), the material strain rate, the column height-to-diameter ratio, the column diameter, the FRP confinement ratio, the diameter-to-thickness ratio of the steel tube, the column void ratio, the embedded length of the steel tube, the infilled steel tube, the top boundary conditions, the axial load level, the vehicle's velocity, and the vehicle's mass on both dynamic and static impact forces. The peak dynamic force (PDF) and the equivalent static force (ESF) were investigated. The ESF is defined as the peak of the twenty-five millisecond moving average (PTMSA). The PTMSAs of the investigated columns were compared to the ESF of the American Association of State Highway and Transportation Officials- Load and Resistance Factor

1 Ph.D. Candidate, Dept. of Civil, Architectural, and Environmental Engineering, Missouri University of Science and Technology, Rolla, MO. 65401; oiafgc@mail.mst.edu

2 Benavides Associate Professor, Dept. of Civil, Architectural, and Environmental Engineering, Missouri University of Science and Technology, Rolla, MO. 65401; elgawadym@mst.edu

§Corresponding author

Design (AASHTO-LRFD; 2,670 kN (600 kips)). The AASHTO-LRFD was found to be non-conservative when the column was collided with a heavy vehicle with a mass of more than 16 tons (35 kips) or a high-speed vehicle with a velocity of more than 112 kph (70 mph).

Keywords: *Bridge Columns, Precast Columns, Composite Columns, Vehicle Collision, Impact Analysis*

Introduction

Very tall concrete bridge columns in seismic areas have usually hollow-core cross-section. The use of hollow-core cross sections in concrete columns reduces both mass and self-weight, thereby also reducing inertial forces. These columns limit the required dimensions of foundations, consequently lowering construction costs.

A new type of hollow-core columns was introduced by Montague (1978), consisting of a concrete wall sandwiched between two generally concentric steel tubes. These columns have been investigated extensively (Fouche and Bruneau 2010; Hajjar 2000; Shakir-Khalil & Illouli 1987). Fiber reinforced polymer (FRP) tubes have been used repeatedly as an alternative to steel tubes in concrete-filled tube columns. The behavior of concrete-filled FRP tube columns has been investigated under extreme loads (Qasrawi et al. 2014; Moon et al. 2013; Sadeghian and Fam 2010; Zhu et al. 2006; Shao and Mirmiran 2005; Fam et al. 2003; Zhang and Shahrooz 1997). More recently, Teng et al. (2004) presented a section similar to Montague et al. (1978) but utilizing FRP as an outer tube and steel as an inner tube, developing the hollow-core fiber reinforced polymer-concrete-steel column (HC-FCS). This system combines and optimizes the

benefits of all three materials: fiber reinforced polymer (FRP), concrete, and steel, in addition to the benefits of the hollow-core concrete columns.

Construction of HC-FCS columns exhibited several advantages over conventional reinforced concrete (RC) columns. The hollow core of the HC-FCS column uses 60 to 75% less material and requires 90% less construction time than the conventional solid column (Abdelkarim et al. 2015). When implemented with precast construction, it also reduces freight cost. An HC-FCS column represents a compact engineering system in which the steel and FRP tubes cooperate as stay-in-place formworks, the steel tube acting as both flexural and shear reinforcement. Both tubes provide continuous confinement for the concrete shell, giving it higher strain, strength, and ductility when compared to the concrete of the conventional RC column.

The FRP confinement pressure (f_l) is essential to characterizing the performance of the confined concrete core. Confinement pressure is the lateral pressure exerted by the FRP tube confining the concrete core when the concrete material starts to expand. The confinement pressure and the confinement ratio are calculated as shown below in equations (1) and (2):

$$Confinement\ pressure\ (f_l) = \frac{2\ E_f\ \varepsilon_f\ t_f}{D} \tag{1}$$

$$Confinement\ ratio\ (CR) = \frac{f_l}{f_c'} \tag{2}$$

where E_f is the elastic modulus of the FRP tube in the confinement direction, ε_f is the ultimate tensile strain of the FRP in the confinement direction, t_f is the FRP tube

thickness, D is the column's diameter, and f_c' the characterized unconfined concrete cylindrical strength at 28 days.

HC-FCS columns under axial compression and flexural loading have been investigated (e.g., Abdelkarim and ElGawady 2014a & 2014b; Teng et al. 2005). The previous studies showed that HC-FCS columns have high flexural strength and displacement ductility. According to the writers' best knowledge, no previous studies have been done investigating HC-FCS columns under vehicle impact loading.

Accidents can have serious repercussions with regard to both human life and transportation systems. Throughout the U.S., vehicles colliding with bridge piers have frequently resulted in partial or complete bridge collapse (Harik et al. 1990; Buth et al. 2010; Agrawal 2011). Lee et al. (2013) stated that vehicle collision was the third cause of bridge failures in the United States between the years of 1980 and 2012 because it was the reason of approximately 15% of bridge failures during this period. Numerous researchers have used LS-DYNA software to investigate the modeling of concrete columns under extreme loads such as impact and earthquakes (Abdelkarim and ElGawady 2015a; Abdelkarim and ElGawady 2014b; Sharma et al. 2012; Fouche and Bruneau 2010; Thilakarathna et al. 2010). In the study of vehicle and bridge column collision, there are two main terms to be calculated: the peak dynamic force (PDF) and the equivalent static force (ESF). The PDF is defined as the maximum contact force between the vehicle and the bridge column. However, no consensus exists among researchers with regard to calculating ESF based on PDF. Abdelkarim and ElGawady (2015b) concluded, based on extensive study, that the best approach to calculating ESF is the peak of the twenty-five millisecond moving average (PTMSA).

All of the previous studies examined the behavior of HC-FCS columns under axial, flexural, and combined axial-flexural loading. This paper introduces detailed finite element analyses to investigate the effects of 14 different parameters on both dynamic and static impact forces. Comparisons were also conducted between the ESF of the AASHTO-LRFD (2,670 kN [600 kips]) and the PTMSA. In addition, this study presents a comparison between the HC-FCS column and the RC column under vehicle collision.

Parametric Study

Finite element (FE) modeling of the HC-FCS columns and vehicle collisions with bridge columns were validated in previous studies (Abdelkarim and ElGawady 2014b; Abdelkarim and ElGawady 2015a). A comprehensive parametric study was conducted to investigate the behavior of the HC-FCS columns numerically during a vehicle collision. If the bridge pier was not located inside the clear zone, which means the pier was not shielded by a crashworthy barrier, the design of the pier must include the collision force. The clear zone is the total roadside border area, beginning at the edge of the traveled way, available for safe use by an errant vehicle (AASHTO Roadside Design Guide, 2011). This study investigated unshielded bridge columns under vehicle collision. The distance between the errant vehicle and the unshielded column was 150 mm (0.5 ft). LS-DYNA software was used to examine 14 different parameters, including the following:

- Concrete material model (elastic and nonlinear)
- Unconfined concrete compressive strength (f_c') ranging from 20.7 MPa (3,000 psi) to 69.0 MPa (10,000 psi)
- Material strain rate (SR, both considered and not considered)

- Column height-to-diameter ratio (H/D_o) ranging from 2.5 to 10.0
- Column diameter (D_o) ranging from 1,200 mm (4.0 ft) to 2,100 mm (7.0 ft)
- The FRP confinement ratio ranging from 0.05 to 0.20
- Diameter-to-thickness ratio of the inner steel tube ranging from 50 to 200
- Column void ratio (inner diameter-to-outer diameter ratio) ranging from 0.67 to 0.9
- Embedded length-to-diameter ratio of the steel tube ranging from 1.0 to 2.0
- Steel tube infilled foam (empty, infilled soft foam, and infilled rigid foam)
- Column top boundary condition (free, superstructure, and hinged)
- Axial load level (P/P_o) ranging from 0% to 10%
- Vehicle velocity (v_r) ranging from 32 kph (20 mph) to 112 kph (70 mph)
- Vehicle mass (m) ranging from 2 tons (4.4 kips) to 30 tons (65 kips)

Thirty-four columns (from C0 to C33) were investigated. Column C0 was used as a reference column. The range of selected variables for the columns with regard to the examined parameters is summarized in Table 1. It should be noted that some of the selected parameters may be not common in practice. They were used, however, to fully understand the column's performance under a wide spectrum of parameters. One parameter was investigated in each group, with the rest being kept constant as in the reference column. For example, the parameter of column void ratio changed by changing the diameter of the inner steel tube. As a result, the steel tube thickness changed to result in the same diameter-to-thickness ratio.

Geometry and FE Columns Modeling

The HC-FCS column consisted of an outer glass FRP tube, an inner steel tube, and concrete sandwiched between them. The inner steel tube was extended inside the footing using an embedded length (L_e), while the FRP tube was stopped at the top of the footing. The steel tube was hollow inside. None of the columns included any shear or flexure reinforcement except the steel tube. The columns investigated in this study were supported on a concrete footing that had a fixed boundary at its bottom.

Fig. 1 illustrates the "C0" reference column components. The reference column had an outer diameter (D_o) of 1,500 mm (5.0 ft). It had an inner steel tube with a diameter (D_i) of 1,200 (47.2 in.) and a thickness of 26.7 mm (1.05 in.) with a diameter-to-thickness ratio (D_i/t_s) of 45. The column void ratio, inner-diameter-to-outer-diameter ratio, was 0.8. The embedded length of the steel tube inside the footing (L_e) was 1,800 mm (70.9 in.), representing 1.5 D_i. The thickness of the outer FRP tube was 5.9 mm (0.23 in.) with a confinement ratio of 0.1. The column's height was 7,620 mm (25.0 ft) with a height-to-diameter ratio (H/D_o) of 5.0. The soil depth above the top of the footing (d_s) was 1,000 mm (3.3 ft). The unconfined concrete cylindrical compressive strength (f_c') was 34.5 MPa (5,000 psi). An axial load (P) was applied on the column representing 5% of P_o where P_o is the axial load capacity of the reinforced concrete solid-cross sectional column that had same diameter of the HC-FCS column and had 1% of longitudinal reinforcements. The P_o was calculated as follows (AASHTO-LRFD 2012):

$$P_o = A_s f_y + 0.85\, f_c'(A_c - A_s) \tag{3}$$

where A_s = the cross-sectional area of the longitudinal reinforcement of the reinforced concrete solid-cross sectional column that had same diameter of the HC-FCS column,

A_c = the cross sectional area of the concrete column, f_y = the yield stress of the steel tube, and f_c' = the cylindrical concrete's unconfined compressive stress.

All of the columns except C24 and C25 were hinged at the top ends. Column C24 was free at the top end, while column C25 had a superstructure attached at its top. The bridge superstructure, presented by El-Tawil et al. (2005), was comprised of a composite steel-concrete box girder. Thirty-six Belytschko-Schwer resultant beam-type (ELFORM_2) elements were used to simulate two adjacent steel girders (Fig. 2). This superstructure's transformed steel cross-sectional area was 80,000 mm^2 (124 in^2). The strong moment of inertia (the I_{yy} about the vertical axis) was 8.3×10^{10} mm^4 (2.0×10^5 in^4), and the weak moment of inertia (the I_{zz} about the horizontal axis) was 2.8×10^{10} mm^4 (6.7×10^4 in^4). The superstructure's two unequal spans were 53,340 mm (175 ft) and 50,290 mm (165 ft), respectively. This superstructure was assumed to be pinned at the far ends. The Hughes-Liu beam-type element (ELFORM_2) was used to simulate the bridge bearings located under the superstructure. These bearings were 37 mm (1.5 in.) thick and 200 mm × 200 mm (8 in. × 8 in.) in the cross-section. The bridge bearing's shear modulus was 0.61 MPa (88.0 psi).

One-point quadrature solid elements were used to model each column's concrete core. This type of element assumes constant stress through the element and determines the element's local deformations using an hourglass control. An hourglass control was used to avoid spurious singular modes (e.g., hourglass modes). The hourglass value for each of the models was taken as the default value 0.10 with an hourglass control type_4 (Flanagan-Belytschko stiffness form). A rigid cylinder that was 200 mm (7.9 in.) in height, modeled by solid elements, was placed atop the column to avoid excessive local

damage to the column's top when the axial loads were applied. Solid elements were used to model the concrete footing.

A surface-to-surface type contact element was used to simulate the interface between the concrete column and the FRP tube. These elements were also used between the concrete column and the steel tube and between the foam inside the steel tube and the steel tube. This type of contact considers the slip and separation that occur between master and slave contact pairs. Hence, slip/debonding is displayed if either occurs between the concrete wall's surface and the tube's surface. This type of contact was also used between the concrete footing and the steel tube. Node-to-surface contact elements were used between the bottom edges of the FRP and steel tubes and the concrete footing. The coefficient of friction for all of the contact elements was taken as 0.6 (Abdelkarim and ElGawady 2014b).

Concrete Material Models

The AASHTO-LRFD considers vehicle impact to be an extreme load. Therefore, a column's nonlinear behavior is both expected and allowed. Hence, a nonlinear concrete material model (mat72RIII) was used for all columns and footings in this study except Column C1. Mat72RIII was investigated in previous studies for vehicle collision with reinforced concrete bridge columns (Abdelkarim and ElGawady 2015a). Given f_c' and ω, the yield failure surfaces of this model were generated automatically. The fractional dilation parameter (ω) that takes into consideration any volumetric change occurring in the concrete was taken as the default value of 0.50 (Abdelkarim and ElGawady 2014b).

Loading strain rate may play an essential role in a structure's response. The dynamic increase factor (DIF) is typically used to describe the increase in concrete strength under dynamic loading as compared to static loading (Malvar and Ross 1998; Bischoff and Perry 1991; Williams 1994; Fu et al. 1991). Malvar and Ross (1998) modified the CEB model code for use with strain rate effects as in equations 4 to 11 (CEB-FIP 1990). They implemented these equations into an LS-DYNA format.

$$DIF_c = \frac{f_c}{f_{cs}} = \left(\frac{\dot{\varepsilon}}{\dot{\varepsilon}_s}\right)^{1.026\,\alpha_s} \qquad \text{for } \dot{\varepsilon} \leq 30\ s^{-1} \tag{4}$$

$$DIF_c = \frac{f_c}{f_{cs}} = \gamma_s \left(\frac{\dot{\varepsilon}}{\dot{\varepsilon}_s}\right)^{0.33} \qquad \text{for } \dot{\varepsilon} > 30\ s^{-1} \tag{5}$$

$$\alpha_s = (5 + 9\frac{f_{cs}}{f_{co}})^{-1} \tag{6}$$

$$log\gamma_s = 6.156\,\alpha_s - 2 \tag{7}$$

Where DIF_c = compressive strength dynamic increase factor

$\dot{\varepsilon}$ = strain rate in the range of 30×10^{-6} to 300 s^{-1}

$\dot{\varepsilon}_s$ = static strain rate of 30×10^{-6} s^{-1},

f_c = the dynamic compressive strength at $\dot{\varepsilon}$

f_{cs} = the static compressive strength at $\dot{\varepsilon}_s$

f_{co} = 10 MPa = 1,450 psi

$$DIF_t = \frac{f_t}{f_{ts}} = \left(\frac{\dot{\varepsilon}}{\dot{\varepsilon}_s}\right)^{\delta} \qquad \text{for } \dot{\varepsilon} \leq 1\ s^{-1} \tag{8}$$

$$DIF_t = \frac{f_t}{f_{ts}} = \beta \left(\frac{\dot{\varepsilon}}{\dot{\varepsilon}_s}\right)^{0.33} \qquad \text{for } \dot{\varepsilon} > 1\ s^{-1} \tag{9}$$

$$\delta = (1 + 8\frac{f_{cs}}{f_{co}})^{-1} \tag{10}$$

$$log\ \beta = 6\ \delta - 2 \tag{11}$$

Where DIF_t = tensile strength dynamic increase factor

f_t = the dynamic tensile strength at $\dot{\varepsilon}$

f_{ts} = the static tensile strength at $\dot{\varepsilon_s}$

$\dot{\varepsilon}$ = strain rate in the range of 10^{-6} to 160 s^{-1}

$\dot{\varepsilon_s}$ = static strain rate of 10^{-6} s^{-1}

This research was conducted to investigate the effects of two different concrete material models, including elastic (mat001) and nonlinear (mat72RIII) models, on the HC-FCS bridge column's response under vehicle impact. The elastic material model was investigated because it permits greater convenience in design. The elastic material was used for the concrete core and footing of Column C1. The elastic modulus and Poisson's ratio are the only parameters required to define an elastic material model. These parameters were also used for the rigid material to identify the sliding interface parameters of the contact elements between the vehicle and the column. The elastic modulus (E) was calculated according to ACI-318 (2011) and considered in the dynamic increase factor (DIF) (E = 4,750 $\sqrt{\text{DIF} * f_c'}$). Poisson's ratio was taken as 0.20 (Mehta and Monteiro 2006).

Steel Tube Material Model

An elasto-plastic constitutive model (mat003-plastic_kinamatic) was used for the steel tube. The following five parameters were needed to define this material model: the elastic modulus (E), the yield stress, Poisson's ratio, the tangent modulus, and the ultimate plastic strain. These parameters were assigned the following values: 200 GPa (29,000

ksi); 420.0 MPa (60,900 psi); 0.30; 1,102 MPa (160 ksi); and 0.12, respectively (Caltrans 2006). Cowper-Symonds's (1957) model was adopted (eqn. 12) to examine the strain rate effect. Parameters p and c were assigned as a means for identifying the strain rate effect. Constants p and c were taken as 5 and 40, respectively (Yan and Yali 2012). For example, substituting these two constants into Cowper-Symonds's equation at a strain rate of 100 s^{-1} produced a dynamic yield stress that was 2.20 times the static yield stress. The elastic modulus of the steel did not change considerably under impact loading (Campbell 1954).

$$f_{yd} = 1 + \left(\frac{\dot{\varepsilon}}{c}\right)^{\frac{1}{p}} \tag{12}$$

where $f_{yd} =$ dynamic yield stress and p and c were taken as 5 and 40, respectively.

FRP Tube Material Model

The FRP material used was modeled as an orthotropic material using "054-enhanced composite damage." There are a number of composite material models available in the LS-DYNA library. However, this material model was selected because it correlated well with experimental results of highway guardrail collision (Bank and Gentry 2001). This material is defined by several engineering constants, elastic modulus (E), shear modulus (G), and Poisson's ratio (PR), in the three principle axes (a, b, and c). The fiber orientation was defined by a vector. In addition, the tension and compression FRP strengths were defined. Table 2 summarizes the properties of the FRP tube referenced by the data sheets of the manufacturer "National Oilwell Varco."

Broutman and Rotem (1975) conducted drop weight tests on both uni-directional and cross-ply E-glass/epoxy composites with different geometries. They found that, under a high loading rate, the composite tensile strength increased by approximately 30% for the uni-directional composites and approximately 45% for the cross-ply composites. However, they also found that the energy absorption produced by the high strain rate created a delamination between laminae.

Gama and Gillespie (2011) used LS-DYNA to investigate thick-section composites. This study used four rate parameters to examine the strain rate effect: Crate1, Crate2, Crate3, and Crate4. Crate1 was used for all strength values. Crate2 was used for in-plane Young's moduli. Crate3 was used for all of the shear moduli, and Crate4 was used for the transverse modulus. They found that a close correlation between the experiments and finite element analysis was achieved when (Crate1= Crate3= Crate4) = 0.03 and Crate2 = 0.00. They noted that, when Crate2= 0.00, no change occurred in the in-plane Young's moduli under impact loading. The dynamic properties/static properties could be calculated using Equations 13 to 17. Applying these equations at a strain rate of 104 s-1 (common for impact loading) (Sierakowsi and Chaturved 1997), yielded a dynamic tensile strength that was approximately 28% higher than the static tensile strength, which is compatible with the drop weight studies that were presented earlier.

$$\boldsymbol{E} = \frac{\{E_{RT}\}}{\{E_0\}} = 1 + \{C_{rate}\} \ln \frac{\{\dot{\bar{\varepsilon}}\}}{\dot{\varepsilon_0}} \tag{13}$$

$$\{E_{RT}\} = \{E1\ E2\ E3\ G12\ G31\ G32\}^T \tag{14}$$

$$\left\{\dot{\bar{\varepsilon}}\right\} = \{|\dot{\varepsilon}_1||\dot{\varepsilon}_2||\dot{\varepsilon}_3||\dot{\varepsilon}_{12}||\dot{\varepsilon}_{31}||\dot{\varepsilon}_{32}|\}^T \quad (15)$$

$$\{C_{rate}\} = \{C_{rate1}\ C_{rate2}\ C_{rate4}\ C_{rate3}\ C_{rate3}\ C_{rate3}\}^T \quad (16)$$

$$\dot{\varepsilon_0}\ (reference\ train\ rate) = 1\ s^{-1} \quad (17)$$

Foam Material Model

The steel tube was infilled with soft and rigid foam in Columns C22 and C23, respectively. A material model of low density foam (mat_057) was used to simulate the foam inside the steel tube. The parameters of this material model are the elastic modulus and stress-strain relationship. The material properties of the soft and rigid foam were collected from Tuwair et al. (2015), as shown in Fig. 3.

FE Vehicles Modeling

Two vehicle models were used in this study: a Ford reduced model (35,353 elements) single unit truck (SUT) and a detailed model (58,313 elements) Chevrolet C2500 Pickup (Fig. 4). These models were downloaded from the NCAC website. Experimental tests involving head-on collisions were conducted to validate each model (Zaouk et al. 1996; Mohan et al. 2003). Both models showed high correlation with the experimental results.

Different vehicle speeds were investigated during this research. The vehicle's initial velocities were between 32 kph (20 mph) and 112 kph (70 mph); most had an initial velocity of 80 kph (50 mph). The interface friction between the vehicle and the ground was taken as 0.9. The mass of the vehicle was between 2 tons (4.4 kips) and 30 tons (65 kips); the most was 8 tons (18 kips). The Chevrolet C2500 Pickup was used for the 2-ton

(4.4 kips) mass, and the Ford SUT was used for the remaining models. The Ford SUT's mass was changed by changing the cargo mass. Automatic_surface_to_surface contact elements by parts, with the contact factor SOFT=1, were used between the vehicle and the HC-FCS columns (Bala 2001). The algorithm Automatic_surface_to_surface is penalty-based and was designed to examine each slave node for penetration through the master surface at every time step. Therefore, if any penetration was found between the parts in contact, a nominal interface spring would apply a force proportional to the penetration depth of these interfaces to eliminate the penetration.

Results and Discussion of the Parametric Study

General Performance

The FE results were reliable when the initial kinetic energy completely transformed into internal energy, hourglass energy, and residual kinetic energy (El-Tawil et al. 2005). The hourglass energy was calculated for each model and was lower than 2.5% of the total (Fig. 5). Therefore, the hourglass control did not affect the accuracy of the results. Fig. 6 illustrates the SUT truck's collision with the HC-FCS bridge column "C0" at a time of 0.1 second.

The typical behavior of the time-impact force relationship of the HC-FCS column under vehicle collision is illustrated in Fig. 7. The first peak force occurred when the vehicle's rail collided with the column. The second peak force on the columns, the peak dynamic force (PDF), was produced by the vehicle's engine. The third peak occurred when the vehicle's cargo (in the Ford SUT only) struck the cabinet and the engine. The fourth peak was produced when the rear wheels left the ground. Each of the columns

reached their PDF at nearly the same time (40 milliseconds) and had zero impact force beyond 220 milliseconds. The PDF of the reference column "C0" was 3,025 kN (680 kips). The PTMSA is the equivalent static force of the impact force, which was calculated as the peak twenty-five millisecond moving average of the time-impact force relation. The PTMSA of Column C0 was 2,310 kN (520 kips). The PTMSAs of all of the investigated columns in this study were lower than the equivalent static force of the AASHTO-LRFD of 2,670 kN (600 kips), except when the vehicle's velocity was 112 kph (70 mph) and the vehicle's mass was higher than 16 tons (30 kips). Table 3 summarizes the PDF and PTMSA for all of the investigated columns. Fig. 8 illustrates the typical behavior of the frontal and side deformations of the FRP and steel tubes. The difference in the displacement of FRP and steel tubes, which represent the deformations of the concrete core and FRP tube, was very low. This behavior indicated that the main resistance of the HC-FCS columns to the vehicle collision came from the inner steel tube. Therefore, none of the investigated columns failed due to FRP rupture.

Concrete Material Models

This section investigated the effect of the selection of a concrete material model on the PDF and PTMSA. Two material models, mat72RIII and mat001, representing nonlinear and elastic behavior, were used for this investigation. Fig. 9(a) illustrates the normalized PDF and PTMSA of the columns with elastic and nonlinear materials. The normalized forces are the PDF and the PTMSA divided by the equivalent static force of the AASHTO-LRFD (2012) of 2,670 kN (600 kips). The PDF of Column C1, which was modeled using an elastic material, was approximately 7% higher than that of Column C0,

which was modeled using a nonlinear material. This finding was expected as the energy dissipation in the case of the elastic material is lower than that of the nonlinear material. However, this difference in PDF between Columns C0 and C1 was not significant. The reason for that was the effect of the FRP confinement, which reduced the nonlinear deformation for the material mat72RIII.

Fig. 10 illustrates that the time-impact load relation of the column with elastic concrete material was steeper than that of the column with nonlinear concrete material. In general, this behavior was because the column response is faster in the case of low deformation than in the case of high deformation. As the PTMSA is an average in a specific time increment, it decreases with steep curves, and vice versa. Therefore, the PTMSA of Column C1, which was modeled using elastic material, was approximately 9% lower than that of Column C0, which was modeled using a nonlinear material. However, this difference in PTMSA between the two columns was not significant. Hence, the study in this section reveals that the elastic material could be used for designing HC-FCS columns under vehicle collision for simplicity.

Unconfined Concrete Compressive Strength (f'_c)

Four values of f'_c, ranging from 20.7 MPa (3,000 psi) to 69.0 MPa (10,000 psi), were investigated. Fig. 9(b) illustrates the normalized PDF and PTMSA of the columns with different values of f'_c. The PDF increased by 9%, and the PTMSA decreased by 6%, when the f'_c increased by 233%. This behavior occurred because the high f'_c reduced or delayed the nonlinear deformation that made the curve steeper.

Strain Rate Effect

The strain rate effect was included in Column C0 and excluded in Column C5 for all of the column's components. Fig. 9(c) illustrates the normalized PDF and PTMSA of Columns C0 and C5. The PDF and PTMSA did not significantly change considering the strain rate effect. This behavior occurred because the strain rate was considerably low, which would not significantly change the material properties.

Column Height-To-Diameter Ratio (H/D_o)

Three values of the column height-to-diameter ratio, ranging from 2.5 to 10, were investigated. Fig. 9(d) illustrates the normalized PDF and PTMSA of the columns with different height-to-diameter ratios. The PDF and the PTMSA were almost constant with the changing height-to-diameter ratio. This behavior occurred because the shear forces from the vehicle collision were more dominant rather than flexural as the collision was close to the support.

Column Diameter (D_o)

Four values of the column's diameter, ranging from 1,200 mm (4.0 ft) to 2,100 mm (7.0 ft), were investigated. Fig. 9(e) illustrates the normalized PDF and PTMSA of the columns with different diameters. The PDF of all of the columns, except for Column C8 with a diameter of 1,200 (4.0 ft), was almost constant. The PDF of Column C8, which had a diameter of 1,200 mm (4.0 ft), was approximately 25% higher than that of Column C0, which had a diameter of 1,500 mm (5.0 ft). This behavior occurred because the steel tube of the low-diameter Column, C8, had a high curvature that increased the lateral

resistance of the steel tube. Hence, the steel tube deformation decreased and, as a result, the energy dissipation decreased, leading to a higher PDF. However, the PTMSA was almost constant with the changing column diameter, which agreed with a previous study conducted by Buth et al. (2010).

FRP Confinement Ratio (f_l/f'_c)

Four values of FRP confinement ratios, ranging from 0.05 to 0.2, were investigated. Fig. 9(f) illustrates the normalized PDF and PTMSA of the columns with different FRP confinement ratios. The PDF and PTMSA of all of the columns were almost constant with the changing FRP confinement ratio. This behavior occurred because the concrete stress was lower or slightly higher than the f'_c, as the main resistance was from the steel tube. Hence, the FRP confinement had almost no effect on the PDF or PTMSA, but it saved the concrete core from spalling.

Diameter-To-Thickness Ratio of the Steel Tube (D_i/t_s)

Five values of diameter-to-thickness (D_i/t_s) ratios for the steel tube, ranging from 50 to 200, were investigated. Fig. 11(a) illustrates the normalized PDF and PTMSA of the columns with different diameter-to-thickness ratios of the steel tube. The PDF decreased nonlinearly by approximately 21% when the D_i/t_s of the steel tube increased by 300%. This behavior occurred because the higher D_i/t_s of the steel tube led to a higher steel tube deformation and a higher energy dissipation. However, the PTMSA was almost constant with the changing D_i/t_s of the steel tube. This behavior occurred because the time-impact

load relation of the column with a low D_i/t_s of the steel tube was steeper than that of the column with a high D_i/t_s of the steel tube (Fig. 12).

Column Void Ratio (D_i/D_o)

Three values of column void ratios (D_i/D_o), ranging from 0.67 to 0.9, were investigated. Fig. 11(b) illustrates the normalized PDF and PTMSA of the columns with different column void ratios. The PDF decreased nonlinearly by approximately 22% when the column void ratio increased by 34%. This behavior occurred because of the effect of the steel tube curvature. The steel tube was flatter for the case of the high void ratio than that of the low void ratio. Hence, the steel tube deformation increased when the steel tube diameter increased. As a result, the energy dissipation increased, leading to a lower PDF. However, the PTMSA increased almost linearly when the column void ratio increased by 34%. This behavior occurred because the time-impact load relation of the column with a low D_i/D_o was steeper than that of the column with a high D_i/D_o (Fig. 13).

Embedded Length-To-Diameter Ratio of Steel Tube (L_e/D_i)

Three values of embedded length-to-diameter (L_e/D_i) ratios of the steel tube, ranging from 1 to 2, were investigated. Fig. 11(c) illustrates the normalized PDF and PTMSA of the columns with different column void ratios. The PDF and PTMSA were almost constant with the changing embedded length. This behavior occurred because the shear forces from the vehicle collision were more dominant rather than flexural as the vehicle collision was close to the support.

Steel Tube Infilled Foam

The steel tube was infilled with soft and rigid foam in Columns C22 and C23, respectively, and the results were compared with those of Column C0 which had an empty steel tube. Fig. 11(d) illustrates the normalized PDF and PTMSA of the columns with different column void ratios. The PDF increased slightly when the steel tube was infilled with foam. This behavior occurred because the infilled foam reduced the steel tube deformation. Figs. 14 and 15 illustrate the frontal and side deformations of the steel tube for the columns with infilled soft and rigid foams, respectively. The frontal deformation of the steel tube was reduced by 3% and 33% when it was infilled with soft and rigid foam, respectively. The side deformation of the steel tube was reduced by 2.5% and 48% when it was infilled with soft and rigid foam, respectively. The PTMSA decreased when the steel tube was infilled with foam. This behavior occurred because the time-impact load relation of the column with the steel tube infilled with foam was steeper than that of the column with an empty steel tube.

Top Boundary Conditions

Three of the column's top boundary conditions, including free, hinged, and superstructure, were investigated. Fig. 11(e) illustrates the normalized PDF and PTMSA of the columns with different top boundary conditions. Changing the column's top boundary condition changed the PDF values slightly because the PDF was induced in a very short period of time. This behavior occurred because the impact loading occurred in a very short time. Hence, the structure did not have enough time to respond. This result is compatible with the study by Chopra (2012) on the pulse shape. If the pulse duration is

much shorter than the natural period (as in impact loading), the structure's response is mainly controlled by the total kinetic energy. However, the maximum lateral displacement of Column C22, which had a free top boundary condition, was significantly higher than those of Columns C0 and C23, which had hinged and superstructure top conditions, respectively. The existence of the superstructure in Column C23 resulted in a top boundary condition similar to that in column C0. The PTMSA was almost constant with the column's changing top boundary condition.

Axial Load Level

Three values of axial load levels, ranging from 0 to 10% of the axial capacity (P_o) of a same diameter reinforced concrete column with a longitudinal reinforcement ratio of 1%, were investigated. Fig. 11(f) illustrates the normalized PDF and PTMSA of the columns with different axial load levels. The PDF and PTMSA were almost constant with the changing axial load level. This behavior occurred because the axial stresses coming from an axial load would mainly be applied on the concrete core with insignificant stresses on the steel tube, because the axial stiffness of the concrete core is much higher than that of the steel tube. However, the vehicle collision was mainly resisted by the steel tube. Therefore, the axial load level did not affect the PDF or the PTMSA for the HC-FCS columns.

Vehicle Velocity

Four vehicle velocities, ranging from 32 kph (20 mph) to 112 kph (70 mph), were investigated. Fig. 16(a) illustrates the normalized PDF and PTMSA of the columns with

different vehicle velocities. The PDF tended to increase nonlinearly when the vehicle's velocity increased. It is of interest that the increase in the PDF is not proportional to the square of the velocity, as in the case of elastic impact problems. Damage to the columns reduced the rate of increase in the PDF. For example, the PDF increased by approximately 200% when the vehicle's velocity increased from 32 kph (20 mph) to 112 kph (70 mph). The PTMSA increased almost linearly by 140% when the vehicle's velocity increased from 56 kph (35 mph) to 112 kph (70 mph). However, the PTMSA was almost constant when the vehicle's velocity increased from 32 kph (20 mph) to 56 kph (35 mph) because the kinetic energy of both cases was considerable. The AASHTO-LRFD under-predicted the equivalent static force when the column was collided with by a high-speed vehicle at a velocity of 112 kph (70 mph). The PTMSA was almost 1.2 times the equivalent static force of the AASHTO-LRFD of 2,670 kN (600 kips) when the column was collided with by a high-speed vehicle at a velocity of 112 kph (70 mph).

Vehicle Mass

Four vehicle masses, ranging from 2 tons (4.4 kips) to 30 tons (65 kips), were investigated. Fig. 16(b) illustrates the normalized PDF and PTMSA of the columns with different vehicle velocities. In general, both the PDF and ESF increased linearly when the vehicle's mass increased. However, the rate of increase was slower than anticipated in elastic impact problems. For example, the PDF increased by approximately 86% when the vehicle's mass increased from 2 tons (4.4 kips) to 30 tons (65 kips). The PDF barely changed when the vehicle's mass increased from 2 tons (4.4 kips) to 8 tons (18 kips) because the energy dissipation, in the form of inelastic deformations, whether in the vehicle or in the column, did not significantly change as the kinetic energy was not

considerably high. The PTMSA increased almost linearly by approximately 410% when the vehicle mass increased from 2 tons (4.4 kips) to 30 tons (65 kips). The AASHTO-LRFD under-predicted the equivalent static force when the column was collided with by the heavy vehicle with a mass greater than 16 tons (35 kips). The PTMSA was almost 2.1 times the equivalent static force of the AASHTO-LRFD of 2,670 kN (600 kips) when the column was collided with by a heavy vehicle with a mass of 30 tons (65 kips).

Comparison between HC-FCS and RC Columns

The column C16 was compared, under vehicle collision with a reinforced concrete (RC) column with the same flexural strength. Both columns had the superstructure of the column C25. The longitudinal steel reinforcement of the RC column was 24 D35 (24 #11) representing up to 1.25% of the concrete cross-sectional area. The RC column's hoop reinforcement was 5 D16 (5 #5). Modeling of the RC column was explained in Abdelkarim and ElGawady (2015a). The RC and HC-FCS columns were collided with by a Ford F800 single unit truck (SUT) with three different velocities of 112 kph (70 mph), 80 kph (50 mph), and 32 kph (20 mph).

Fig. 17 illustrates the PDF and PTMSA of the investigated columns. The PDF of the HC-FCS column was lower than that of the RC column by approximately 40% and 28% when it was collided with by a vehicle with a velocity of 112 kph (70 mph) and 80 kph (50 mph), respectively (Fig. 17a). However, the PDFs of the HC-FCS and RC columns were almost the same when they were collided with by a vehicle travelling with a velocity of 32 kph (20 mph). The PTMSA of the HC-FCS column was lower than that of the RC column by approximately 20% when it was collided with by a vehicle with a

velocity of 112 kph (70 mph) (Fig. 17b). However, the PTMSAs of the HC-FCS and RC columns were almost the same when they were collided with by a vehicle travelling with a velocity of 80 kph (50 mph) or 32 kph (20 mph). Hence, the equation (18) to estimate the ESF of vehicle collision with bridge column as presented by Abdelkarim and ElGawady (2015b) would be applicable for HC-FCS columns when struck by vehicles traveling with velocities of up to 80 kph (50 mph). After this speed, the equation overestimates the ESF of vehicle collisions with the HC-FCS columns.

$$KEB_{ESF} = 33\sqrt{m\ v_r^2} = 46\sqrt{KE} \tag{18}$$

where m = the vehicle mass in ton, v_r = the vehicle velocity in m/s, and KE = kinetic energy of the vehicle in kN.m.

The concrete spalling occurred during the vehicle collision with the RC column because of the high local strain. However, the FRP tube in the HC-FCS column protected the concrete from spalling and increased the ultimate compressive strain by approximately 5 times than that of the RC column.

Summary and Findings

The behavior of the HC-FCS columns under vehicle collision was presented. The peak dynamic force (PDF) and the equivalent static force (ESF) were evaluated through an extensive parametric study. The ESF was defined as the peak of the 25 millisecond moving average (PTMSA). The extensive parametric study investigated the effects of 14 different parameters: the concrete material model, the unconfined concrete compressive strength (f_c'), the material strain rate, the column height-to-diameter ratio, the column

diameter, the FRP confinement ratio, the diameter-to-thickness ratio of steel tube, the column void ratio, the embedded length of the steel tube, the infilled steel tube, the top boundary conditions, the axial load level, the vehicle's velocity, and the vehicle's mass on both dynamic and static impact forces. This study revealed the following findings:

1. The main resistance of the HC-FCS columns to the vehicle collision came from the inner steel tube.
2. The AASHTO-LRFD was found to be non-conservative when the column was collided with heavy vehicles that weigh more than 16 tons (35 kips) at speeds greater than 112 kph (70 mph).
3. For simplicity, the elastic material could be used to design HC-FCS columns under vehicle collision.
4. The frontal deformation of the steel tube was reduced by 3% and 33% when it was infilled with soft and rigid foams, respectively. The side deformation of the steel tube was reduced by 2.5% and 48% when it was infilled with soft and rigid foam, respectively.
5. Generally, the PDF increased when the f_c', vehicle velocity and vehicle mass increased and when the steel tube was infilled with foam. It decreased when the diameter-to-thickness ratio of the steel tube and the column void ratio increased. However, it was not affected by changing the strain rate effect, column height-to-diameter ratio, column outer diameter, FRP confinement ratio, steel tube embedded length, top boundary condition of the column, or axial load level.
6. Generally, the PTMSA increased when the column void ratio, vehicle velocity, and vehicle mass increased. It decreased when the f_c' increased and when the steel tube was infilled with foam. However, it was not affected by changes to the strain

rate effect, column height-to-diameter ratio, column outer diameter, FRP confinement ratio, diameter-to-thickness ratio of the steel tube, steel tube embedded length, top boundary condition of the column, or axial load level.

7. The PDF of the HC-FCS column was lower than that of the RC column by approximately 40% and 28% when it was collided with by a vehicle at a velocity of 112 kph (70 mph) and 80 kph (50 mph), respectively.
8. The PDFs of the HC-FCS and RC columns were almost the same when they were collided with by a vehicle travelling with a velocity of 32 kph (20 mph).
9. The PTMSA of the HC-FCS column was lower than that of the RC column by approximately 20% when it was collided with by a vehicle with a velocity of 112 kph (70 mph).
10. The PTMSAs of the HC-FCS and RC columns were almost the same when they were collided with by vehicles travelling with velocities of 80 kph (50 mph) or 32 kph (20 mph).
11. The equation ($KEB_{ESF} = 33\sqrt{m\, v_r^2} = 46\sqrt{KE}$) to estimate the ESF of a vehicle's collision with a bridge column as presented by Abdelkarim and ElGawady (2015b) would be applicable for the HC-FCS columns struck by a vehicle with a velocity of up to 80 kph (50 mph). After this speed, the equation overestimates the ESF of collision with the HC-FCS columns.

Acknowledgement

This research was conducted at Missouri University of Science and Technology and was partially supported by Missouri Department of Transportation (MoDOT) and Mid-

American Transportation Center (MATC). Their support is gratefully appreciated. However, any opinions, findings, conclusions, and recommendations presented in this paper are those of the authors and do not necessarily reflect the views of sponsors.

References

AASHTO, (2012). AASHTO-LRFD Bridge Design Specifications – Customary US Units, sixth edition, Washington, DC.

Abdelkarim, O., Gheni, A., Anumolu, S., Wang, S., ElGawady, M. (2015). "Hollow-Core FRP-Concrete-Steel Bridge Columns under Extreme Loading." Missouri Department of Transportation (MoDOT), Project No. TR201408, Report No. cmr15-008, April.

Abdelkarim, O. and ElGawady, M. (2014a). "Behavior of Hybrid FRP-Concrete-Steel Double-Skin Tubes Subjected to Cyclic Axial Compression." Structures Congress 2014: pp. 1002-1013.

Abdelkarim, O. and ElGawady, M. (2014b). "Analytical and Finite-Element Modeling of FRP-Concrete-Steel Double-Skin Tubular Columns." J. Bridge Eng. , 10.1061/(ASCE)BE.1943-5592.0000700 , B4014005.

Abdelkarim, O. and ElGawady, M. (2015a). "Impact Analysis of Vehicle Collision with Reinforced Concrete Bridge Columns." Transportation Research Board (TRB) conference, Washington Dc, 15-4461.

Abdelkarim, O. and ElGawady, M. (2015b). "Vehicle Collision with Reinforced Concrete Bridge Columns." Proceedings of the Fifth International Workshop on Performance, Protection & Strengthening of Structures under Extreme Loading, Michigan, June, pp. 628-635.

ACI Committee 318 (2011). "Building Code Requirements for Structural Concrete (ACI318-11) and Commentary (318R-11)." American Concrete Institute, Farmington Hills, Mich., pp. 509.

Agrawal, A.K. (2011). "Bridge Vehicle Impact Assessment: Final Report." University Transportation Research Center and New York State Department of Transportation.

Bala, S. (2001). "Contact Modeling in LS-DYNA." Livermore Software Technology Corporation.

Bank, L. C. and Gentry, T. R. (2001). "Development of a pultruded composite material highway guardrail." Composites Part A: Applied Science and Manufacturing, 32(9), 1329-1338.

Bischoff, P.H., Perry, S.H., "Compressive Behavior of Concrete at High Strain Rates." Materials and Structures, Vol. 24, 1991, pp. 425-450.

Broutman, L. J., and Rotem. A. (1975). "Impact strength and toughness of fiber composite materials." Foreign Object Impact Damage to Composites: pp. 114-133.

Buth, C. E., Williams, W. F., Brackin, M. S., Lord, D., Geedipally, S. R., and Abu-Odeh, A. Y. (2010). "Analysis of Large Truck Collisions with Bridge Piers: Phase 1." Texas Department of Transportation Research and Technology Implementation Office, 9-4973-1.

California Department of Transportation. (2006). "Seismic Design Criteria." California Department of Transportation, Rev. 1.4.

Campbell, J.D. (1954). "The yield of mild steel under impact loading." Journal of the Mechanics and Physics of Solids, 3, 54-62.

Chopra, A. K. (2012). "Dynamics of Structures- Theory and Applications to Earthquake Engineering." Prentice Hall, Upper Saddle River, NJ, USA.

Comité Euro-International du Béton. (1993). "CEB-FIP Model Code 1990." Redwood Books, Trowbridge, Wiltshire, UK.

Cowper, G. R. and Symonds, P. S. (1957). "Strain Hardening and Strain Rate Effects in Impact Loading of Cantilever Beams." Brown University, App. Math. Report No. 28.

El-Tawil, S., Severino, E., and Fonseca, P. (2005). "Vehicle Collision with Bridge Piers." J. Bridge Eng., 10(3), 345-353.

Fam, A., Flisak, B., Rizkalla, S. (2003). "Experimental and analytical modeling of concrete-filled fiber-reinforced polymer tubes subjected to combined bending and axial loads." ACI Structural Journal, 100 (4), pp. 499-509.

Fouche, P., Bruneau, M. (2010). "Non-Linear Analysis of Multi-Hazard Performance of Cylindrical Concrete Filled Steel Tubes Bridge Piers." Proceedings of 8th International Conference on Short and Medium Span Bridges, Canada.

Fu, H.C., Erki, M.A., Seckin, M. (1991). "Review of Effects of Loading Rate on Reinforced Concrete." Journal of Stru. Eng., Vol. 117, No. 12, December, pp. 3660-3679.

Gama, BA., Gillespie, JW. (2011). "Finite element modeling of impact, damage evolution and penetration of thick-section composites." International Journal of Impact Engineering, 38 (4), pp. 181-197.

Hajjar J. (2000). "Concrete-filled steel tube columns under earthquake loads." Structural Engineering and Materials; 2(1):72–82.

Harik, I., Shaaban, A., Gesund, H., Valli, G., and Wang, S. (1990). "United States Bridge Failures, 1951–1988." J. Perform. Constr. Facil., 4(4), 272–277.

Lee, G. C., Mohan, S., Huang, C., and Fard, B. N. (2013). "A Study of US Bridge Failures (1980-2012)." MCEER Technical Report 13-0008, Buffalo, NY.

LS-DYNA; "theory manual for version 971." (2006). Livermore Software Technology Corporation.

Malvar, L. J. and Ross, C. A. (1998). "Review of Strain Rate Effects for Concrete in Tension." ACI Materials Journal, 95, 735-739.

Malvar, L., Crawford, J., Wesevich, J., and Simons, D. (1997). "A plasticity concrete material model for DYNA3D." Int. J. Impact Eng., 19(9–10), 847–873.

Mehta, K.P., Monteiro, P.J.M. (2006). "CONCRETE: Microstructure, Properties, and Materials." 3rd Edition, McGraw-Hill Inc., United States of America, pp. 660.

Mohan, P., Marzougui, D., Kan, C. (2003). "Validation of a Single Unit Truck Model for Roadside Hardware Impacts." NCAC, the George Washington University.

Montague, P., (1978). "Experimental behavior of double-skinned, composite, circular cylindrical-shells under external-pressure." Journal of Mechanical Engineering Science, 20(1), pp. 21–34.

Moon, J., Lehman, D. E., Roeder, C. W., and Lee, H. E. (2013). "Strength of Circular Concrete-Filled Tubes with and without Internal Reinforcement under Combined Loading." Journal of Structural Engineering, 139(12).

Qasrawi, Y., Heffernan, P. J., & Fam, A. (2014). "Performance of Concrete-Filled FRP Tubes under Field Close-in Blast Loading." J. Compos. Constr., 10.1061/(ASCE)CC.1943-5614.0000502 , 04014067.

Roadside Design Guide. (2011). "American Association of State Highway and Transportation Officials." Washington, DC.

Sadeghian, P. and Fam, A. (2010). "Bond-Slip Analytical Formulation toward Optimal Embedment of Concrete-Filled Circular FRP Tubes into Concrete Footings." J. Eng. Mech., 136(4), 524–533.

Shakir-Khalil, H., and Illouli, S. (1987). "Composite columns of concentric steel tubes." Proc., Conf. on the Design and Construction of Non-Conventional Structures, Vol. 1, London, pp. 73–82.

Sharma, H., Hurlebaus, S., Gardoni, P. (2012). "Performance-based response evaluation of reinforced concrete columns subject to vehicle impact." Inter. Journal of Impact Eng., (43), 52-62.

Shao, Y. and Mirmiran, A. (2005). "Experimental Investigation of Cyclic Behavior of Concrete-Filled Fiber Reinforced Polymer Tubes." J. Compos. Constr., 9(3), 263–273.

Sierakowsi, R. L. and Chaturved, S. K. (1997). "Dynamic Loading and Characterization of Fiber-Reinforced Composites." John Wiley & Sons, Inc., New York, USA.

Teng, J.G., Yu, T., and Wong, Y.L. (2004). "Behavior of Hybrid FRP-Concrete-Steel Double-Skin Tubular Columns." Proc. 2nd Int. Conf. on FRP Composites in Civil Engineering, Adelaide, Australia, 811-818.

Teng, J.G., Yu, T., Wong, Y.L., and Dong, S.L. (2005). "Innovative FRP-Steel-Concrete Hybrid Columns." Advances in Steel Structures, 1, 545-554.

Thilakarathna, H.M.I., Thambiratnam, D.P., Dhanasekar, M., Perera, N. (2010). "Numerical simulation of axially loaded concrete columns under transverse impact and vulnerability assessment." Inter. Journal of Impact Eng., (37), 1100-1112.

Tuwair, H., Hopkins, M., Volz, J., ElGawady, M. A., Mohamed, M., Chandrashekhara, K., & Birman, V. (2015). "Evaluation of sandwich panels with various polyurethane foam-cores and ribs." Composites Part B: Engineering, 79, 262-276.

Williams, M.S. (1994). "Modeling of Local Impact Effects on Plain and Reinforced Concrete." ACI Structural Journal, Vol. 91, No. 2, March-April, pp. 178-187.

Yan, X. and Yali, S. (2012). "Impact Behaviors of CFT and CFRP Confined CFT Stub Columns." J. Compos. Constr., 16(6), 662–670.

Zaouk, A. K., Bedewi, N. E., Kan, C. D., and Marzoughi, D. (1996). "Evaluation of a Multi-purpose Pick-up Truck Model Using Full Scale Crash Data with Application to Highway Barrier Impact." 29th Inter. Sym. on Auto. Tech. and Auto., Florence, Italy.

Zhang, B., Teng, J. G. and Yu, T. (2012). "Behaviour of hybrid double-skin tubular columns subjected to combined axial compression and cyclic lateral loading." Sixth International Conference on FRP Composites in Civil Engineering (pp. 1-7). Rome, Italy.

Zhang, W. and Shahrooz, B. M. (1997). "Analytical and Experimental Studies into Behavior of Concrete-Filled Tubular Columns." Report No. UC-CII 97/01, Cincinnati Infrastructure Institute, Department of Civil and Environmental Engineering, University of Cincinnati, College of Engineering, Cincinnati, Ohio, May.

Zhu, Z., Ahmad, I., and Mirmiran, A. (2006). “Seismic performance of concrete-filled FRP tube columns for bridge substructure.” J. Bridge Eng., 11(3), 359–370.

Table 1. Summary of the examined columns' parameters

Column	Concrete Material	f_c', MPa (psi)	SR	H/D_o	D_o, m (ft)	CR	D_i/t_s steel tube ratio	Void ratio (D_i/D_o)	Steel Tube embedded length (L_e/D_i)	Steel tube infilled	Top Boundary Condition	Axial load level of P_o	V_c, kph (mph)	m, ton (kip)
C0	Nonlinear	34.5 (5,000)	C	5	1.5 (5.0)	0.1	75	0.8	1.5	Empty	Hinged	5%	80 (50)	8 (18)
C1	Elastic													
C2	Nonlinear	20.7 (3,000)												
C3		48.3 (7,000)												
C4		69.0 (10,000)												
C5		34.5 (5,000)	N.C.											
C6			C	2.5										
C7				10										
C8				5	1.2 (4.0)									
C9					1.8 (6.0)									
C10					2.1 (7.0)									
C11					1.5 (5)	0.05								
C12						0.15								
C13						0.2								
C14						0.1	50							
C15							100							
C16							150							
C17							200							

Table 1. Summary of the examined columns' parameters (cont'd)

C18	Nonlinear	34.5 (5,000)	C	5	1.5 (5)	0.1	75	0.67	1.5	Empty	Hinged	5%	80 (50)	8 (18)
C19								0.9						
C20								0.8	1					
C21									2					
C22									1.5	Soft foam				
C23										Rigid foam				
C24										Empty	Free			
C25											Superstructure			
C26											Hinged	0%		
C27												10%		
C28												5%	112 (70)	
C29													56 (35)	
C30													32 (20)	
C31													80 (50)	2 (4.4)
C32														16 (35)
C33														30 (65)

D_o = column diameter, D_i = steel tube diameter, H = column height, L_e = steel tube embedded length, CR = FRP confinement ratio, SR = strain rate, NC = Not Considered, C = Considered, v_r = vehicle velocity, m = vehicle mass.

Table 2. FRP tubes properties

	Axial compression elastic modulus (E_a, GPa (ksi))	Axial ultimate stress (f_{ar}, MPa, psi))	Hoop elastic modulus (E_h, GPa, ksi))	Hoop rupture stress (f_{hr}, psi)
FRP tube	4.7 (677)	83.8 (12,150)	20.8 (3,020)	276.9 (40,150)

Table 3. Summary of the FE results

Variables		Column	Forces		Normalized forces	
Parameter	Value		PDF (kN)	PTMSA (kN)	PDF	PTMSA
Concrete material model	Nonlinear	C0	3,027	2,310	1.13	0.87
	Elastic	C1	3,231	2,121	1.21	0.79
f'c (MPa)	20.7	C2	2,840	2,250	1.06	0.84
	48.3	C3	3,001	2,106	1.12	0.79
	69.0	C4	3,106	2,108	1.16	0.79
Strain rate effect	Not considered	C5	2,892	2,187	1.08	0.82
Height-to-diameter ratio	2.5	C6	2,957	2,122	1.11	0.79
	10	C7	3,106	2,101	1.16	0.79
Column diameter (m)	1.2	C8	3,753	2,438	1.41	0.91
	1.8	C9	3,124	2,385	1.17	0.89
	2.1	C10	3,137	2,193	1.17	0.82
FRP confinement ratio	0.05	C11	2,858	2,182	1.07	0.82
	0.15	C12	2,941	2,087	1.10	0.78
	0.20	C13	2,979	2,204	1.12	0.83
Steel tube D_i/t_s ratio	50	C14	3,266	2,154	1.22	0.81
	100	C15	2,751	2,184	1.03	0.82
	150	C16	2,755	2,292	1.03	0.86
	200	C17	2,700	2,224	1.01	0.83
Void ratio (D_i/D)	0.67	C18	3,439	1,998	1.29	0.75
	0.90	C19	2,823	2,303	1.06	0.86
Steel tube embedded length-to-steel diameter	1.0	C20	2,904	2,179	1.09	0.82
	2.0	C21	2,907	2,257	1.09	0.85
Steel tube infilled	Soft foam	C22	2,983	2,162	1.12	0.81
	Rigid foam	C23	3,158	2,094	1.18	0.78
Top boundary condition	Free	C24	2,853	2,310	1.07	0.87
	Superstructure	C25	2,882	2,172	1.08	0.81
Axial load level	No load	C26	2,901	2,153	1.09	0.81
	10% of P_o	C27	2,963	2,177	1.11	0.82
Vehicle velocity (kph)	112	C28	5,199	3,153	1.95	1.18
	56	C29	2,174	1,336	0.81	0.50
	32	C30	1,752	1,316	0.66	0.49
Vehicle mass (ton)	2	C31	3,480	1,080	1.30	0.40
	16	C32	5,152	4,532	1.93	1.70
	30	C33	6,463	5,489	2.42	2.06

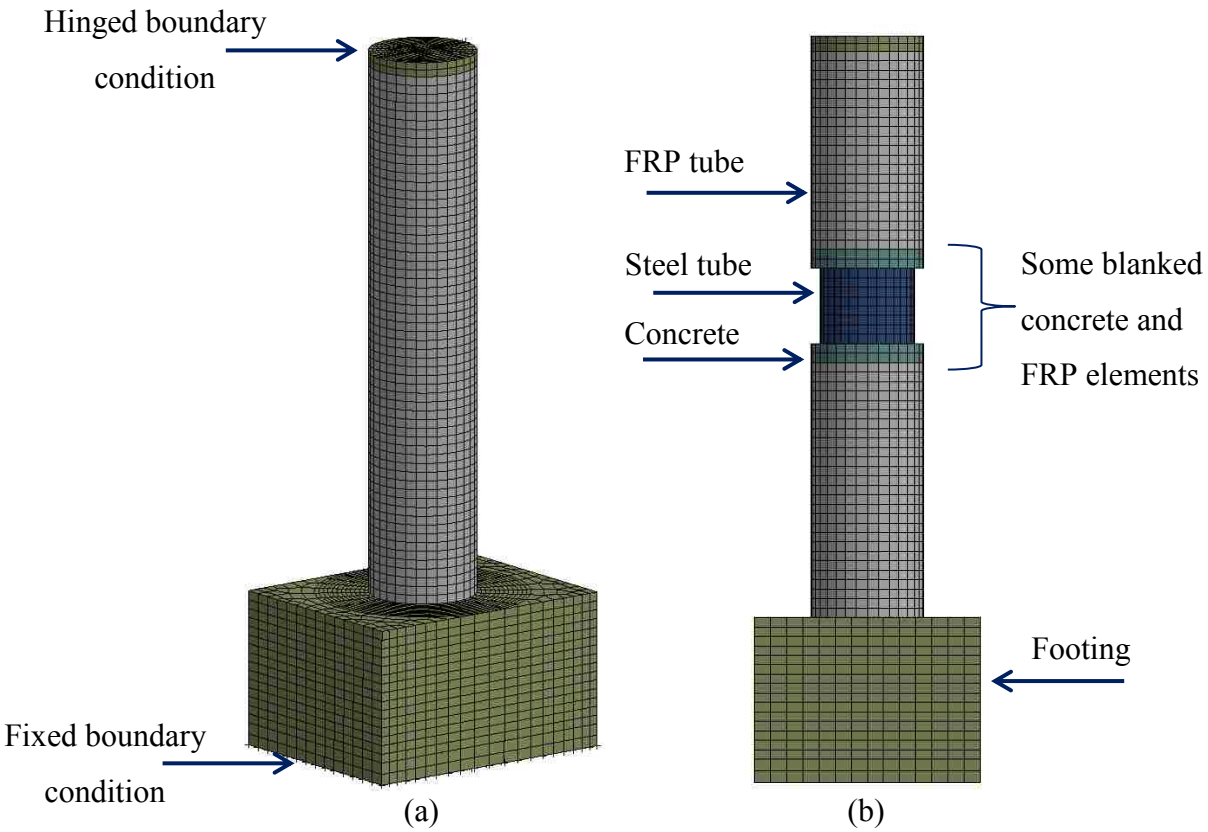

Fig. 1. FE model of the bridge column "C0" for the parametric study: (a) 3D-view, (b) detailed side view of the column components

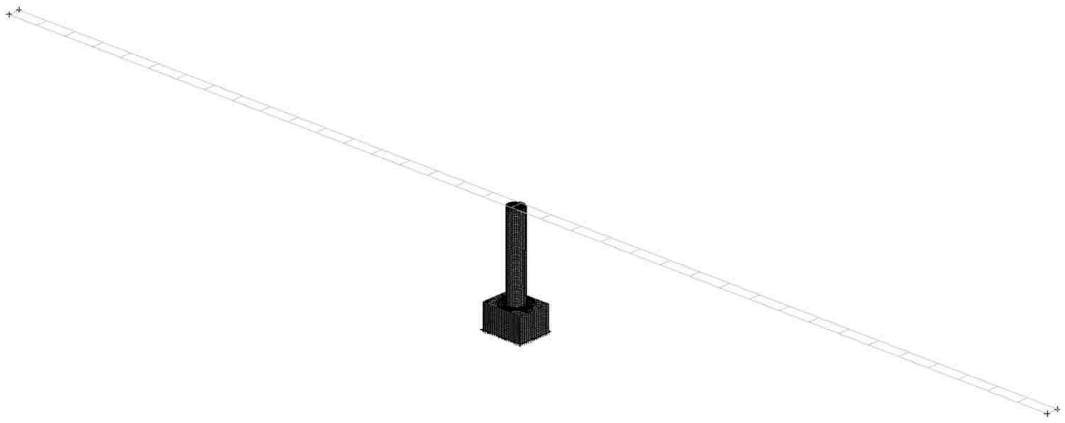

Fig. 2. 3-D view of the column C25 with superstructure

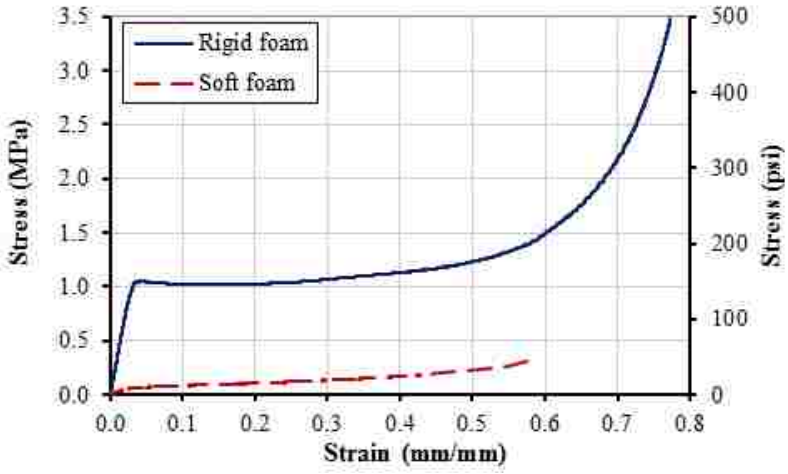

Fig. 3. Stress-strain relationship of the rigid and soft foams (Tuwair et al. 2015)

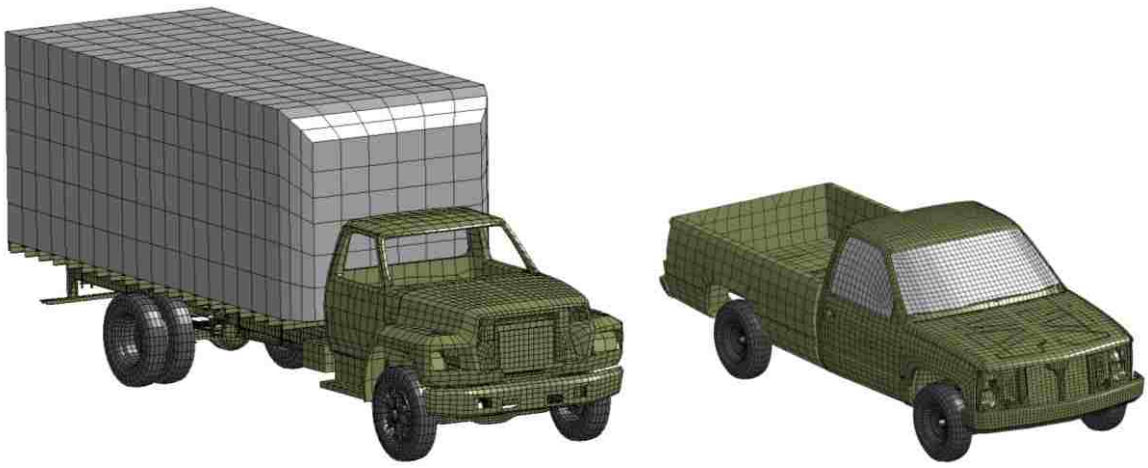

(a) (b)

Fig. 4. 3D-view of the FE model: (a) the Ford single unit truck, (b) Chevrolet pickup detailed model

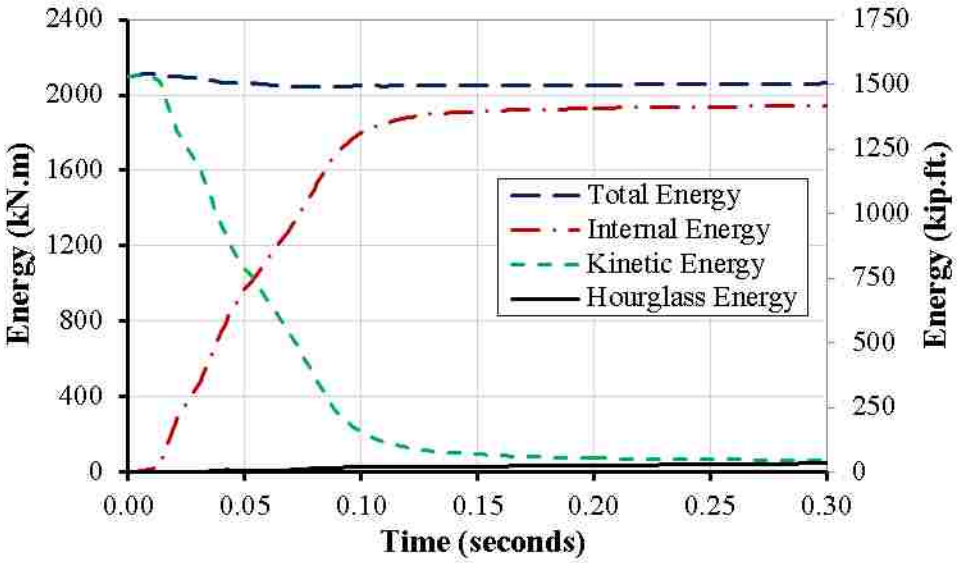

Fig. 5. Time-energies relations of the FE model C0

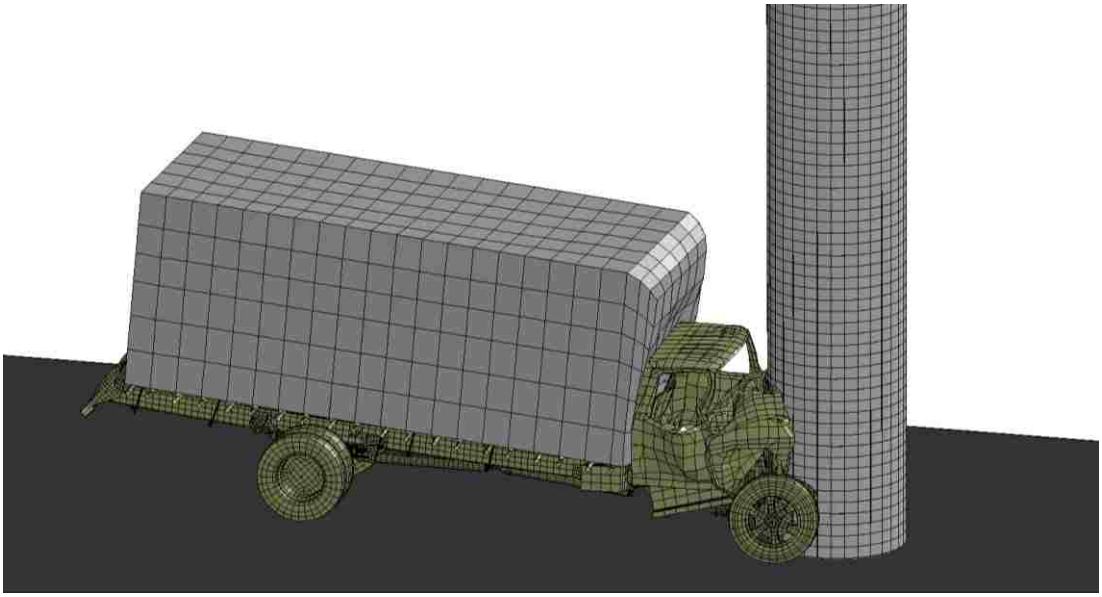

Fig. 6. Vehicle collision with the HC-FCS column at 0.1 second

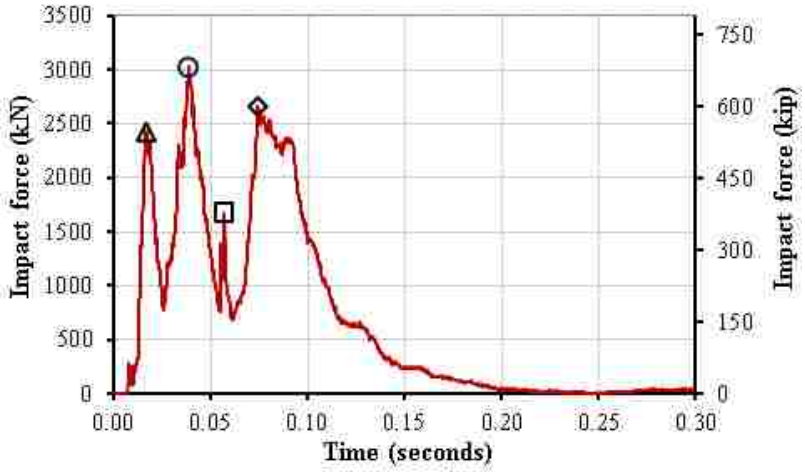

Fig. 7. Time-Impact force of the vehicle collision with the column C0

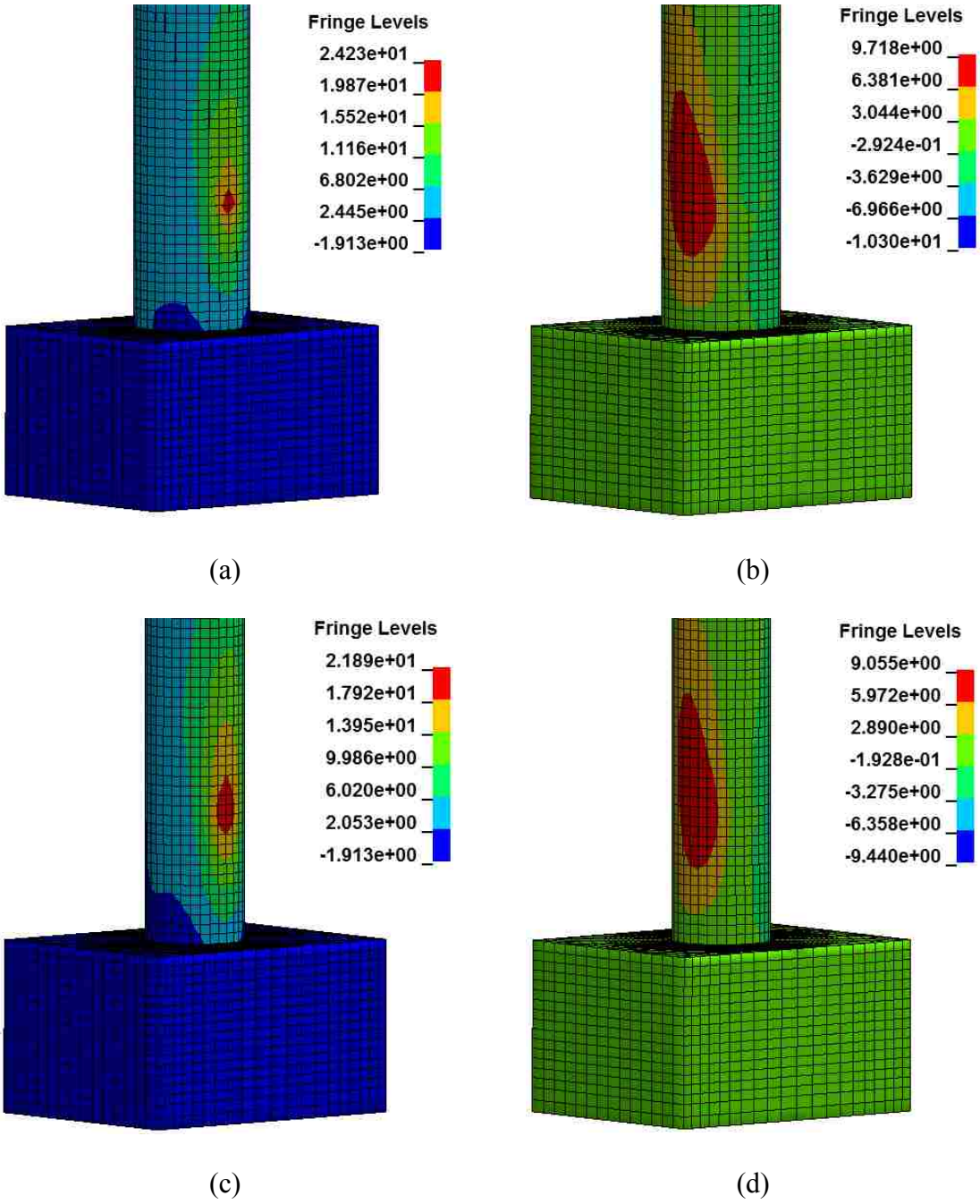

Fig. 8. Column C0 displacement contours of: (a) FRP head-on direction, (b) FRP side direction, (c) steel head-on direction, and (d) steel side direction at time of the PDF of 0.04 second, units are in mm (1 mm = 0.04 inch)

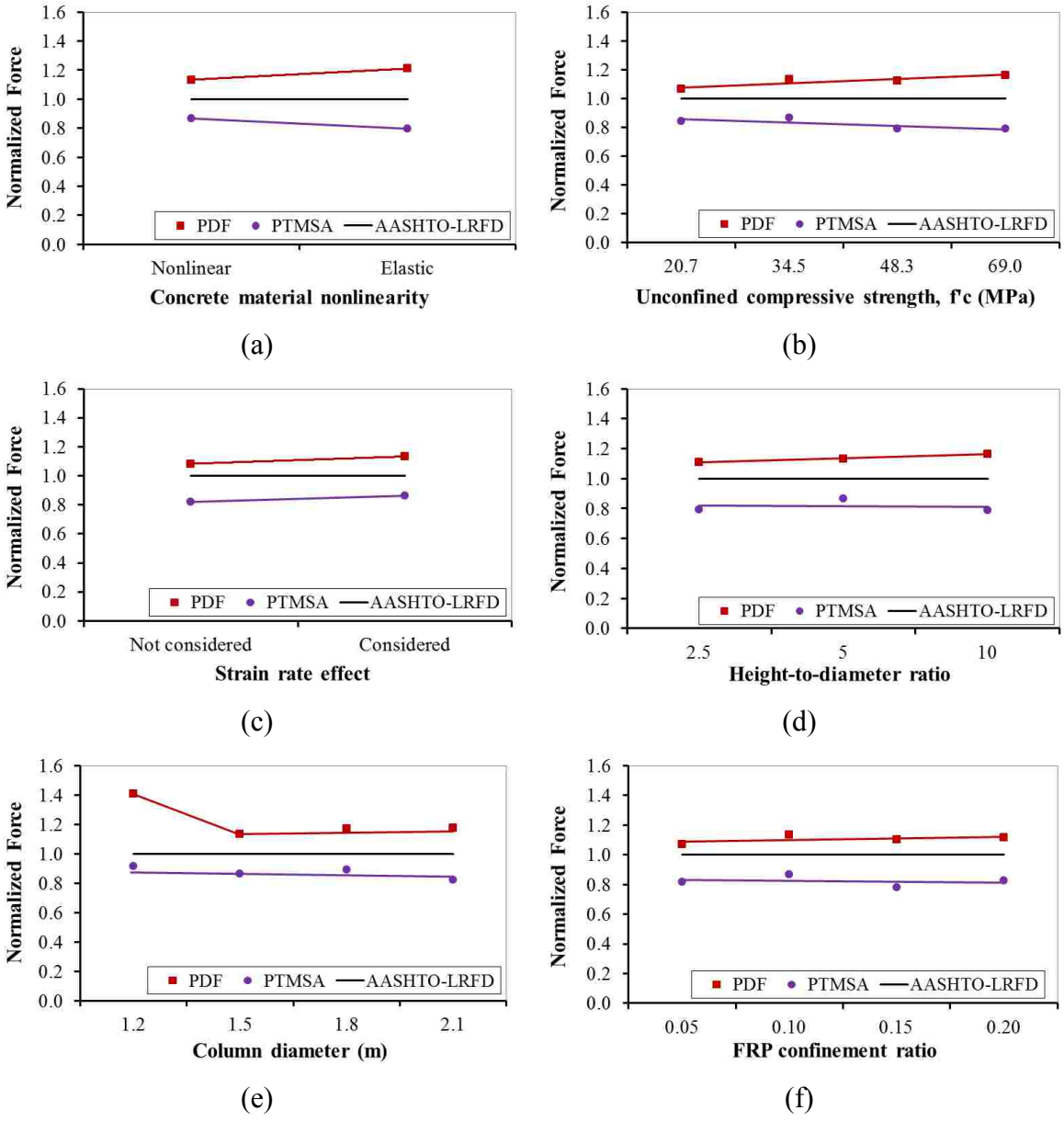

Fig. 9. Effects of (a) concrete material nonlinearity, (b) f_c', (c) strain rate, (d) height-to-diameter ratio, (e) column diameter, and (f) FRP confinement ratio on PDF and ESF

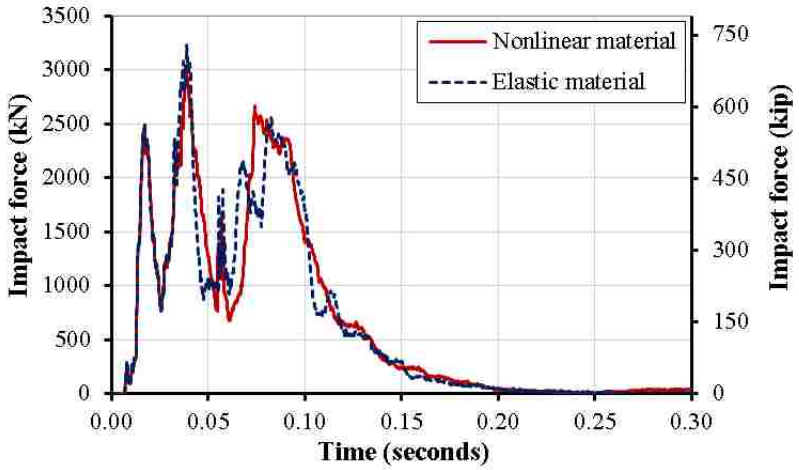

Fig. 10. Time-Impact force of the vehicle collision with the columns with concrete nonlinear and linear materials

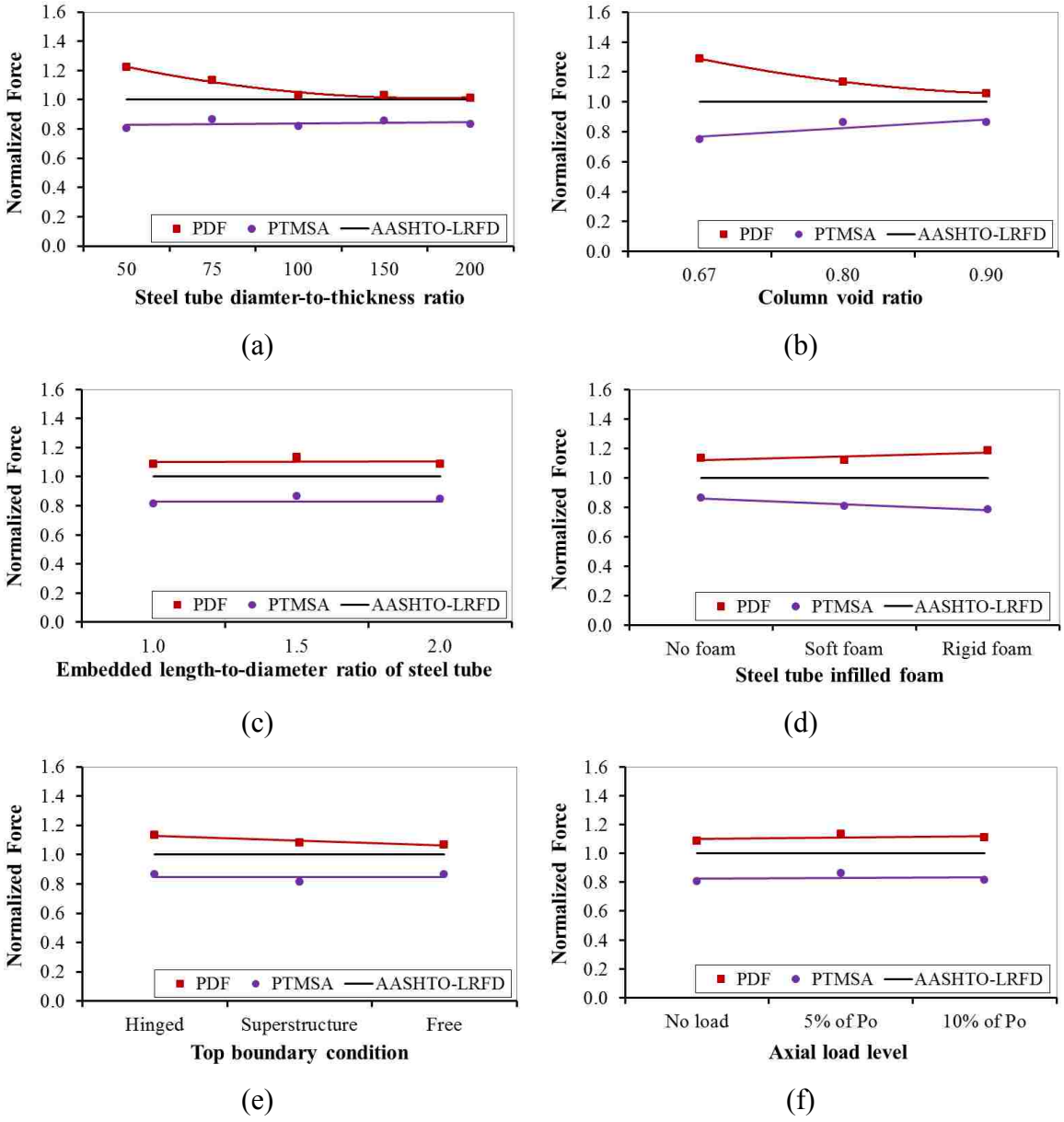

Fig. 11. Effects of (a) steel tube diameter-to-thickness ratio, (b) column void ratio, (c) embedded length-to-diameter ratio of steel tube, (d) steel tube infilled foam, (e) top boundary condition, and (f) axial load level on PDF and ESF

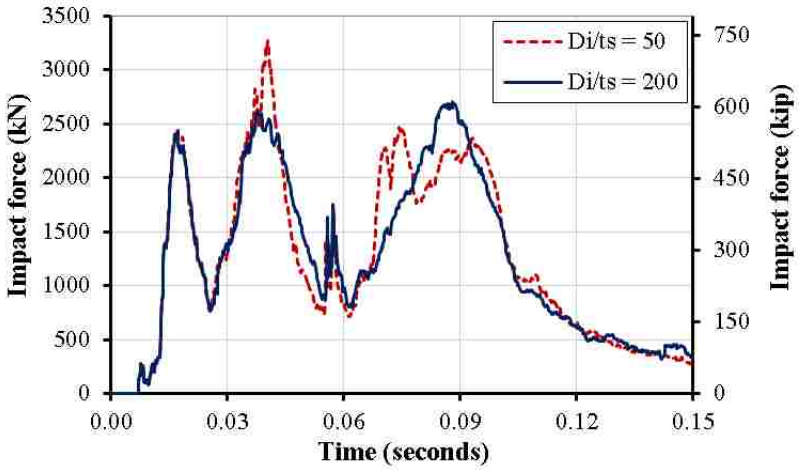

Fig. 12. Time-Impact force of the vehicle collision with the columns with concrete high and low diameter-to-thickness ratio of the steel tube

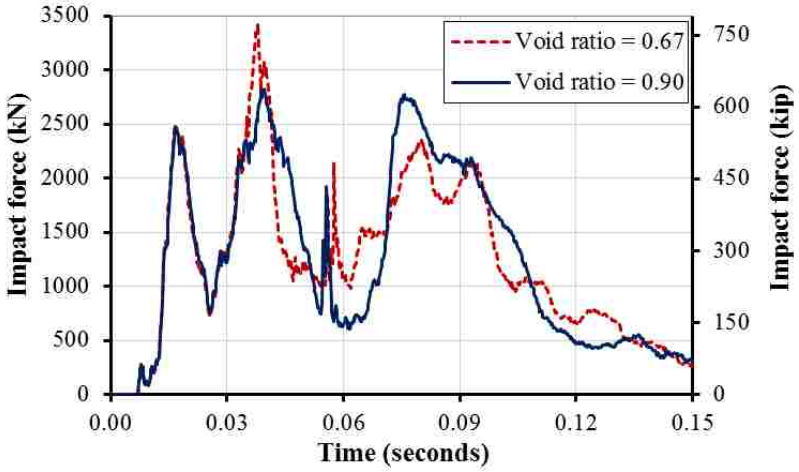

Fig. 13. Time-Impact force of the vehicle collision with the columns with concrete high and low column void ratio

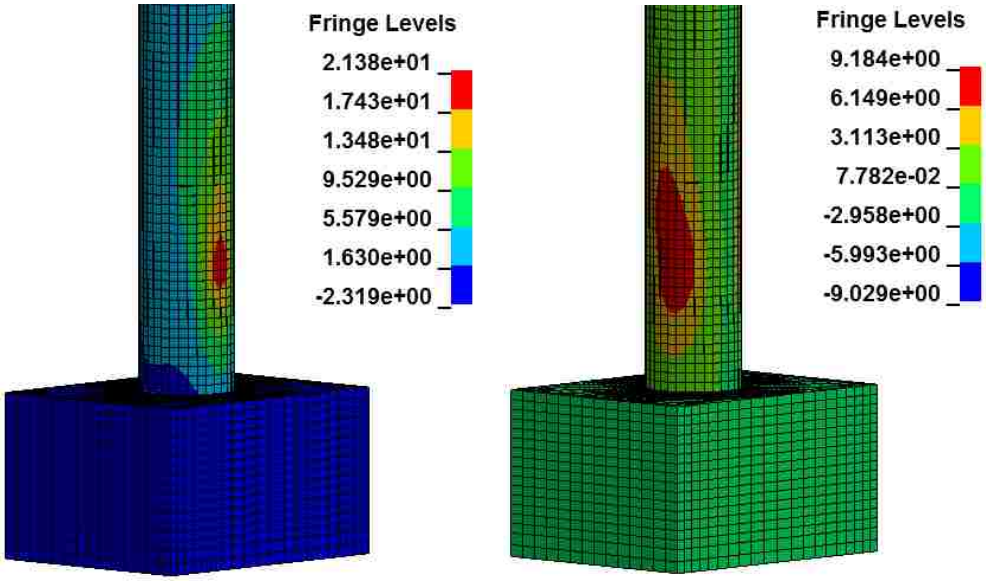

(a) (b)

Fig. 14. Column C22, steel tube infilled soft foam, displacement contours of: (a) steel tube-frontal direction and (b) steel tube-side direction at time of the PDF of 0.04 second, units are in mm (1 mm = 0.04 inch)

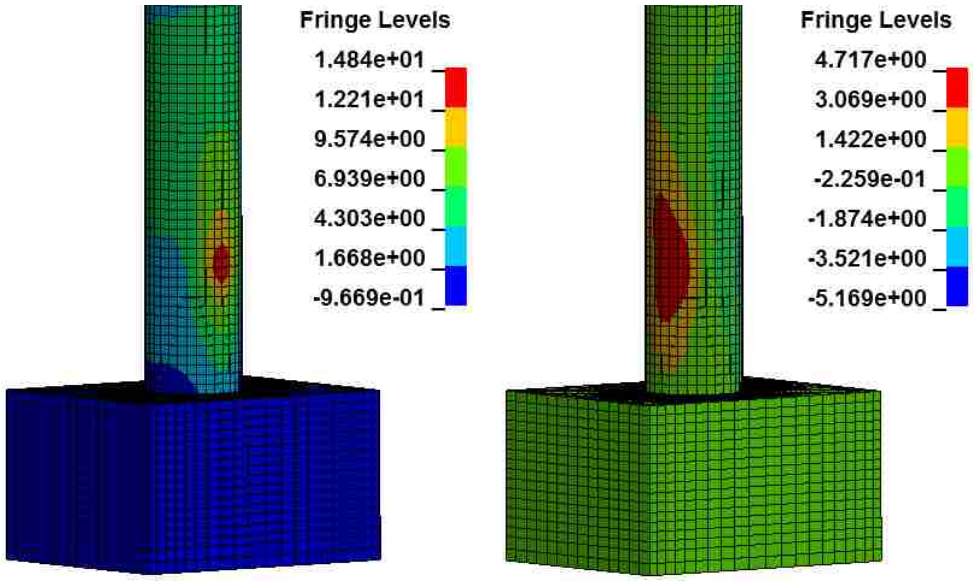

(a) (b)

Fig. 15. Column C23, steel tube infilled rigid foam, displacement contours of: (a) steel tube-frontal direction and (b) steel tube-side direction at time of the PDF of 0.04 second, units are in mm (1 mm = 0.04 inch)

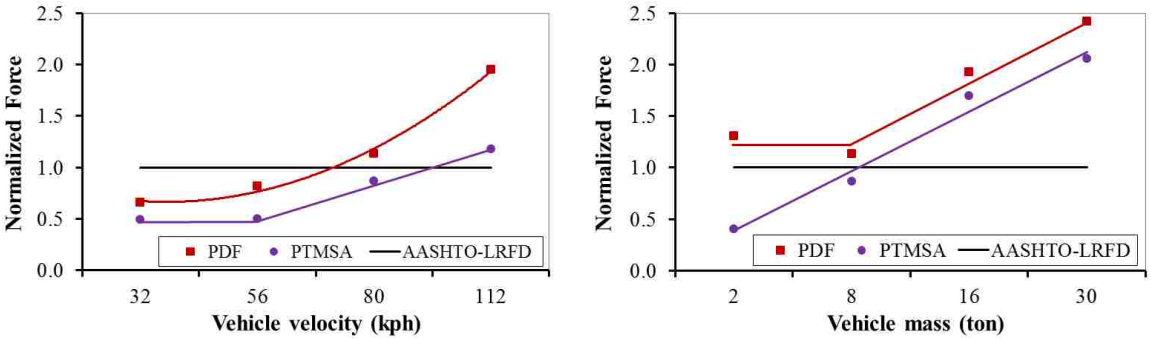

(a) (b)

Fig. 16. Effects of (a) vehicle velocity and (b) vehicle mass on PDF and ESF

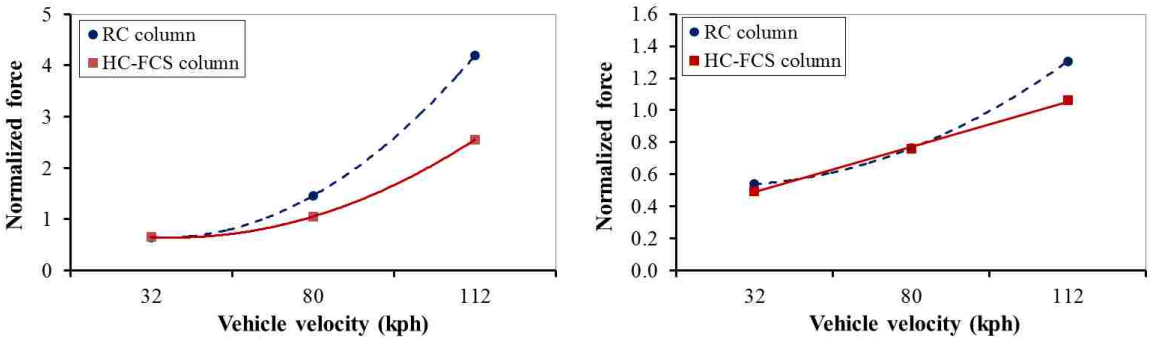

(a) (b)

Fig. 17. The HC-FCS versus RC columns at different vehicle's velocities: (a) PDF and (b) PTMSA

SECTION

3. FINDINGS, CONCLUSIONS, AND RECOMMENDATIONS FOR FUTURE WORK

3.1. FINDINGS AND CONCLUSIONS

This dissertation presented the behavior of HC-FCS columns under axial, combined axial-flexural, and vehicle collision loadings. The effects of using different steel tube diameter-to-thickness ratio (D/t), outer FRP tubes with different orientations, and different concrete wall thickness, on the behavior of HC-FCS columns under axial loading were investigated. HC-FCS columns with wet lay-up FRP tubes having $\pm$ 45° exhibited high level of axial strain capacity than that of the unconfined concrete. However, the increase in strength due to confinement was minimal.

HC-FCS columns with wet lay-up FRP tubes having $\pm$ 45° and 0° (hybrid FRP) exhibited high axial strengths and strains. The failure of the HC-FCS columns with hybrid FRP tubes consisted of two stages. The first stage was the rupture of the unidirectional FRP (outer tube) and the second stage was the reorientation of the $\pm$ 45° FRP exhibiting high axial strains. HC-FCS columns having steel tubes of high D/t ratio was not effective in confining the concrete shell.

Five large scale columns, a conventionally reinforced concrete (RC) column having solid cross section and four HC-FCS columns were investigated during this study. Each column had an outer diameter of 24 inch and a column's aspect ratio, height-to-diameter ratio, of 4.0. The steel tube was extended inside the footing with an embedded length of 1.6-1.8 times the steel tube diameter. While the FRP tube only confined the

concrete wall thickness and truncated at the top of the footing level. The hollow steel tube was the only reinforcement for shear and flexure inside the HC-FCS column. The HC-FCS column exhibited high lateral drift reaching 15.2% and failed gradually due to concrete crushing, steel tube local buckling, followed by FRP rupture. The reference RC column failed at drift of 10.9% due to rebar fracture. The HC-FCS columns dissipated energy under seismic loading reaching to 1.9 times that of the conventional RC column.

Finite element models were developed and validated against experimental results of small-scale column available in the literature. The proposed model was able to predict the behaviors of the large-scale columns that were tested during this research. The Karagozian and Case Concrete Damage Model Release 3 (K&C model), with automatically generated parameters, produces good results for concrete modelling, including high strength concrete. An analytical model based on Navier-Bernoulli's assumptions and strains compatibility was also used to predict the HC-FCS's strength. Based on the finite element analyses and analytical model, it is concluded that:

- The behavior of HC-FCS column is complex and is controlled by the interaction of the stiffness of the steel tube, concrete wall, and FRP. Local buckling occurred in all of the specimens investigated using the finite element analyses, which triggered the rupture of the HC-FCS system. The rate of local buckling propagation depends on the FRP confinement ratio, the steel tube diameter/ steel tube thickness (D/t), concrete unconfined compressive strength, and the concrete wall thickness.

- Two modes of failure were defined, namely, steel/concrete compression failure and FRP rupture. Compression failure is relatively gradual while failure due to FRP rupture is quite abrupt.
- The bending strength increases as the applied axial load, concrete compressive strength, and number of FRP layers increase.
- Keeping the column outer diameter constant and decreasing the concrete wall thickness and/or D/t, increases the column flexural strength.
- The columns' drifts increase as the applied axial load, unconfined concrete compressive strength, and steel tube D/t decrease. The columns' drifts increase as the FRP layers increase.
- The flexural strength slightly increases as the number of FRP layers increases regardless of the steel tube D/t ratio within the range of the parameters investigated in this study.

A detailed description of finite element modeling of vehicle collision with RC bridge columns using LS-DYNA software was presented in this dissertation. Evaluation of the peak dynamic force (PDF) and the equivalent static force (ESF) through an extensive parametric study were conducted. The extensive parametric study investigated the effects of concrete material model, maximum unconfined concrete compressive stress (f_c'), material strain rate, percentage of longitudinal reinforcement, hoop reinforcement, column span-to-depth ratio, column diameter, the top boundary conditions, axial load level, vehicle's velocity, vehicle's mass, distance between the errant vehicle and bridge column, and soil depth above the top of footing on the PDF and ESF. Three approaches were considered during the course of this research to investigate the ESF. In the first

approach, SB_{ESF}, the ESF was defined as the force needed to produce the same maximum displacement by a collision event at the point of impact. In the second approach, EC_{ESF}, the ESF was calculated by Eurocode. In the third approach, PTMSA, the ESF was defined as the peak of the 25 millisecond moving average. This study revealed the following findings:

1. The AASHTO-LRFD was found to be non-conservative when the column was collided with heavy vehicles of a weight more than 35 kips or high speed vehicle more than 70 mph. In another terms, the AASHTO-LRFD nonconservative for KE higher than 1,800 kip.ft. The AASHTO-LRFD predicted 85% of the columns' performance and predicted only 1 out of 4 of the failed columns.
2. A new equation for estimating the ESF based on the vehicle's mass and velocity ($KEB_{ESF} = 33\sqrt{m\ v_r^2}$) with accuracy more than 90% was developed. This approach will allow Departments of Transportation (DOTs) to design different bridge columns to different impact forces depends on the anticipated truck loads and velocities.
3. This dissertation simplified the Eurocode equation for estimating the ESF based on the vehicle's mass and velocity ($MB_{ESF} = 130\sqrt{m\ v_r}$) with accuracy more than 90%.
4. Approximately 12% of the investigated columns failed while 15% and 73% of the columns were assigned to performance levels severe and minor damage, respectively.
5. PTMSA approach was the best approach for predicting the columns' performance by 100% and 4 out of 4 of the failed columns while SBESF predicted 94% of the

columns' performance and 4 out of 4 of the failed columns. Furthermore, ECESF predicted 94% of the columns' performance and 2 out of 4 of the failed columns.

6. This study indicated that columns that are 48.0 inch in diameter and smaller are the most vulnerable for shear failure contradicting the AASHTO-LRFD (2012) which states that columns that are 30.0 inch in diameter and smaller are the most vulnerable.
7. Generally, the PDF increases when the longitudinal reinforcement ratio, hoop reinforcement volumetric ratio, column diameter, axial load level, vehicle velocity, and vehicle mass increase and when the strain rate effect is considered. While it decreases when the damage of the column and the clear zone distance increase. However, it is not affected by changing f_c', column top boundary condition, and soil depth.
8. The relation between the PDF and the column's span-to-depth ratio was nonlinear.

The behavior of the HC-FCS columns under vehicle collision was presented. The peak dynamic force (PDF) and the equivalent static force (ESF) were evaluated through an extensive parametric study. The ESF was defined as the peak of the 25 millisecond moving average (PTMSA). The extensive parametric study investigated the effects of 14 different parameters: the concrete material model, the unconfined concrete compressive strength (f_c'), the material strain rate, the column height-to-diameter ratio, the column diameter, the FRP confinement ratio, the diameter-to-thickness ratio of steel tube, the column void ratio, the embedded length of the steel tube, the infilled steel tube, the top boundary conditions, the axial load level, the vehicle's velocity, and the vehicle's mass on both dynamic and static impact forces. This study revealed the following findings:

1. The main resistance of the HC-FCS columns to the vehicle collision came from the inner steel tube.
2. The AASHTO-LRFD was found to be non-conservative when the column was collided with heavy vehicles that weigh more than 16 tons (35 kips) at speeds greater than 112 kph (70 mph).
3. For simplicity, the elastic material could be used to design HC-FCS columns under vehicle collision.
4. The frontal deformation of the steel tube was reduced by 3% and 33% when it was infilled with soft and rigid foams, respectively. The side deformation of the steel tube was reduced by 2.5% and 48% when it was infilled with soft and rigid foam, respectively.
5. Generally, the PDF increased when the f_c', vehicle velocity and vehicle mass increased and when the steel tube was infilled with foam. It decreased when the diameter-to-thickness ratio of the steel tube and the column void ratio increased. However, it was not affected by changing the strain rate effect, column height-to-diameter ratio, column outer diameter, FRP confinement ratio, steel tube embedded length, top boundary condition of the column, or axial load level.
6. Generally, the PTMSA increased when the column void ratio, vehicle velocity, and vehicle mass increased. It decreased when the f_c' increased and when the steel tube was infilled with foam. However, it was not affected by changes to the strain rate effect, column height-to-diameter ratio, column outer diameter, FRP confinement ratio, diameter-to-thickness ratio of the steel tube, steel tube embedded length, top boundary condition of the column, or axial load level.

7. The PDF of the HC-FCS column was lower than that of the RC column by approximately 40% and 28% when it was collided with by a vehicle at a velocity of 112 kph (70 mph) and 80 kph (50 mph), respectively.
8. The PDFs of the HC-FCS and RC columns were almost the same when they were collided with by a vehicle travelling with a velocity of 32 kph (20 mph).
9. The PTMSA of the HC-FCS column was lower than that of the RC column by approximately 20% when it was collided with by a vehicle with a velocity of 112 kph (70 mph).
10. The PTMSAs of the HC-FCS and RC columns were almost the same when they were collided with by vehicles travelling with velocities of 80 kph (50 mph) or 32 kph (20 mph).
11. The equation ($KEB_{ESF} = 33\sqrt{m\ v_r^2} = 46\sqrt{KE}$) to estimate the ESF of a vehicle's collision with a bridge column as presented by Abdelkarim and ElGawady (2015b) would be applicable for the HC-FCS columns struck by a vehicle with a velocity of up to 80 kph (50 mph). After this speed, the equation overestimates the ESF of collision with the HC-FCS columns.

3.2. RECOMMENDATIONS FOR FUTURE WORK

Extensive research was carried out during the course of this project, including testing small-scale columns, large-scale columns, analytical modeling, and finite element modeling under lateral and vehicle impact. A few issues need to be addressed before field implementation of HC-FCS. Future work is required to address the following issues:

- Shear strength of HC-FCS should be investigated for short columns.

- More experimental studies on determination of the required development length of the steel tube to avoid pull-out of the tube from footing should be conducted.
- HC-FCS columns with infilled-steel tube with concrete or other filling material should be investigated.
- HC-FCS columns with thin steel and FRP tubes should be investigated under different loadings attempting to reduce the materials costs.
- Developing and testing of a cap-beam column connection.
- Determination of torsion strength of the column. Skewed and curved bridges may induce considerable torsion on the columns.
- Performance of durability studies of the steel encased into the concrete and FRP tube is required.
- Fire resistance of the HC-FCS columns is important to be investigated.
- Optimization of the construction cost of the HC-FCS column. Cost analysis and comparisons with conventional concrete columns need to be carried out. Then, the price needs to be optimized.

APPENDIX A

FIGURES OF SMALL-SCALE COLUMNS

(a) (b)

Figure A.1. Rupture of the hybrid FRP: (a) rupture of the outer unidirectional FRP only and (b) rupture of the 45^{o} FRP after the unidirectional FRP

(a) (b)

(c)

Figure A.2. Steel tube buckling: (a) steel tube with the concrete cone, (b) steel tube alone, and (b) top view of the steel tube

APPENDIX B

FIGURES OF LARGE-SCALE COLUMNS

There are two options to construct the HC-FCS columns. The first option; building the precast HC-FCS column in the precast yard, then install it on the reinforcement cage of the footing, and finally cast-in-place the concrete footing (Fig. B.1). The second option; building the precast HC-FCS column in the precast yard during casting-in-place of the footing with a certain void, then install the precast column into the footing's void, and finally grouting the gap between the footing and the steel tube (Fig. B.2). The void diameter (D_o') is larger than the column's diameter (D_o) to free access for grouting. Option "1" has lower number of tasks for construction but the tasks are series while option "2" has higher number of tasks for construction but the tasks are parallel.

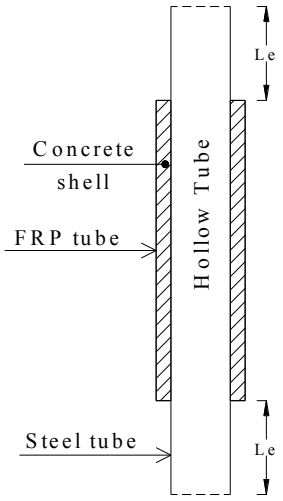

Step 1: Build pre-cast HC-FCS column

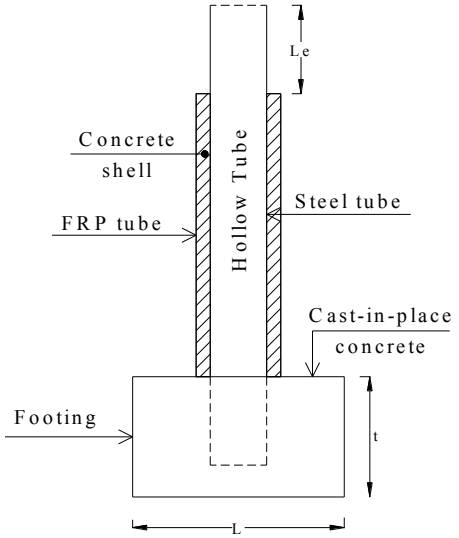

Step 2: Install pre-cast column on the footing cage then cast-in-place the footing

Figure B.1. Construction of HC-FCS column: Option "1"

Step 1: Build pre-cast HC-FCS column as in OPTION "1"

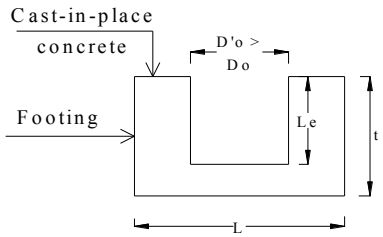

Step 2: Cast-in-place the footing with void of dimensions D_o' x L_e

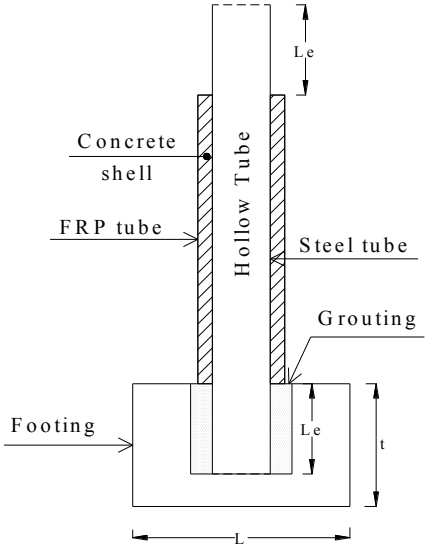

Step 3: Install pre-cast column on the footing's void then concrete grouting to fill the gap between the steel tube and the footing

Figure B.2. Construction of HC-FCS column: Option "2"

(a)

(b)

Figure B.3. Preparing reinforcement cages: (a) footing and (b) RC-column

(a)

(b)

Figure B.4. Install reinforcement cages into formwork: (a) footing, (b) RC-column

(a) (b) (c)

Figure B.5. Install the steel tube into the footing: (a) moving the steel tube, (b) putting the steel tube into the footing, (c) verticality check of the steel tube

Figure B.6. Fixing the steel tube before pouring the footing

(a)

(b)

Figure B.7. Concrete pouring of the footing: (a) during pouring and (b) after pouring

Figure B.8. Install the formwork of the RC-column and the FRP tube for the HC-FCS column

(a)

(b)

(d)

(c)

Figure B.9. Concrete pouring of the columns: (a) and (b) flow slump, (c) pouring concrete into the columns, and (d) concrete showed no segregation after pouring

(a)

(b)

Figure B.10. Install the formwork of the columns' heads: (a) placing the formwork and (b) scaffolding and tying the formwork

Install reinforcement cage

Concrete pouring

Figure B.11. Install the reinforcement cage of the column head and concrete pouring

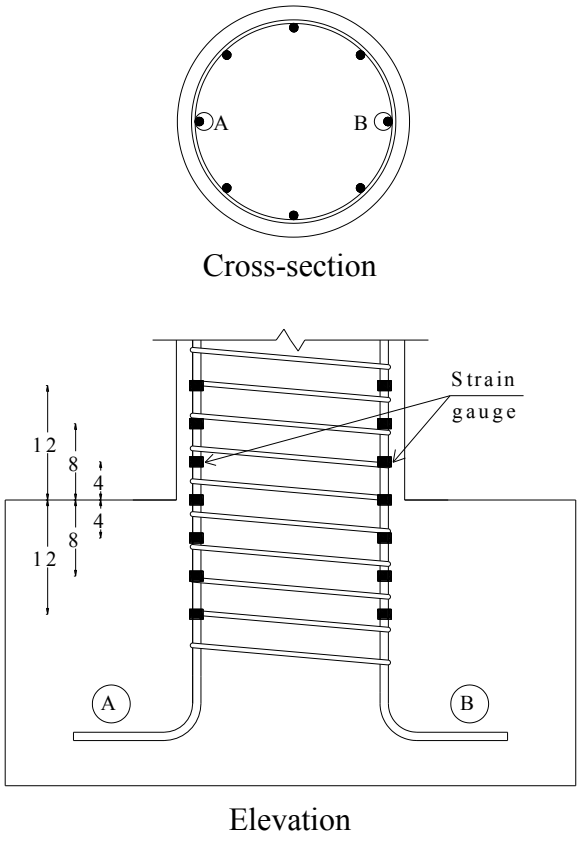

Figure B.12. Install strain gauges on two longitudinal rebars of the RC-column

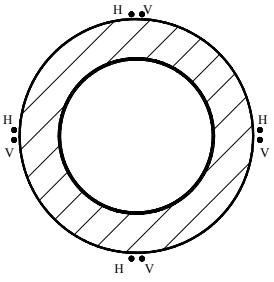

Cross-section

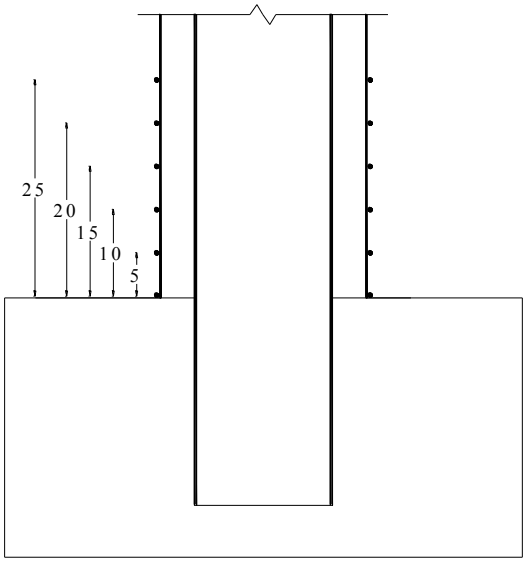

Elevation

Figure B.13. Install strain gauges on FRP tubes

Figure B.14. Install vibrating wire strain gauges in the concrete wall thickness

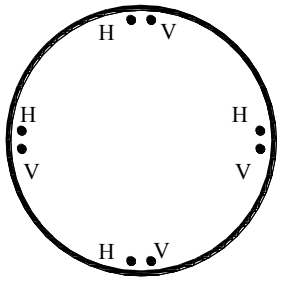

H: horizontal strain gauge
V: vertical strain gauge

(a)

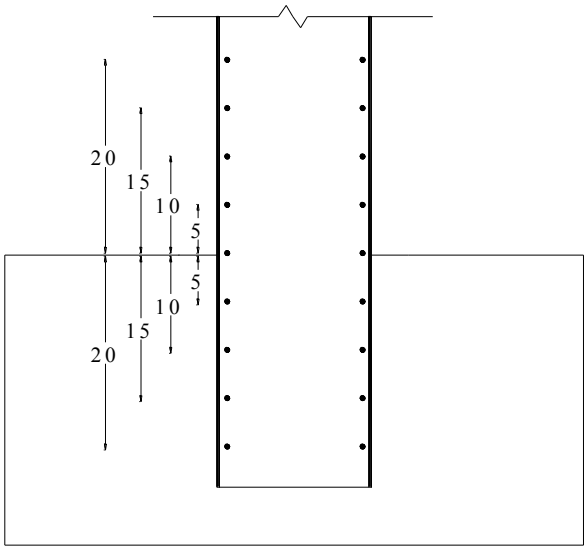

(b)

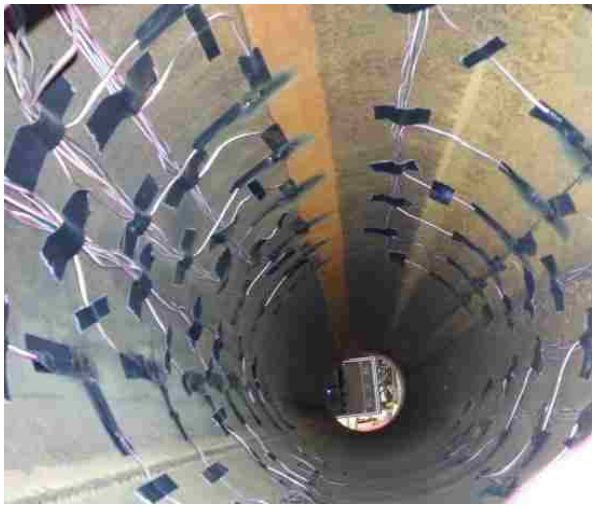

(c)

Figure B.15. Install strain gauges inside steel tubes: (a) arrangement in cross-section, (b) arrangement along the height, and (c) inserting strain gauges into steel tube

Figure B.16. Install webcams inside the steel tubes

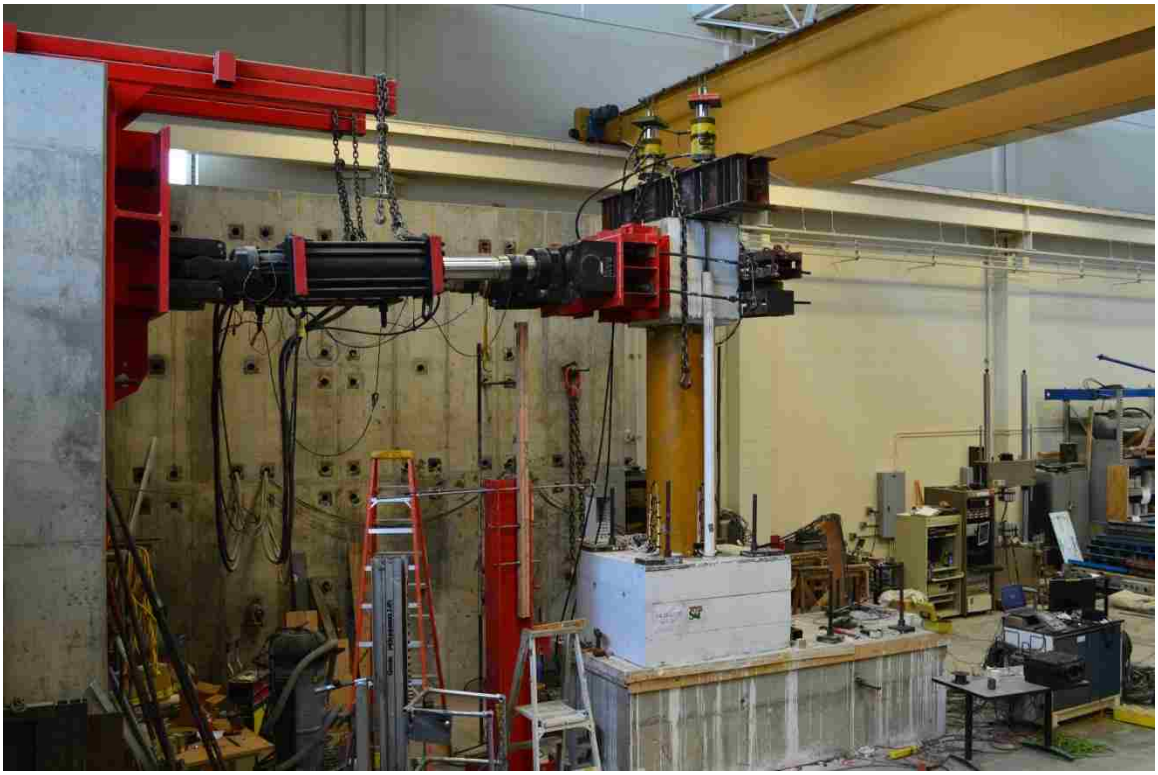

Figure B.17. Large-scale column test setup

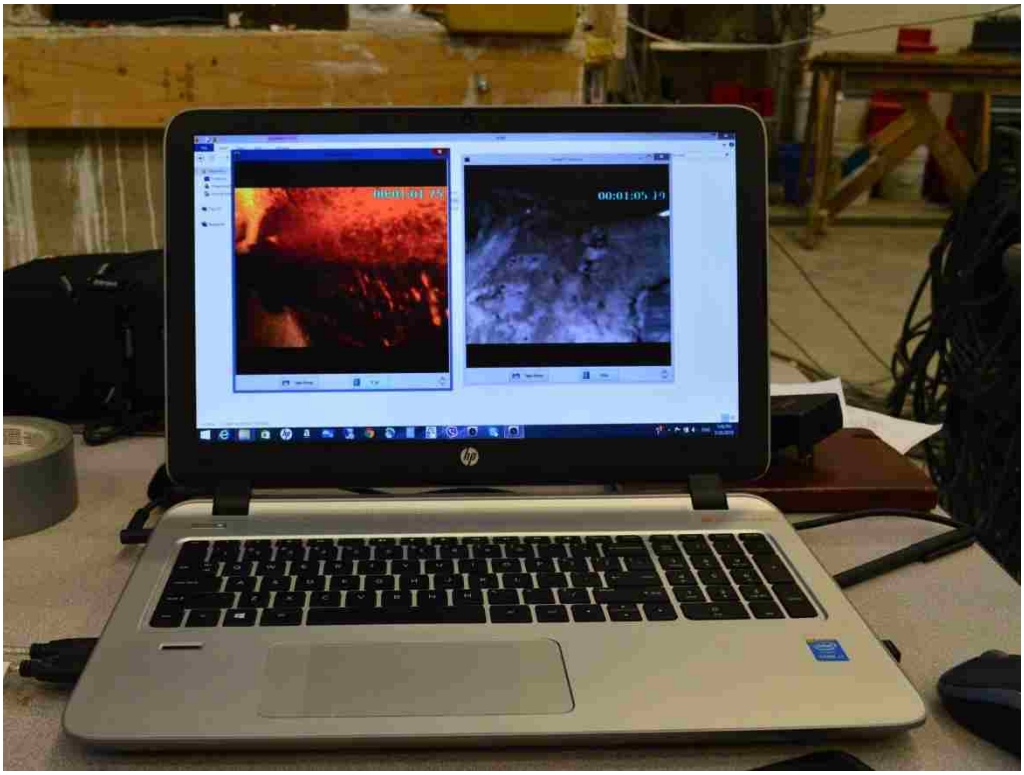

Figure B.18. Monitoring the steel tube deformations from inside through webcams

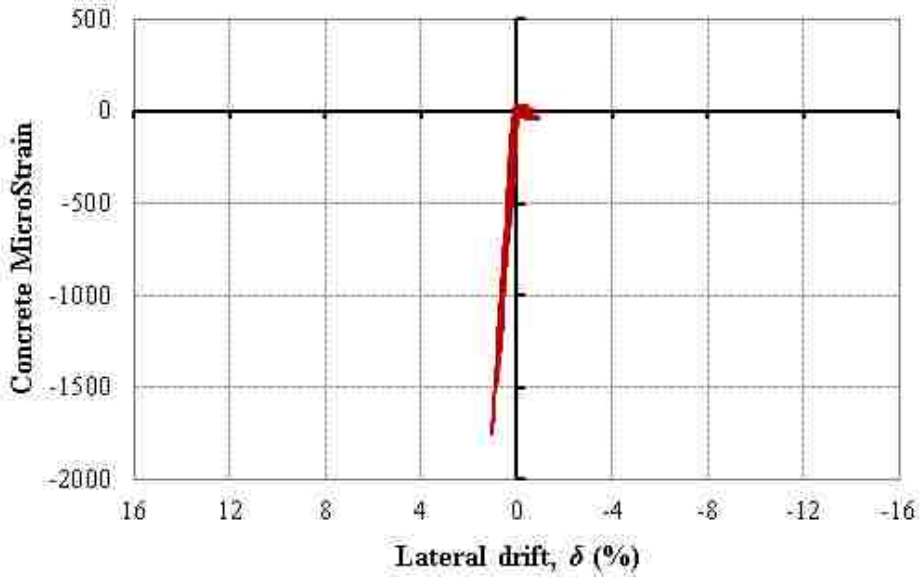

(a)

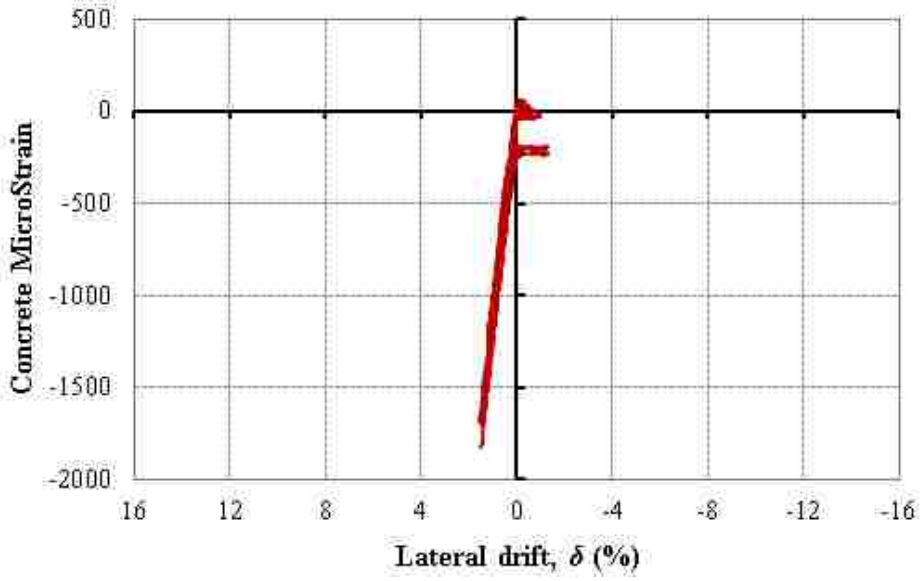

(b)

Figure B.19. Lateral drift-concrete strain relation for: (a) the F4-24-P124 column and (b) the F4-24-E344 column

Three standard coupons were cut longitudinally from a steel tube for tensile tests according to ASTM A1067. The steel coupon tests were conducted under a displacement control of 0.76 mm/min. (0.03 inch/min). Two vertical and horizontal strain gauges were attached to the mid height of the steel coupons (Fig. B.20a). All of the steel coupons failed by yielding at the neck before fracturing (Fig. B.20c).

According to ASTM D3039, three longitudinal FRP coupons were cut from each type of FRP tube. One vertical and one horizontal strain gauge were attached to the front and back surfaces of each FRP coupon at the mid height (Fig. B.20b). Each FRP coupon was subjected to a tensile test with a displacement loading rate of 1.27 mm/min. (0.05 in/min.). All of the FRP coupons failed by debonding between the FRP layers without fiber rupture, as shown in Fig. B.20c. The ultimate stress was 9,500 psi (65.5 MPa) (Fig. B.21). The saturated FRP with a fiber orientation at 53^o has a structure that depends on fibers in two perpendicular directions [$\pm 53^o$] with adhesive material between them. Therefore, this type of laminate works globally. As a result, the fibers did not work in the coupon test. The width of the strip is only 25 mm (1.0 inch), so there is no fiber continuity. Therefore, the properties of the FRP were referenced based on the manufacturer data sheet.

(a) (b) (c)

Figure B.20. Coupon tests: (a) steel coup during the test, (b) FRP coupon during the test, and (c) steel and FRP coupons ruptures

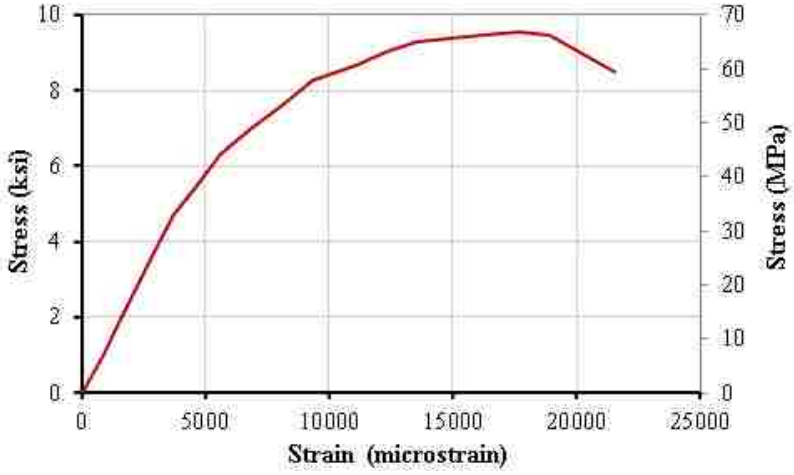

Figure B.21. Strain-stress curve for FRP coupon

Figure B.22 illustrates the normalized residual drift (NRD)-lateral drift relation for all columns. The residual drift is the permanent drift when the column return back to zero lateral force during the unloading cycling (Fig. B.23). The normalized residual drift was calculated as the residual drift in a given cycle divided by the peak lateral drift in this cycle. In general, the F4-24-RC and F4-24-E324 columns behaved quite similar beyond drift of 2%. Before drift of 2%, the F4-24-E324 has constant NRD of 10% while the NRD of F4-24-RC nonlinearly increased to NRD of 10% at drift of 2%. Beyond drift of 2%, the NRD of both columns nonlinearly increased. At the failure of the columns, the NRD reached to 70%. The NRD of the F4-24-P124 column was lower than that of the F4-24-E324 column. This occurred since the F4-24-P124 had thinner FRP tube. Hence, the concrete dilation occurred toward the FRP tube rather than the steel tube, which reduced the local buckling of the steel tube and hence reduced the residual drift.

Figure B.24 illustrates the equivalent viscous damping (ζ)-lateral drift relation for all of the columns. The ζ is one of the essential parameters of the displacement-based seismic design method. The ζ increases when the displacement or curvature ductility increases (Priestley et al. 1995). The ζ was calculated using equation 2 (Jacobsen 1930):

$$\zeta = \frac{1}{4\pi}\frac{A1}{A2}$$

where A1 = the dissipated energy of each hysteretic loop (Fig. B.23a) and A2 = the strain energy for each cyclic step which is the elastic stored energy in the system (Fig. B.23b). The ζ of all of the columns in the elastic stage was between 0.02 and 0.07. The HC-FCS columns had a higher ζ comparable to that of the F4-24-RC column.

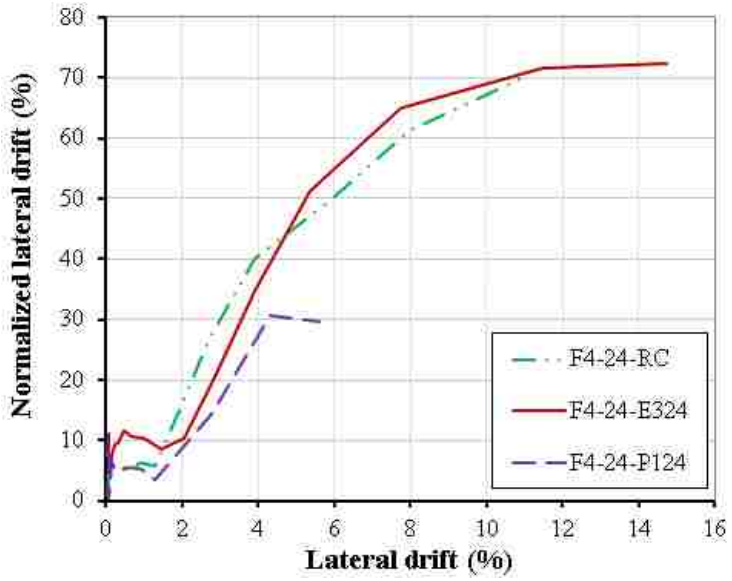

Figure B.22. Normalized residual drift-lateral drift relation of two HC-FCS columns versus the reinforced concrete (RC) column

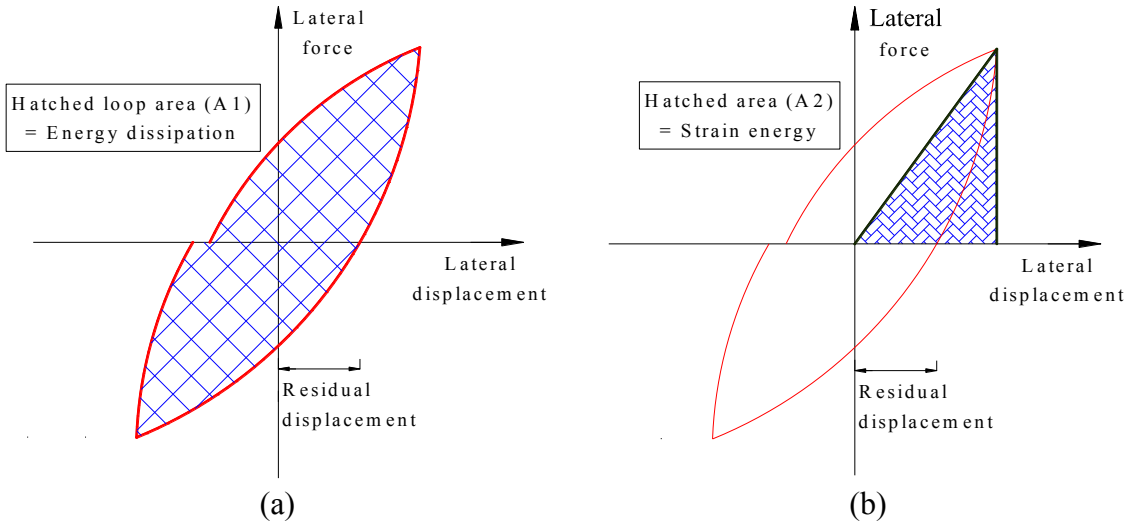

Figure B.23. Determination of the energy dissipation and equivalent viscous damping: (a) Loop energy dissipation, and (b) Strain energy

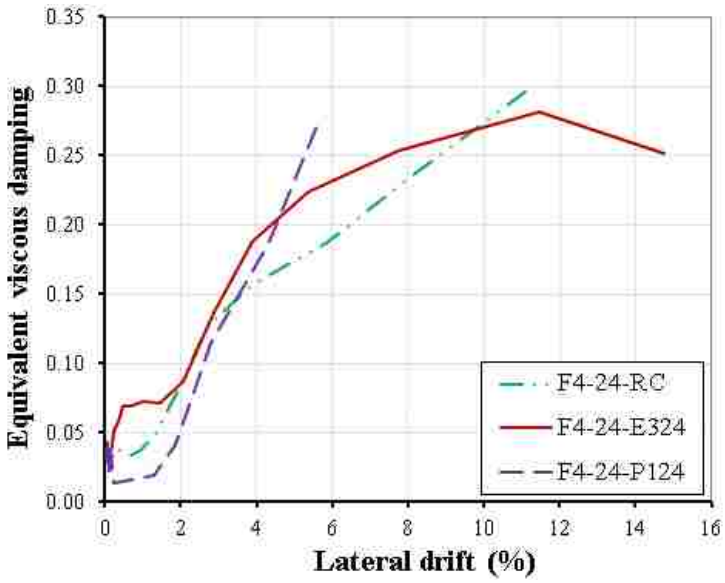

Figure B.24. Equivalent viscous damping-lateral drift relation of two HC-FCS columns versus the reinforced concrete (RC) column

APPENDIX C

FIGURES OF VEHICLE COLLISION WITH REINFORCED CONCRETE (RC) BRIDGE COLUMNS

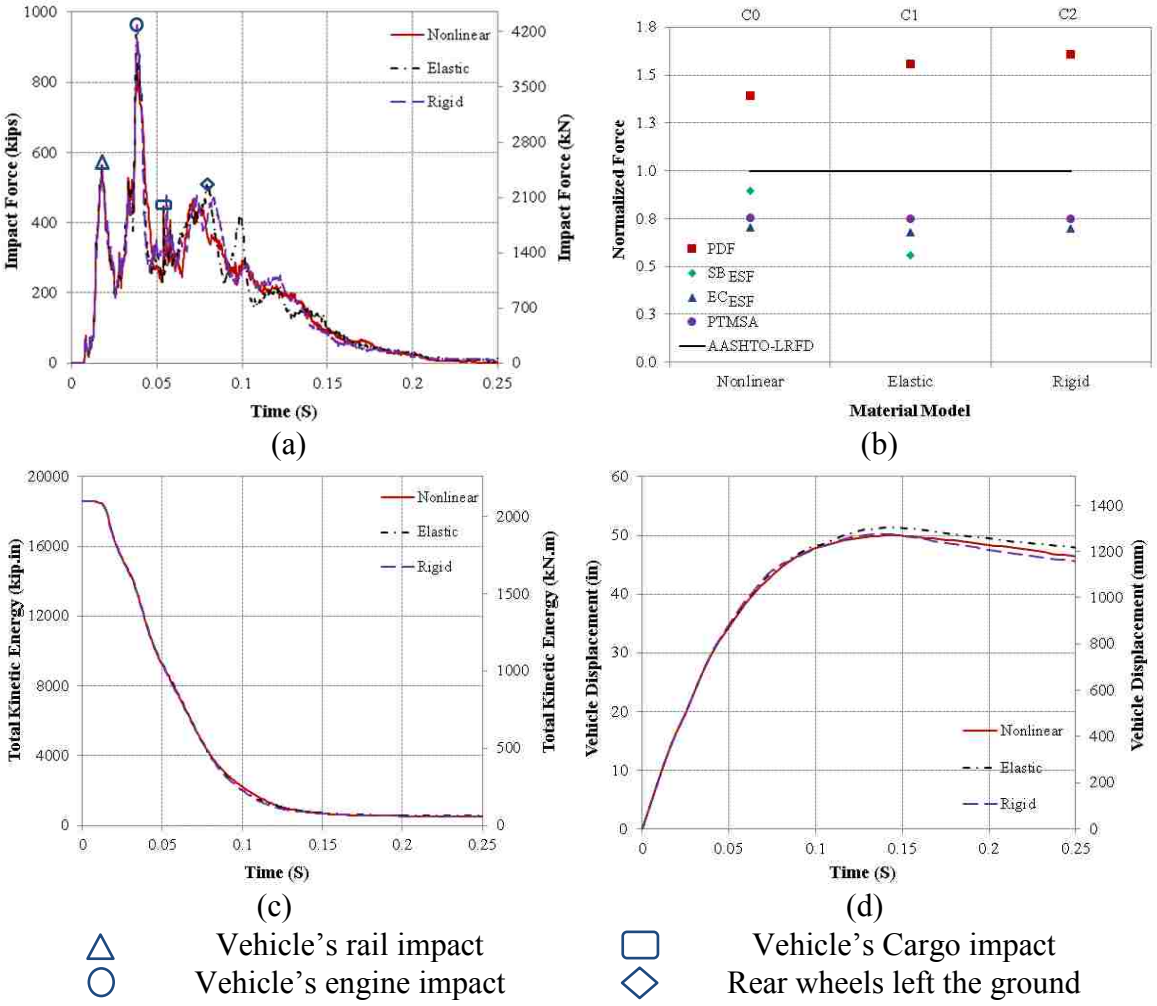

Figure C.1. Effects of various concrete material models: (a) Time-Impact force, (b) PDF vs. ESF vs. AASHTO-LRFD, (c) Time-Total kinetic energy, and (d) Time-Vehicle displacement.

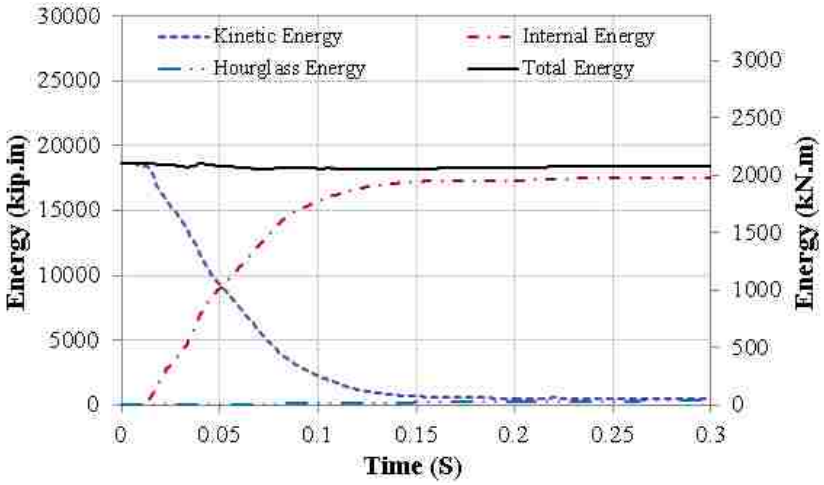

Figure C.2. Time-energies relations of the FE model C0

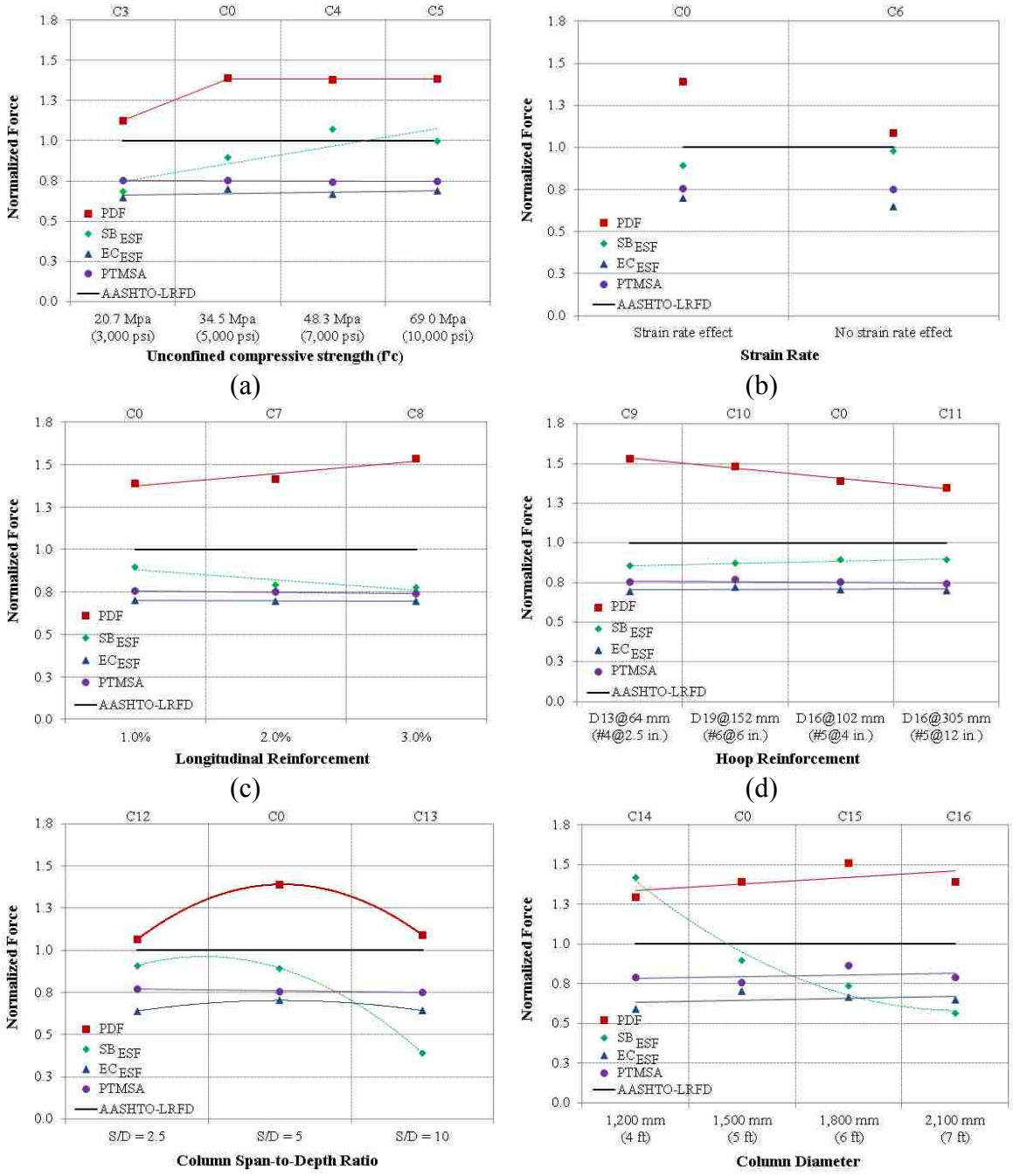

Figure C.3. Effects of (a) f'_c, (b) strain rate, (c) longitudinal reinforcements ratio, (d) hoop reinforcements ratio, (e) span-to-depth ratio, and (f) column diameters on PDF and ESF

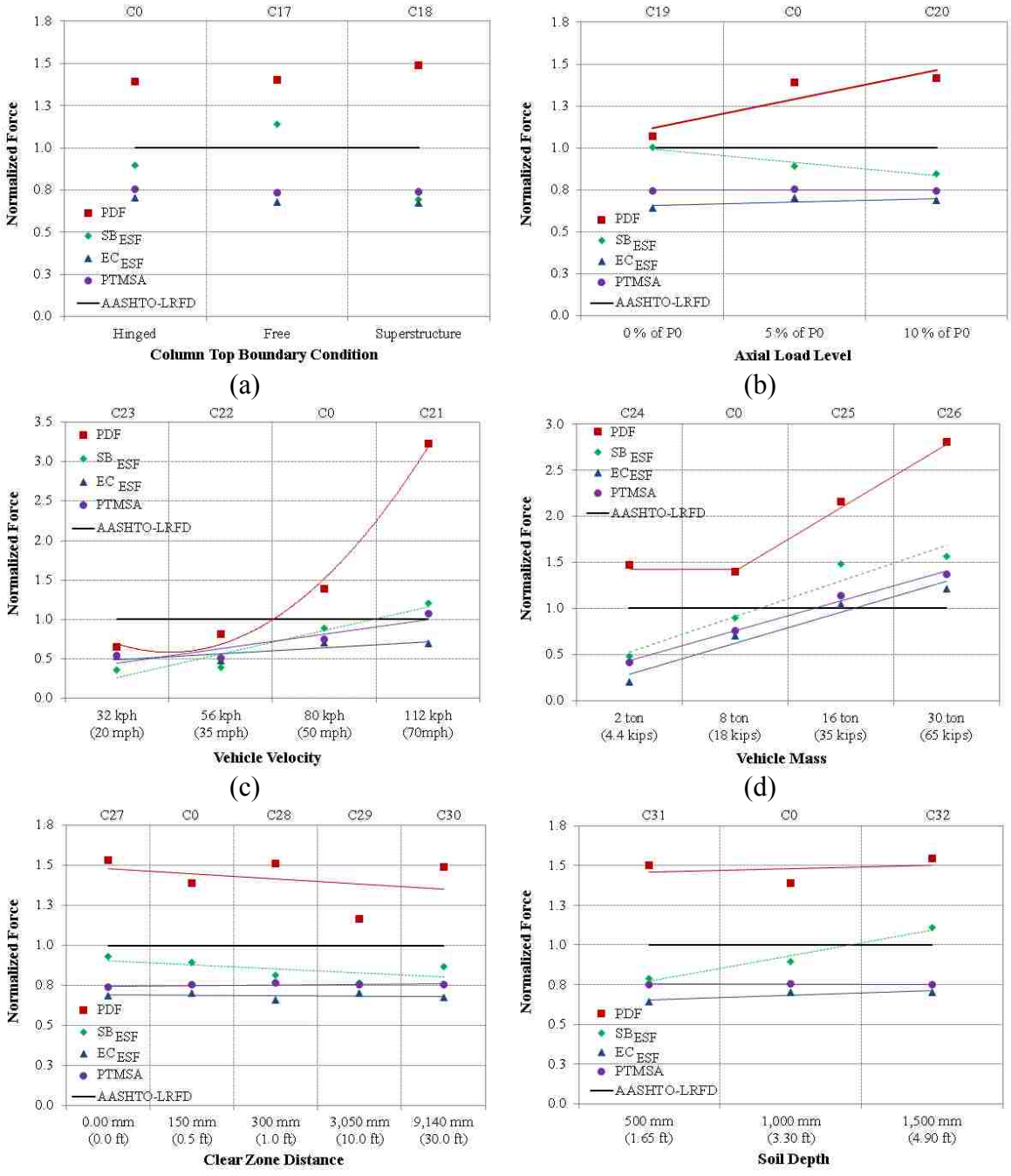

Figure C.4. Effects of (a) top boundary conditions, (b) axial load level (c) vehicle velocities, (d) vehicle masses, (e) clear zone distance, and (f) soil depth above the top of column footing on PDF and ESF

APPENDIX D

CONCRETE-FILLED-LARGE DEFORMABLE FRP TUBULAR COLUMNS UNDER AXIAL COMPRESSIVE LOADING

This appendix includes a journal paper investigates the qualification of a new FRP to be used in HC-FCS columns in future research. This paper has been published in the *journal of fibers* published by Multidisciplinary Digital Publishing Institute (MDPI).

CONCRETE-FILLED-LARGE DEFORMABLE FRP TUBULAR COLUMNS UNDER AXIAL COMPRESSIVE LOADING

Omar I. Abdelkarim [1], and Mohamed A. ElGawady[2, *, †]

[1] Ph.D. Candidate, Dept. of Civil, Architectural, and Environmental Engineering, Missouri University of Science and Technology, Rolla, MO, 65401, USA; oiafgc@mst.edu

[2] Benavides Associate Professor, Dept. of Civil, Architectural, and Environmental Engineering, Missouri University of Science and Technology, Rolla, MO, 65401, USA; elgawadym@mst.edu

* Authors to whom correspondence should be addressed; E-Mail: elgawadym@mst.edu; Tel.: +1-573-341-6947

Academic Editor: Mahmoud Reda Taha

Received: 29 August 2015 / Accepted: 28 September 2015 / Published: 14 October 2015

Abstract

The behavior of concrete-filled fiber tubes (CFFT) polymers under axial compressive loading was investigated. Unlike the traditional fiber reinforced polymers (FRP) such as carbon, glass, aramid, etc., the FRP tubes in this study were designed using large rupture strains FRP which are made of recycled materials such as plastic bottles; hence, large rupture strain (LRS) FRP composites are environmentally friendly and can be used in the context of green construction. This study performed finite element (FE) analysis using LS-DYNA software to conduct an extensive parametric study on CFFT. The effects of the FRP confinement ratio, the unconfined concrete compressive strength (f_c'), column size, and column aspect ratio on the behavior of the CFFT under axial compressive loading were investigated during this study. A comparison between the behavior of the

CFFTs with LRS-FRP and those with traditional FRP (carbon and glass) with a high range of confinement ratios was conducted as well. A new hybrid FRP system combined with traditional and LRS-FRP is proposed. Generally, the CFFTs with LRS-FRP showed a remarkable behavior under axial loading in strength and ultimate strain. Equations to estimate the concrete dilation parameter and dilation angle of the CFFTs with LRS-FRP tubes and hybrid FRP tubes are suggested.

Keywords: Concrete-filled tube; Large deformable FRP; Large rupture strain; Hybrid FRP; LS-DYNA.

1. Introduction

Green buildings are environmentally sound buildings. The ideal green project preserves and restores the habitat that is vital for sustaining life by acting as a net producer and exporter of resources, materials, energy, and water rather than being a net consumer. The Environmental Protection Agency (EPA) suggests using recycled industrial goods such as demolition debris in construction projects for green buildings. Energy efficient building materials and appliances are promoted in the United States through energy rebate programs. However, using green materials in construction is usually costly. Recently, new fiber reinforced polymer (FRP) composites have been manufactured from recycled plastic bottles. They were introduced as alternatives to traditional FRPs such as glass, aramid, and carbon FRP. The new FRP composites are much cheaper than the traditional FRPs. These new FRP composites are made of polyethylene terephthalate (PET) and polyethylene naphthalate (PEN) fibers. The traditional FRP composites have linear elastic stress-strain relationships with a rupture

failure strain ranged around 1.0% to 2.5%. However, the new FRP composites have bilinear stress-strain relationships with elastic modulus and tangent modulus. This bilinear stress-strain relation is because of the effect of amorphous phase motion and macromolecular chains sliding between LRS fibers and matrix [1]. However, the elastic modulus of the new FRP composites is, in general, lower than that of the traditional FRPs. They have much larger rupture strains, usually larger than 6.0%. Therefore, the new FRP composites were called large rupture strain FRPs (LRS-FRPs). PET polymers keep their mechanical strengths up to a temperature of 150- 175°C [2].

Use of the FRP in new structures has grown rapidly in the past two decades. The main purpose of using FRP is to enhance the strength and ductility of a structural member. Concrete-filled FRP tubes (CFFTs) have many benefits such as light weight-to-strength ratio, high confinement, and corrosion resistance. The FRP tube acts as a stay-in-place formwork, confines the concrete structural element, and increase its compressive strength. Several researchers investigated the behavior of CFFT columns using the traditional FRP tubes under different loadings [3-10]. Recently, some experimental works have been conducted to investigate the performance of the LRS-FRPs in jacketing concrete members to examine their behavior under different loading such as axial, flexural, shear loadings [1,11-15]. The researches have shown that the concrete members had remarkable behavior using LRS-FRP jacketing. However, the new FRPs should be investigated with different aspects such as: their fire resistance and their performance under impact and durability loadings. Their behavior with different matrices and their bonding with concrete members should be investigated as well. As these new FRPs have high tensile strains, they would be a good solution for prestressed FRP, wrapping

masonry structures, and using them for flexural bars. Also, no previous studies were conducted to determine the benefits of combining both traditional and new FRPs in a hybrid system.

The FRP confinement pressure (f_l) and the concrete dilation angle (ψ) are essential parameters in characterizing the performance of concrete under compression stress in the CFFTs. Confinement pressure is the lateral pressure from the FRP tube that confines the concrete core when the concrete material starts to expand. The confinement pressure and the confinement ratio can be calculated using equations (1) and (2). The dilation angle is defined as the inclination of the failure surface towards the hydrostatic axis. Physically, the dilation angle is interpreted as a concrete internal friction. The dilation angle varies depending on the axial stress level and the FRP jacketing stiffness [16,17]. However, previous studies used the dilation angle to vary with the FRP jacketing stiffness and to be a constant value under varied axial load levels in the finite element analysis [18-20]. The finite element results of these studies agreed with the experimental results with reasonable accuracy. For unconfined concrete material, the dilation angle is usually taken between 36^o to 40^o with an average value of 38^o [21-23].

$$Confinement\ pressure\ (f_l) = \frac{2\ E_f\ \varepsilon_f\ t_f}{D} \tag{1}$$

$$Confinement\ ratio\ (CR) = \frac{f_l}{f_c'} \tag{2}$$

Where E_f is the elastic modulus of the FRP tube in the confinement direction, ε_f is the ultimate tensile strain of the FRP in the confinement direction, t_f is the FRP tube

thickness, D is the column's diameter, and f_c' the characterized concrete cylindrical strength at 28 days.

An extensive finite element (FE) study is presented to investigate the behavior of the CFFTs using LRS-FRP under axial compressive loading. LS-DYNA software [24] was used during this study. A high range of confinement ratios was investigated for the traditional FRP and LRS-FRP. A new state-of-the-art CFFT columns using hybrid FRP tubes combined with traditional FRP and LRS-FRP are introduced. In addition, the effect of the concrete strength (f_c'), columns size, and column aspect ratio on the behavior of the CFFT were studied. This study introduces recommendations for using of the most effective FRP type in CFFT tubes. A new equation to estimate the dilation angle for the CFFT column with LRS-FRP tubes is suggested.

2. Finite Element Model Validation

FE modeling was used to analyze the behavior of CFFT with LRS-FRP under axial loading. The LS-DYNA 971 R3 software was used to design and validate the models against the experimental results that were gathered from twelve CFFT columns with LRS-FRP by Dai et al. [13]. Each column had a circular cross-section with an outer diameter of 150 mm and a height of 300 mm. These columns had a concrete compressive strength (f_c') that was between 32.5 and 39.2 MPa. Either PET-FRP or PEN-FRP was used to manufacture the FRP tubes (Table 1). These models were next used to conduct a parametric study investigating the differences between LRS-FRP, tradition FRP, and hybrid system of a combination of both by analyzing the effects of the confinement ratio, column's size, and the column's aspect ratio on the CFFT behavior under axial loading.

2.1 Geometry

The concrete cylinder and steel plates were modeled using solid elements (Figure 1). The outer FRP tube was simulated using shell elements. All solid elements were modeled with constant-stress and a one-point quadrature to reduce the computational time. Hourglass control was used to avoid spurious singular modes (i.e., hourglass modes) for solid elements. The hourglass value for all models was taken as the default value of 0.10. Surface-to-surface contact elements were used to simulate the interface between the concrete cylinder and the outer FRP tube. Node-to-surface contact elements were used between the rigid plates and the cylinder. The coefficient of friction for all of the contact elements was taken as 0.6 [25].

2.2 Concrete material model

Different material models are available in LS-DYNA to simulate concrete materials. Because the Karagozian and Case Concrete Damage Model Release 3 (K&C model) exhibited good agreement with the experimental results collected in previous studies, it was chosen for this study (e.g., [25]). The model was developed based on the theory of plasticity. The model has three shear failure surfaces: yield, maximum, and residual [26]. This material model has eighty parameters that can be either user defined or automatically generated. This study used the automatic generation option for the failure surface where f_c' was the main input to the model. Another input to the model, the fractional dilation parameter (ω), considers any volumetric change in concrete. The fractional dilation parameter is related to the dilation angle by Equation 3. Youssf et al. [20] suggested an equation (4) to calculate the dilation parameter to the CFFT with

traditional FRP. Youssef et al.'s equation was modified to propose a new equation (5) to calculate the dilation parameter of the CFFT with LRS-FRP based on the validation of the experimental results. In the case of a conventional concrete column without FRP confinement, the equation yields a dilation parameter of a constant value of 0.8, which is approximately equal to Tan 38^{o}. This result agreed with the common value of the dilation angle of the concrete material without FRP confinement. The dilation parameter for the hybrid system of a combination of the LRS-FRP and the traditional FRP was equal to the summation of the two dilation parameters (Equation 6).

$$\text{Dilation parameter } (\omega) = tan\ (\psi) \tag{3}$$

$$\text{Dilation parameter in case of traditional FRP } (\omega_1) = \text{-0.195 ln } (\frac{E_{f1}}{f_c'}) + 0.6115 \tag{4}$$

$$\text{Dilation parameter in case of LRS-FRP } (\omega_2) = \frac{0.8-0.015\ E_1/f_c'}{1+0.075\ E_1/f_c'} \tag{5}$$

$$\text{Dilation parameter in case of combination of traditional and LRS-FRP } (\omega_3) = (\text{-0.195 ln } (\frac{E_{f1}}{f_c'}) + 0.6115) + \frac{0.8-0.015\ E_1/f_c^{'}}{1+0.075\ E_1/f_c^{'}} \tag{6}$$

$$E_1 = \frac{2\ E_{f2}\ t_f}{D} \tag{7}$$

Where E_1 is the confinement modulus ratio, E_{f1} is the elastic modulus of the traditional FRP, E_{f2} is the tangent modulus of the LRS-FRP, t_f is the thickness of the FRP, D is the column's diameter, and f_c' is the characteristic cylindrical concrete strength at 28 days.

2.3 FRP material model

The material properties of PET-FRP and PEN-FRP composites have been studied by Dai et al. [13]. Such types of FRP have approximate bilinear stress-strain relationships that can be described in terms of two moduli of elasticity: the initial elastic modulus (E_{f1}) and the tangent modulus (E_{f2}). The material properties of PET-FRP and PEN-FRP are summarized in Table 2. The material properties of the glass and carbon FRP referenced in the manufacturer data sheet of Tyfo® SEH-51 and Tyfo® SCH-41 are summarized as well in Table 2. FRP composites were modeled as orthotropic materials using "108-ortho_elastic_plastic" material for LRS-FRP to simulate the bilinear behavior. Material model "002-orthotropic-elastic" was used for the traditional FRP to simulate the linear behavior. The "108-ortho_elastic_plastic" material model combines orthotropic, elastic, and plastic behaviors for shells only. This material is defined by the engineering constants: elastic modulus (E_{f1}), tangent modulus (Ef_2), shear modulus (G), and Poisson's ratio (PR) in the two principle axes (a and b). Additionally, the fiber orientation is defined by a vector. However, the tangent modulus does not exist in the material model of "002-orthotropic-elastic". Failure criterion for FRP composites was defined using "000-add_erosion," to assign the ultimate strain of FRP in the "EFFEPS" card.

2.4 Loading and boundary conditions

Displacements and rotations in all directions were prevented at the bottom of the bottom plate. Displacements in X and Y directions were prevented for all of the nodes of the top plate. Monotonic downward (negative Z direction) displacement loading was

applied on the top plate for axial compressive loading until failure occurred. Failure was defined as the rupture of the FRP or the crushing of the concrete cylinder.

2.5 Validation results

Figure 2 illustrates the axial strain-axial stress relationships for all of the cylinders gathered from the FE and the experimental results. The axial strain of each cylinder was obtained by dividing the axial displacement of the loading plate by the cylinder's height of 300 mm. The axial stress of each cylinder was obtained by dividing the axial reactions at the bottom of the bottom plate by the cross-sectional area of the cylinder. All simulated columns behaved in a manner similar to the tested cylinders until failure. All of the cylinders failed by FRP rupture whether in the experimental or FE category (Figure 3). The FE's average error rates in predicting the ultimate axial stress and ultimate axial strain were 9% and 10%, respectively. The error was calculated as the absolute value of the difference between the experimental results and the FE results divided by the experimental results.

The FE predicted accurately the initial stiffness and stiffness degradation of all of the cylinders until the axial stress reached the unconfined concrete cylindrical strength (f_c'). After this stress, the FE differentiated a little in values with the experimental results until failure. This difference in values was because the dilation angle was taken as a constant value in the FE. However, it would change with the axial stress level. However, the effect of the dilation did not significantly affect the overall behavior as the accuracy in predicting the ultimate strain was 91%, and the accuracy in predicting the ultimate stress was 90%.

3. Parametric Study

The LRS-FRP is a new composite that has only recently been investigated. Once the finite element model was validated, a comprehensive parametric study was conducted to numerically investigate the behavior of the CFFTs with LRS-FRP. The behavior of the CFFT using different FRP types, including traditional FRP and LRS-FRP, was investigated. A new hybrid system of FRP composites was investigated by combining traditional FRP with LRS-FRP to confine the concrete. The influence of fiber stacking sequences was investigated by placing the PET-FRP layers in the inner surface of the FRP tube and placing the traditional FRP in the outer tube for some columns and vice versa for others. In addition, the effects of the confinement ratio, the unconfined concrete nominal compressive strength (f_c'), the column's size, and the column's aspect ratio were investigated.

All of the investigated columns had a diameter of 150 mm, a height of 300 mm, and an aspect ratio of 2 except columns C44 to C48. Four different column sizes with aspect ratios of 2 were investigated during this study. The diameters X heights ranged from 150 mm X 300 mm to 1,500 mm X 3,000 mm. Three different column aspect ratios ranging from 2 to 10 were investigated. Seven different confinement ratios ranging from 0.3 to 1.2 were investigated for PET-FRP, PEN-FRP, Glass-FRP, and Carbon-FRP. Five concrete cylindrical compressive strengths (f_c') ranging from 27.6 MPa to 82.8 MPa were examined. Each parameter was studied independently, resulting in an analysis of 49 columns. Table 3 summarizes the investigated columns' variables.

3.1 LRS-FRP versus traditional FRP

The CFFTs with LRS-FRP and with traditional FRP were investigated with different confinement ratios ranging from 0.3 to 1.2. Figure 3 illustrates the typical axial strain-normalized strength behavior of the CFFTs with LRS-FRP and with traditional FRP. The normalized strength was calculated as the axial stress divided by the f_c'. All of the columns failed by FRP rupture. However, the CFFTs with traditional FRP behaved, as expected, with bilinear strain-stress relationships. The CFFTs with LRS-FRP behaved with trilinear behavior. This behavior of CFFTs with LRS-FRP was because of the effect of the bilinear behavior on the LRS-FRP instead of the linear behavior in the traditional FRP. All of the columns had the same initial stiffness. The reason was that the effect of the FRP confinement did not appear until the axial stress reached to almost the f_c' when the concrete volume change started to become positive (expansion; reference). The CFFTs with traditional FRP continued with the secant modulus until failure occurred. The CFFTs with LRS-FRP showed a stiffness degradation after axial strain of approximately 0.016 and 0.013 for PEN-FRP and PET-FRP, respectively. The CFFTs with LRS-FRP showed higher ultimate strain and lower secant stiffness than those with traditional FRP. As expected, the CFFTs with carbon FRP tubes showed higher secant stiffness and lower ultimate strain. The CFFTs with PET-FRP showed higher ultimate strain and lower secant stiffness. The CFFTs with LRS-FRP showed a higher strength than those with traditional FRP. The reason was the high hoop rupture strain of the LRS-FRP reached 8.7 times that of the carbon FRP and 2.9 times that of the glass FRP. The axial strength of the CFFTs with PEN-FRP and PET-FRP was almost the same.

However, the axial strength of the CFFT with PET-FRP was approximately 1.25 times that of the CFFT with PEN-FRP.

Figure 4 illustrates the relation between the confinement ratio and the normalized strength and between the confinement ratio and the ultimate axial strain for all of the FRP composites. This figure illustrates the efficiency of the different types of FRP in normalized strength and ultimate axial strain at the same confinement ratio. It is very clear in the figure that the CFFTs with LRS-FRP were more efficient than those with traditional FRP. This clearly indicated the great effect high rupture strain had on the confinement.

Figure 5 illustrates the axial strain-normalized strength for the CFFTs with traditional FRP, LRS-FRP, and hybrid FRP with the same confinement ratio of 1.2. Fiber stacking sequences were investigated by placing PET-FRP in the inner surface of the FRP tube and placing glass or carbon FRPs in the outer surface and vice versa. Figure 5(a) illustrates the PET, glass, and hybrid PET/glass where the PET was in the inner surface. In general, placing the LRS-FRP in the inner surface and the traditional FRP in the outer surface revealed a better performance than placing the traditional FRP in the inner surface. The reason for this behavior was that the rupture strain of the traditional FRP is much lower than that of the traditional FRP. Therefore, the traditional FRP ruptured earlier than the LRS-FRP. Hence, when the traditional FRP was placed in the inner surface, the LRS-FRP was controlled by the traditional FRP rupture strain, and it ruptured directly after the rupture of the traditional FRP. However, when the traditional FRP was placed in the outer surface, the LRS-FRP was controlled by it, and it continued until ruptured with high hoop strains. Therefore, the hybrid FRP of PET/traditional FRP

reached higher hoop strains than the traditional FRP. However, the hybrid FRP ruptured at a lower strain than that of the LRS-FRP alone because of the synergistic effect from hybridization.

In general, the hybrid of PET/glass performed better than PET/carbon. The reason for that was the large difference in rupture strains between the PET and carbon. In general, the axial strain-normalized strength relation of the CFFTs with hybrid FRP was nonlinear instead of bilinear in the case of LRS-FRP alone. The relation was linear in the case of traditional FRP alone. The strength and ultimate axial strain of the CFFTs with hybrid FRP increased when the traditional FRP was increased. This indicated that using few layers of LRS-FRP with the traditional FRP would improve the CFFT's performance a lot. However, the difference in the confinement ratio contribution of the LRS-FRP has to be considerable in order to avoid sudden failure as in the case of (PET-I+Carbon) in Figure 5(c). When the carbon FRP reached its ultimate strain (1% only), it failed and one layer of PET-FRP was not enough to continue to confine the concrete core, which led to rupture of the PET layer as well.

3.2 Unconfined concrete compressive strength ($\boldsymbol{f'_c}$)

Five columns were studied with different concrete unconfined compressive strengths (f'_c) ranging from 27.6 MPa to 82.8 MPa. Figure 6 illustrates the axial strain-normalized strength relation of the CFFTs with different f'_c. In general, changing the f'_c did not affect the normalized strength or the ultimate axial strain because the columns had the same FRP confinement ratios. However, when the concrete core was high-strength ($f'_c \geq 55.2$ MPa), the strength and ultimate axial strain were inversely proportional with the f'_c. The

lateral concrete expansion is dependent on the concrete mechanical properties. Therefore, the lateral expansion of high-strength concrete is significantly higher than that of the normal strength concrete, which reduces the effect of FRP confinement. The ultimate axial strain and the normalized strength decreased by 14.6% and 9.0%, respectively when the f_c' of the high-strength concrete increased by 25% (from 55.2 MPa to 69.0 MPa). The ultimate axial strain and the normalized strength decreased by 21.1% and 24.9%, respectively when the f_c' of the high-strength concrete increased by 50% (from 55.2 MPa to 82.8 MPa).

3.3 Column size

Four columns with sizes ranging from 150mm X 300mm to 1,500mm X 3,000mm were studied. Figure 7 illustrates the axial strain-normalized strength relation of the CFFTs with different column sizes. In general, the strength was reduced when the column size was increased as the FRP confinement could not affect the whole cross-section. Figure 8 shows the axial stress distribution of all of the columns in the mid and top cross-sections. It is very clear that the FRP confinement affected a zone along the outer perimeter in the cross-section, and this zone decreased when the column diameter increased. However, the behavior of the columns with dimensions of 150mm X 300mm and 200mm X 400mm was almost the same in axial strain-normalized strength as the behavior in cross-section. This behavior was because both dimensions were considerably low for a confinement ratio of 1.2.

3.4 Column aspect ratio

Three columns with different column aspect (height-to-diameter) ratios ranging from 2 to 10 were studied. Figure 9 illustrates the axial strain-normalized strength relation of the CFFTs with different aspect ratios. The ultimate axial strain and axial strength decreased when the column's aspect ratio increased. The column with an aspect ratio of 2 failed by FRP rupture. However, the columns with aspect ratios of 5 and 10 failed by compression failure. Figure 10 illustrates the column's deformation for different aspect ratios. Figure 10(a) illustrates the global buckling that occurred in the column with an aspect ratio of 10, leading to compression failure. Figure 10(b) illustrates the deformation of the column, with an aspect ratio of 5, that bulged in the top and bottom thirds leading to compression failure. Figures 10(c) and 10(d) illustrate the common failure of the confined short column of FRP rupture at the middle part. The ultimate axial strain decreased by 26% and the axial strength of the CFFT with LRS-FRP decreased by 48% when the aspect ratio increased from 2 to 5. The ultimate axial strain decreased by 63% and the axial strength of the CFFT with LRS-FRP decreased by 58% when the aspect ratio increased from 2 to 10.

4. Findings and Conclusions

The behavior of the concrete-filled fiber tubes (CFFT) with new high deformable fiber reinforced polymers under axial compressive loading was investigated. Unlike the traditional fiber reinforced polymers (FRP) like carbon, glass, aramid, etc., the new FRP composites have a large rupture strain and are made with cheap materials. The large rupture strain (LRS) FRP composites are made with polyethylene naphthalate (PEN) and

polyethylene terephthalate (PET) fibers. The PEN and PET fibers can be used in green buildings. They are environmentally friendly as they are made from recycled materials (e.g. bottles). They have a high ultimate strain (> 5.0%), however their elastic modulus is low. This study used finite element (FE) analysis using LS-DYNA software to conduct an extensive parametric study to investigate the behavior of the CFFTs with the LRS-FRP under axial compressive loading.

Forty-nine columns were investigated to determine important factors may affect the behavior of the CFFTs under axial compressive loading. A high range of FRP confinement ratios was investigated. In addition, the effects of the unconfined concrete compressive strength (f_c'), column size, and column aspect ratio on the behavior of the CFFT were studied. A comparison between the behavior of the CFFTs with LRS-FRP and the traditional FRP (carbon and glass) with a high range of confinement ratios was conducted as well. This paper introduced a new state-of-the-art hybrid FRP to be used for the CFFT columns by investigating different combinations of traditional FRP with LRS-FRP. Generally, the CFFTs with LRS-FRP showed a remarkable behavior under axial loading in strength and ultimate strain. The LRS-FRP composites were more efficient than the traditional FRP composites in strength and ultimate strain. The behavior of the hybrid FRP with a stacking sequence of LRS/glass (inner/outer of the tube) showed much better behavior in strength than the traditional FRP or the LRS-FRP. However, this hybrid FRP showed a higher ultimate axial strain than the traditional FRP. The LRS alone was better in the ultimate axial strain. A new equation to estimate the concrete dilation parameter and dilation angle of the CFFT columns with LRS-FRP tubes or hybrid FRP tubes was suggested.

Acknowledgments

This research was supported by the National University Transportation Center (NUTC) at Missouri University of Science and Technology (Missouri S&T). However, any opinions, findings, conclusions, and recommendations presented in this paper are those of the authors and do not necessarily reflect the views of the sponsors.

Author Contributions

Omar Abdelkarim carried out the finite element modeling presented in this manuscript. Dr. Mohamed ElGawady was the initiator of the research idea and supervisor of all of the technical work reported in this manuscript.

Conflicts of Interest

The authors declare no conflict of interest.

References

1. Lechat, C.; Bunsell, A.R.; Davies, P. Tensile and creep behaviour of polyethylene terephthalate and polyethylene naphthalate fibres. *Journal of Materials Science* **2011**, *46*, 528-533.

2. Venkatachalam, S.; Nayak, S.G.; Labde, J.V.; Gharal, P.R.; Rao, K.; Kelkar, A.K. Degradation and recyclability of poly (ethylene terephthalate). *Edited by Hosam El-Din M. Saleh* **2012**, 107.

3. Qasrawi, Y.; Heffernan, P.J.; Fam, A. Performance of concrete-filled frp tubes under field close-in blast loading. *Journal of Composites for Construction* **2014**.

4. Moon, J.; Lehman, D.E.; Roeder, C.W.; Lee, H.-E. Strength of circular concrete-filled tubes with and without internal reinforcement under combined loading. *Journal of Structural Engineering* **2012**, *139*, 04013012.

5. ElGawady, M.A.; Sha'lan, A. Seismic behavior of self-centering precast segmental bridge bents. *Journal of Bridge Engineering* **2010**, *16*, 328-339.

6. Sadeghian, P.; Fam, A. Bond-slip analytical formulation toward optimal embedment of concrete-filled circular frp tubes into concrete footings. *Journal of engineering mechanics* **2010**, *136*, 524-533.

7. ElGawady, M.; Booker, A.J.; Dawood, H.M. Seismic behavior of posttensioned concrete-filled fiber tubes. *Journal of Composites for Construction* **2010**, *14*, 616-628.

8. Shao, Y.; Mirmiran, A. Experimental investigation of cyclic behavior of concrete-filled fiber reinforced polymer tubes. *Journal of Composites for Construction* **2005**, *9*, 263-273.

9. Fam, A.; Flisak, B.; Rizkalla, S. Experimental and analytical modeling of concrete-filled frp tubes subjected to combined bending and axial loads. *ACI Struct. J* **2003**, *100*, 499-509.

10. Zhang, W.; Shahrooz, B.M. *Analytical and experimental studies into behavior of concrete-filled tubular columns*. Cincinnati Infrastructure Institute, University of Cincinnati: 1997.

11. Ispir, M. Monotonic and cyclic compression tests on concrete confined with pet-frp. *Journal of Composites for Construction* **2014**, *19*, 04014034.

12. Bai, Y.-L.; Dai, J.-G.; Teng, J. Cyclic compressive behavior of concrete confined with large rupture strain frp composites. *Journal of Composites for Construction* **2013**, *18*, 04013025.

13. Dai, J.-G.; Bai, Y.-L.; Teng, J. Behavior and modeling of concrete confined with frp composites of large deformability. *Journal of Composites for Construction* **2011**.

14. Anggawidjaja, D.; Ueda, T.; Dai, J.; Nakai, H. Deformation capacity of rc piers wrapped by new fiber-reinforced polymer with large fracture strain. *Cement and Concrete Composites* **2006**, *28*, 914-927.

15. Jirawattanasomkul, T.; Dai, J.-G.; Zhang, D.; Senda, M.; Ueda, T. Experimental study on shear behavior of reinforced-concrete members fully wrapped with large rupture-strain frp composites. *Journal of Composites for Construction* **2013**, *18*, A4013009.

16. Mirmiran, A.; Zagers, K.; Yuan, W. Nonlinear finite element modeling of concrete confined by fiber composites. *Finite Elements in Analysis and Design* **2000**, *35*, 79-96.

17. Yu, T.; Teng, J.; Wong, Y.; Dong, S. Finite element modeling of confined concrete-i: Drucker–prager type plasticity model. *Engineering Structures* **2010**, *32*, 665-679.

18. Rousakis, T.C.; Karabinis, A.I.; Kiousis, P.D.; Tepfers, R. Analytical modelling of plastic behaviour of uniformly frp confined concrete members. *Composites Part B: Engineering* **2008**, *39*, 1104-1113.

19. Karabinis, A.I.; Rousakis, T.C.; Manolitsi, G.E. 3d finite-element analysis of substandard rc columns strengthened by fiber-reinforced polymer sheets. *Journal of Composites for Construction* **2008**, *12*, 531-540.

20. Youssf, O.; ElGawady, M.A.; Mills, J.E.; Ma, X. Finite element modelling and dilation of frp-confined concrete columns. *Engineering Structures* **2014**, *79*, 70-85.

21. Jankowiak, T.; Lodygowski, T. Identification of parameters of concrete damage plasticity constitutive model. *Foundations of civil and environmental engineering* **2005**, *6*, 53-69.

22. Kmiecik, P.; Kamiński, M. Modelling of reinforced concrete structures and composite structures with concrete strength degradation taken into consideration. *Archives of civil and mechanical engineering* **2011**, *11*, 623-636.

23. Rezazadeh, M.; Costa, I.; Barros, J. Influence of prestress level on nsm cfrp laminates for the flexural strengthening of rc beams. *Composite Structures* **2014**, *116*, 489-500.

24. Hallquist, J.O. Ls-dyna theory manual. *Livermore software Technology corporation* **2006**, *3*.

25. Abdelkarim, O.I.; ElGawady, M.A. Analytical and finite-element modeling of frp-concrete-steel double-skin tubular columns. *Journal of Bridge Engineering* **2014**.

26. Malvar, L.J.; Crawford, J.E.; Wesevich, J.W.; Simons, D. A plasticity concrete material model for dyna3d. *International Journal of Impact Engineering* **1997**, *19*, 847-873.

Table 1. Summary of cylinders variables (Modified from Dai et al. 2011, © ASCE)

Cylinder label	Diameter (mm) X height (mm)	f'_c (MPa)	FRP type	No. of layers	Total thickness (mm)
PEN-600-I	150 x 300	39.2	PEN-600	One	0.85
PEN-600-II				Two	1.70
PEN-600-III				Three	2.54
PET-600-I		32.5	PET-600	One	0.84
PET-600-II				Two	1.68
PET-600-III				Three	2.52
PET-900-I		39.2	PET-900	One	1.26
PET-900-II				Two	2.52
PET-900-III				Three	3.79

Table 2. Material properties of FRP composites (part of this reproduced after Dai et al. [12] ©ASCE)

FRP Type	E_{f1} (GPa)	E_{f2} (GPa)	Tensile strength (MPa)	Rupture strain (%)
PET-FRP	17.9	8.3	750	8.7
PEN-FRP	27.0	12.0	760	6.3
Glass-FRP	26.1	—	575	2.2
Carbon-FRP	95.8	—	986	1.0

Table 3. Parametric study columns' variables

Parameter	Col. label	Diameter (mm)	Height (mm)	Aspect ratio	LRS-FRP thick. (mm)	Traditional FRP thickness (mm)	$f_c^{'}$ (MPa)	CR	ω
PET-FRP	C0	150	300	2	3.4	0	27.6	1.20	0.29
	C1	150	300	2	2.97	0	27.6	1.05	0.33
	C2	150	300	2	2.55	0	27.6	0.90	0.37
	C3	150	300	2	2.13	0	27.6	0.75	0.41
	C4	150	300	2	1.7	0	27.6	0.60	0.46
	C5	150	300	2	1.28	0	27.6	0.45	0.52
	C6	150	300	2	0.85	0	27.6	0.30	0.60
PEN-FRP	C7	150	300	2	3.1	0	27.6	1.20	0.23
	C8	150	300	2	2.7	0	27.6	1.05	0.26
	C9	150	300	2	2.32	0	27.6	0.90	0.30
	C10	150	300	2	1.92	0	27.6	0.75	0.34
	C11	150	300	2	1.54	0	27.6	0.60	0.40
	C12	150	300	2	1.15	0	27.6	0.45	0.47
	C13	150	300	2	0.78	0	27.6	0.30	0.55
GLASS-FRP	C14	150	300	2	0	4.33	27.6	1.20	-0.17
	C15	150	300	2	0	3.8	27.6	1.05	-0.14
	C16	150	300	2	0	3.25	27.6	0.90	-0.11
	C17	150	300	2	0	2.7	27.6	0.75	-0.08
	C18	150	300	2	0	2.15	27.6	0.60	-0.03
	C19	150	300	2	0	1.62	27.6	0.45	0.02
	C20	150	300	2	0	1.07	27.6	0.30	0.10
CARBON-FRP	C21	150	300	2	0	2.6	27.6	1.20	-0.32
	C22	150	300	2	0	2.27	27.6	1.05	-0.30
	C23	150	300	2	0	1.94	27.6	0.90	-0.27
	C24	150	300	2	0	1.62	27.6	0.75	-0.23
	C25	150	300	2	0	1.3	27.6	0.60	-0.19
	C26	150	300	2	0	0.98	27.6	0.45	-0.13
	C27	150	300	2	0	0.65	27.6	0.30	-0.05

Table 3. Parametric study columns' variables (cont'd)

PET/Glass (inside/ outside)	C28	150	300	2	2.55	1.07	27.6	1.20	0.47
	C29	150	300	2	1.7	2.15	27.6	1.20	0.43
	C30	150	300	2	0.85	3.25	27.6	1.20	0.48
Glass/PET (inside/ outside)	C31	150	300	2	2.55	1.07	27.6	1.20	0.47
	C32	150	300	2	1.7	2.15	27.6	1.20	0.43
	C33	150	300	2	0.85	3.25	27.6	1.20	0.48
PET/Carbon (inside/ outside)	C34	150	300	2	2.55	0.65	27.6	1.20	0.31
	C35	150	300	2	1.7	1.3	27.6	1.20	0.27
	C36	150	300	2	0.85	1.95	27.6	1.20	0.33
Carbon/PET (inside/ outside)	C37	150	300	2	2.55	0.65	27.6	1.20	0.31
	C38	150	300	2	1.7	1.3	27.6	1.20	0.27
	C39	150	300	2	0.85	1.95	27.6	1.20	0.33
Concrete Strength (f_c')	C40	150	300	2	5.1	0	41.4	1.20	0.29
	C41	150	300	2	6.8	0	55.2	1.20	0.29
	C42	150	300	2	8.5	0	69	1.20	0.29
	C43	150	300	2	10.2	0	82.8	1.20	0.29
Column size	C44	200	400	2	4.55	0	27.6	1.20	0.29
	C45	300	600	2	6.8	0	27.6	1.20	0.29
	C46	1500	3000	2	34	0	27.6	1.20	0.29
Column aspect ratio	C47	300	1500	5	6.8	0	27.6	1.20	0.29
	C48	300	3000	10	6.8	0	27.6	1.20	0.29

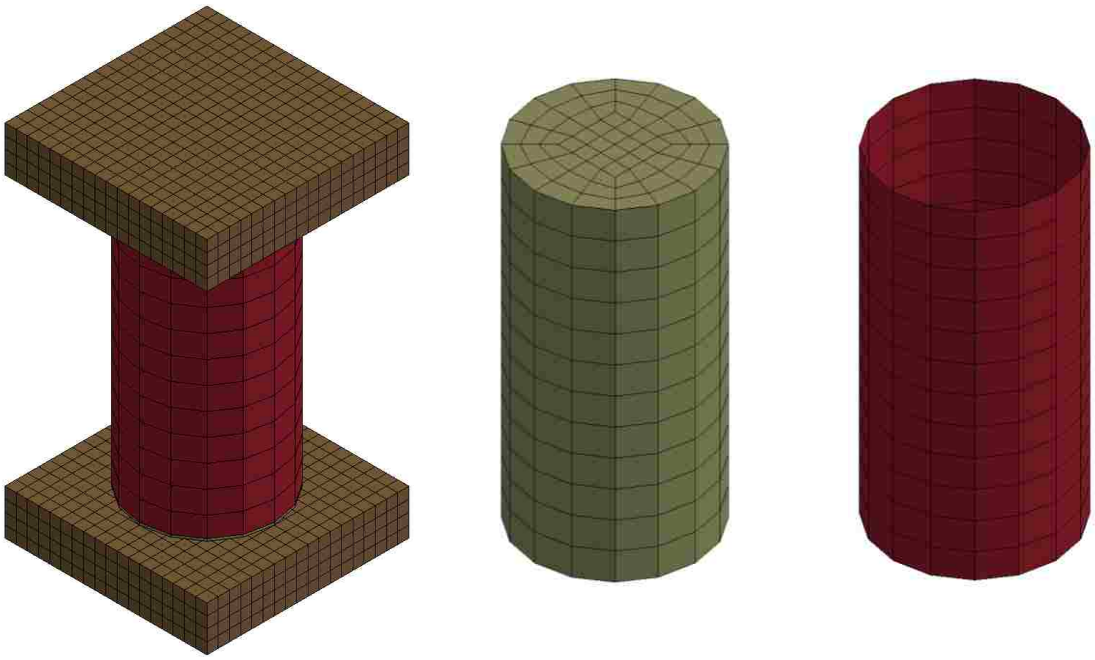

(a) (b) (c)

Figure 1. Finite element model components: (**a**) 3-D view, (**b**) concrete cylinder, and (**c**) FRP tube

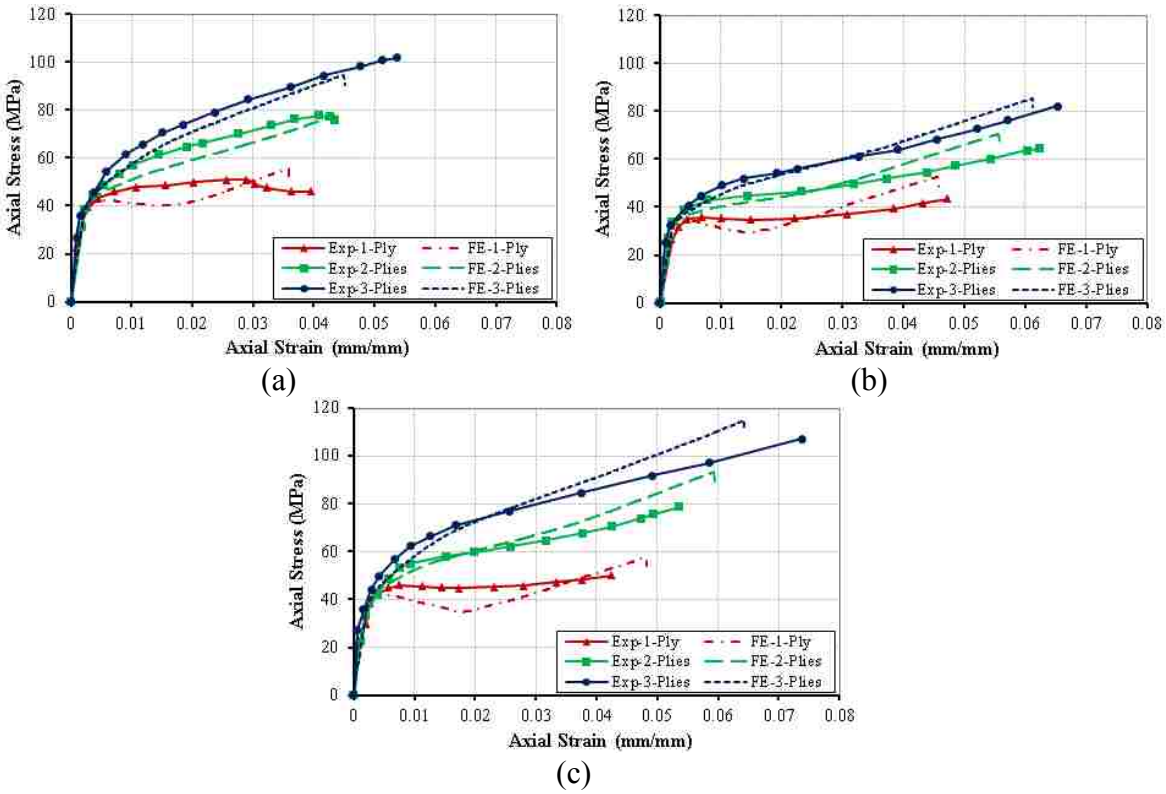

Figure 2. FE results versus experimental results by Dai et al. [12] of the CFFT with: (**a**) PEN-FRP-600, (**b**) PET-FRP-600, and (**c**) PET-FRP-900

(a) (b)

Figure 3. FRP rupture in FE analysis and experimental work by Dai et al. [12] ©ASCE of the PEN-600-I: (**a**) Experimental and (**b**) FE

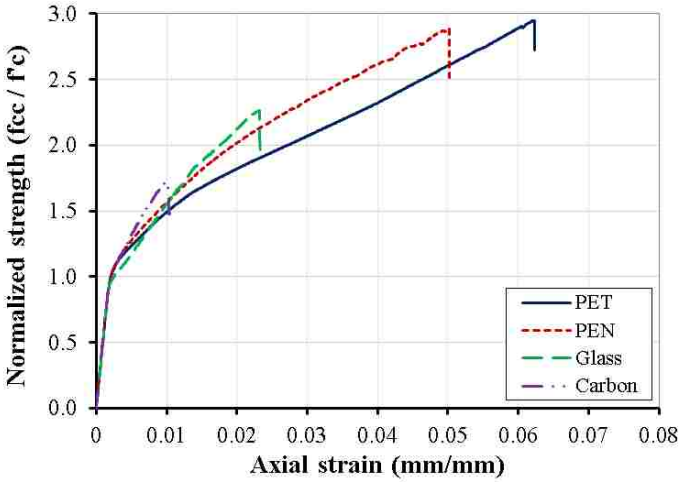

Figure 4. Axial strain-normalized strength (f_{cc}/f_c') relationship for PET, PEN, Glass, and Carbon FRP with same confinement ratio of 0.9

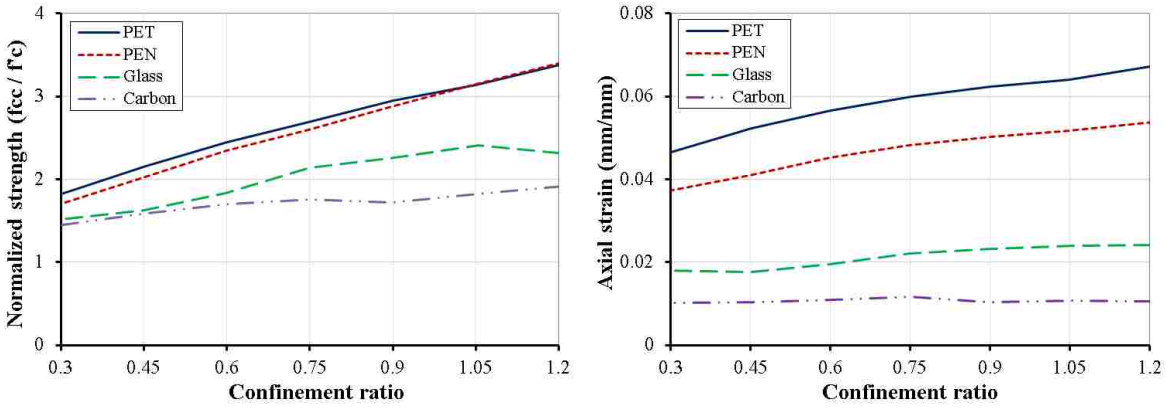

(a) (b)

Figure 5. Efficiency of the traditional versus LRS-FRP composites in: (**a**) normalized axial strength, (**b**) axial strain

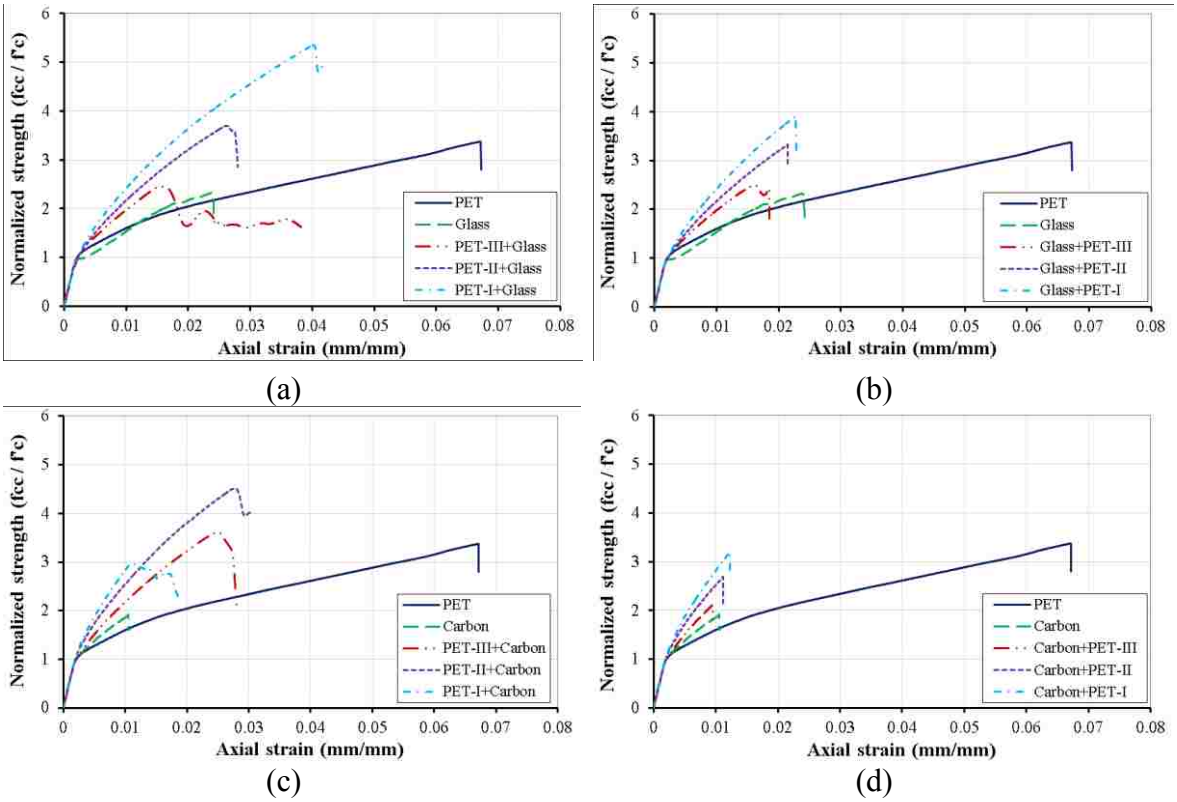

Figure 6. Axial strain-normalized strength relationship of the traditional, LRS, and hybrid FRP: (**a**) PET/Glass-FRP, (**b**) Glass/PET, (**c**) PET/Carbon-FRP, and (**d**) Carbon/PET-FRP

Note: PET/Glass-FRP is the stacking sequence of inside/outside FRP and vice versa

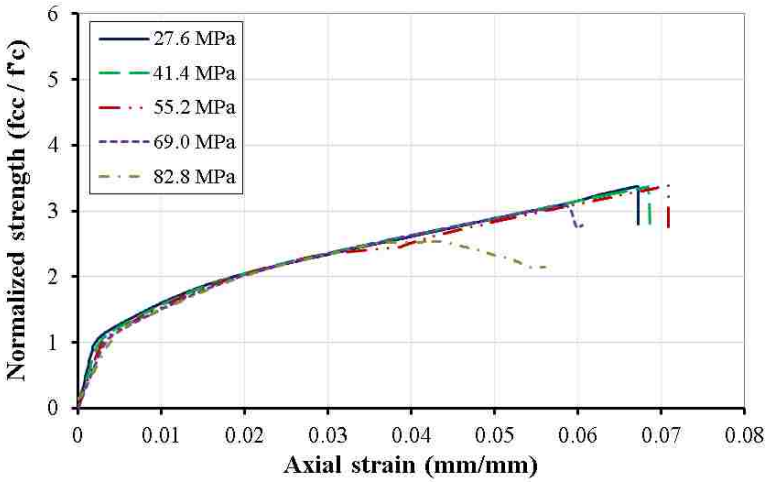

Figure 7. Axial strain-normalized strength relationship of CFFT with LRS-FRP with different concrete compressive strength (f_c')

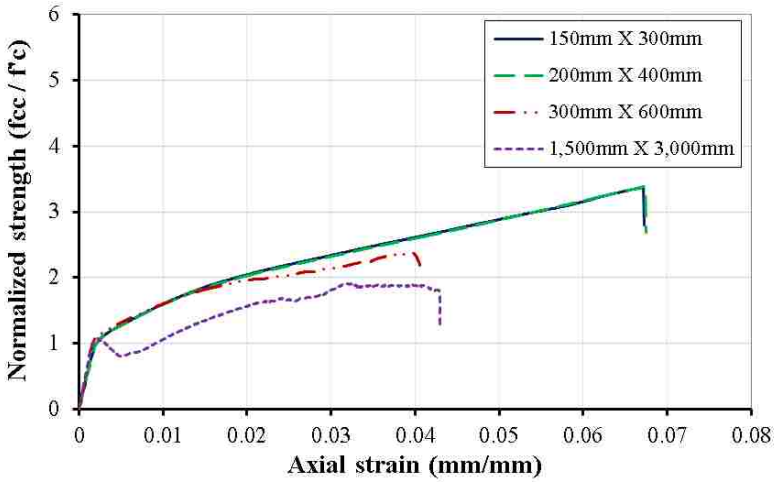

Figure 8. Axial strain-normalized strength relationship of CFFT with LRS-FRP with different column sizes

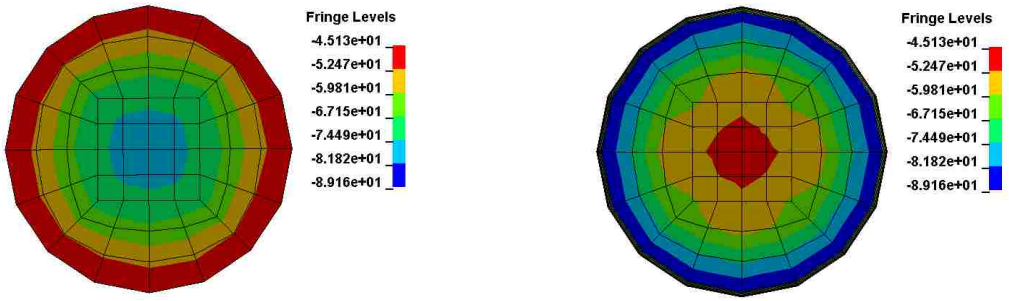

Mid cross-section Top cross-section

(a)

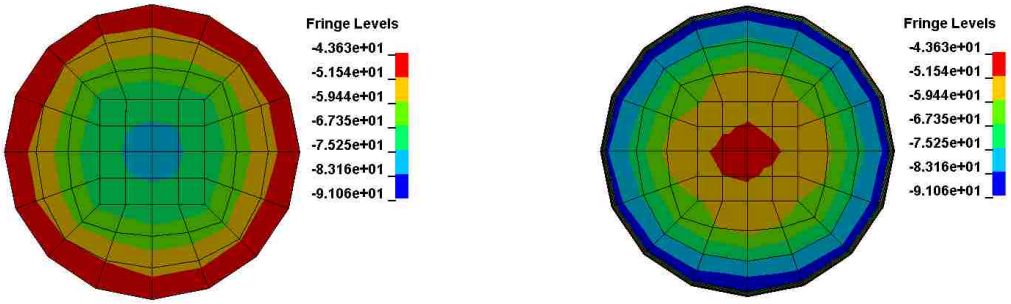

Mid cross-section Top cross-section

(b)

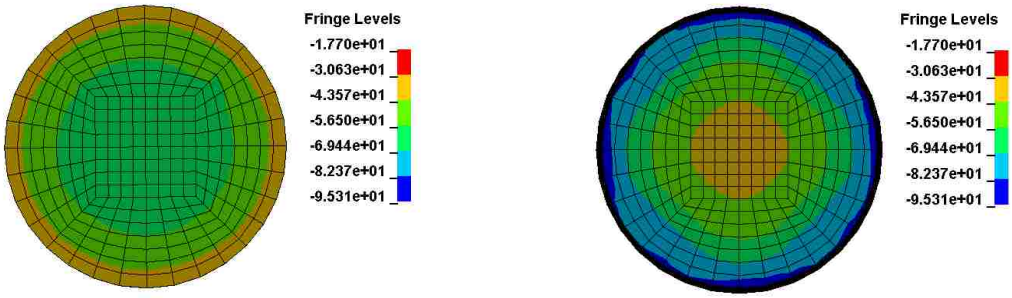

Mid cross-section Top cross-section

(c)

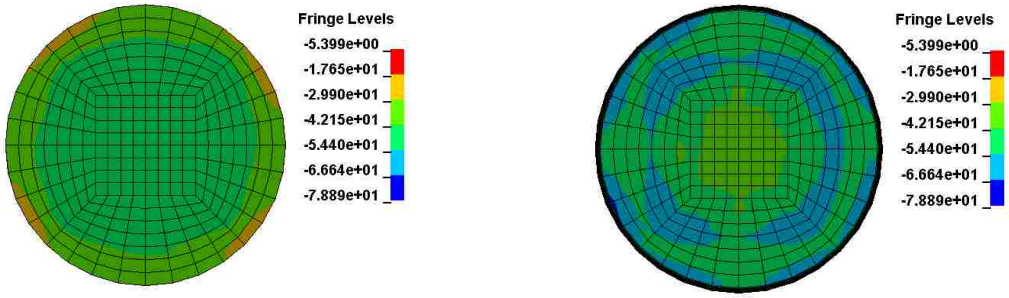

Mid cross-section Top cross-section

(d)

Figure 9. Axial stress in cross-section of the columns of sizes: (**a**) 150mm X 300mm, (**b**) 200mm X 100mm, (**c**) 300mm X 600mm, and (**d**) 1,500mm X 3,000mm

Note: Fringe levels shows the axial stresses legend in MPa

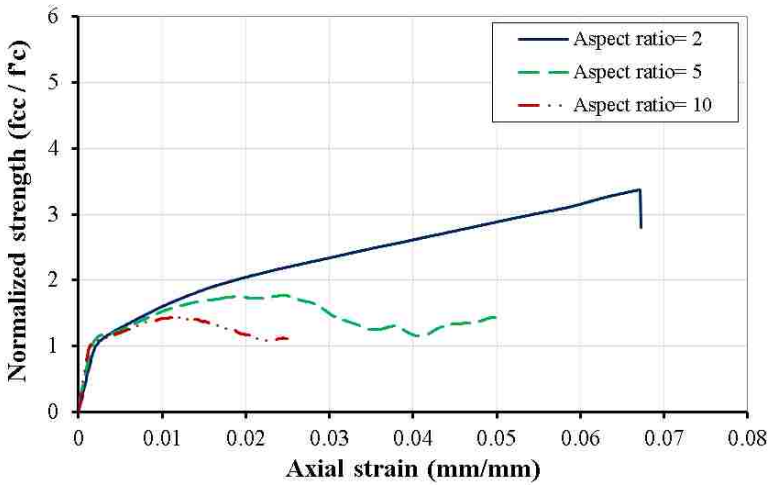

Figure 10. Axial strain-normalized strength relationship of CFFT with LRS-FRP with different column aspect ratios

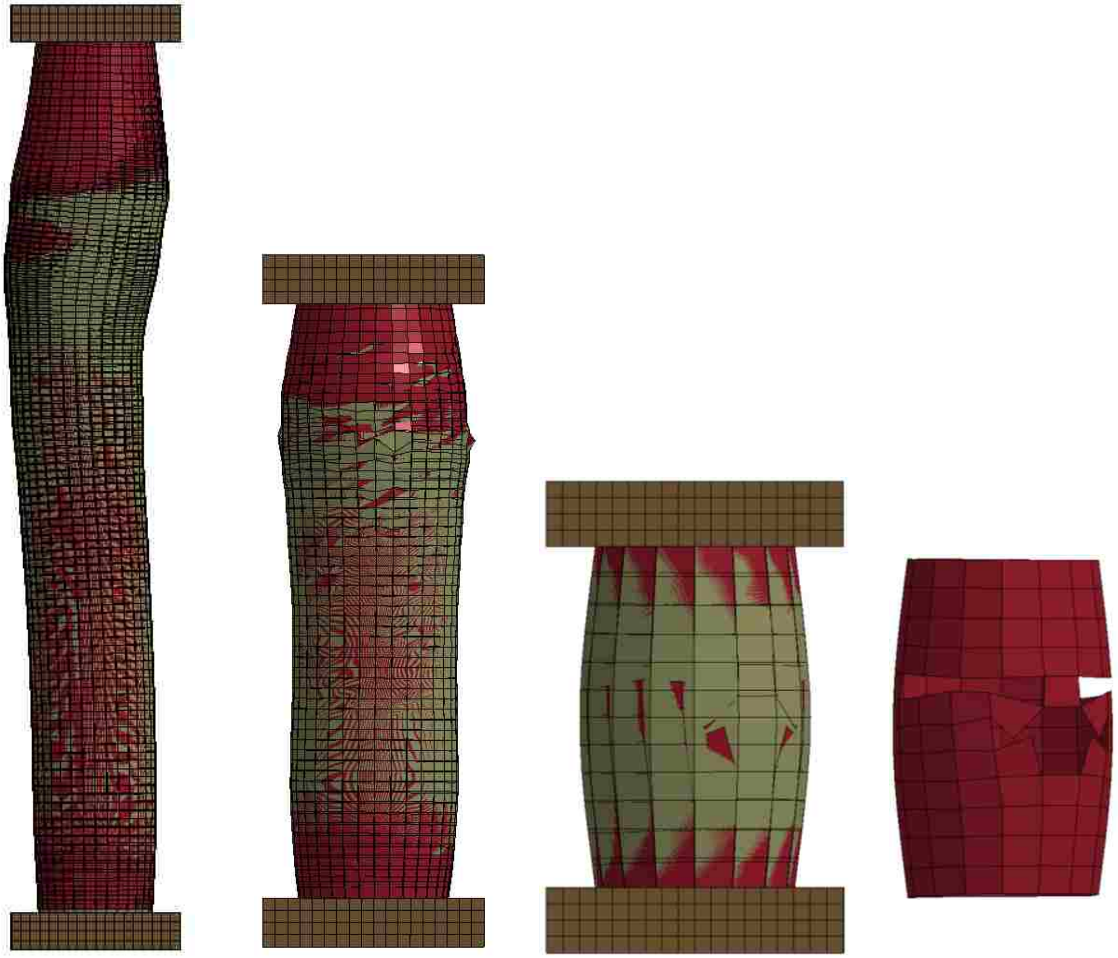

(a) (b) (c) (d)

Figure 11. Column deformation with different aspect ratios: (**a**) aspect ratio of 10, (**b**) aspect ratio of 5, (**c**) aspect ratio of 2, and (**d**) FRP rupture of column with aspect ratio of 2

REFERENCES

AASHTO, (2012). AASHTO-LRFD Bridge Design Specifications – Customary US Units, sixth edition, Washington, DC.

AASHTO, (2010). AASHTO-LRFD Bridge Design Specifications – Customary US Units, fifth edition, Washington, DC.

Abdelkarim, O. and ElGawady, M. (2014a). "Behavior of Hybrid FRP-Concrete-Steel Double-Skin Tubes Subjected to Cyclic Axial Compression." Structures Congress 2014: pp. 1002-1013.

Abdelkarim, O. and ElGawady, M. (2014b). "Analytical and Finite-Element Modeling of FRP-Concrete-Steel Double-Skin Tubular Columns." J. Bridge Eng., 10.1061/(ASCE)BE.1943-5592.0000700 , B4014005.

Agrawal, A. K., Liu, G., and Alampalli, S. (2013). "Effects of Truck Impacts on Bridge Piers." Advanced Materials Research, 639-640, pp.13-25.

Agrawal, A.K. (2011). "Bridge Vehicle Impact Assessment: Final Report." University Transportation Research Center and New York State Department of Transportation.

Albitar, M., Ozbakkaloglu, T., and Louk Fanggi, B. (2015). "Behavior of FRP-HSC-Steel Double-Skin Tubular Columns under Cyclic Axial Compression." J. Compos. Constr., 19(2), 04014041.

Buth, C. E., Brackin, M. S., Williams, W. F., and Fry, G.T. (2011). "Collision Loads On Bridge Piers: Phase 2." Texas Department of Transportation Research and Technology Implementation Office, Report 9-4973-2.

Buth, C. E., Williams, W. F., Brackin, M. S., Lord, D., Geedipally, S. R., and Abu-Odeh, A. Y. (2010). "Analysis of Large Truck Collisions with Bridge Piers: Phase 1." Texas Department of Transportation Research and Technology Implementation Office, 9-4973-1.

ElGawady, M. and Sha'lan, A. (2011). "Seismic Behavior of Self-Centering Precast Segmental Bridge Bents." J. Bridge Eng., 16(3), 328–339.

ElGawady, M., Booker, A., and Dawood, H. (2010). "Seismic Behavior of Posttensioned Concrete-Filled Fiber Tubes." J. Compos. Constr., 14(5), 616–628.

ElGawady, M. and Dawood, H. (2012). "Analysis of segmental piers consisted of concrete filled FRP tubes." Engineering Structures, Vol. 38, pp. 142-152.

El-Tawil, S., Severino, E., and Fonseca, P. (2005). "Vehicle Collision with Bridge Piers." J. Bridge Eng., 10(3), 345-353.

Eurocode 1 (2002). "Actions on structures – Part 1-1: General actions – Densities, self-weight, imposed loads for buildings." Final Draft prEN 1991-1-1, October.

Dawood, H. M. and ElGawady, M. (2013). "Performance-based seismic design of unbonded precast post-tensioned concrete filled GFRP tube piers." Composites Part B: Engineering, 44(1), 357-367.

Fouche, P., Bruneau, M. (2010). "Non-Linear Analysis of Multi-Hazard Performance of Cylindrical Concrete Filled Steel Tubes Bridge Piers." Proceedings of 8th International Conference on Short and Medium Span Bridges, Canada.

Hajjar J. (2000). "Concrete-filled steel tube columns under earthquake loads." Structural Engineering and Materials; 2(1):72–82.

Han, L.H., Tao, Z., Liao, F.Y., and Xu, Y. (2010). "Tests on Cyclic Performance of FRP-Concrete –Steel Double-Skin Tubular Columns." *Thin-Walled Structures*, 4, 430-439.

Harik, I., Shaaban, A., Gesund, H., Valli, G., and Wang, S. (1990). "United States Bridge Failures, 1951–1988." J. Perform. Constr. Facil., 4(4), 272–277.

Hoshikuma, J., and Priestley, M. J. N. (2000). "Flexural behavior of circular hollow columns with a single layer of reinforcement under seismic loading." Report No. SSRP-2000/13, University of California, San Diego, La Jolla, CA.

Huang, H., Han, L. H., Zhao, X. (2013). "Investigation on concrete filled double skin steel tubes (CFDSTs) under pure torsion." Journal of Constructional Steel Research, Volume 90, 221-234.

Jacobsen, L. S. (1930). “Steady forced vibrations as influenced by damping.” Trans. ASME, 50(4), 169–181.

Lee, J., Choi, J., Hwang, D., and Kwahk, I. (2014). “Seismic Performance of Circular Hollow RC Bridge Columns.” KSCE Journal of Civil Engineering, Vol. 19(5), pp. 1456-1467.

Lee, G. C., Mohan, S., Huang, C., and Fard, B. N. (2013). “A Study of US Bridge Failures (1980-2012).” MCEER Technical Report 13-0008, Buffalo, NY.

McGrath, J.J. (2013). “Replacement of Missouri Route M Overpass Creamed by Freight-Train Crash in Scott County Estimated to Cost about $3 Million: Accident is the Third Railroad Mishap in Four Months in Rockview- May 26, 2013.” International Business times, http://www.ibtimes.com/replacement-missouri-route-m-overpass-creamed-freight-train-crash-scott-county-estimated-cost-about, Accessed by July, 2014.

Mander, J. B., Priestley, M. J. N., Park, R. (1983). “Behavior of Ductile Hollow Reinforced Concrete Columns.” Bulletin of the New Zealand National Society for Earthquake Engineering, Vol. 16, No. 4, December, pp. 273-290.

Montague, P., (1978). “Experimental behavior of double-skinned, composite, circular cylindrical-shells under external-pressure.” Journal of Mechanical Engineering Science, 20(1), pp. 21–34.

Moon, J., Lehman, D., Roeder, C., and Lee, H. (2013). “Strength of Circular Concrete-Filled Tubes with and without Internal Reinforcement under Combined Loading.” J. Structural Engineering, 139(12).

Ozbakkaloglu, T. and Idris, Y. (2014). “Seismic Behavior of FRP-High-Strength Concrete–Steel Double-Skin Tubular Columns.” J. Struct. Eng., 140(6), 04014019.

Priestley, M.J.N., Seible, F., Calvi, M. (1995.) “Seismic Design and Retrofit of Bridges.” John Wiley & Sons, Inc., New York, NY, September, pp. 672.

Shakir-Khalil, H., and Illouli, S. 1987. "Composite columns of concentric steel tubes." Proc., Conf. on the Design and Construction of Non-Conventional Structures, Vol. 1, London, pp. 73–82.

Sharma, H., Hurlebaus, S., Gardoni, P. (2012). "Performance-based response evaluation of reinforced concrete columns subject to vehicle impact." Inter. Journal of Impact Eng., (43), 52-62.

Shin, M. and Andrawes, B. (2010). "Experimental Investigation of Actively Confined Concrete Using ShapeMemory Alloys." J. Eng. Struct. 32:3, 656-664.

Sierakowsi, R. L. and Chaturved, S. K. (1997). "Dynamic Loading and Characterization of Fiber-Reinforced Composites." John Wiley & Sons, Inc., New York, USA.

Teng, J. G., Yu, T., Wong, Y. L., and Dong, S. L. (2007). "Hybrid FRP concrete-steel tubular columns: Concept and behavior." Constr. Build. Mater., 21(4), 846–854.

Teng, J.G., Yu, T., Wong, Y.L., and Dong, S.L. (2005). "Innovative FRP-Steel-Concrete Hybrid Columns." Advances in Steel Structures, 1, 545-554.

Teng, J.G., Yu, T., and Wong, Y.L. (2004). "Behavior of Hybrid FRP-Concrete-Steel Double-Skin Tubular Columns." *Proc. 2nd Int. Conf. on FRP Composites in Civil Engineering*, Adelaide, Australia, 811-818.

Thilakarathna, H.M.I., Thambiratnam, D.P., Dhanasekar, M., Perera, N. (2010). "Numerical simulation of axially loaded concrete columns under transverse impact and vulnerability assessment." Inter. Journal of Impact Eng., (37), 1100-1112.

Wong, Y. L., Yu, T., Teng, J. G., and Dong, S. L. (2008). "Behavior of FRP-confined concrete in annular section columns." Compos. B Eng., 39(3), 451–466.

Yagishita F, Kitoh H, Sugimoto M, Tanihira T, Sonoda K. (2000). "Double-skin composite tubular columns subjected cyclic horizontal force and constant axial force." Proceedings of the Sixth ASCCS Conference, Los Angeles, USA, March 22–24, pp. 497–503.

Yu, T., Teng, J., and Wong, Y. (2010). "Stress-Strain Behavior of Concrete in Hybrid FRP-Concrete-Steel Double-Skin Tubular Columns." *J. Struct. Eng.*, 136(4), 379–389.

Yu, T., Wong, Y., Teng, J., Dong, S., and Lam, E. (2006). "Flexural Behavior of Hybrid FRP-Concrete-Steel Double-Skin Tubular Members." J. Compos. Constr., 10(5), 443–452.

Zhang, B., Teng, J. G. and Yu, T. (2012). "Behaviour of hybrid double-skin tubular columns subjected to combined axial compression and cyclic lateral loading." *Sixth International Conference on FRP Composites in Civil Engineering* (pp. 1-7). Rome, Italy.

Zhu, Z., Ahmad, I., and Mirmiran, A. (2006). "Seismic performance of concrete-filled FRP tube columns for bridge substructure." J. Bridge Eng., 11(3), 359–370.

VITA

Omar Idris Abdelkarim was born on July 15th, 1984 in Sharqia, Egypt. In 2006, he received his Bachelor of Science in Civil Engineering with grade of excellent with honor from Ain Shams University, Cairo, Egypt. After graduation with a Bachelor's degree, he worked as a lecturer assistant in Ain Shams University for six years. He taught a course of "Design of concrete structures." He also worked as a bridge designer as a *part time* for "Dar Alhandasah Shair and Partners" for five years. He designed, reviewed, and evaluated a number of infrastructure projects to be constructed in different countries (e.g., Saudi Arabia, Qatar, Kuwait, etc.). In 2010, he received his Master of Science in Civil Engineering in particular of Structural Engineering from Ain Shams University. During his Master research, he conducted a study on strengthening of concrete segmental bridge girders using fiber reinforced polymer laminates. In December 2015, he received his Doctor of Philosophy (Ph.D.) from the Missouri University of Science and Technology.